

Wandering in the Background:
A Cosmic Microwave Background Explorer

by

Wayne Hu

A.B. (Princeton University) 1990

M.A. (University of California at Berkeley) 1992

A thesis submitted in partial satisfaction of the
requirements for the degree of

Doctor of Philosophy

in

Physics

in the

GRADUATE DIVISION

of the

UNIVERSITY of CALIFORNIA at BERKELEY

Committee in charge:

Professor Joseph Silk, Chair

Professor Marc Davis

Professor Hyron Spinrad

1995

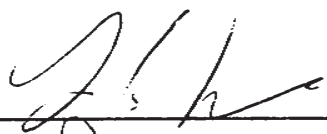
Wandering in the Background:
A Cosmic Microwave Background Explorer


by
Wayne Hu

Doctor of Philosophy in Physics
University of California at Berkeley
Professor Joseph Silk, Chair

We develop and examine the principles governing the formation of distortions in the cosmic microwave background. Perturbations in the frequency or spectral distribution of the background probe the thermal history of the universe, whereas those in the angular temperature distribution probe its dynamics and geometry. Stressing model independent results, we show how the microwave background can be used to extract information on the mass density, vacuum density, baryon content, radiation content, expansion rate and some aspects of structure formation in the universe. To address these issues, we develop elements of relativistic kinetic and perturbation theory as they become necessary for the description of the particle and gravitational interactions of the photons. Subtle issues such as fluctuation representation, or gauge, normal mode analysis in an open geometry, and second order effects are considered in detail. Employing analytic and numerical results, we construct anisotropies in a critical, open, and cosmological constant universe with adiabatic and/or isocurvature initial conditions allowing for possible early reionization. We find that anisotropy formation is a simple process governed by the Compton scattering of photons off electrons and their gravitational coupling to the other particle species in the universe.

The thesis of Wayne Hu is approved:

 5/17/95

Chair  Date 5/16/95

 5/16/95
Date

University of California, Berkeley

1995

Wandering in the Background:
A Cosmic Microwave Background Explorer

© copyright 1995

by

Wayne Hu

To Chuang-tzu,

Said the disciple, "After I heard your words, one year and I ran wild, two years and I was tame, three years and positions interchanged, four years and things settled down, five years and things came to me . . ."

-Chuang-tzu, 27

From Chuang-tzu,

I hear that there is a sacred tortoise which has been dead for three thousand years. His Majesty keeps it wrapped up in a box at the top of the hall in the ancestral shrine. Would this tortoise rather be dead, to be honored as preserved bones, or would it rather be alive and dragging its tail in the mud... Away with you! I shall drag my tail in the mud.

-Chuang-tzu, 17

Contents

List of Figures	viii
List of Tables	x
Preface	xi
Acknowledgements	xiii
1 Overview	1
1.1 Cosmological Background	1
1.1.1 Perfection and Its Implications	2
1.1.2 Imperfection and Its Applications	4
1.2 Anisotropy Formation	6
1.2.1 Acoustic Oscillations	8
1.2.2 Baryon Drag	10
1.2.3 Doppler Effect	11
1.2.4 Potential Evolution	11
1.2.5 Photon Diffusion Damping	14
1.2.6 Integrated Sachs-Wolfe Effect	15
1.2.7 Projection Effects	16
1.3 Anisotropy Spectrum	18
1.4 Robustness to Initial Conditions	20
1.5 Reionization	22
2 The Boltzmann Equation	25
2.1 Gravitational Interactions	26
2.1.1 Metric Fluctuations	26
2.1.2 Gravitational Redshift and Dilation	27
2.1.3 Collisionless Brightness Equation	30
2.2 Compton Scattering	31
2.2.1 Collision Integral	32
2.2.2 Individual Terms	35
2.2.3 Generalized Kompaneets Equation	40
2.2.4 Collisional Brightness Equation	41

3	Thermalization and Spectral Distortions	42
3.1	Collision Equations	43
3.1.1	Compton Scattering Revisited	43
3.1.2	Electron Temperature Evolution	44
3.1.3	Bremsstrahlung and Double Compton Scattering	45
3.2	Thermalization Optical Depths and Rates	46
3.2.1	Comptonization	47
3.2.2	Chemical Potential Formation	52
3.2.3	Blackbody Formation	54
3.3	Low Frequency Evolution	56
3.3.1	Chemical Potential Era	58
3.3.2	Chemical Potential Freeze Out	60
3.3.3	Negative Chemical Potentials	63
3.3.4	Balanced Injection	63
3.4	High Frequency Evolution	65
3.4.1	Analytic Approximations	65
3.4.2	Numerical Results	68
3.5	Comparisons and Constraints	72
3.5.1	Observational Data	72
3.5.2	Constraints on Decaying Particles	73
3.5.3	Dissipation of Acoustic Waves	75
4	Multifluid Perturbation Theory	80
4.1	Normal Mode Decomposition	81
4.1.1	Laplacian Eigenfunctions	81
4.1.2	Radial Representation	82
4.1.3	Completeness and Super Curvature Modes	83
4.1.4	Higher Angular Functions	86
4.2	Newtonian Gauge Evolution	87
4.2.1	Metric Fluctuations	87
4.2.2	Conservation Equations	88
4.2.3	Total Matter and Its Components	92
4.2.4	Radiation	93
4.2.5	Matter	94
4.2.6	Einstein Equations	95
4.3	Gauge	96
4.3.1	Gauge Transformations	98
4.3.2	Newtonian Gauge	99
4.3.3	Synchronous Gauge	100
4.3.4	Total Matter Gauge	103
4.3.5	Hybrid Formulation	104

5	Perturbation Evolution	106
5.1	Superhorizon Evolution	107
5.1.1	Total Matter Equation	107
5.1.2	General Solution	108
5.1.3	Initial Conditions	111
5.1.4	Component Evolution	113
5.1.5	Discussion	116
5.2	Subhorizon Evolution before Recombination	116
5.2.1	Analytic Acoustic Solutions	117
5.2.2	Driven Acoustic Oscillations	120
5.2.3	Damped Acoustic Oscillations	123
5.3	Matter Evolution after Recombination	126
5.3.1	Compton Drag	126
5.3.2	Reionization in Isocurvature Models	128
6	Primary Anisotropies	130
6.1	Overview	130
6.1.1	Anisotropy Sources	131
6.1.2	Projection and Free Streaming	132
6.1.3	Mathematical Description	133
6.2	Sachs-Wolfe Effect	134
6.2.1	Ordinary Sachs-Wolfe Effect	136
6.2.2	Integrated Sachs-Wolfe Effect	138
6.2.3	Adiabatic $\Omega_0 = 1$ models	140
6.2.4	Adiabatic Λ Models	143
6.2.5	Adiabatic Open Models	146
6.2.6	Isocurvature Λ and Open Models	148
6.3	Acoustic Peaks	151
6.3.1	Mathematical Description	151
6.3.2	Location of the Peaks	153
6.3.3	Heights of the Peaks	155
6.3.4	Diffusion Damping at Recombination	156
7	Secondary Anisotropies	160
7.1	Linear Contributions	161
7.1.1	Reionization Damping	161
7.1.2	<i>COBE</i> Constraints on PIB Models	163
7.1.3	Anisotropy Regeneration	167
7.1.4	Cancellation Damping	171
7.1.5	Minimal PIB Anisotropies	173
7.2	Second Order Contributions	175
7.2.1	Generalized Doppler Effect	175
7.2.2	Vishniac Effect	177
7.2.3	Other Second Order Effects	180
7.3	Beyond Perturbation Theory: A Survey	183

7.4	Final Thoughts	185
A	Toward Higher Accuracy: A CDM Example	187
A.1	Refining the Gravitational Potentials	188
A.1.1	Neutrino Anisotropic Stress	188
A.1.2	Small Scale Radiation Feedback	191
A.2	Analytic Construction to 5% Accuracy	193
A.2.1	Explicit Tight Coupling Solutions	193
A.2.2	Recombination Revisited	195
A.2.3	Analytic Results	197
A.3	Toward 1% Accuracy	200
A.3.1	Polarization Damping	200
A.3.2	Helium Recombination	204
A.3.3	Gravity Waves	205
A.3.4	Massive Neutrinos	206
B	Useful Quantities and Relations	209
B.1	FRW Parameters	209
B.2	Time Variables	211
B.2.1	Scale Factor and Redshift	211
B.2.2	Conformal Time	213
B.2.3	Coordinate Time	213
B.2.4	Growth Function	215
B.2.5	Optical Depth	215
B.3	Critical Scales	216
B.3.1	Physical Scales	216
B.3.2	Angular Scales	217
B.4	Normalization Conventions	219
B.4.1	Power Spectra	219
B.4.2	Anisotropies	220
B.4.3	Large Scale Structure	222
B.5	Symbol Index	223
	Bibliography	226

List of Figures

1.1	FIRAS Spectral Measurement	2
1.2	DMR Anisotropy Map	3
1.3	Anisotropies: Theory and Experiment	7
1.4	Acoustic Oscillations	9
1.5	Differential Redshift and Dilation	12
1.6	Photon Diffusion	14
1.7	Projection Effect	17
1.8	Total Anisotropy Spectrum	19
1.9	Cancellation Mechanism	21
1.10	Vishniac Mechanism	23
2.1	Scattering Geometry	32
3.1	Compton- y distortion	48
3.2	Thermalization from y to μ	50
3.3	Critical Frequencies and Redshifts	57
3.4	Low Frequency Evolution	59
3.5	Low Frequency Spectrum	61
3.6	Negative Chemical Potentials	62
3.7	Balanced Injection	64
3.8	Positive Chemical Potential Evolution	68
3.9	Negative Chemical Potential Evolution	69
3.10	Comparison with Observational Data	71
3.11	Rayleigh-Jeans Baryon Dependence	73
3.12	Particle Decay Constraints	74
3.13	Diffusion Dissipation and Limits on n	78
4.1	Open Radial Eigenfunctions	85
4.2	Gauge Ambiguity	98
5.1	Large Scale Adiabatic Evolution	112
5.2	Large Scale Isocurvature Evolution	115
5.3	Acoustic Oscillations	119
5.4	Small Scale Isocurvature Evolution	124

5.5	Compton Drag and Standard Recombination	127
5.6	Compton Drag and Reionization	128
6.1	Sachs-Wolfe Evolution	135
6.2	ISW Effect	139
6.3	$\Omega_0 = 1$ Radiation Transfer Function	141
6.4	$\Omega_0 = 1$ Early ISW Spectrum	142
6.5	Λ Adiabatic Radiation Transfer Function	143
6.6	Λ Late ISW Spectrum	144
6.7	Analytic Decomposition: Adiabatic Models	146
6.8	Open Adiabatic Radiation Transfer Function	147
6.9	Open Adiabatic Spectrum	148
6.10	Isocurvature Radiation Transfer Function	149
6.11	Analytic Decomposition: Isocurvature Models	150
6.12	Aliasing Effect	151
6.13	The m Dependence of Isocurvature Spectra	152
6.14	Fluctuations at Last Scattering	153
6.15	Acoustic Peak Location	154
6.16	Acoustic Peak Heights	156
6.17	Diffusion Damping	157
6.18	Damping Scale	158
7.1	Reionization Damping Evolution	162
7.2	Reionization Damped Spectrum	163
7.3	PIB Matter Power Spectrum	164
7.4	Constraints on PIB Models	165
7.5	First Order Doppler Effect	170
7.6	Cancellation Damping	172
7.7	Minimal PIB Anisotropies	174
7.8	Vishniac Effect	178
7.9	PIB Vishniac Power Spectrum	179
7.10	Quadratic Doppler Effect	182
A.1	Gravitational Potential Evolution	192
A.2	Visibility Function	195
A.3	Analytic Separation of Effects	198
A.4	Comparison of Analytic and Numerical Results	199
A.5	Polarization Generation	200
A.6	Polarization Damping	202
A.7	Helium Recombination	204
A.8	Gravity Wave Spectrum	205
A.9	Number of Massless Neutrinos	207

List of Tables

B.1	Physical Constants and Conversion Factors	210
B.2	Critical Redshifts	212
B.3	Anisotropy Data Points	221
B.4	Commonly Used Symbols	225

Preface

If you have a great tree and think it's a pity it's so useless, Why not plant it in the middle of nowhere in the wilds which spread out, and go rambling away aimlessly at its side, wander around and fall asleep in its shade?

–Chuang-tzu, 1¹

A mere three years ago when I started work on the cosmic microwave background (CMB) with Joe Silk, anisotropies had not yet been discovered. The theory of anisotropy formation was considered arcana and earned barely a mention in the standard textbooks of the time. With the number of detections now in the double digits, CMB anisotropies have joined spectral distortions, light element abundances, and large scale structure measurements as some of our most powerful observational probes of cosmology. The depth that even the interested non-specialist needs to understand the principles governing fluctuations in the CMB has consequently increased. This work begins the task of assembling the material necessary for a modern understanding of the CMB. Of course, the whole task is beyond the scope of a 200 some page dissertation assembled in a month's time! I make no claims of completeness. Rather, I develop a handful of general principles that seem to me may have lasting interest. As a consequence, I do not treat in any detail CMB constraints on specific cosmological models, except where necessary to illustrate general points. Moreover, important issues of statistical analysis related to the current generation of experiments are not covered here. I happily refer the interested reader to the excellent “companion thesis” by Emory Bunn [21].

Chapter 1 is provided as a qualitative and hopefully intuitive introduction to the subject. The formal development begins in chapter 2 with relativistic kinetic theory and continues in chapter 4 with relativistic perturbation theory. Readers who are familiar with these subjects should skip to their applications: spectral distortions in chapter 3 and density perturbation evolution in chapter 5. Given its importance, anisotropy formation occupies the rest of this work. Again, I stress robust features that may survive the current generation of models. I discuss how these features may be used to probe general cosmological issues such as the matter content, dynamics, and geometry of the universe. Advanced topics such as radiation feedback effects, polarization, and the details of recombination are saved for

¹Translations of the *Chuang-tzu* throughout are adapted from [65].

Appendix A. Appendix B gathers together useful material scattered throughout the text.

Some topics are covered at greater depth than others. Some will be of more interest to the specialist than to the general cosmologist. This thesis is nowhere near as homogeneous as the subject it purports to study (though it may be as directionless)! Wander through its pages and perhaps you will find it of some use – if nothing else, for its soporific qualities.

Wayne Hu

Berkeley, California

April 1995

Acknowledgments

First and foremost I would like to thank my advisor Joe Silk for his constant flow of ideas, support and encouragement. He introduced me to all the right people and helped me gain exposure in the field. I would also like to thank the whole Berkeley CMB group. This thesis has arisen in large part through discussions and collaborations with them. Specifically, Ted Bunn deserves special credit for putting up with me as an officemate in general and my dumb statistical questions in particular. Douglas Scott started me out in the anisotropy game and taught me a good part of my working knowledge of astronomy and cosmology. Naoshi Sugiyama devoted much time and effort to share with me his expertise in the CMB. Our many fruitful collaborations form the basis of the latter half of this work. Martin White lent his critical skills in helping me develop and refine the material here. I would also like to thank Naoshi and Martin for allowing me to use results from their Boltzmann codes. Marc Davis and Hy Spinrad provided me with the ideal set of comments on a draft of this thesis.

My officemates Lexi Moustakas and Dan Stevens provided me with a daily dose of entertaining conversations on a variety of off-the-wall subjects. Dan, as the patron saint of coffee, also supplied me with much needed caffeine during the writing of this work. Matt Craig and David Schlegel endured many rehearsals of my “cute pictures” talk. David Weinberg earns my special thanks for giving that talk more credit than it probably deserved! Marc Kamionkowski and David Spergel urged me to aim high. Max Tegmark threatened me with monetary gain had I *not* finished this work on time. Dan Plonsey saved one of my chapters from encryption hell. Eric Gawiser proofread several chapters. Ann Takizawa, who knows everything there is to know about UC Berkeley, saved me on many occasions from missing important deadlines.

Tom Donnelly taught me that even physicists can “get huge.” The I-house bunch, especially Justin Bendich, Dan Krejsa and Raymond Yee, provided memorable dinner conversations and an outlet for the frustrations of the early years. Even more so than his physics acumen, Dan’s baking skills made him an ideal roommate. Via email, Mike Aguilar and the rest of the college crew watched my progress from a writer of hat-obsessed bad poetry to jargon-filled bad prose. Finally, Meow Vatanatumrak selectively *impeded* progress on this work. Her diabolical tactics helped me better enjoy my stay at Berkeley.

Chapter 1

Overview

Is the azure of the sky its true color? Or is it that the distance into which we are looking is infinite? The P'eng never stops flying higher till everything below looks the same as above: heat-hazes, dust-storms, the breath which living things blow at each other ...

—Chuang-tzu, 1

1.1 Cosmological Background

With the discovery of the cosmic microwave background (CMB) by Penzias and Wilson in 1965 [128], modern cosmology was born. Long the realm of armchair philosophers, the study of the origins and evolution of the universe became a physical science with falsifiable theories. As light from an earlier epoch, the CMB provides evidence that has proven many a cosmological theory wrong. Still, cosmology has remained a data-starved field until quite recently. Unlike its brethren disciplines, experimentation is not possible. Given access to this one universe alone, one must piece together the principles of its formation out of what observations of it are possible. The task is made even more challenging due to the enormous range of physical and temporal scales involved.

We are now at the threshold of a new era in cosmology. With telescopes probing ever earlier epochs and larger volumes, we are making rapid progress in improving the quantity and quality of data. Cosmology is at last becoming a precision science. Once again the CMB is taking a central place in this transition. Launched in late 1989, the *COBE* satellite ushered in the era of precision cosmology. It has revealed in the CMB a perfect thermal or blackbody spectrum of temperature $T_0 = 2.726 \pm 0.010\text{K}$ (95% CL), with

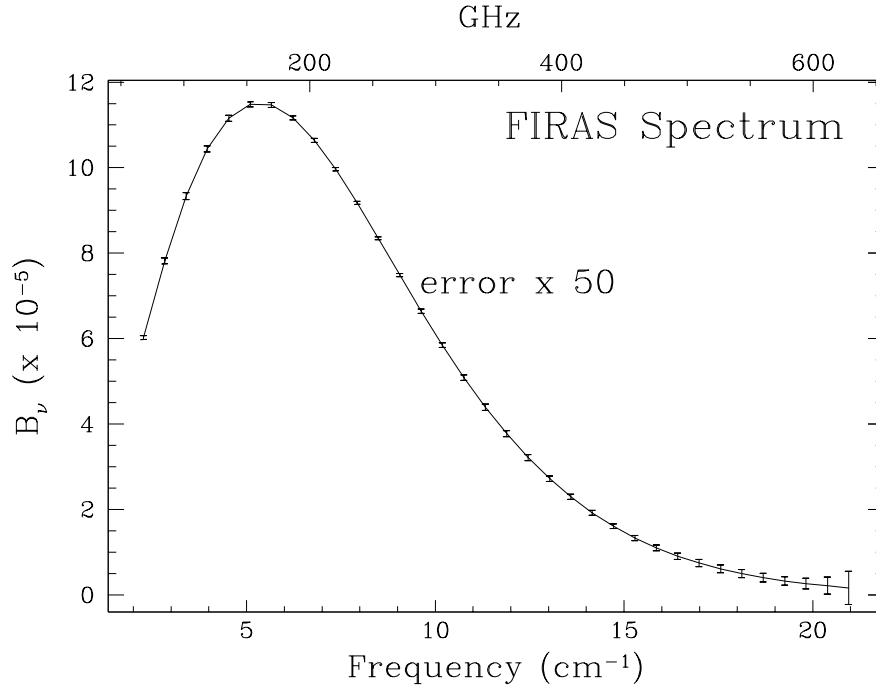


Figure 1.1: FIRAS Spectral Measurement

To the precision of the *COBE* FIRAS instrument [116], the CMB spectrum is a perfect blackbody with a maximum deviation of no more than 3×10^{-4} and a noise weighted rms deviation of under 5×10^{-5} of its peak intensity. No spectral distortions have been measured to date excluding nearly all options for its formation except in the early stages of a hot big bang. Plotted here is the intensity in $\text{ergs cm}^{-2} \text{s}^{-1} \text{sr}^{-1} \text{cm}$.

deviations no more than several parts in 10^4 [116], and temperature anisotropies at the level of one part in 10^5 [153].

1.1.1 Perfection and Its Implications

Observe the void – its emptiness emits a pure light.

–Chuang-tzu, 4

The cosmic microwave background spectrum and anisotropy: near perfection and slight imperfection. The implications of the former run deep; the applications of the latter are broad. A thermal radiation background is a definite and almost unique prediction of the big bang cosmology. Why is the spectrum thermal at 2.7K, a much lower temperature than most astronomical matter in the universe? Let us recall the basic facts and premises upon which the big bang model is built. Light from distant galaxies is redshifted in proportion to

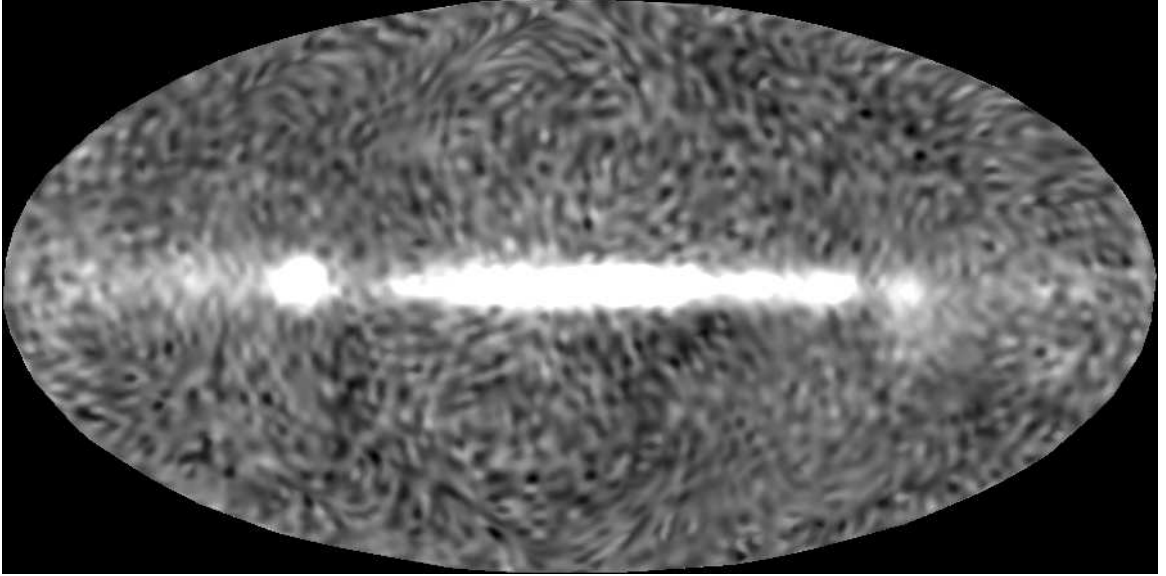


Figure 1.2: DMR Anisotropy Map

Anisotropies in the CMB as detected by the *COBE* DMR experiment at an rms level of $\Delta T/T = \mathcal{O}(10^{-5})$. While the raw data set is noisy and suffers galactic contamination (bright center band), filtering reveals a detection of high significance and importance to our understanding of structure formation in the universe. Map courtesy of E. Bunn.

their distance. In the big bang model, this is interpreted as a consequence of the universal expansion of the universe. Due to the light travel time, distant sources emitted their light long ago when the universe was smaller. During the expansion, the wavelengths of photons are stretched and particle number densities drop leading to the low temperature and photon density observed in the background today. Conversely, extrapolating backwards in time, we infer that the universe began in a hot dense state. As we discuss in more detail in §3, at sufficiently high temperatures interactions between particles were rapid enough to bring the universe into a state of thermal equilibrium. This and the fact that adiabatic cooling from the expansion preserves the thermal spectrum explains the blackbody nature of the observed spectrum (see Fig. 1.1). No other model for cosmology yet proposed can account for the stunningly thermal spectrum. Even in the big bang model, the lack of distortions to the spectrum provides serious constraints on physical and astrophysical processes that could have occurred between the thermalization redshift $z \simeq 10^7$ and the present, *i.e.* very nearly the *whole* history of the universe.

The second pillar upon which the big bang model stands is the large scale homogeneity and isotropy of the universe. Originally only a hypothesis based on simplicity and a Copernican desire not to occupy a preferred position in the universe, this “cosmological principle” finds its validation most dramatically in the radio source catalogue of Gregory and Condon [66] and in the extreme isotropy of the CMB. Aside from a dipole anisotropy of $3.343 \pm 0.016\text{mK}$ (95% CL) [152], almost certainly due to the Doppler effect from our own motion, the CMB is isotropic at the level of one part in 10^5 .

In fact, the high degree of isotropy has long been a puzzle to cosmologists. The CMB last interacted with the matter through Compton scattering as long ago as redshift $z \simeq 10^3$, when the photons no longer had the energy to keep hydrogen photoionized, and no later than z of a few tens if hydrogen was ionized by some external source. Our extrapolation backwards to this early time tells us that the patches of sky off which the CMB last scattered should not have been in causal contact at that time. This seemingly acausal isotropy of the CMB temperature is called the *horizon problem*. The most promising solution to date, called the inflationary scenario, postulates an early phase of rapid expansion that separates originally causally connected regions by the vast distances necessary to account for the large scale isotropy of the CMB. Alternatively, it may be just a boundary condition of the universe imposed by unknown physics at the Planck epoch.

Potentially more troubling to cosmologists is the fact that the universe at small scales is manifestly inhomogeneous as the distribution of galaxies and indeed our own existence implies. In the big bang model, perturbations grow by gravitational instability slowly due to the expansion, *i.e.* power law rather than exponential growth (see §4, §5). Even though the CMB bears the imprint of an earlier and less evolved epoch, fluctuations must be present at the $10^{-6} - 10^{-5}$ level to be consistent with the simple gravitational instability model. The announcement by the *COBE* DMR group of the first detection of CMB anisotropies was thus met with expressions of relief and elation by cosmologists.

1.1.2 Imperfection and Its Applications

Said Hui-Shih to Chuang-tzu: ‘This talk of yours is big but useless.’

–Chuang-tzu, 1

As is often the case in physics, the deviations are of greater practical interest than the mean. While measurements of the thermal nature and isotropy of the CMB reveal strong support for the general hot big bang scenario, they are shed no light upon the details of

the cosmological model. Anisotropies on the other hand bear the imprint, filtered through the dynamics and geometry of the expanding universe, of the fluctuations which eventually led to structure formation in the universe. CMB anisotropies can therefore shed light on not only the mysteries of structure formation but also such fundamental quantities as the expansion rate, matter content and geometry of the universe. Let us briefly review the current status of some of these unresolved issues.

Hubble's law states that the observed redshift scales with distance as $z = H_0 d$ due to the uniform expansion. Measurement of the proportionality constant, the so-called Hubble constant, is notoriously difficult due to the need to obtain absolute distances to galaxies. The uncertainty is usually parameterized as $H_0 = 100h \text{ km s}^{-1} \text{ Mpc}^{-1}$ where observations roughly require $0.5 \gtrsim h \gtrsim 1$. High values of the Hubble constant $h \simeq 0.8$ seem currently favored by many distance scale calibrations (see [89] for a review and [56] for recent advances), but the issue is far from settled (see *e.g.* [139]). Because H_0 sets the expansion time scale $H_0^{-1} \simeq 10h^{-1} \text{ Gyr}$, its measurement is crucial in determining the age of the universe. Through the theory of stellar evolution, globular clusters are inferred to be as old as $14 \pm 2 \text{ Gyr}$ [140, 141] which may lead to an age crisis if H_0 turns out to be in the upper range of modern measurements.

How acute the age crisis might be depends on the second major source of dispute: the density of the universe. Because mass tends to decelerate the expansion, a higher energy density implies a younger universe. The mass is usually parameterized by Ω_0 which is the energy density in units of the critical density $\rho_{crit} = 3H_0^2/8\pi G = 1.879 \times 10^{-29} h^2 \text{ g cm}^{-3}$. There is also the possibility that vacuum energy and pressure, *i.e.* the cosmological constant Λ , can provide an acceleration of the expansion leading to an arbitrarily old universe. A universe with $\Omega_0 + \Omega_\Lambda = 1$ is special in that it is the only one that is spatially flat. Dynamical measurements of the mass in the halo of galaxies from their velocity dispersion implies that $\Omega_0 \gtrsim 0.1 - 0.3$. The inequality results from the fact that these measurements cannot probe the amount of mass that is not clustered with galaxies. Large scale velocity fields can test larger regions and though the situation to date is far from clear, current measurements tend to yield slightly higher values for Ω_0 (see *e.g.* [156] for a recent review).

Let us examine the constituents of the total density. Luminous matter in the form of stars in the central part of galaxies only accounts for $\Omega_* \simeq 0.004$ of the critical density. Compared with dynamical measurements, this indicates that most of the matter in the universe is dark. On the other hand, the CMB energy density $\Omega_\gamma h^2 = 2.38 \times 10^{-5} \Theta_{2.7}^4$,

where $\Theta_{2.7} = T_0/2.7\text{K}$. Although negligible today, in the early universe it increases in importance relative to the matter energy density ρ_m since $\rho_\gamma/\rho_m \propto 1+z$ due to the redshift. With the photon density thus fixed through the CMB temperature, primordial nucleosynthesis and observations of the light element abundances imply that the baryon fraction is low $\Omega_b h^2 = 0.01 - 0.02$ [151, 171]. A significant amount of non-baryonic dark matter is apparently present in the universe. The amount and nature of dark matter in the universe has significant consequences for structure formation. The most crucial aspect of its nature for these purposes is the mass of its constituent particles. Collisionless dark matter, unlike baryonic matter, does not suffer dissipative processes. Thus the particle mass determines whether their rms velocity is high enough to escape gravitational collapse.

CMB anisotropies can provide information on all these fundamental issues and more. Since the issue of anisotropy formation is of such central importance, its systematic development occupies the greater part of this work §4–7. Gravitational and Compton coupling of the CMB represent intertwining themes that recur throughout these chapters. It is therefore useful to give here a brief exposition of these concepts, their importance for anisotropy formation, and their implications for cosmology [85].

1.2 Anisotropy Formation

*Words are for catching ideas; once you've caught the idea, you can forget about the words.
Where can I find a man who knows how to forget about words so that I might have a few words
with him?*

–Chuang-tzu, 26

Fluctuations in the total matter density, which includes decoupled species such as the neutrinos and possibly collisionless dark matter, interact with the photons through the gravitational potentials they create. These same fluctuations grow by gravitational attraction, *i.e.* infall into their own potential wells, to eventually form large scale structure in the universe. Their presence in the early universe is also responsible for anisotropy formation.

Before redshift $z_* \simeq 1000$, the CMB was hot enough to ionize hydrogen. Compton scattering off electrons, which are in turn linked to the protons through Coulomb interactions, strongly couples the photons to the baryons and establishes a photon-baryon fluid. Photon pressure resists compression of the fluid by gravitational infall and sets up acoustic oscillations. At z_* , recombination produces neutral hydrogen and the photons last scat-

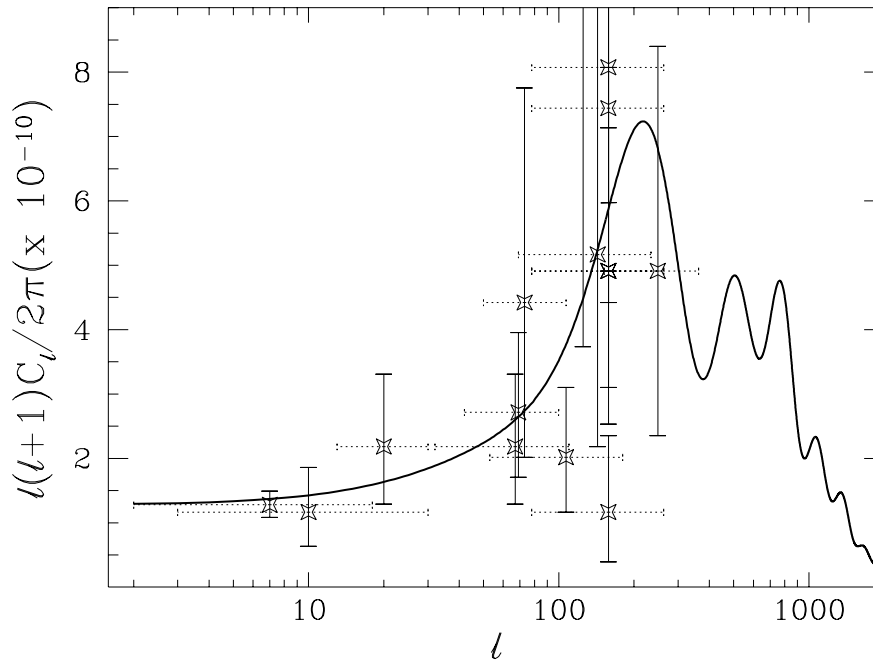


Figure 1.3: Anisotropies: Theory and Experiment

Anisotropy data of current CMB experiments from Tab. B.3 compiled by [146]. Dotted horizontal “error bars” are the half power angular range of the experiment. Overplotted is the predicted anisotropy power spectrum C_ℓ in a typical model: standard CDM with $\Omega_0 = 1$, $h = 0.5$, $\Omega_B = 0.05$, scale invariant scalar initial fluctuations, and arbitrary normalization. The corresponding angle on the sky is approximately $100/\ell$ degrees.

ter. Regions of compression and rarefaction at this epoch represent hot and cold spots respectively. Photons also suffer gravitational redshifts from climbing out of the potentials on the last scattering surface. The resultant fluctuations appear to the observer today as anisotropies on the sky. By developing the simple picture outlined above in greater detail, we show how realistic anisotropies such as those depicted in Fig 1.3 are formed.

Notation

Although sky maps such as Fig. 1.2 are visually impressive, the anisotropy must be analyzed statistically. For gaussian fluctuations, the statistical content is encapsulated in the two point temperature correlation function, or equivalently its angular decomposition into Legendre moments C_ℓ . In Fig. 1.3, we show a typical prediction for the anisotropy power spectrum C_ℓ compared with the current state of observations.

Predictions for C_ℓ are obtained by tracking the evolution of temperature fluctu-

ations. Their equations of motion take on a simple form when decomposed into normal modes. These are plane waves for a flat geometry, referred to in this chapter as such even when considering their open geometry generalization (see §4.1.1 and [71, 175]). We represent temperature fluctuations in Newtonian form, which simplifies concepts such as infall and redshift, by defining them on the spatial hypersurfaces of the conformal Newtonian gauge (see §4.3).

Under the gravitational force F , a temperature perturbation $\Theta_0 = \Delta T/T$ of comoving wavenumber k evolves almost as a simple harmonic oscillator before recombination [82] $(1 + R)\ddot{\Theta}_0 + \frac{k^2}{3}\Theta_0 \simeq F$. The overdots represent derivatives with respect to conformal time $\eta = \int(1+z)dt$ with $c = 1$ and $R = 3\rho_b/4\rho_\gamma = 3.0 \times 10^4(1+z)^{-1}\Omega_b h^2$ accounts for the baryonic contribution to the effective mass of the oscillator. Notice that the restoring force from photon pressure is independent of the baryon content. The frequency of the oscillator is constructed out of these quantities as $\omega = kc_s$ where the sound speed c_s , which measures the resistance of the fluid to compression, is $c_s \equiv \dot{p}/\dot{\rho} = 1/\sqrt{3(1+R)}$. The oscillator equation can thus be rewritten as $\ddot{\Theta}_0 + k^2 c_s^2 \Theta_0 \simeq F/(1+R)$.

Let us now consider the gravitational driving force $F/(1+R) \simeq -k^2\Psi/3 - \ddot{\Phi}$, where Ψ is the Newtonian gravitational potential, obtained from density fluctuations via the generalized Poisson equation, and $\Phi \simeq -\Psi$ is the perturbation to the space curvature. They also represent plane wave fluctuations in the time-time and space-space metric components respectively. The sign convention reflects the fact that overdensities create positive space curvature and negative potentials, *i.e.* potential wells. In real space though, a single plane wave represents both overdense *and* underdense regions. We use the former to guide intuition since the distinction is only in sign.

1.2.1 Acoustic Oscillations

Let us first consider temperature fluctuations before recombination in the case of a *static* potential [48, 15, 92]. Although only appropriate for a universe which has *always* been matter dominated, it illustrates the general nature of the acoustic oscillations. In this case, $F = -k^2(1+R)\Psi/3$ and represents the usual driving force of gravity that leads to infall into potential wells. Since big bang nucleosynthesis implies that the baryon density is low, $\Omega_b h^2 \simeq 0.01 - 0.02$, as a first approximation assume that $R \ll 1$ and the photons completely dominate the fluid $c_s \simeq 1/\sqrt{3}$.

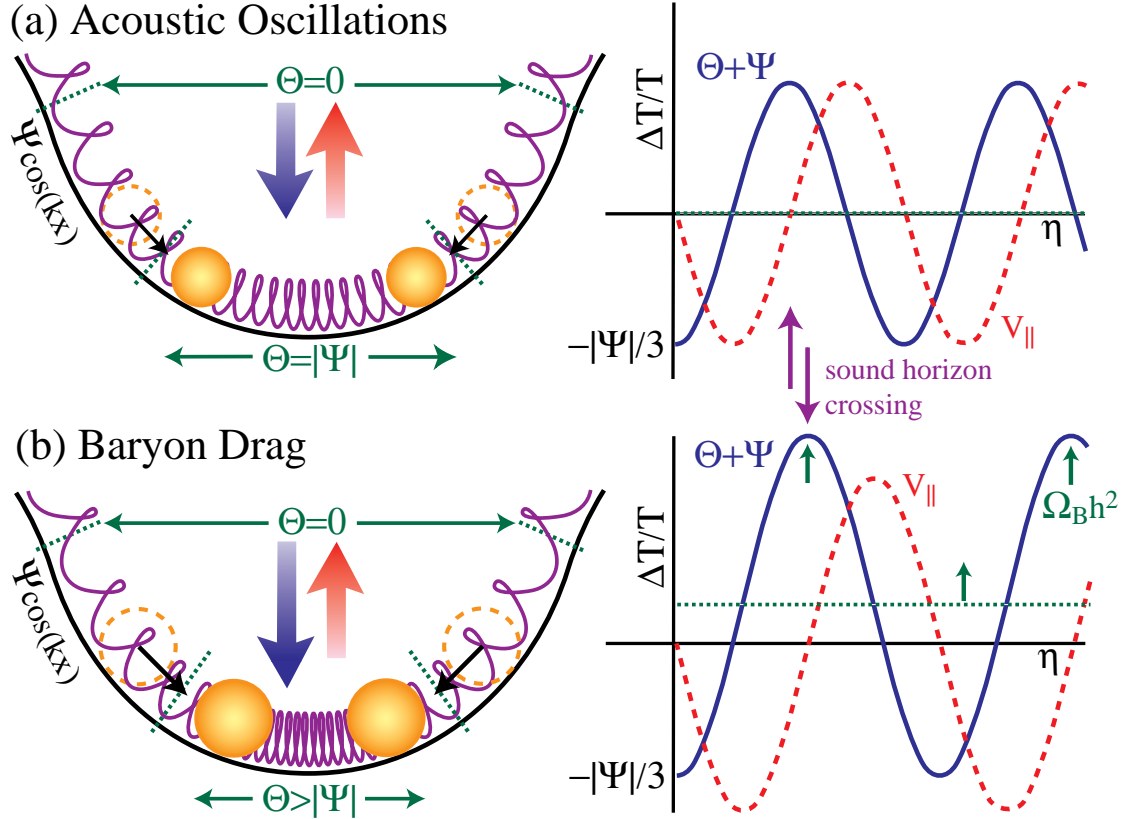


Figure 1.4: Acoustic Oscillations

(a) Photon-dominated system. Fluid compression through gravitational infall is resisted by photon pressure setting up acoustic oscillations. Displayed here is a potential well in real space $-\pi/2 \lesssim kx \lesssim \pi/2$. Gravity displaces the zero point so that at the bottom of the well, the temperature is $\Theta_0 = |\Psi| = -\Psi$ at equilibrium with $\Psi/3$ excursions. This displacement is exactly cancelled by the redshift Ψ a photon experiences climbing out from the bottom of the potential well. Velocity oscillations lead to a Doppler effect 90 degrees phase shifted from the temperature perturbation. (b) Photon-baryon system. Baryons increase the gravitating mass, causing more infall and a net zero point displacement, even after redshift. Temperature crests (compression) are enhanced over troughs (rarefaction) and velocity contributions.

Gravitational infall compresses the fluid until resistance from photon pressure reverses the motion. Since the gravitational force is constant in this case, it merely shifts the zero point of the oscillation to $\Theta_0 = -\Psi$. To determine the amplitude of the oscillations, we must first fix the initial conditions. The relation between the matter density fluctuations and the potential $\delta_m(0) = -2\Psi$ is fixed by demanding consistency with the Poisson and Euler equations. Let us assume adiabatic initial conditions for the photons $\Theta_0(0) = \frac{1}{3}\delta_m(0) = -\frac{2}{3}\Psi$ and $\dot{\Theta}_0(0) = 0$ (see Fig. 1.4a). In this case, the photons follow the matter, making the temperature higher inside a potential well. The effective initial displacement of $\Theta_0(0) + \Psi = \frac{1}{3}\Psi$ then evolves as $\Theta_0(\eta) = \frac{1}{3}\Psi\cos(kc_s\eta) - \Psi$. At last scattering η_* , the photons decouple from the baryons and stream out of potential wells suffering gravitational redshifts equal to Ψ . We thus call $\Theta_0 + \Psi$ the *effective* temperature fluctuation. Here the redshift exactly cancels the zero point displacement since gravitational infall and redshift are one and the same for a photon-dominated system.

The phase of the oscillation at last scattering determines the effective fluctuation. Since the oscillation frequency $\omega = kc_s$, the critical wavenumber $k = \pi/c_s\eta_*$ is essentially at the scale of the *sound horizon* $c_s\eta_*$ (see Fig 1.4). Larger wavelengths will not have evolved from the initial conditions and possess $\frac{1}{3}\Psi$ fluctuations after gravitational redshift. This combination of the intrinsic temperature fluctuation and the gravitational redshift is the well known Sachs-Wolfe effect [138]. Shorter wavelength fluctuations can be frozen at different phases of the oscillation. Since fluctuations as a function of k go as $\cos(kc_s\eta_*)$ at last scattering, there will be a harmonic series of temperature *fluctuation* peaks with $k_m = m\pi/c_s\eta_*$ for the m th peak. Odd peaks thus represent the compression phase (temperature crests), whereas even peaks represent the rarefaction phase (temperature troughs), inside the potential wells.

1.2.2 Baryon Drag

Though effectively pressureless, the baryons still contribute to the inertial and gravitational mass of the fluid $m_{\text{eff}} = 1 + R$. This changes the balance of pressure and gravity as baryons drag the photons into potential wells. As the baryon content R is increased, gravitational infall leads to greater compression of the fluid, *i.e.* a further displacement of the oscillation zero point (see Fig. 1.4b). Since the redshift is not affected by the baryon content, this relative shift remains after last scattering to enhance all peaks from compression over

those from rarefaction. If the baryon photon ratio R were constant, $\Theta(\eta) + \Psi = \frac{1}{3}\Psi(1 + 3R)\cos(kc_s\eta) - R\Psi$, with compressional peaks a factor of $(1 + 6R)$ over the $R = 0$ case. In reality, the effect is reduced since $R \rightarrow 0$ at early times.

Finally the *evolution* of the effective mass has a effect of its own. In classical mechanics, the ratio of energy $E = \frac{1}{2}m_{\text{eff}}\omega^2 A^2$ to frequency of an oscillator ω is an adiabatic invariant. Thus for the slow changes in $\omega \propto (1 + R)^{-1/2}$, the amplitude of the oscillation varies as $A \propto (1 + R)^{-1/4}$. Since $R(\eta_*) = 30\Omega_b h^2 \lesssim 1$ at recombination, this is ordinarily not a strong effect.

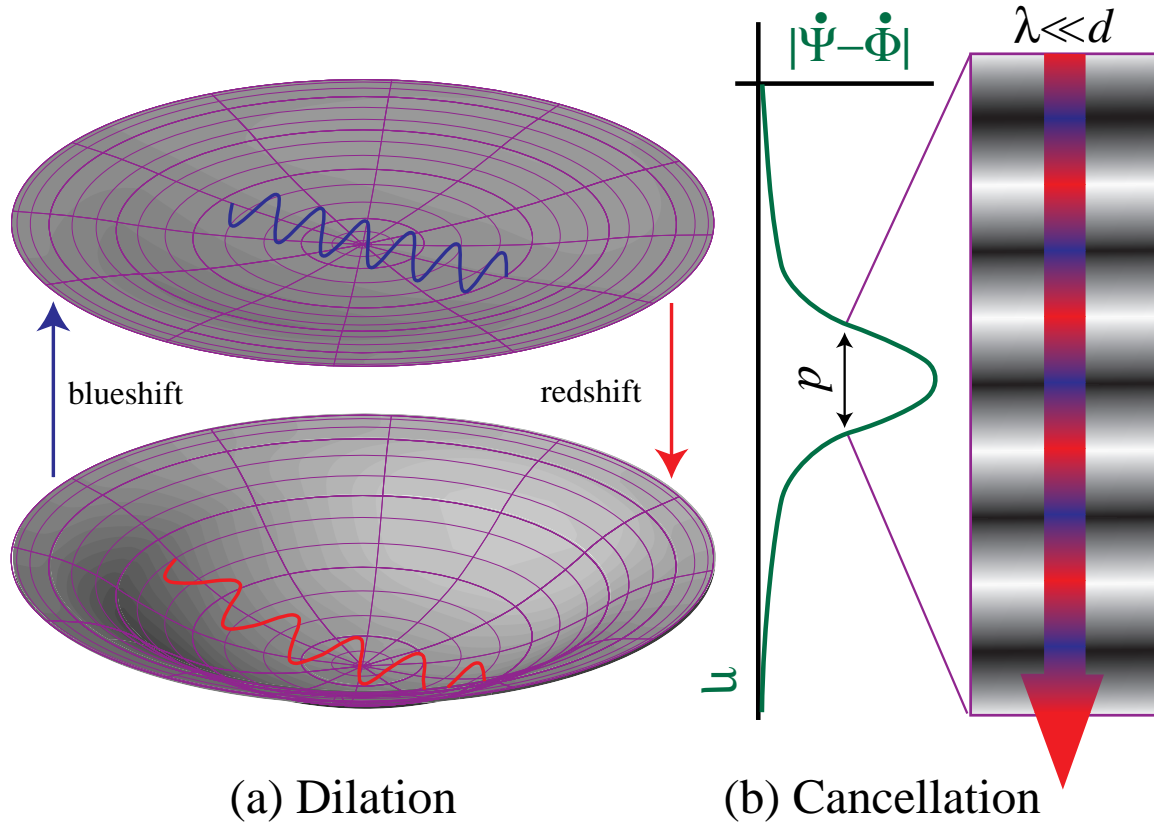
1.2.3 Doppler Effect

Since the turning points are at the extrema, the fluid velocity oscillates 90 degrees out of phase with the density (see Fig. 1.4a). Its motion relative to the observer causes a Doppler shift. Whereas the observer velocity creates a pure dipole anisotropy on the sky, the fluid velocity causes a spatial temperature variation $V_\gamma/\sqrt{3}$ on the last scattering surface from its line of sight component. For a photon-dominated $c_s \simeq 1/\sqrt{3}$ fluid, the velocity contribution is equal in amplitude to the density effect [48, 92]. This photon-intrinsic Doppler shift should be distinguished from the scattering-induced Doppler shift of reionized scenarios (see §7.1.3 and [162]).

The addition of baryons significantly changes the relative velocity contribution. As the effective mass increases, conservation of energy requires that the velocity decreases for the same initial temperature displacement. Thus the *relative* amplitude of the velocity scales as c_s . In the toy model of a constant baryon-photon density ratio R , the oscillation becomes $V_\gamma/\sqrt{3} = \frac{1}{3}\Psi(1 + 3R)(1 + R)^{-1/2}\sin(kc_s\eta)$. Notice that velocity oscillations are symmetric around zero leading to even more prominent compressional peaks (see Fig. 1.4b). Even in a universe with $\Omega_b h^2$ given by nucleosynthesis, R is sufficiently large to make velocity contributions subdominant.

1.2.4 Potential Evolution

All realistic models involve potentials which are time-dependent, leading to a non-trivial gravitational driving force that can greatly enhance the prominence of the acoustic peaks [82, 83]. We have hitherto assumed that matter dominates the energy density. In reality, radiation dominates above the redshift of equality $z_{eq} = 2.4 \times 10^4 \Omega_0 h^2$, assuming



(a) Dilation

(b) Cancellation

Figure 1.5: Differential Redshift and Dilation

Gravitational redshift and dilation effects in a time dependent potential. Time variability occurs whenever the matter is not the sole dynamical factor and thus probes $\Omega_0 h^2$, Ω_Λ , $1 - \Omega_0 - \Omega_\Lambda$ and any isocurvature perturbations. (a) Decay of the potential $|\Psi|$ decreases the gravitational redshift leading to an effective blueshift in the well. The implied curvature perturbation $|\Phi|$ decay represents a “contraction of space” which blueshifts photons through time dilation, nearly doubling the Ψ effect. (b) In the free streaming limit after last scattering, these two mechanisms combine to form the ISW effect. Redshift-blueshift cancellation cuts off contributions at small scales where the photon traverses many wavelengths during the decay.

the usual three flavors of massless neutrinos. The feedback from radiation perturbations into the gravitational potential makes the CMB sensitive to the matter-radiation ratio in the background *and* the fluctuations.

Consider first adiabatic initial conditions as before. Inside the sound horizon, radiation pressure prevents gravitational infall during radiation domination. Energy density fluctuations consequently can no longer maintain a constant gravitational potential. Counterintuitively, this decaying potential can actually enhance temperature fluctuations through its near resonant driving force. Since the potential decays after sound horizon crossing, it mimics $\cos(kc_s\eta)$ for $kc_s\eta \lesssim \pi$. Consequently, it drives the first compression without a counterbalancing effect on the subsequent rarefaction or gravitational redshift.

Moreover, there is another effect. Recall that the space curvature perturbation follows the potential as $\Phi \simeq -\Psi$. Since the forcing function $F/(1+R) \simeq -\ddot{\Phi} - k^2\Psi/3$, a changing Φ also drives oscillations. As Φ is a perturbation to the spatial metric, its change induces a time-dilation effect which is wholly analogous to the cosmological redshift due to the expansion. Heuristically, the overdensities which establish the potential well “stretch” the space-time fabric (see Fig. 1.5a). As the potential well decays, it re-contracts. Photons which are caught in this contraction find their wavelength similarly contracted, *i.e.* blueshifted. Thus a differential change in Φ leads to a dilation effect, $\dot{\Theta}_0 = -\dot{\Phi}$, and consequently a forcing effect on $\ddot{\Theta}_0$ of $-\ddot{\Phi}$ as required.

If Ψ were exactly $\cos(kc_s\eta)$, then $\ddot{\Phi}$ would double the driving force. Detailed calculation shows that the oscillation amplitude is boosted to $\simeq 5$ times the Sachs-Wolfe effect of $\frac{1}{3}\Psi$ (see §5.2.2). Only short wavelengths, which cross the sound horizon during the radiation-dominated epoch, experience this enhancement. For $\Omega_0 h^2 \simeq 0.25$, the sound horizon at equality is several times smaller than that at last scattering. Hence delaying equality, by lowering $\Omega_0 h^2$ or increasing the number of relativistic species, boosts the amplitude of oscillations for the first few peaks. Finally, the decay of the potential Ψ also removes the zero point shift and thus lifts the pattern of alternating heights for the peaks.

As a second example of forced oscillations, consider isocurvature perturbations. In this case, the matter alone carries the initial fluctuations, *i.e.* $\Theta_0(0) = 0$ and since the radiation dominates the energy density, $\Phi(0) = 0 = \Psi(0)$ as well. However $\dot{\Theta}(0) \neq 0$ and is set to counteract the gravitational attraction of the matter. Consequently, the potential grows to be significant only near sound horizon crossing and subsequently decreases if the universe is radiation dominated. The forcing function resembles $\sin(kc_s\eta)$ and thus drives

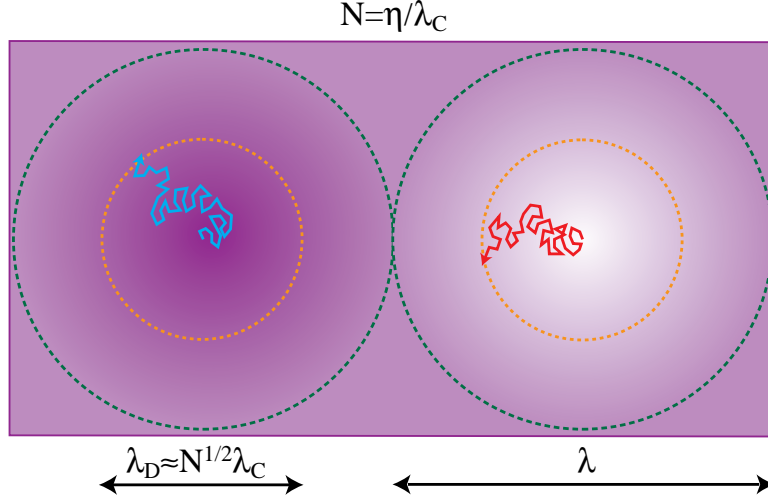


Figure 1.6: Photon Diffusion

Photon diffusion mixes hot photons from overdense regions and cold photons from underdense regions as the diffusion length λ_D exceeds the wavelength λ . Scattering averages the two and rapidly damps anisotropies. The diffusion length is given by a random walk of stepsize the Compton mean free path λ_C . The number of steps the photon traverses in the age of the universe η is η / λ_C . Thus the diffusion length scales as $\lambda_D \simeq N^{1/2} \lambda_C = (\eta \lambda_C)^{1/2}$. The Compton mean free path increases near recombination causing extensive damping at last scattering.

the sine harmonic of oscillations. Furthermore, since fluctuations are initially established to counter gravity, infall enhances *even* rather than odd peaks. Outside the sound horizon, dilation implies that $\Theta_0(\eta_*) = -\Phi(\eta_*)$, creating a Sachs-Wolfe effect of $[\Theta_0 + \Psi](\eta_*) \simeq 2\Psi(\eta_*)$.

1.2.5 Photon Diffusion Damping

In reality, the photons and baryons are not perfectly coupled since the photons possess a mean free path in the baryons λ_C due to Compton scattering. As the photons random walk through the baryons, hot spots and cold spots are mixed (see Fig. 1.6). Fluctuations thereafter remain only in the unscattered fraction causing a near exponential decrease in amplitude as the diffusion length $\lambda_D \sim \sqrt{N} \lambda_C = \sqrt{\eta \lambda_C}$ overtakes the wavelength [150].

At last scattering, the ionization fraction x_e decreases due to recombination, thus increasing the mean free path of the photons $\lambda_C \propto (x_e n_b)^{-1}$. The effective diffusion scale is therefore extremely sensitive to the ionization history in addition to the baryon number density n_b . Subtle effects during and even before last scattering can have a measurable effect on the damping [93, 77]. Moreover, if last scattering is delayed, *e.g.* by early reionization,

diffusion continues and can destroy all the acoustic peaks (see §7.1). Assuming a standard recombination ionization history however, the approximate scaling can be obtained from the Saha equation for the ionization at fixed redshift or temperature, $x_e \propto (\Omega_b h^2)^{-1/2}$. The final damping length therefore approximately scales as $\lambda_D(\eta_*) \propto \eta_*^{1/2} (\Omega_b h^2)^{-1/4}$. For high $\Omega_b h^2$ models, this scaling must be modified due to the high Lyman- α opacity at recombination [84].

1.2.6 Integrated Sachs-Wolfe Effect

After last scattering, the photons free stream toward the observer. Only gravitational effects can further alter the temperature. The differential redshift from $\dot{\Psi}$ and dilation from $\dot{\Phi}$ discussed above must be integrated along the trajectory of the photons. We thus call the combination the *integrated* Sachs-Wolfe (ISW) effect [138]. For adiabatic models, it can contribute via the potential decay for modes that cross the sound horizon between last scattering and full matter domination. In isocurvature models, potential *growth* outside the sound horizon makes the ISW effect dominate over the Sachs-Wolfe effect for all wavelengths larger than the sound horizon at η_* (see §6.2.6). Because these effects are sensitive to the radiation content and occur primarily at early times, we call them *early* ISW effects. In an open or Λ model, the universe enters a rapid expansion phase once matter no longer dominates the expansion. We call the effect of the resultant potential decay the *late* ISW effect.

One additional subtlety is introduced in ISW effects. If the potential decays while the photon is in an underdense region, it will suffer an effective redshift rather than a blueshift. Contributions from overdense and underdense regions will cancel and damp the ISW effect if the decay time is much greater than the light travel time across a wavelength (see Fig. 1.5). The damping does not occur for the *early* ISW effect. Since it arises when the perturbations are outside or just crossing the horizon, the time scale for the decay is always less than, or comparable to, the light travel time across a wavelength. For the late ISW effect, decay takes on the order of an expansion time at curvature or Λ domination independent of the wavelength. Thus, cancellation leads to a gradual damping in k of contributions as the wavelength becomes smaller than the horizon at the decay epoch. For a fixed Ω_0 , the decay epoch occurs much later in flat $\Omega_\Lambda + \Omega_0 = 1$ models than open ones. Consequently, Λ models will suffer cancellation of late ISW contributions at a much larger

scale than open models [98]. In summary, the epoch that the universe exits the radiation ($\Omega_0 h^2$) and matter-dominated phase ($\Omega_\Lambda, 1 - \Omega_0 - \Omega_\Lambda$) is imprinted on the CMB by the early and late ISW effects respectively.

1.2.7 Projection Effects

We have been considering the generation of temperature fluctuations in space. However, what one actually observes are temperature anisotropies on the sky. The connection between the two is that a spatial fluctuation on a distant surface, say at last scattering for the acoustic effects, appears as an anisotropy on the sky. Three quantities go into this conversion: the spectrum of spatial fluctuations, the distance to the surface of their generation, and curvature or lensing in light propagation to the observer (see Fig. 1.7).

For the acoustic contributions, the k modes that reach extrema in their oscillation at last scattering form a harmonic series of peaks related to the sound horizon. This in turn is approximately $\eta_*/\{1 + C[1 + R(\eta_*)]^{1/2}\}$, where $R(\eta_*) = 30\Omega_b h^2$ and $C \simeq \sqrt{3} - 1$. Since $\Omega_b h^2$ must be low to satisfy nucleosynthesis constraints, the sound horizon will scale roughly as the particle horizon η_* . The particle horizon at last scattering itself scales as $\eta_* \propto (\Omega_0 h^2)^{-1/2} f_R$. Here $f_R = [1 + (24\Omega_0 h^2)^{-1}]^{1/2} - (24\Omega_0 h^2)^{-1/2}$ and is near unity if the universe is matter dominated at η_* . For low $\Omega_0 h^2$, radiation allows for more rapid early expansion and consequently a smaller horizon scale. In a flat Λ universe, the distance to the last scattering surface scales approximately as $\eta_0 \propto (\Omega_0 h^2)^{-1/2} f_\Lambda$ with $f_\Lambda = 1 + 0.085 \ln \Omega_0$. Notice that the two behave similarly at high $\Omega_0 h^2$. Since the acoustic angle $\theta_A \propto \eta_*/\eta_0$, the leading term $(\Omega_0 h^2)^{-1/2}$ has no effect. Slowly varying corrections from f_R/f_Λ decreases the angular scale somewhat as $\Omega_0 h^2$ is lowered. On the other hand, the damping scale subtends an angle $\theta_D \simeq \lambda_D/\eta_0 \propto (\Omega_0 h^2)^{1/4} (\Omega_b h^2)^{-1/4} f_R^{1/2}/f_\Lambda$. Even in a low $\Omega_0 h^2$ universe θ_D is only weakly dependent on h unlike θ_A the acoustic scale.

By far the most dramatic effect is due to *background* curvature in the universe [158]. If the universe is open, photons curve on their geodesics such that a given scale subtends a much smaller angle in the sky than in a flat universe. In a $\Lambda = 0$ universe, the angle-distance relation yields $\theta_A \propto \eta_* \Omega_0 h$, *i.e.* $\propto \Omega_0^{1/2} f_R$. Likewise, the damping scale subtends an angle $\theta_D \propto \lambda_D \Omega_0 h$, *i.e.* $\propto \Omega_0^{3/4} \Omega_b^{-1/4} f_R^{1/2}$. At *asymptotically* high and low $\Omega_0 h^2$, $f_R \simeq 1$ and $f_R \propto (\Omega_0 h^2)^{1/2}$ respectively, so that there is a weak but different scaling with h and strong but similar scaling with Ω_0 for the two angles. The latter should be an

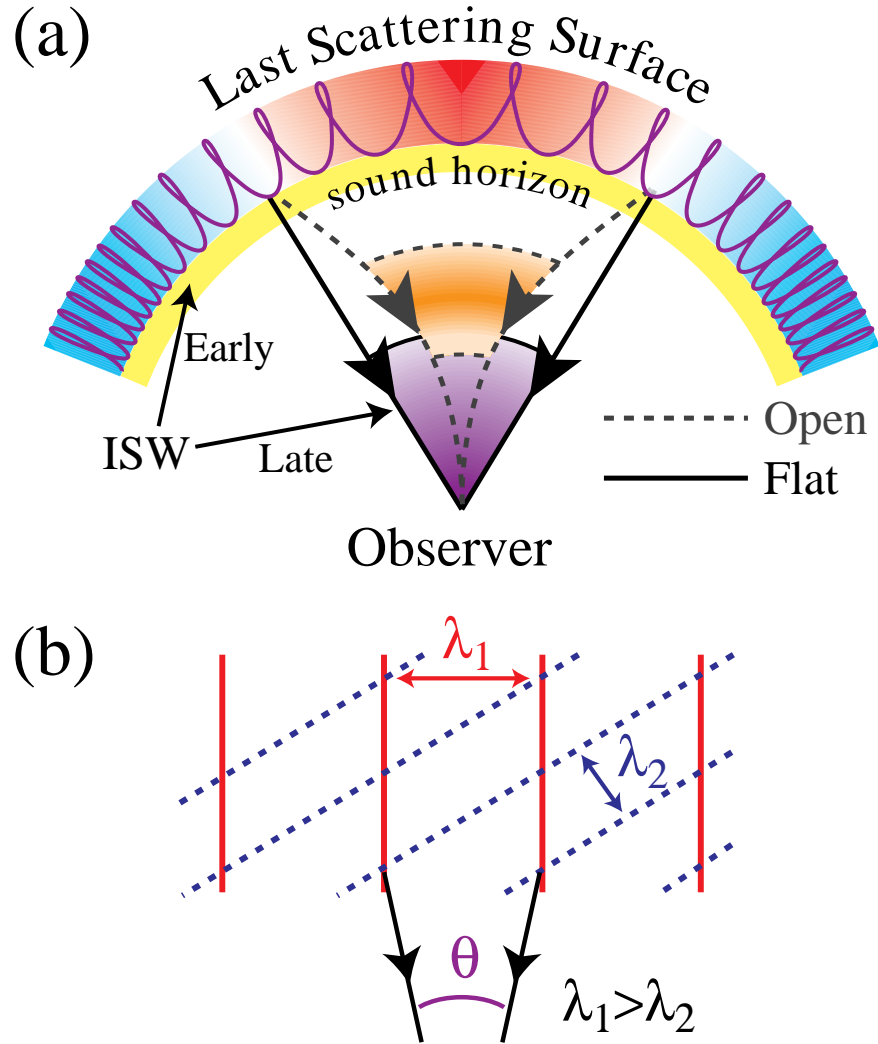


Figure 1.7: Projection Effect

(a) Acoustic contributions exhibit a series of peaks with decreasing angle beginning at the angular scale the sound horizon subtends at last scattering. This scale decreases significantly as the curvature increases due to geodesic deviation. Contributions after last scattering, come from a smaller physical scale for the same angular scale, which pushes the late ISW effect of flat Λ and open models to larger angles. (b) The orientation of the plane wave projected on the surface of last scattering leads to aliasing of power from shorter wavelengths onto larger angles. This smooths out sharp features and prevents a steeply rising (blue) anisotropy spectrum.

easily measurable effect [96].

Contributions from after last scattering, such as the ISW effects, arise from a distance closer to us. A given scale thus subtends a larger angle on the sky (see Fig. 1.7). Their later formation also implies that the radiation correction factor f_R will be smaller. For example, the angle subtended by the adiabatic early ISW effect scales nearly as $\Omega_0^{1/2}$ in a $\Lambda = 0$ universe even at low $\Omega_0 h^2$.

The above discussion implicitly assumes an one-to-one correspondence of linear scale onto angle that is strictly only true if the wavevector is perpendicular to the line of sight. In reality, the orientation of the wavevector leads to aliasing of different, in fact larger, angles for a given wavelength (see Fig. 1.7b). This is particularly important for Doppler contributions which vanish for the perpendicular mode (see §7.1.4). Moreover if there is a lack of long wavelength power, *e.g.* in typical baryon isocurvature models, large angle anisotropies are dominated by aliasing of power from short wavelengths. Consequently, the angular power spectrum may be less blue than the spatial power spectrum (see §6.2.6). On the other hand, for so called “scale invariant” or equal weighting of k modes, aliasing tends to smear out sharp features but does not change the general structure of the real to angular space mapping. It is evident that gravitational lensing from the curvature *fluctuations* of overdense and underdense regions has a similar but usually smaller effect [148].

1.3 Anisotropy Spectrum

Anisotropy formation is a simple process that is governed by gravitational effects on the photon-baryon fluid and the photons alone before and after last scattering respectively. The component contributions contain detailed information on classical cosmological parameters. Let us now put them together to form the total anisotropy spectrum.

The popular scale invariant adiabatic models provide a useful example of how cosmological information is encoded into the anisotropy spectrum. Specifically by scale invariant, we mean that the logarithmic contribution to the gravitational potential is initially constant in k . For open universes, this is only one of several reasonable choices near the curvature scale [95, 110, 134, 20]. In Fig. 1.8, we display a schematic representation of the anisotropy spectrum which separates the various effects discussed above and identifies their dependence on the background cosmology.

Changing the overall dynamics from $\Omega_0 = 1$ through flat Λ models to open models

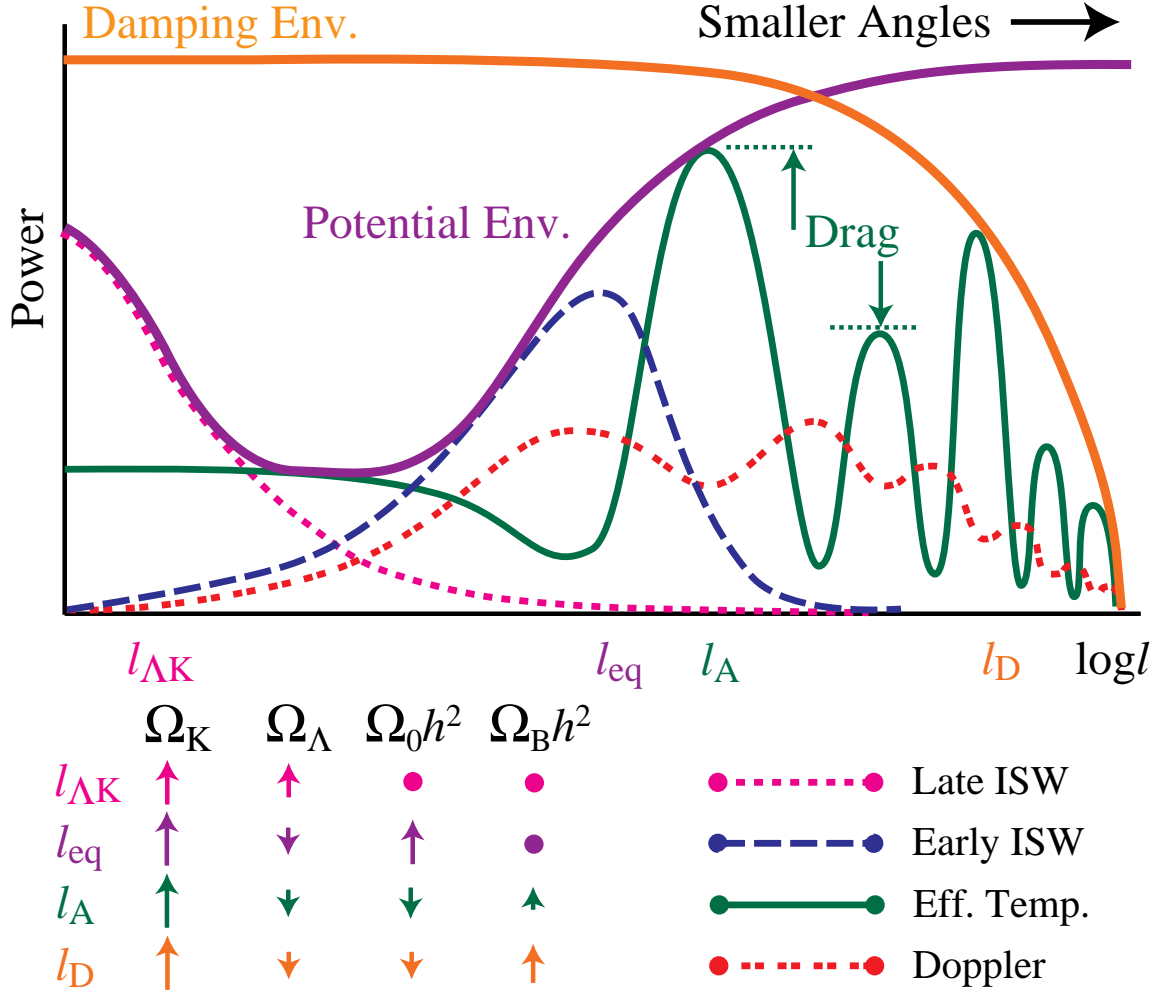


Figure 1.8: Total Anisotropy Spectrum

A schematic representation for scale invariant adiabatic scalar models. Features in open models are shifted to significantly smaller angles compared with Λ and $\Omega_0 = 1$ models, represented here as a shift in the ℓ axis beginning at the quadrupole $\ell = 2$. The monopole and dipole fluctuations are unobservable due to the mean temperature and peculiar velocity at the point of observation. The effective temperature at last scattering $[\Theta + \Psi](\eta_*)$ includes the gravitational redshift effect $\Psi(\eta_*)$. At large scales, the effective temperature goes to $\Psi(\eta_*)/3$ and is called the Sachs-Wolfe (SW) contribution. In reality, small scale acoustic contributions from the effective temperature and velocity are smoothed out somewhat in ℓ due to projection effects (see Fig. 1.7).

is similar to shifting the spectrum in angular space toward smaller angles. Beginning at the largest angles, the ISW effect from late potential decay dominates in $\Omega_0 \ll 1$ models. Cancellation suppresses contributions for wavelengths smaller than the particle horizon at the exit from matter domination. This damping extends to larger angles in Λ than in open models affecting even the quadrupole. At scales much larger than the sound horizon at η_* and particle horizon at equality, the effective temperature, or Sachs-Wolfe effect, is $[\Theta + \Psi](\eta_*) \simeq \frac{1}{3}\Psi(\eta_*)$. Shifting equality through $\Omega_0 h^2$ changes the redshift contribution $\Psi(\eta_*)$. For scales just above the sound horizon, the early ISW effect boosts fluctuations as the relative radiation content is increased by lowering $\Omega_0 h^2$. In sufficiently low Ω_0 open models, the late and early ISW effects merge and entirely dominate over the last scattering surface effects at large angles.

The first of a series of peaks from the acoustic oscillations appear on the sound horizon at η_* . In the total spectrum, the first acoustic peak merges with the early ISW effect. A lower $\Omega_0 h^2$ thus serves to broaden out and change the angular scaling of this combined feature. The acoustic peak heights also depend strongly on $\Omega_0 h^2$ for the first few peaks due to the driving effects of infall and dilation. Furthermore, greater infall due to the baryons allows more gravitational zero point shifting if $\Omega_0 h^2$ is sufficiently high to maintain the potentials. Odd peaks will thus be enhanced over the even, as well as velocity contributions, with increasing $\Omega_b h^2$. The location of the peaks is dependent on the sound horizon, distance to last scattering, and the curvature. In a low $\Omega_b h^2$, high $\Omega_0 h^2$ universe, it is sensitive only to the curvature $1 - \Omega_0 - \Omega_\Lambda$. Finally, the physics of recombination sets the diffusion damping scale which cuts off the series of acoustic peaks.

1.4 Robustness to Initial Conditions

How robust are anisotropies to model changes? Obviously, changing the initial spectrum will significantly modify the spectrum. For example, isocurvature conditions and tilt can alter the relative contributions of the various effects. The lack of super-curvature modes in open inflationary models can also suppress the low order multipoles [111]. On the other hand, they may be boosted by gravitational wave ISW contributions [168, 37].

Acoustic oscillations however are unavoidable, if there are potential perturbations before last scattering. Even exotic models such as defect-induced fluctuations should give rise to acoustic contributions of some form. Since adiabatic and isocurvature conditions

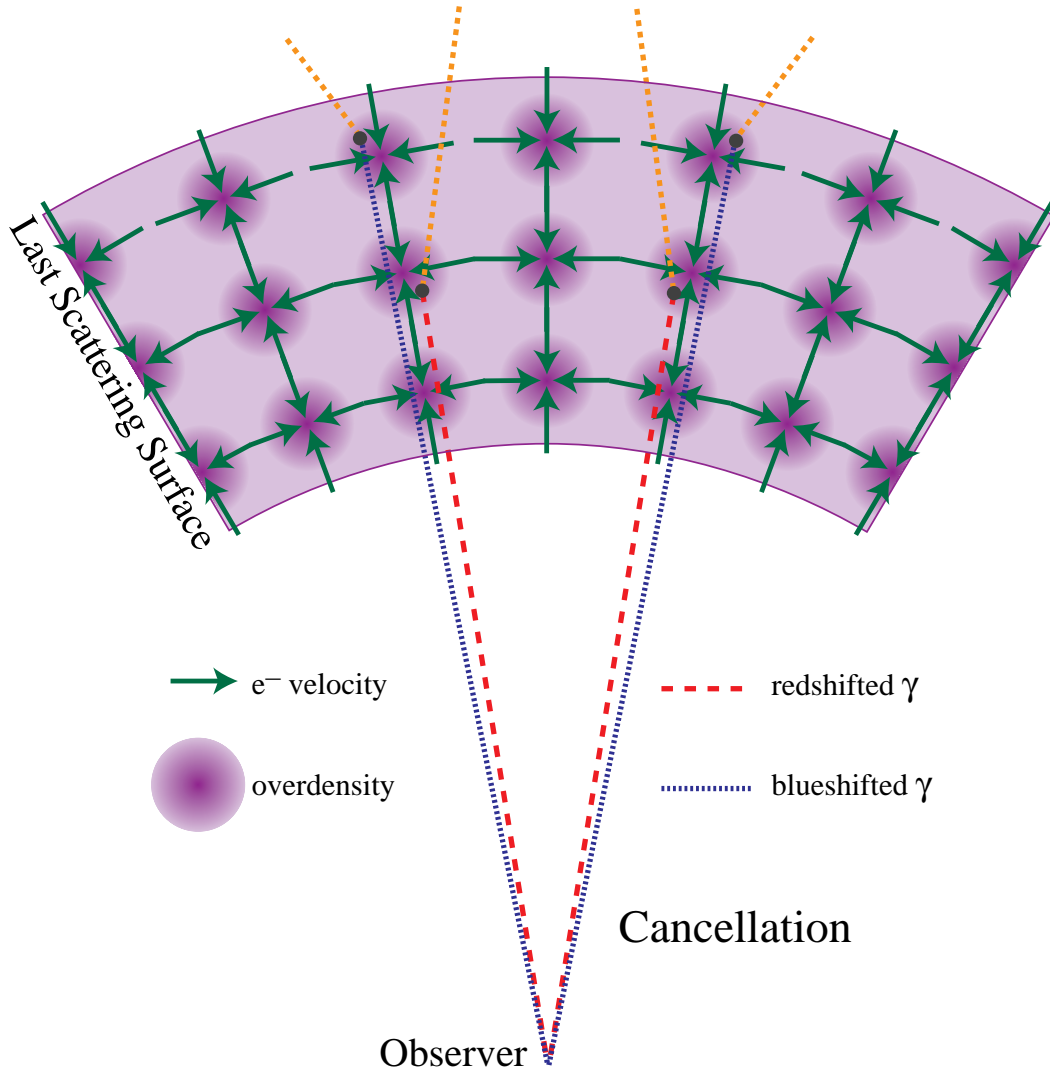


Figure 1.9: Cancellation Mechanism

If the coherence scale, *i.e.* wavelength, of the perturbation is under the thickness of the last scattering surface, the photons suffer alternating Doppler shifts depending on whether the photon last scattered in the fore or rear of the perturbation. The small scale Doppler effect is therefore severely cancelled.

drive two different harmonics, they can be distinguished by the relation between the peaks and the sound horizon at last scattering [83]. The *locations* of the peaks are then dependent only on the background cosmology, *i.e.* mainly on the curvature but also on a combination of $\Omega_b h^2$, Ω_Λ and $\Omega_0 h^2$. On the other hand, the difference in heights between odd and even peaks is a reasonably robust probe of the baryon-photon ratio, *i.e.* $\Omega_b h^2$, relative to the matter-radiation ratio at last scattering, *i.e.* $\Omega_0 h^2$ and possibly even the number of massless neutrinos. Finally, the damping scale probes the baryon content and the detailed physics of recombination. If acoustic oscillations are detected in the anisotropy data, clearly we will be able to measure many parameters of classical cosmology.

1.5 Reionization

The one caveat to these considerations is that reionization can completely erase the acoustic oscillations. In a model with sufficiently early reionization, *i.e.* $z_i \gg 10$, the photon diffusion length grows to be the horizon scale at the new last scattering surface and consequently damps all of the peaks. In models such as CDM, structure forms late and early reionization is highly unlikely. However, it is worthwhile to consider its general effects on the CMB in the event that structure formation proceeded by a qualitatively different route.

CMB fluctuations can be regenerated once the baryons are released from Compton drag to evolve independently $z_d = 160(\Omega_0 h^2)^{1/5} x_e^{-2/5}$ (see §7.1.3). Baryonic infall into potential wells leads to electron bulk velocities which induce Doppler shifts in the scattered photons. If the universe remains ionized, last scattering effectively occurs when the Compton scattering time exceeds the expansion time. Thus the thickness of the last scattering surface is on the order of the horizon size at last scattering. At small scales, this thickness spans many wavelengths of the perturbation. Photons that last scatter from the fore and rear of the perturbation encounter electrons with oppositely directed infall velocities (see Fig. 1.9). Just like the late ISW effect, the net contribution will be cancelled at small scales.

Cancellation is particularly severe for the linear theory Doppler effect (see §7.1.4). This implies that higher order terms in perturbation theory will dominate the anisotropy at small scales. As we show in §7.2, the dominant second order effect is due to a coupling of density and velocity perturbations called the Vishniac effect [121, 169]. It arises since the probability of a photon scattering off an overdensity is higher due to the increased electron

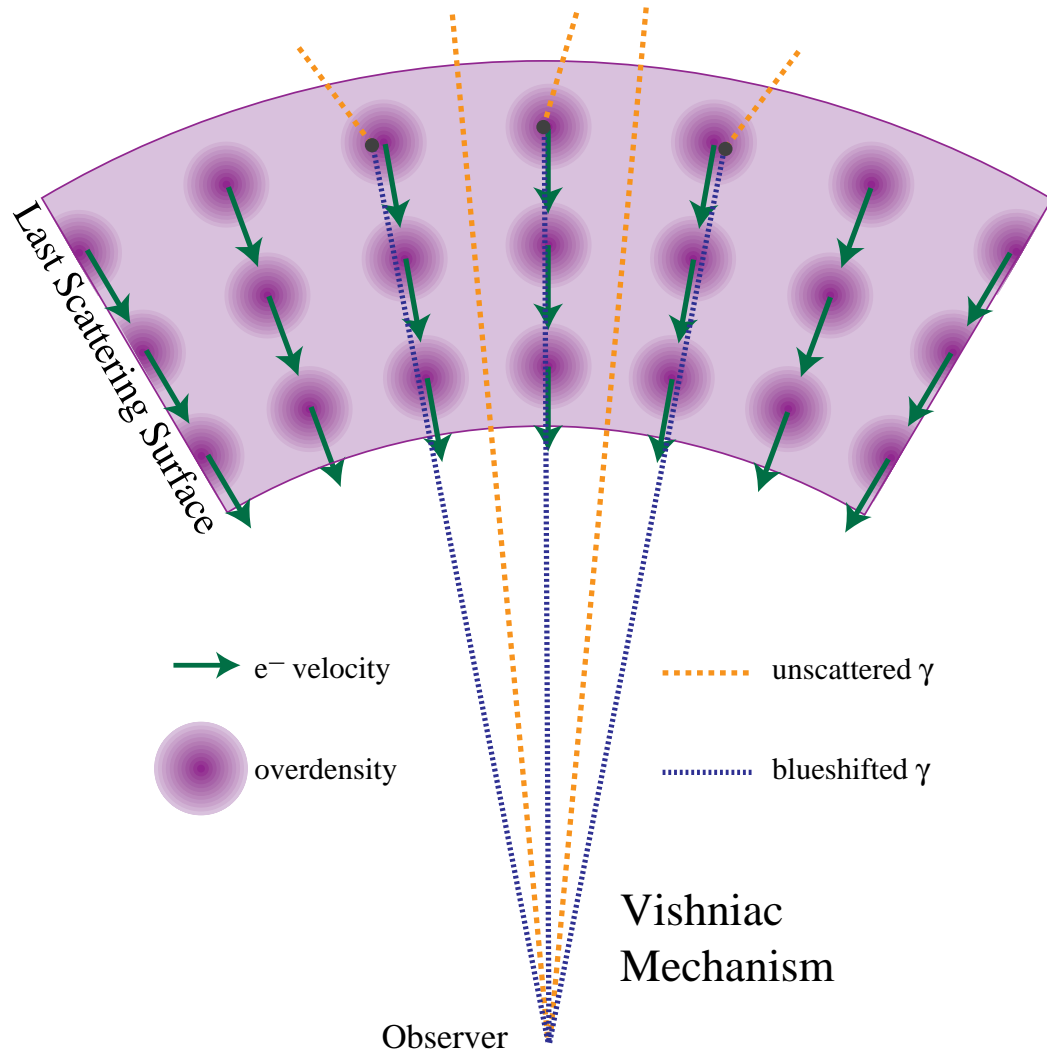


Figure 1.10: Vishniac Mechanism

In an overdense region, the free electron density is higher. This increases the probability of scattering. If these overdense regions are also caught in a large scale bulk flow, this can lead to a small scale variation in the temperature through preferential scattering. The Vishniac mechanism thus relies on a coupling of large and small scale perturbation modes.

density. If the overdense regions are also caught in a larger scale bulk flow, this can yield an anisotropy on the scale of the overdensity since a greater fraction of the photons suffer Doppler kicks along lines of sight that intersect overdensities (see Fig. 1.10). Since the effect depends on a coupling of modes, it is extremely sensitive to the shape and amplitude of the baryon power spectrum. Furthermore, the horizon size at last scattering is imprinted as the cancelled scale of the first order effect. Thus in the case of early reionization, the CMB can be used as a sensitive probe of the model for structure formation and the ionization history of the universe, but yields little model-independent information on the classical cosmological parameters. These secondary anisotropies are thus complementary to the primary ones. It is possible that the observed spectrum will contain an admixture of the two if reionization occurs but is not sufficiently early.

Chapter 2

The Boltzmann Equation

Wonderful, the process which fashions and transforms us! What is it going to turn you into next, in what direction will it use you to go?

–Chuang-tzu, 6

The study of the formation and evolution of CMB fluctuations in both real and frequency space begins with the radiative transport, or Boltzmann equation. In this pedagogically motivated chapter, we will examine its derivation. The Boltzmann equation written in abstract form as

$$\frac{df}{dt} = C[f] \quad (2.1)$$

contains a collisionless part df/dt , which deals with the effects of gravity on the photon distribution function f , and collision terms $C[f]$, which account for its interactions with other species in the universe. The collision terms in the Boltzmann equation have several important effects. Most importantly, Compton scattering couples the photons and baryons, keeping the two in kinetic equilibrium. This process along with interactions that create and destroy photons determines the extent to which the CMB can be thermalized. We will examine these issues more fully in §3 where we consider spectral distortions. Compton scattering also governs the evolution of inhomogeneities in the CMB temperature which lead to anisotropies on the sky. This will be the topic of §6 and §7.

In this chapter, we will first examine gravitational interactions and show that the photon energy is affected by gradients in the gravitational potential, *i.e.* the gravitational redshift, and changes in the spatial metric, *i.e.* the cosmological redshift from the scale factor and dilation effects due to the space curvature perturbation. Compton scattering in its non-relativistic limit can be broken down in a perturbative expansion based on the

energy transfer between the photons and electrons. We will examine the importance of each term in turn and derive its effects on spectral distortions and temperature inhomogeneities in the CMB.

2.1 Gravitational Interactions

Gravity is the ultimate source of spatial fluctuations in the photon distribution and the cause of the adiabatic cooling of the photon temperature from the expansion. Its effects are described by the collisionless Boltzmann, or Liouville, equation which controls the evolution of the photon distribution $f(x, p)$ as the photons stream along their geodesics. Here x and p are the 4-position and 4-momentum of the photons respectively. It is given by

$$\frac{df}{dt} = \frac{\partial f}{\partial x^\mu} \frac{dx^\mu}{dt} + \frac{\partial f}{\partial p^\mu} \frac{dp^\mu}{dt} = 0. \quad (2.2)$$

In other words, the phase space density of photons is conserved along its trajectory. The gravitational effects are hidden in the time dependence of the photon momentum. The solution to equation (2.2) is non-trivial since the photons propagate in a metric distorted by the lumpy distribution of matter. To evaluate its effect explicitly, we need to examine the geodesic equation in the presence of arbitrary perturbations.

2.1.1 Metric Fluctuations

The big bang model assumes that the universe is homogeneous and isotropic on the large scale. All such cases can be described by the Friedman-Robertson-Walker metric, where the line element takes the form

$$ds^2 = g_{\mu\nu} dx^\mu dx^\nu = -dt^2 + (a/a_0)^2 \gamma_{ij} dx^i dx^j, \quad (2.3)$$

with γ_{ij} as the background three-metric on a space of constant curvature $K = -H_0^2(1 - \Omega_0 - \Omega_\Lambda)$ and the scale factor is related to the redshift by $a/a_0 = (1 + z)^{-1}$. We will be mainly interested in the flat $K = 0$ and negatively curved (open) $K < 0$ cases. For these cases, a convenient representation of the three-metric which we will have occasion to use is the radial representation

$$\gamma_{ij} dx^i dx^j = -K^{-1} [d\chi^2 + \sinh^2 \chi (d\theta^2 + \sin^2 \theta d\phi^2)], \quad (2.4)$$

where the radial coordinate is scaled to the curvature length $(-K)^{-1/2}$.

Small scalar perturbations to the background metric can in general be expressed by two spatially varying functions. The exact form of the metric fluctuations varies with the choice of hypersurface on which these perturbations are defined, *i.e.* the gauge. We will discuss the subtleties involving the choice of gauge in §4.3. For now, let us derive the evolution equations for the photons using the conformal Newtonian gauge where the metric takes the form

$$\begin{aligned} g_{00} &= -[1 + 2\Psi(\mathbf{x}, t)], \\ g_{ij} &= (a/a_0)^2[1 + 2\Phi(\mathbf{x}, t)]\gamma_{ij}. \end{aligned} \quad (2.5)$$

Note that Ψ can be interpreted as a Newtonian potential. Φ is the fractional perturbation to the spatial curvature as the form of equation (2.4) shows. As we shall see in §4.2.6, they are related by the Einstein equations as $\Phi = -\Psi$ when pressure may be neglected. We will therefore often loosely refer to both as “gravitational potentials.”

The geodesic equation for the photons is

$$\frac{d^2x^\mu}{d\lambda^2} + \Gamma^\mu_{\alpha\beta} \frac{dx^\alpha}{d\lambda} \frac{dx^\beta}{d\lambda} = 0, \quad (2.6)$$

where Γ is the Christoffel symbol. The affine parameter λ is chosen such that the photon energy satisfies $p^0 = dx^0/d\lambda$. Since the photon momentum is given by

$$\frac{p^i}{p^0} = \frac{dx^i}{dt}, \quad (2.7)$$

the geodesic equation then becomes

$$\frac{dp^i}{dt} = g^{i\nu} \left(\frac{1}{2} \frac{\partial g_{\alpha\beta}}{\partial x^\nu} - \frac{\partial g_{\nu\alpha}}{\partial x^\beta} \right) \frac{p^\alpha p^\beta}{p^0}. \quad (2.8)$$

This equation determines the gravitational effects on the photons in the presence of perturbations as we shall now show.

2.1.2 Gravitational Redshift and Dilation

Let us rewrite the Boltzmann equation in terms of the energy p and direction of propagation of the photons γ^i in a frame that is locally orthonormal on constant time hypersurfaces,

$$\frac{\partial f}{\partial t} + \frac{\partial f}{\partial x^i} \frac{dx^i}{dt} + \frac{\partial f}{\partial p} \frac{dp}{dt} + \frac{\partial f}{\partial \gamma^i} \frac{d\gamma^i}{dt} = 0. \quad (2.9)$$

Notice that $d\gamma^i/dt \neq 0$ only in the presence of curvature from K or Φ because otherwise photon geodesics are straight lines. Since the anisotropy $\partial f/\partial\gamma^i$ is already first order in the perturbation, it may be dropped if the background curvature $K = 0$. In the presence of negative curvature, it makes photon geodesics deviate from each other exponentially with distance. Two photons which are observed to have a given angular separation were in the past separated by a larger (comoving) physical distance than euclidean analysis would imply. We shall see that this property allows the curvature of the universe to be essentially read off of anisotropies in the CMB. Formal elements of this effect are discussed in §4.2.4.

On the other hand, the redshift term dp/dt is important in all cases – even in the absence of perturbations. Since static curvature effects are unimportant in determining the redshift contributions, we will assume in the following that the background three-metric is flat, *i.e.* $\gamma_{ij} = \delta_{ij}$ without loss of generality. The energy and direction of propagation are explicitly given by

$$p^2 = p^i p_i, \quad \gamma^i = \frac{a}{a_0} \frac{p^i}{p} (1 + \Phi), \quad (2.10)$$

which implies $p^0 = (1 + \Psi)p$. The geodesic equation (2.8) then yields to first order in the fluctuations

$$\frac{1}{p} \frac{dp^0}{dt} = - \left(\frac{\partial\Psi}{\partial t} + \frac{da}{dt} \frac{1}{a} (1 - \Psi) + \frac{\partial\Phi}{\partial t} + 2 \frac{\partial\Psi}{\partial x^i} \frac{a_0}{a} \gamma^i \right). \quad (2.11)$$

From this relation, we obtain

$$\begin{aligned} \frac{1}{p} \frac{dp}{dt} &= \frac{1}{p} \frac{dp^0}{dt} (1 + \Psi) + \frac{\partial\Psi}{\partial t} + \frac{\partial\Psi}{\partial x^i} \frac{dx^i}{dt} \\ &= - \left(\frac{da}{dt} \frac{1}{a} + \frac{\partial\Phi}{\partial t} + \frac{\partial\Psi}{\partial x^i} \frac{a_0}{a} \gamma^i \right), \end{aligned} \quad (2.12)$$

which governs the gravitational and cosmological redshift effects on the photons.

Now let us discuss the physical interpretation of the energy equation (2.12). Consider first a small region where we can neglect the spatial variation of Ψ and Φ . In the presence of a gravitational potential, clocks naturally ticking at intervals Δt run slow by the dilation factor (see *e.g.* [173]),

$$\delta t = (-g_{00})^{-1/2} \Delta t \simeq (1 - \Psi) \Delta t. \quad (2.13)$$

For light emitted from the point 1, crests leave spaced by $\delta t_1 = [1 - \Psi(t_1)] \Delta t$. If they arrive at the origin spaced by δt_0 , they should be compared with a local oscillator with crests spaced as $[1 - \Psi(t_0)] \Delta t$, *i.e.* the shift in frequency (energy) is

$$\frac{p_1}{p_0} = [1 + \Psi(t_1) - \Psi(t_0)] \frac{\delta t_1}{\delta t_0}. \quad (2.14)$$

Now we have to calculate the in-transit delay factor $\delta t_1/\delta t_0$. Since null geodesics from the origin are radial in the FRW metric, choose angular coordinates such that along the $\chi(t)$ geodesic

$$-(1 + 2\Psi)dt^2 + (a/a_0)^2(-K)^{-1}(1 + 2\Phi)d\chi^2 = 0. \quad (2.15)$$

A wave crest emitted at (t_1, χ_1) is received at $(t_0, 0)$ where the two are related by

$$\int_{t_1}^{t_0} (1 + \Psi - \Phi) \frac{a_0}{a} dt = \int_0^{\chi_1} (-K)^{1/2} d\chi. \quad (2.16)$$

At χ_1 , the source emits a second crest after δt_1 which is received at the origin at $t_0 + \delta t_0$ where

$$\int_{t_1}^{t_0} (1 + \Psi - \Phi) \frac{a_0}{a} dt = \int_{t_1 + \delta t_1}^{t_0 + \delta t_0} (1 + \Psi - \Phi) \frac{a_0}{a} dt. \quad (2.17)$$

This can be manipulated to give

$$\int_{t_1}^{t_1 + \delta t_1} (1 + \Psi - \Phi) \frac{a_0}{a} dt = \int_{t_0}^{t_0 + \delta t_0} (1 + \Psi - \Phi) \frac{a_0}{a} dt, \quad (2.18)$$

or

$$\frac{\delta t_1}{\delta t_0} = \frac{a(t_1) [1 - \Psi(t_1) + \Phi(t_1)]}{a(t_0) [1 - \Psi(t_0) + \Phi(t_0)]}. \quad (2.19)$$

Inserting this into equation (2.14), the ratio of energies becomes

$$\frac{p_1}{p_0} = \frac{a(t_1) [1 + \Phi(t_1)]}{a(t_0) [1 + \Phi(t_0)]}. \quad (2.20)$$

Notice that the space curvature Φ but *not* the Newtonian potential Ψ enters this expression. This is easy to interpret. Heuristically, the wavelength of the photon itself scales with the space-space component of the metric, *i.e.* $a(1 + \Phi)$. In the background, this leads to the universal redshift of photons with the expansion. The presence of a space curvature perturbation Φ also stretches space. We shall see that it arises from density fluctuations through the Einstein equations (see §4.2.6). Overdense regions create positive curvature and underdense regions negative curvature. From equation (2.20), the rate of change of the energy is therefore given by

$$\frac{1}{p} \frac{\partial p}{\partial t} = -\frac{da}{dt} \frac{1}{a} - \frac{\partial \Phi}{\partial t}, \quad (2.21)$$

which explains two of three of the terms in equation (2.12).

Now let us consider the effects of spatial variations. Equation (2.14) becomes

$$\frac{p_1}{p_0} = [1 + \Psi(t_1, \chi_1) - \Psi(t_0, 0)] \frac{\delta t_1}{\delta t_0}. \quad (2.22)$$

The additional factor here is the potential difference in space. Photons suffer gravitational redshifts climbing in and out of potentials. Thus the gradient of the potential along the direction of propagation leads to a redshift of the photons, *i.e.*

$$\begin{aligned} \frac{1}{p} \frac{\partial p}{\partial x^i} \frac{dx^i}{dt} &= -\frac{\partial \Psi}{\partial x^i} \frac{dx^i}{dt} \\ &= -\frac{\partial \Psi}{\partial x^i} \frac{a_0}{a} \gamma^i, \end{aligned} \quad (2.23)$$

as required. This explains why a uniform Ψ does not lead to an effect on the photon energy and completes the physical interpretation of equation (2.12).

2.1.3 Collisionless Brightness Equation

The fractional shift in frequency from gravitational effects is independent of frequency $p' = p(1 + \delta p/p)$. Thus, a blackbody distribution will remain a blackbody,

$$\begin{aligned} f'(p') &= f(p) = \{\exp[p'/T(1 + \delta p/p)] - 1\}^{-1} \\ &= \{\exp[p'/T'] - 1\}^{-1}, \end{aligned} \quad (2.24)$$

with a temperature shift $\delta T/T = \delta p/p$. Let us therefore integrate the collisionless Boltzmann equation over energy, *i.e.* define

$$4\Theta \equiv \frac{1}{\pi^2 \rho_\gamma} \int p^3 dp f - 1 = \frac{\delta \rho_\gamma}{\rho_\gamma}, \quad (2.25)$$

where ρ_γ is the spatially and directionally averaged energy density of the photons. Since $\rho_\gamma \propto T^4$, $\Theta(\eta, \mathbf{x}, \gamma)$ is the fractional temperature fluctuation for a blackbody.

Employing equation (2.12) in (2.9) and integrating over frequencies, we obtain the collisionless Boltzmann (or brightness) equation,

$$\dot{\Theta} + \gamma^i \frac{\partial}{\partial x^i} (\Theta + \Psi) + \dot{\gamma}^i \frac{\partial}{\partial \gamma^i} \Theta + \dot{\Phi} = 0, \quad (2.26)$$

where the overdots represent derivatives with respect to conformal time $d\eta = dt/a$. Notice that since the potential $\Psi(\eta, \mathbf{x})$ is not an explicit function of angle γ and $\dot{\gamma}^i = \dot{x}^i$, we can write this in a more compact and suggestive form,

$$\frac{d}{d\eta} [\Theta + \Psi](\eta, \mathbf{x}, \gamma) = \dot{\Psi} - \dot{\Phi}, \quad (2.27)$$

which also shows that in a static potential $\Theta + \Psi$ is conserved. Thus the temperature fluctuation is just given by the potential difference:

$$\Theta(\eta_0, \mathbf{x}_0, \gamma_0) = \Theta(\eta_1, \mathbf{x}_1, \gamma_1) + [\Psi(\eta_1, \mathbf{x}_1) - \Psi(\eta_0, \mathbf{x}_0)]. \quad (2.28)$$

This is the Sachs-Wolfe effect [138] in its simplest form.

2.2 Compton Scattering

Compton scattering $\gamma(p) + e(q) \leftrightarrow \gamma(p') + e(q')$ dominates the interaction of CMB photons with electrons. By allowing energy exchange between the photons and electrons, it is the primary mechanism for the thermalization of the CMB. It also governs the mutual evolution of photon and baryon inhomogeneities before last scattering. The goal of this section is to derive its collision term in the Boltzmann equation to second order in the small energy transfer due to scattering. The approach taken here provides a coherent framework for all Compton scattering effects. In the proper limits, the equation derived below reduces to more familiar forms, *e.g.* the Kompaneets equation in the homogeneous and isotropic limit and the temperature Boltzmann equation for blackbody spectra. Furthermore, new truly second order effects such as the quadratic Doppler effect which mix spectral distortions and anisotropies result [75].

We make the following assumptions in deriving the equations:

1. The Thomson limit applies, *i.e.* the fractional energy transfer $\delta p/p \ll 1$ in the rest frame of the background radiation.
2. The radiation is unpolarized and remains so.
3. The density of electrons is low so that Pauli suppression terms may be ignored.
4. The electron distribution is thermal about some bulk flow velocity determined by the baryons \mathbf{v}_b .

Approximations (1), (3), and (4) are valid for most situations of cosmological interest. The approximation regarding polarization is not strictly true. Polarization is generated at the last scattering surface by Compton scattering of anisotropic radiation. However, since anisotropies themselves tend to be small, polarization is only generated at the $\sim 10\%$ level compared with temperature perturbations [93]. The feedback effect into the temperature only represents a $\sim 5\%$ correction to the temperature evolution and thus is only important for high precision calculations. We will consider its effects in greater detail in Appendix §A.3.1.

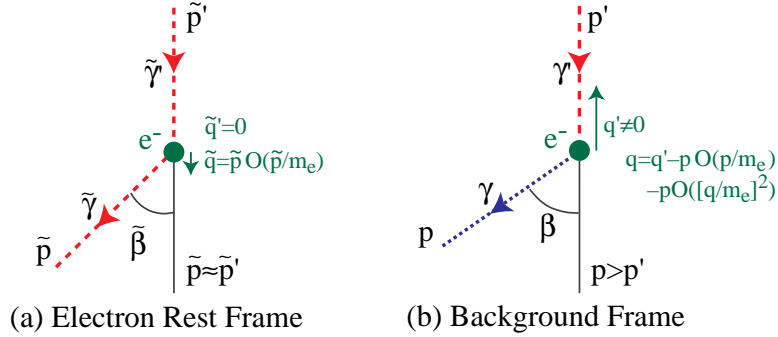


Figure 2.1: Scattering Geometry

In the electron rest frame, scattering only transfers energy to order $\mathcal{O}(\tilde{p}/m_e)$ due to the recoil of the electron. The Doppler shift into the background frame however induces a dipole which is aligned with the electron velocity. Dash length represents the photon wavelength. Aside from the energy shift due to recoil, the quadratic Doppler effect transfers energy to the photons $\delta p/p = \mathcal{O}[v_e^2 = (q/m_e)^2]$. The change in scattering angle is due to relativistic beaming effects.

2.2.1 Collision Integral

Again employing a locally orthonormal, *i.e.* Minkowski, frame we may in general express the collision term as [11]

$$\begin{aligned}
 C[f] = & \frac{1}{2E(p)} \int Dq Dq' Dp' (2\pi)^4 \delta^{(4)}(p + q - p' - q') |M|^2 \\
 & \times \left\{ g(t, \mathbf{x}, \mathbf{q}') f(t, \mathbf{x}, \mathbf{p}') [1 + f(t, \mathbf{x}, \mathbf{p})] \right. \\
 & \left. - g(t, \mathbf{x}, \mathbf{q}) f(t, \mathbf{x}, \mathbf{p}) [1 + f(t, \mathbf{x}, \mathbf{p}')] \right\}, \tag{2.29}
 \end{aligned}$$

where $|M|^2$ is the Lorentz invariant matrix element, $f(t, \mathbf{x}, \mathbf{p})$ is the photon distribution function, $g(t, \mathbf{x}, \mathbf{q})$ is the electron distribution function and

$$Dq = \frac{d^3q}{(2\pi)^3 2E(q)}, \tag{2.30}$$

is the Lorentz invariant phase space element. The terms in equation (2.29) which contain the distribution functions are just the contributions from scattering into and out of the momentum state \mathbf{p} including stimulated emission effects.

We will assume that the electrons are thermally distributed about some bulk flow velocity \mathbf{v}_b ,

$$g(t, \mathbf{x}, \mathbf{q}) = (2\pi)^3 x_e n_e (2\pi m_e T_e)^{-3/2} \exp \left\{ \frac{-[\mathbf{q} - m_e \mathbf{v}_b]^2}{2m_e T_e} \right\}, \tag{2.31}$$

where x_e is the ionization fraction, n_e is the electron number density, m_e is the electron mass, and we employ units with $c = \hbar = k_B = 1$ here and throughout. Expressed in the rest frame of the electron, the matrix element for Compton scattering summed over polarization is given by [113]

$$|M|^2 = 2(4\pi)^2 \alpha^2 \left[\frac{\tilde{p}'}{\tilde{p}} + \frac{\tilde{p}}{\tilde{p}'} - \sin^2 \tilde{\beta} \right], \quad (2.32)$$

where the tilde denotes quantities in the rest frame of the electron, α is the fine structure constant, and $\cos \tilde{\beta} = \tilde{\gamma} \cdot \tilde{\gamma}'$ is the scattering angle (see Fig. 2.1). The Lorentz transformation gives

$$\frac{p}{\tilde{p}} = \frac{\sqrt{1 - q^2/m_e^2}}{1 - \mathbf{p} \cdot \mathbf{q}/pm_e}, \quad (2.33)$$

and the identity $\tilde{p}_\mu \tilde{p}'^\mu = p_\mu p'^\mu$ relates the scattering angles.

We now expand in the energy transfer $p - p'$ from scattering. There are several small quantities involved in this expansion. It is worthwhile to compare these terms. To first order, there is only the bulk velocity of the electrons v_b . In second order, many more terms appear. The quantity T_e/m_e characterizes the kinetic energy of the electrons and is to be compared with p/m_e or essentially $T/m_e \simeq 5 \times 10^{-10}(1 + z_*)$, where T is the temperature of the photons. Before a redshift $z_{cool} \simeq 8.0(\Omega_0 h^2)^{1/5} x_e^{-2/5}$, where x_e is the ionization fraction (this corresponds to $z \gtrsim 500(\Omega_b h^2)^{2/5}$ for standard recombination), the tight coupling between photons and electrons via Compton scattering requires these two temperatures to be comparable (see §3.2.1). At lower redshifts, it is possible that $T_e \gg T$, which produces distortions in the radiation via the Sunyaev-Zel'dovich (SZ) effect as discussed in section §3.2.1. Note that the term T_e/m_e may also be thought of as the average thermal velocity squared $\langle v_{\text{therm}}^2 \rangle = 3T_e/m_e$. This is to be compared with the bulk velocity squared v_b^2 and will depend on the specific means of ionization. Terms of order $(q/m_e)^2$ contain both effects.

Let us evaluate the collision integral keeping track of the order of the terms. The matrix element expressed in terms of the corresponding quantities in the frame of the radiation is

$$|M|^2 = 2(4\pi)^2 \alpha^2 \left(\mathcal{M}_0 + \mathcal{M}_{q/m_e} + \mathcal{M}_{(q/m_e)^2} + \mathcal{M}_{(qp/m_e^2)} + \mathcal{M}_{(p/m_e)^2} \right) + h.o., \quad (2.34)$$

where

$$\begin{aligned} \mathcal{M}_0 &= 1 + \cos^2 \beta, \\ \mathcal{M}_{q/m_e} &= -2\cos\beta(1 - \cos\beta) \left[\frac{\mathbf{q} \cdot \mathbf{p}}{m_e p} + \frac{\mathbf{q} \cdot \mathbf{p}'}{m_e p'} \right], \end{aligned}$$

$$\begin{aligned}
\mathcal{M}_{(q/m_e)^2} &= \cos\beta(1 - \cos\beta)\frac{q^2}{m_e^2}, \\
\mathcal{M}_{qp/m_e^2} &= (1 - \cos\beta)(1 - 3\cos\beta)\left[\frac{\mathbf{q} \cdot \mathbf{p}}{m_e p} + \frac{\mathbf{q} \cdot \mathbf{p}'}{m_e p'}\right]^2 \\
&\quad + 2\cos\beta(1 - \cos\beta)\frac{(\mathbf{q} \cdot \mathbf{p})(\mathbf{q} \cdot \mathbf{p}')}{m_e^2 pp'}, \\
\mathcal{M}_{(p/m_e)^2} &= (1 - \cos\beta)^2\frac{p^2}{m_e^2}.
\end{aligned} \tag{2.35}$$

Notice that the zeroth order term gives an angular dependence of $1 + \cos^2\beta$ which is the familiar Thomson cross section result.

Likewise, the electron energies can be expressed as

$$\frac{1}{E_q E'_q} = \frac{1}{m_e^2} [1 - \mathcal{E}_{(q/m_e)^2} - \mathcal{E}_{qp/m_e^2} - \mathcal{E}_{(p/m_e)^2}], \tag{2.36}$$

where

$$\begin{aligned}
\mathcal{E}_{(q/m_e)^2} &= \frac{q^2}{m_e^2}, \\
\mathcal{E}_{qp/m_e^2} &= \frac{(\mathbf{p} - \mathbf{p}') \cdot \mathbf{q}}{m_e^2}, \\
\mathcal{E}_{(p/m_e)^2} &= \frac{(\mathbf{p} - \mathbf{p}')^2}{2m_e^2}.
\end{aligned} \tag{2.37}$$

The following identities are very useful for the calculation. Expansion to second order in energy transfer can be handled in a quite compact way by ‘‘Taylor expanding’’ the delta function for energy conservation in $\delta p = q - q'$,

$$\begin{aligned}
\delta(p + q - p' - q') &= \delta(p - p') + (\mathcal{D}_{q/m_e} + \mathcal{D}_{p/m_e})p \left[\frac{\partial}{\partial p'} \delta(p - p') \right] \\
&\quad + \frac{1}{2}(\mathcal{D}_{q/m_e} + \mathcal{D}_{p/m_e})^2 p^2 \left[\frac{\partial^2}{\partial p'^2} \delta(p - p') \right] + h.o.,
\end{aligned} \tag{2.38}$$

where

$$\begin{aligned}
\mathcal{D}_{q/m_e} &= \frac{1}{m_e p} (\mathbf{p} - \mathbf{p}') \cdot \mathbf{q}, \\
\mathcal{D}_{p/m_e} &= \frac{1}{m_e p} (\mathbf{p} - \mathbf{p}')^2.
\end{aligned} \tag{2.39}$$

This is of course defined and justified by integration by parts. Integrals over the electron distribution function are trivial,

$$\int \frac{d^3 \mathbf{q}}{(2\pi)^3} g(\mathbf{q}) = x_e n_e,$$

$$\begin{aligned} \int \frac{d^3 \mathbf{q}}{(2\pi)^3} q^i g(\mathbf{q}) &= m_e v_b^i x_e n_e, \\ \int \frac{d^3 \mathbf{q}}{(2\pi)^3} q^i q^j g(\mathbf{q}) &= m_e^2 v_b^i v_b^j x_e n_e + m_e T_e \delta^{ij} x_e n_e. \end{aligned} \quad (2.40)$$

Thus while the terms of $\mathcal{O}(q/m_e) \rightarrow \mathcal{O}(v_b)$, the $\mathcal{O}(q^2/m_e^2)$ terms give two contributions: $\mathcal{O}(v_b^2)$ due to the bulk velocity and $\mathcal{O}(T_e/m_e)$ from the thermal velocity.

The result of integrating over the electron momenta can be written

$$C[f] = \frac{d\tau}{dt} \int dp' \frac{p'}{p} \int \frac{d\Omega'}{4\pi} \frac{3}{4} \left[\mathcal{C}_0 + \mathcal{C}_{p/m_e} + \mathcal{C}_{v_b} + \mathcal{C}_{v_b^2} + \mathcal{C}_{T_e/m_e} + \mathcal{C}_{v_b p/m_e} + \mathcal{C}_{(p/m_e)^2} \right], \quad (2.41)$$

where we have kept terms to second order in $\delta p/p$ and the optical depth to Thomson scattering τ is defined through the scattering rate

$$\frac{d\tau}{dt} \equiv x_e n_e \sigma_T, \quad (2.42)$$

with

$$\sigma_T = 8\pi\alpha^2/3m_e^2, \quad (2.43)$$

as the Thomson cross section. Equation (2.41) may be considered as the source equation for all first and second order Compton scattering effects.

2.2.2 Individual Terms

In most cases of interest, only a few of the terms in equation (2.41) will ever contribute. Let us now consider each in turn. It will be useful to define two combinations of distribution functions

$$\begin{aligned} F_1(t, \mathbf{x}, \mathbf{p}, \mathbf{p}') &= f(t, \mathbf{x}, \mathbf{p}') - f(t, \mathbf{x}, \mathbf{p}), \\ F_2(t, \mathbf{x}, \mathbf{p}, \mathbf{p}') &= f(t, \mathbf{x}, \mathbf{p}) + 2f(t, \mathbf{x}, \mathbf{p})f(t, \mathbf{x}, \mathbf{p}') + f(t, \mathbf{x}, \mathbf{p}'), \end{aligned} \quad (2.44)$$

which will appear in the explicit evaluation of the collision term.

(a) Anisotropy Suppression: \mathcal{C}_0

Scattering makes the photon distribution isotropic in the electron rest frame. Microphysically this is accomplished via scattering into and out of a given direction. Since the electron velocity is assumed to be first order in the perturbation, to zeroth order scattering

makes the radiation isotropic $\delta f \equiv f - f_0 \rightarrow 0$, where f_0 is the isotropic component of the distribution function.

Its primary function then is the suppression of anisotropies as seen by the scatterers. Since isotropic perturbations are not damped, *inhomogeneities* in the distribution persist. Inhomogeneities at a distance are seen as anisotropies provided there are no intermediate scattering events, *i.e.* they are on the last scattering surface. They are the dominant source of primary anisotropies (see §6) and an important contributor to secondary anisotropies (see §7.1.3).

Explicitly the suppression term is

$$C_0 = \delta(p - p') \left(1 + \cos^2\beta\right) F_1(t, \mathbf{x}, \mathbf{p}, \mathbf{p}'). \quad (2.45)$$

Inserting this into equation (2.41) for the integration over incoming angles and noting that $\cos\beta = \boldsymbol{\gamma} \cdot \boldsymbol{\gamma}'$, we obtain the contribution

$$C_0[f] = \frac{d\tau}{dt} [(f_0 - f) + \gamma_i \gamma_j f^{ij}], \quad (2.46)$$

where f_0 is the isotropic component of the distribution and the f^{ij} are proportional to the quadrupole moments of the distribution

$$f^{ij}(t, \mathbf{x}, p) = \frac{3}{4} \int \frac{d\Omega}{4\pi} (\gamma^i \gamma^j - \frac{1}{3} \delta^{ij}) f. \quad (2.47)$$

The angular dependence of Compton scattering sources a quadrupole anisotropy damp more slowly than the higher moments.¹ Even so C_0 vanishes only if the distribution is isotropic $f = f_0$. Furthermore, since the zeroth order effect of scattering is to isotropize the distribution, in most cases any anisotropy is at most first order in the perturbative expansion. This enormously simplifies the form of the other terms.

(b) Linear and Quadratic Doppler Effect: C_{v_b} and $C_{v_b^2}$

Aside from the small electron recoil (see c), the kinematics of Thomson scattering require that no energy be transferred in the rest frame of the electron *i.e.* $\tilde{p}' = \tilde{p}$. Nevertheless, the transformation from and back into the background frame induces a Doppler shift,

$$\frac{\delta p}{p} = \frac{1 - \mathbf{v}_b \cdot \boldsymbol{\gamma}'}{1 - \mathbf{v}_b \cdot \boldsymbol{\gamma}} - 1 = \mathbf{v}_b \cdot (\boldsymbol{\gamma} - \boldsymbol{\gamma}') + (\mathbf{v}_b \cdot \boldsymbol{\gamma}) \mathbf{v}_b \cdot (\boldsymbol{\gamma} - \boldsymbol{\gamma}') + \mathcal{O}(v_b^3). \quad (2.48)$$

¹This can generate viscosity in the photon-baryon fluid and affects diffusion damping of anisotropies as we show in Appendix A.3.1.

Notice that in addition to the usual linear term, there is also a term quadratic in v_b . Furthermore, quadratic contributions do not disappear upon averaging over incoming and outgoing directions. They represent a net energy gain and/or loss by the CMB.

Let us first consider the case that scattering is rapid, *e.g.* before recombination, such that all CMB photons scatter before traversing a coherence scale of the velocity field. After averaging over incoming directions the net first order contribution is $\delta p/p = \boldsymbol{\gamma} \cdot \mathbf{v}_b$. As one might expect, this is just the Doppler shifted signal we expect from radiation that is isotropic in the electron rest frame. The spectrum therefore is a blackbody with a dipole signature \mathbf{v}_γ in angle: $\delta T/T = \boldsymbol{\gamma} \cdot \mathbf{v}_\gamma = \boldsymbol{\gamma} \cdot \mathbf{v}_b$. To $\mathcal{O}(v_b^2)$, there is a net energy transfer. Scattering brings the photons into kinetic equilibrium with the electrons. This equalization amounts to an energy gain by the photons if $v_\gamma < v_b$, and a loss in the opposite case. The energy transfer occurs only until kinetic equilibrium is attained. In other words, once the photons are isotropic in the electron rest frame $\mathbf{v}_\gamma = \mathbf{v}_b$, scattering has no further effect.

On the other hand, if the mean free path of the photons due to Compton scattering is much greater than the typical coherence scale of the velocity, the photons are in the diffusion limit. This can occur in reionized scenarios. Scattering is not rapid enough to ever make the distribution isotropic in the local rest frame of the electrons. Say some fraction $d\tau = n_e \sigma_T dt$ of the CMB scatters within a coherence scale. Then the Doppler shift will be reduced to $\boldsymbol{\gamma} \cdot \mathbf{v}_b d\tau$ and the energy transfer will be of order $\mathcal{O}(v_b^2 d\tau)$. As the photons continue to scatter, the first order Doppler term vanishes since redshifts and blueshifts from regions with different orientations of the electron velocity will mainly cancel (see §7.1.4). The second order term will however be positive definite: $\mathcal{O}(\int v_b^2 d\tau)$.

Is the resultant spectrum also a blackbody? In averaging over angles and space above, we have really superimposed many Doppler shifts for individual scattering events. Therefore the resulting spectrum is a superposition of blackbodies with a range of temperatures $\Delta T/T = \mathcal{O}(v_b)$. Zel'dovich, Illarionov, & Sunyaev [182] have shown that this sort of superposition leads to spectral distortions of the Compton- y type with $y = \mathcal{O}(v_b^2)$ (see §3.2.1).

Now let us write down the explicit form of these effects. The linear term is given by

$$c_{v_b} = \left\{ \left[\frac{\partial}{\partial p'} \delta(p - p') \right] (1 + \cos^2 \beta) \mathbf{v}_b \cdot (\mathbf{p} - \mathbf{p}') \right.$$

$$-\delta(p - p')2\cos\beta(1 - \cos\beta) \left[\frac{\mathbf{v}_b \cdot \mathbf{P}}{p} + \frac{\mathbf{v}_b \cdot \mathbf{P}'}{p'} \right] \Big\} F_1(t, \mathbf{x}, \mathbf{p}, \mathbf{p}'). \quad (2.49)$$

Assuming that the anisotropy is at most first order in the perturbation $\delta f \equiv f - f_0 \lesssim \mathcal{O}(v_b)$, the contribution to the collision term can be explicitly evaluated as

$$C_{v_b}[f] = -\frac{d\tau}{dt} \left[(\boldsymbol{\gamma} \cdot \mathbf{v}_b) p \frac{\partial f_0}{\partial p} - \mathcal{O}(\delta f v_b) \right]. \quad (2.50)$$

The $\mathcal{O}(\delta f v_b)$ term is not necessarily small compared with other second order terms. However, we already know its effect. If scattering is sufficiently rapid, the anisotropy δf will be a dipole corresponding to the electron velocity \mathbf{v}_b . In this case, its effects will cancel the $\mathcal{O}(v_b^2)$ quadratic term. Notice that to first order equilibrium will be reached between the zeroth and first order terms when

$$f_0 - f - p(\boldsymbol{\gamma} \cdot \mathbf{v}_b) \frac{\partial f}{\partial p} = \mathcal{O}(v_b^2), \quad (2.51)$$

assuming negligible quadrupole. For a blackbody, $T(\partial f / \partial T) = -p(\partial f / \partial p)$. Thus the equilibrium configuration represents a temperature shift $\delta T / T = \boldsymbol{\gamma} \cdot \mathbf{v}_b$. This formally shows that the $\mathcal{O}(v_b)$ term makes the photons isotropic in the baryon rest frame.

The quadratic term, given explicitly by

$$\begin{aligned} C_{v_b^2} = & \frac{1}{2} \left[\frac{\partial^2}{\partial p'^2} \delta(p - p') \right] (1 + \cos^2\beta) [\mathbf{v}_b \cdot (\mathbf{p} - \mathbf{p}')]^2 F_1(t, \mathbf{x}, \mathbf{p}, \mathbf{p}') \\ & - \left[\frac{\partial}{\partial p'} \delta(p - p') \right] 2\cos\beta(1 - \cos\beta) \left[\frac{\mathbf{v}_b \cdot \mathbf{P}}{p} + \frac{\mathbf{v}_b \cdot \mathbf{P}'}{p'} \right] \mathbf{v}_b \cdot (\mathbf{p} - \mathbf{p}') F_1(t, \mathbf{x}, \mathbf{p}, \mathbf{p}') \\ & + \delta(p - p') \left\{ - (1 - 2\cos\beta + 3\cos^2\beta) v_b^2 + 2\cos\beta(1 - \cos\beta) \frac{(\mathbf{v}_b \cdot \mathbf{P})(\mathbf{v}_b \cdot \mathbf{P}')}{pp'} \right. \\ & \left. + (1 - \cos\beta)(1 - 3\cos\beta) \left[\frac{\mathbf{v}_b \cdot \mathbf{P}}{p} + \frac{\mathbf{v}_b \cdot \mathbf{P}'}{p'} \right]^2 \right\} F_1(t, \mathbf{x}, \mathbf{p}, \mathbf{p}'), \end{aligned} \quad (2.52)$$

can also be evaluated under the assumption of small anisotropy,

$$C_{v_b^2}[f] = \frac{d\tau}{dt} \left\{ \left[(\boldsymbol{\gamma} \cdot \mathbf{v}_b)^2 + v_b^2 \right] p \frac{\partial f}{\partial p} + \left[\frac{11}{20} (\boldsymbol{\gamma} \cdot \mathbf{v}_b)^2 + \frac{3}{20} v_b^2 \right] p^2 \frac{\partial^2 f}{\partial p^2} \right\}. \quad (2.53)$$

(c) Thermal Doppler Effect and Recoil: C_{T_e/m_e} and C_{p/m_e}

Of course, we have artificially separated out the bulk and thermal components of the electron velocity. The thermal velocity leads to a quadratic Doppler effect exactly as described above if we make the replacement $\langle v_b^2 \rangle \rightarrow \langle v_{\text{therm}}^2 \rangle = 3T_e/m_e$. For an isotropic

distribution of photons, this leads to the familiar Sunyaev-Zel'dovich (SZ) effect [162]. The SZ effect can therefore be understood as the second order spectral distortion and energy transfer due to the superposition of Doppler shifts from individual scattering events off electrons in thermal motion. It can also be naturally interpreted macrophysically: hot electrons transfer energy to the photons via Compton scattering. Since the number of photons is conserved in the scattering, spectral distortions must result. Low energy photons are shifted upward in frequency, leading to the Rayleigh-Jeans depletion and the Wien tail enhancement characteristic of Compton- y distortions. We will consider this process in more detail in §3.2.1.

If the photons have energies comparable to the electrons (*i.e.* the electron and photon temperatures are nearly equal), there is also a significant correction due to the recoil of the electron. The scattering kinematics tell us that

$$\frac{\tilde{p}'}{\tilde{p}} = \left[1 + \frac{\tilde{p}}{m_e}(1 - \cos\tilde{\beta}) \right]^{-1}. \quad (2.54)$$

Thus to lowest order, the recoil effects are $\mathcal{O}(p/m_e)$. Together with the thermal Doppler effect, these terms form the familiar Kompaneets equation in the limit where the radiation is isotropic and drive the photons toward kinetic equilibrium as a Bose-Einstein distribution of temperature T_e (see §3.2.2). A blackbody distribution cannot generally be established since Compton scattering requires conservation of the photon number.

Explicitly, the recoil term

$$\mathcal{C}_{p/m_e} = - \left[\frac{\partial}{\partial p'} \delta(p - p') \right] \left(1 + \cos^2\beta \right) \frac{(\mathbf{p} - \mathbf{p}')^2}{2m_e} F_2(t, \mathbf{x}, \mathbf{p}, \mathbf{p}'), \quad (2.55)$$

yields

$$C_{T_e/m_e}[f] = \frac{d\tau}{dt} \frac{p}{m_e} \left[4f(1 + f) + (1 + 2f)f \frac{\partial f}{\partial p} \right]; \quad (2.56)$$

whereas the thermal term

$$\begin{aligned} \mathcal{C}_{T_e/m_e} = & \left\{ \left[\frac{\partial^2}{\partial p'^2} \delta(p - p') \right] \left(1 + \cos^2\beta \right) \frac{(\mathbf{p} - \mathbf{p}')^2}{2} - \left[\frac{\partial}{\partial p'} \delta(p - p') \right] 2\cos\beta \right. \\ & \left. \times (1 - \cos^2\beta)(p - p')\delta(p - p')[4\cos^3\beta - 9\cos^2\beta - 1] \right\} \frac{T_e}{m_e} F_1(t, \mathbf{x}, \mathbf{p}, \mathbf{p}'), \end{aligned} \quad (2.57)$$

gives

$$C_{T_e/m_e}[f] = \frac{d\tau}{dt} \frac{T_e}{m_e} \left(4p \frac{\partial f}{\partial p} + p^2 \frac{\partial^2 f}{\partial p^2} \right). \quad (2.58)$$

(d) Higher Order Recoil Effects: $C_{v_b p/m_e}$ and $C_{(p/m_e)^2}$

These terms represent the next order in corrections due to the recoil effect. Explicit forms are provided in [75]. In almost all cases, they are entirely negligible. Specifically, for most cosmological models, the baryon bulk flow grows by gravitational instability and is small until relatively recently. On the other hand the photon energy redshifts with the expansion and is more important early on. Thus their cross term is never important for cosmology. Furthermore, since there is no cancellation in the $C_{p/m}$ term, $C_{(p/m)^2}$ will never produce the dominant effect. We will hereafter drop these terms in our consideration.

2.2.3 Generalized Kompaneets Equation

Even for an initially anisotropic radiation field, multiple scattering off electrons will have the zeroth order effect of erasing the anisotropy. Therefore when the optical depth is high, we can approximate the radiation field as nearly isotropic. Under the assumption of full isotropy, the individual effects from equations (2.50), (2.53), (2.56) and (2.58) combine to form the collision term

$$C[f] = \frac{d\tau}{dt} \left\{ -\boldsymbol{\gamma} \cdot \mathbf{v}_b p \frac{\partial f}{\partial p} + \left([(\boldsymbol{\gamma} \cdot \mathbf{v}_b)^2 + v_b^2] p \frac{\partial f}{\partial p} + \left[\frac{3}{20} v_b^2 + \frac{11}{20} (\boldsymbol{\gamma} \cdot \mathbf{v}_b)^2 \right] \right. \right. \quad (2.59)$$

$$\left. \left. \times p^2 \frac{\partial^2 f}{\partial p^2} \right) + \frac{1}{m_e p^2} \frac{\partial}{\partial p} \left[p^4 \left\{ T_e \frac{\partial f}{\partial p} + f(1+f) \right\} \right] \right\}. \quad (2.60)$$

The first and second terms represent the linear and quadratic Doppler effects respectively. The final term is the usual Kompaneets equation. Notice that in the limit of many scattering regions, we can average over the direction of the electron velocity. The first order linear Doppler effect primarily cancels in this case. We can then reduce equation (2.59) to

$$C[f] = \frac{d\tau}{dt} \left\{ \frac{\langle v_b^2 \rangle}{3} \frac{1}{p^2} \frac{\partial}{\partial p} \left[p^4 \frac{\partial f}{\partial p} \right] + \frac{1}{m_e p^2} \frac{\partial}{\partial p} \left[p^4 \left\{ T_e \frac{\partial f}{\partial p} + f(1+f) \right\} \right] \right\}. \quad (2.61)$$

Under the replacement $\langle v_{\text{therm}}^2 \rangle = 3T_e/m \rightarrow v_b^2$, the SZ (thermal Doppler) portion of the Kompaneets equation and quadratic Doppler equation have the same form. Thus, spectral distortions due to bulk flow have exactly the same form as SZ distortions and can be characterized by the Compton- y parameter (see §3.2.1) given in its full form by

$$y = \int \frac{d\tau}{dt} \left[\frac{1}{3} \langle v_b^2(t) \rangle + \frac{T_e - T}{m_e} \right] dt \quad v_b \gg v_\gamma. \quad (2.62)$$

The appearance of the photon temperature T in equation (2.62) is due to the recoil terms in the Kompaneets equation.

The quadratic Doppler effect only contributes when the electron velocity is much greater than the photon dipole or bulk velocity. Just as the thermal term vanishes when the temperatures are equal, the “kinetic” part vanishes if the bulk velocities are equal. The effect therefore contributes only in the diffusion limit where the photons can be approximated a weakly anisotropic distribution diffusing through independently moving baryons. However above redshift $z_d \simeq 160(\Omega_0 h^2)^{1/5} x_e^{-2/5}$ (see §5.3.1), Compton drag on the electrons keeps the electrons coupled to the photons and requires $v_b \sim v_\gamma$. For a fully ionized, *COBE* normalized CDM model, integrating (2.62) up until the drag epoch yields a quadratic Doppler contribution of CDM equal to $y(z_d) \simeq 5 \times 10^{-7}$, almost two orders of magnitude below the current limits. Almost certainly the thermal effect in clusters will completely mask this effect. We will henceforth ignore its contributions when discussing spectral distortions.

2.2.4 Collisional Brightness Equation

We have shown that if the photons and baryons are in equilibrium, the effects which create spectral distortions vanish. In this case, we may integrate over the spectrum to form the temperature perturbation. Combining the collisional zeroth and $\mathcal{O}(v_b)$ parts, equations (2.46) and (2.50) respectively, with equation (2.26) for the collisionless part, we obtain for the temperature perturbation evolution in conformal time $\Theta(\eta, \mathbf{x}, \boldsymbol{\gamma})$

$$\dot{\Theta} + \gamma^i \frac{\partial}{\partial x^i} (\Theta + \Psi) + \dot{\gamma}^i \frac{\partial}{\partial \gamma^i} \Theta + \dot{\Phi} = \dot{\tau} (\Theta_0 - \Theta - \gamma_i v_b^i + \frac{1}{16} \gamma_i \gamma_j \Pi_\gamma^{ij}), \quad (2.63)$$

where

$$\begin{aligned} \Pi_\gamma^{ij} &= \frac{4}{\pi^2 \rho_\gamma} \int p^3 dp f^{ij}(\eta, \mathbf{x}) \\ &= \frac{1}{\pi^2 \rho_\gamma} \int p^3 dp \int \frac{d\Omega}{4\pi} (3\gamma^i \gamma^j - \delta^{ij}) f(\eta, \mathbf{x}, \boldsymbol{\gamma}) \\ &= \int \frac{d\Omega}{4\pi} (3\gamma^i \gamma^j - \delta^{ij}) 4\Theta(\eta, \mathbf{x}, \boldsymbol{\gamma}). \end{aligned} \quad (2.64)$$

The quantities Π_γ^{ij} are the quadrupole moments of the energy distribution. Since the pressure $p_\gamma = \frac{1}{3}\rho_\gamma$, they are related to the anisotropic stress. To generalize this relation to open universes, merely replace the flat space metric δ^{ij} with γ^{ij} . Equation (2.63) is the fundamental equation for primary anisotropy formation (see §6). We will revisit second order effects in §7 when we discuss reionized scenarios.

Chapter 3

Thermalization and Spectral Distortions

To be continuously transformed with other things is to be untransformed once and for all.

–Chuang-tzu, 25

The CMB exhibits a perfect blackbody form to the precision of current measurements. The deviations from the intensity of a blackbody are no more than 3×10^{-4} of the peak intensity [116]. The question arises: how does the blackbody spectrum form and how is it maintained? We have seen in Chapter 2 that spectral distortions occur when the photons and electrons are not in equilibrium. Many processes may thus contribute to spectral distortions. For example, energy may be dumped into the CMB through out-of-equilibrium particle decays, dissipation of turbulence and acoustic waves in the density fluctuations, early phase transition relics such as unstable domain walls or strings, and any astrophysical process that heat the electrons. Moreover, full thermalization of distortions requires the creation and annihilation of photons. The relevant interactions for cosmology, bremsstrahlung (*e.g.* [39]) and double Compton scattering [107], are ineffective below a redshift of $z \lesssim 10^7$. Thus spectral distortions are the earliest *direct* observational probe of cosmology.

There is always the possibility that an experimental determination of distortions from a blackbody spectrum will be confirmed: historically, there have been several false alarms, and even at present, the low frequency measurements continue to show marginally significant evidence of distortion. To understand the implications of the presence or absence of spectral distortions, we undertake here a thorough analytic and numerical study [79] of

thermalization processes in the early universe.

3.1 Collision Equations

3.1.1 Compton Scattering Revisited

By far, the dominant interaction that thermally couples photons and electrons before recombination is Compton scattering. Assuming homogeneity and isotropy, we can reduce the collisionless Boltzmann equation (2.9) and the Compton collision term (2.59) to

$$\frac{\partial f}{\partial t} - \frac{\partial f}{\partial p} \frac{da}{dt} \frac{1}{a} = \frac{1}{mp^2} \frac{d\tau}{dt} \frac{\partial}{\partial p} \left[p^4 \left(T_e \frac{\partial f}{\partial p} + f(1+f) \right) \right], \quad (3.1)$$

where recall that $d\tau/dt = x_e n_e \sigma_T$. For convenience, we can transform variables into a dimensionless energy $x_p = p/T_e$, not to be confused with x_e the ionization fraction. The Boltzmann equation then becomes

$$\left(\frac{\partial f}{\partial t} \right)_K = \left(\frac{d\tau}{dt} \frac{T_e}{m_e} \right) \frac{1}{x_p^2} \frac{\partial}{\partial x_p} \left[x_p^4 \left(\frac{\partial f}{\partial x_p} + f + f^2 \right) \right] + x_p \frac{\partial f}{\partial x_p} \frac{\partial}{\partial t} \left(\ln \frac{T_e}{T_0(1+z)} \right). \quad (3.2)$$

As we shall see, early on the electron temperature is tightly coupled to the photon temperature and thus scales with the expansion as $T_e \propto (1+z)$. In the late universe, the expansion time is long enough so that during the scattering by say, hot electrons in clusters, the expansion may be ignored. Hence the last term is usually negligible. Dropping this term, we obtain the standard form of the Kompaneets equation.

Compton scattering cannot change the number of photons, but can only redistribute them in frequency. This may be directly verified by integrating the Kompaneets equation (3.2) to form the change in the total number density n_γ :

$$\left(\frac{da^3 n_\gamma}{dt} \right)_K \propto \int dx_p x_p^2 \left(\frac{\partial f}{\partial t} \right)_K = 0. \quad (3.3)$$

The energy density evolution can likewise be obtained from integration of equation (3.1) over frequency

$$\frac{1}{a^4 \rho_\gamma} \frac{\partial a^4 \rho_\gamma}{\partial t} = 4 \frac{d\tau}{dt} \frac{1}{m_e} \left(T_e - \frac{1}{4\rho_\gamma \pi^2} \int_0^\infty p^4 f(1+f) dp \right), \quad (3.4)$$

where the first and second terms on the right represent the energy transfer from the thermal Doppler and recoil effects respectively.

3.1.2 Electron Temperature Evolution

The electron distribution is correspondingly coupled to the photons by Compton scattering. Since Coulomb interactions with the baryons are extremely rapid, the distribution is to good approximation Maxwellian at all times and has the same temperature as the baryons. We can determine the evolution of the electron temperature by considering the first law of thermodynamics for the photon-electron-baryon system

$$d(\rho a^3) + p da^3 = dQ, \quad (3.5)$$

where dQ is a source external to the system. With $p_\gamma = \frac{1}{3}\rho_\gamma$, $\rho_e = m_e + \frac{3}{2}n_e T_e$, $p_e = n_e T_e$ and similarly for the hydrogen and helium nuclei, this reduces to

$$a^3 d\rho_\gamma + \frac{4}{3}\rho_\gamma da^3 + \frac{3}{2}a^3(x_e n_e + n_H + n_{He})dT_e + (x_e n_e + n_H + n_{He})T_e da^3 = dQ. \quad (3.6)$$

where n_H and n_{He} are the total number density in ionized and neutral hydrogen and helium. If Y_p is the primordial helium mass fraction, then

$$\begin{aligned} n_e &= (1 - Y_p/2)n_b, \\ n_H &= (1 - Y_p)n_b, \\ n_{He} &= (Y_p/4)n_b. \end{aligned} \quad (3.7)$$

Thus, with equation (3.4), the evolution equation for the electron temperature becomes

$$\begin{aligned} \frac{dT_e}{dt} &= \frac{1}{3n_b}[(1 + x_e)/2 - (3 + 2x_e)Y_p/2]^{-1} \left(\frac{q}{a^3} - \frac{1}{a^4} \frac{da^4 \rho_\gamma}{dt} \right) - 2 \frac{da}{dt} \frac{1}{a} T_e \\ &= \frac{q}{3a^3 n_b} [(1 + x_e)/2 - (3 + 2x_e)Y_p/2]^{-1} - 2 \frac{da}{dt} \frac{1}{a} T_e \\ &\quad - \frac{1}{t_{e\gamma}} \left(T_e - \frac{1}{4\rho_\gamma \pi^2} \int_0^\infty p^4 f(1 + f) dp \right), \end{aligned} \quad (3.8)$$

where the rate of energy injection per comoving volume $q = a^{-3}dQ/dt$, and

$$t_{e\gamma} = \frac{3}{4} \frac{m_e}{\sigma_T \rho_\gamma} f_{cool}, \quad (3.9)$$

with

$$f_{cool} = [(1 + x_e)/2 - (3 + 2x_e)Y_p/8](1 - Y_p/2)^{-1} x_e^{-1}, \quad (3.10)$$

which has the limiting forms

$$x_e(1 - Y_p/2)f_{cool} = \begin{cases} (1 - 5Y_p/8) & x_e = 1 \\ \frac{1}{2}(1 - 3Y_p/4) & x_e \ll 1 \end{cases} \quad (3.11)$$

Thus the electron temperature is determined by a balance of adiabatic cooling from the expansion, heating from external sources q , and Compton cooling from the CMB. In the early universe, the latter wins as we shall see.

3.1.3 Bremsstrahlung and Double Compton Scattering

For cosmology, the most effective photon number changing processes are bremsstrahlung, $e^- + X \rightarrow e^- + X + \gamma$ (where X is an ion), and inelastic, henceforth referred to as double Compton scattering $e^- + \gamma \rightarrow e^- + \gamma + \gamma$. The kinetic equation for bremsstrahlung takes the form [107]:

$$\left(\frac{\partial f}{\partial t}\right)_{br} = Q_{br} \frac{d\tau}{dt} \frac{g(x_p)}{e^{x_p}} \frac{1}{x_p^3} [1 - (e^{x_p} - 1)f], \quad (3.12)$$

where

$$Q_{br} = \sqrt{\frac{2}{\pi}} \left(\frac{T_e}{m_e}\right)^{-1/2} \alpha T_e^{-3} \sum n_i Z_i^2. \quad (3.13)$$

Here n_i is the number density of ions with atomic number Z_i , and α is the fine structure constant. For a H + He plasma, $\sum n_i Z_i^2 = [x_H + (x_{He} - x_H)Y_p]n_b \simeq x_e n_b$ if the hydrogen and helium are similarly ionized. The Gaunt factor is given by,

$$g(x_p) \simeq \begin{cases} \ln(2.25/x_p), & x_p \leq 0.37, \\ \pi/\sqrt{3}, & x_p \geq 0.37. \end{cases} \quad (3.14)$$

We can re-express this in a particularly suggestive form

$$\left(\frac{\partial f}{\partial t}\right)_{br} = t_{br}^{-1} \left[\frac{1}{e^{x_p} - 1} - f \right], \quad (3.15)$$

where

$$t_{br} = 3.81 \times 10^{23} \frac{e^{x_p}}{g(x_p)} \frac{x_p^3}{e^{x_p} - 1} (1 - Y_p/2)^{-1} (x_e \Omega_b h^2)^{-2} \Theta_{2.7}^{7/2} \left(\frac{T_e}{T}\right)^{7/2} z^{-5/2} \text{s}, \quad (3.16)$$

where $\Theta_{2.7} = T_0/2.7\text{K}$. Apparently, this is the time scale on which bremsstrahlung can establish a blackbody distribution $f = (e^{x_p} - 1)^{-1}$ at frequency x_p .

Much of the early work on the thermalization problem [162, 185, 29, 87, 88] assumed that bremsstrahlung is the dominant photon-creating process in the early universe. As we can see from the scaling of equation (3.16), in the low baryon density universe implied by the nucleosynthesis constraint $\Omega_b h^2 = 0.01 - 0.02$, bremsstrahlung is rather inefficient.

Double Compton scattering cannot be neglected under such conditions. Lightman [107] first derived the kinetic equation for double Compton scattering:

$$\left(\frac{\partial f}{\partial t}\right)_{dc} = \frac{d\tau}{dt} \frac{4\alpha}{3\pi} \left(\frac{T_e}{m_e}\right)^2 \frac{1}{x_p^3} [1 - (e^{x_p} - 1)f] \int dx_p x_p^4 (1 + f) f \quad (3.17)$$

$$= t_{dc}^{-1} \frac{I(t)}{I_P} \left[\frac{1}{e^{x_p} - 1} - f \right], \quad (3.18)$$

where

$$t_{dc} = 6.96 \times 10^{39} \frac{x_p^3}{e^{x_p} - 1} I_P^{-1} (1 - Y_p/2)^{-1} (x_e \Omega_b h^2)^{-1} \Theta_{2.7}^{-2} \left(\frac{T_e}{T}\right)^{-2} z^{-5} \text{s}, \quad (3.19)$$

and

$$I(t) = \int dx_p x_p^4 (1 + f) f. \quad (3.20)$$

Note that since $(1 + f_P)f_P = -\partial f/\partial x_p$, integration by parts yields $I(t) = I_P = 4\pi^4/15$ for a blackbody of temperature T_e . Equation (3.17) is only strictly valid for $x_p < 1$ since its derivation assumes that the photon produced is lower in energy than the incoming photon. Double Compton scattering is, of course, inefficient at creating photons above the mean energy of the photons in the spectrum. However, we will only be concerned with the effects of double Compton scattering in the low frequency regime where it is efficient. Comparing equations (3.16) and (3.19) for the time-scales, we see that in a low $\Omega_b h^2$ universe and at high redshifts, double Compton scattering will dominate over bremsstrahlung. We will quantify this statement in §3.2.3.

The full kinetic equation to lowest order now reads

$$\left(\frac{\partial f}{\partial t}\right) = \left(\frac{\partial f}{\partial t}\right)_K + \left(\frac{\partial f}{\partial t}\right)_{dc} + \left(\frac{\partial f}{\partial t}\right)_{br}. \quad (3.21)$$

Evolution of an arbitrary spectrum under this kinetic equation must in general be solved numerically. To do so, we employ a fully implicit iterative modified Youngs approach [105].

3.2 Thermalization Optical Depths and Rates

Although the Compton scattering time,

$$t_C = \left(\frac{d\tau}{dt}\right)^{-1} = 4.47 \times 10^{18} (1 + z)^{-3} (1 - Y_P/2)^{-1} (x_e \Omega_b h^2)^{-1} \text{s}, \quad (3.22)$$

from equation (3.1) is quite short compared with most other time scales, its thermalization abilities are hindered by two properties:

1. There is no energy transfer in the Thompson limit. Energy exchange only occurs to $\mathcal{O}(v_e^2)$, *i.e.* $\mathcal{O}(T_e/m_e)$.
2. There is no change in photon number by Compton scattering.

We will first examine the effects of energy transfer and define an optical depth to Comptonization. At low Comptonization optical depth, the effect of Compton scattering is to transfer any excess thermal energy from the electrons to the photons. At higher optical depth, energy exchange can bring the whole distribution to kinetic equilibrium and create a Bose-Einstein distribution. Since Compton scattering does not change the photon number, a blackbody distribution cannot be attained unless the optical depth to absorption/emission from bremsstrahlung and double Compton scattering is high. We quantify these arguments below.

3.2.1 Comptonization

The time scale for energy exchange through Compton scattering is given by equation (3.4) as

$$t_K = \left(4 \frac{d\tau}{dt} \frac{T_e}{m_e}\right)^{-1} = 2.45 \times 10^{27} (1 - Y_p/2)^{-1} (\Omega_b h^2)^{-1} \Theta_{2.7}^{-1} \left(\frac{T_e}{T}\right)^{-1} (1+z)^{-4} \text{s}. \quad (3.23)$$

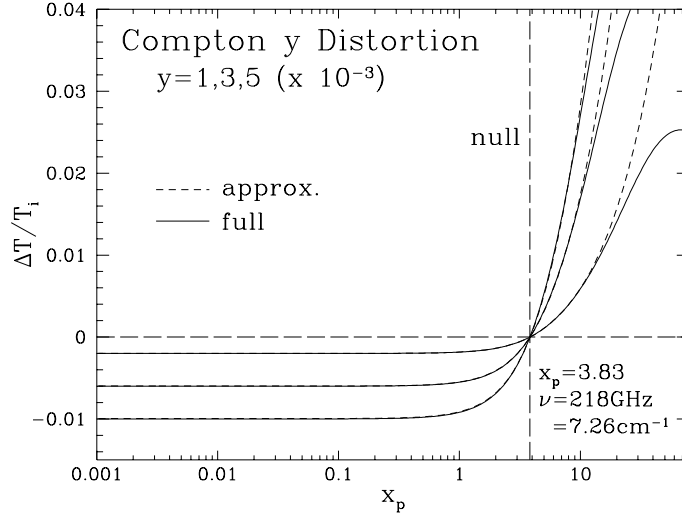
Notice that the rate increases with the free electron density and temperature. Conversely, the time scale associated with changes in electron energy from Compton scattering is controlled by the photon density. From equation (3.9), the Compton cooling rate is

$$\begin{aligned} t_{cool} &= \frac{3}{4} \frac{m_e}{\sigma_T \rho_\gamma} f_{cool} \\ &= 7.66 \times 10^{19} f_{cool} \Theta_{2.7}^{-4} (1+z)^{-4} \text{s}, \end{aligned} \quad (3.24)$$

where recall f_{cool} was defined in equation (3.10). The difference in the time scales reflects the fact that $n_\gamma \gg n_e$ since a given electron scatters more frequently with photons than a given photon with electrons. Alternatively, the heat capacity of the photons is much greater than that of the electrons.

There are two other rates associated with the evolution of the electron energy. The expansion causes adiabatic cooling in the electrons on the Hubble time scale

$$t_{exp} \equiv H^{-1} = \frac{a}{da/dt} \simeq 4.88 \times 10^{19} (z + z_{eq} + 2)^{-1/2} \Theta_{2.7}^{-2} (1+z)^{-3/2} \text{s}, \quad (3.25)$$

Figure 3.1: Compton- y distortion

Compton upscattering by hot electrons leaves a constant Rayleigh-Jeans decrement of $y \equiv (\Delta T/T)_{RJ}$ and a Wien excess that is overestimated by equation (3.31) as compared with the diffusion integral (3.30). The crossover is at $x_p = 3.83$ and is independent of y and allows a clean separation between y distorted and temperature shifted spectra.

where recall that the redshift of equality $z_{eq} = 4.20 \times 10^4 \Omega_0 h^2 \Theta_{2.7}^{-4} (1 - f_\nu)$ with f_ν as the neutrino fraction $f_\nu = \rho_\nu / (\rho_\nu + \rho_\gamma)$. The Compton and expansion cooling rates are equal at redshift

$$1 + z_{cool} = 9.08 \Theta_{2.7}^{-16/5} (\Omega_0 h^2)^{1/5} f_{cool}^{2/5}. \quad (3.26)$$

Thus for an ionized plasma, Compton cooling dominates until late times. However, astrophysical or other processes can continuously inject energy into the electrons at some rate q associated perhaps with structure formation. There are two limits of Comptonization to consider then: when the energy injection is strong such that $T_e \gg T$ and when it is weak and the system is dominated by Compton cooling.

a. Hot Electrons and Compton- y Distortions

If the electrons are strongly heated, $T_e/m_e \gg p/m_e$ at the peak of the spectrum, and we can ignore the recoil term in equation (3.4),

$$\frac{1}{a^4 \rho_\gamma} \frac{\partial a^4 \rho_\gamma}{\partial t} = t_K^{-1}. \quad (3.27)$$

This suggests that we may define the “optical depth” to Comptonization, as

$$\tau_K = \int dt/t_K = \int 4 \frac{d\tau}{dt} \frac{T_e}{m_e} dt. \quad (3.28)$$

The fractional energy distortion from Comptonization thus becomes $\delta\rho_\gamma/\rho_\gamma = \tau_K$.

With this parameter, the Kompaneets equation itself takes on a simple form if recoil is neglected,

$$\frac{\partial f}{\partial \tau_K} = \frac{4}{x_p^2} \frac{\partial}{\partial x_p} \left(x_p^4 \frac{\partial f}{\partial x_p} \right), \quad (3.29)$$

which is merely a diffusion equation in energy corresponding to the upscattering in frequency from the thermal Doppler effect. This equation has the exact solution [185]

$$f(\tau_K, x_p) = \frac{1}{\sqrt{\pi\tau_K}} \int_0^\infty f(0, w) \exp\left(-\frac{(\ln x_p - \ln w + 3\tau_K/4)^2}{\tau_K}\right) \frac{dw}{w}. \quad (3.30)$$

For an initial spectrum $f(0, x_p)$ of a blackbody, small deviations can alternately be solved iteratively by inserting $f(0, x_p)$ on the right hand side of (3.29). This yields the characteristic “Compton- y distortion” [185]

$$\frac{\delta f}{f} = y \frac{x_p e^{x_p}}{e^{x_p} - 1} \left[x_p \left(\frac{e^{x_p} + 1}{e^{x_p} - 1} \right) - 4 \right], \quad (3.31)$$

where here $y = \tau_K/4$. This approximation breaks down in the Wien limit where fractional deviations from a blackbody can be quite large due to exponential suppression in f (see Fig. 3.1). In the $x_p \ll 1$ Rayleigh-Jeans limit, this becomes $\delta f/f = (\delta T/T)_{RJ} = -2y = -\tau_K/2$ and reflects the fact that upscattering causes a photon deficit at low energies.

The Comptonization optical depth $\tau_K/4 = y \sim (T_e/m_e)\tau$ is generally smaller than the Compton optical depth τ . However if the electrons are sufficiently hot, distortions are measurable. In clusters of galaxies, $\tau \simeq 0.01 - 0.1$ but $T_e \simeq 1 - 10$ keV yielding a distortion of the type given by equation (3.31) with $y \simeq 10^{-5} - 10^{-3}$. This is the cluster Sunyaev-Zel’dovich effect [162]. Distortions in the upper portion of this range represent a significant Rayleigh-Jeans decrement and have been detected in several bright X-ray clusters [90, 13]. It can be cleanly separated from distortionless temperature shifts through the Doppler and gravitational redshift effects by its spectral signature. In particular, note that independent of the value of y , there is a null in the distortion at $x_p \simeq 3.8$. On the other hand, no isotropic or average y -distortion has yet been detected on the sky, $y < 2.5 \times 10^{-5}$ (95% CL) [116]. This places serious constraints on the amount of global reheating and ionization allowable and consequently on some models of structure formation (see §7.1.2).

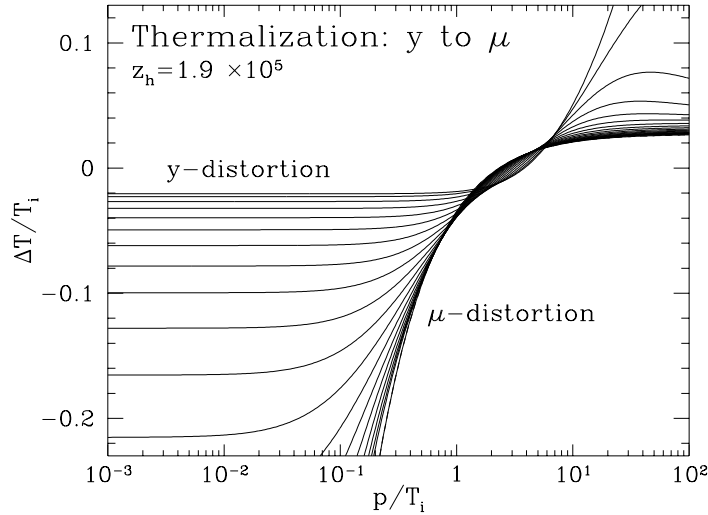


Figure 3.2: Thermalization from y to μ

An initial y -distortion at $z = 1.9 \times 10^5$ with the characteristic Rayleigh-Jeans suppression thermalizes to a Bose-Einstein distribution as both low-frequency and high-frequency photons are shifted to $x_p \sim 1$ by Compton scattering. Curves are equally spaced in redshift between $z = 1.9 \times 10^5 - 0.1 \times 10^5$ from highest to lowest $(\Delta T/T)_{RJ}$. Bremsstrahlung and double Compton scattering have been artificially turned off.

b. Compton Cooled Limit

Before z_{cool} , Compton cooling is so efficient that the electrons are strongly thermally coupled to the photons. In this case, the electron and photon temperature never deviates by a large amount, and we must retain the recoil terms in the Kompaneets equation. If the spectrum is initially blackbody before some injection of energy, we may employ iterative techniques to solve the equation. A blackbody spectrum of temperature T satisfies $f + f^2 = -(\partial f / \partial p)T$. Thus for small deviations from a blackbody, the Kompaneets equation takes the form of the diffusion equation (3.29) if instead of $y = \tau_K/4$ we employ

$$y = \int \frac{d\tau}{dt} \frac{T_e - T}{m_e} dt. \quad (3.32)$$

Thus we see that small deviations from a blackbody due to heating of the electrons can always be expressed as a Compton- y distortion of the form (3.31) below the Wien tail and before the Comptonization optical depth becomes large.

If $\tau_K \gg 1$, energy exchange brings the distribution into kinetic equilibrium (see Fig. 3.2). Since Compton scattering conserves photon number, the kinetic equilibrium

solution is a Bose-Einstein spectrum at the electron temperature,

$$f_{BE} = \frac{1}{e^{x_p + \mu} - 1}, \quad (3.33)$$

where μ is the dimensionless chemical potential. If $T_e \simeq T$, then this occurs near

$$\tau_K \simeq \frac{1}{2} \frac{t_{exp}}{t_K} \simeq \frac{1}{2} \left(\frac{z}{z_K} \right)^2 \simeq 1, \quad (3.34)$$

assuming radiation domination. Here

$$z_K \simeq 7.09 \times 10^3 (1 - Y_p/2)^{-1/2} (x_e \Omega_b h^2)^{-1/2} \Theta_{2.7}^{1/2}. \quad (3.35)$$

Notice that z_K is the redshift at which the energy exchange time scale t_K equals the expansion time scale t_{exp} . Rate comparison thus serves as a simple and useful rule of thumb for estimation purposes. In reality, a pure Bose-Einstein distribution will form for [24]

$$z \gtrsim 4\sqrt{2}z_K, \quad (3.36)$$

whereas only if

$$z \lesssim z_K/8 \quad (3.37)$$

will the spectrum be adequately described as a Compton- y distortion of equation (3.31). In the intermediate regime, the distortion appears as the Rayleigh-Jeans decrement of the y distortion but a less substantial Wien enhancement (see Fig. 3.2).

After external electron heating stops, the electron temperature rapidly approaches its equilibrium value [130, 184],

$$T_e = \frac{1}{4} \frac{\int p^4 f(f+1) dp}{\int p^3 f dp}, \quad (3.38)$$

by Compton cooling off an arbitrary photon distribution. The total energy density of the photons, except for expansion, henceforth does not change as it evolves,

$$\left(\frac{da^4 \rho_\gamma}{dt} \right)_K = 0, \quad (3.39)$$

as we can see from equation (3.4). It is easy to check that if $f = f_{BE}$, a Bose-Einstein distribution at temperature T ,

$$f_{BE}(1 + f_{BE}) = -\frac{\partial f_{BE}}{\partial p} T \quad (3.40)$$

and equation (3.38) implies $T_e = T$, as one would expect in the equilibrium state.

3.2.2 Chemical Potential Formation

Let us consider the Bose-Einstein distribution and its formation more carefully. Spectral distortions leave the regime of Comptonization when the optical depth to energy transfer $\tau_K \simeq 1$ or $z \gtrsim z_K$. In the absence of external sources, Compton scattering does not change the number [equation (3.3)] or energy [equation (3.39)] density of the photons during the era when the electrons are thermally coupled. Thus any external energy injection can be characterized by two quantities: the fractional number density of photons $\delta n_\gamma/n_\gamma$ and energy density $\delta \rho_\gamma/\rho_\gamma$ involved. Moreover, the equilibrium distribution is described by a single number, the chemical potential μ , and collapses this two dimensional parameter space onto one. There will therefore be some degeneracy between number and energy injection. Let us quantify this.

The energy in a Bose-Einstein distribution can be expressed as

$$\rho_{\gamma BE} = \frac{1}{\pi^2} \int f_{BE} p^3 dp = \rho_{\gamma P}(T_e) \psi(\mu), \quad (3.41)$$

where

$$\psi(\mu) \simeq \begin{cases} \frac{6}{I_3} \exp(-\mu), & \mu \gg 1, \\ 1 - 3 \frac{I_2}{I_3} \mu, & \mu \ll 1, \end{cases} \quad (3.42)$$

and $\rho_{\gamma P}(T_e) = I_3 T_e^4 / \pi^2 = a T_e^4 = 4 \sigma_B T_e^4$, the energy density of blackbody radiation, with $\sigma_B = \pi^2 k_B^2 / 60 \hbar^3 c^2 = \pi^2 / 60$ as the Stefan-Boltzmann constant. Similarly, the number density is given by

$$n_{\gamma BE} = \frac{1}{\pi^2} \int f_{BE} p^2 dp = n_{\gamma P}(T_e) \phi(\mu), \quad (3.43)$$

where

$$\phi(\mu) \simeq \begin{cases} \frac{2}{I_2} \exp(-\mu), & \mu \gg 1, \\ 1 - 2 \frac{I_1}{I_2} \mu, & \mu \ll 1, \end{cases} \quad (3.44)$$

with $n_{\gamma P}(T) = (I_2/I_3) a T^3 = I_2 T^3 / \pi^2$. Here the constants I_n are defined by the Riemann Zeta function as follows: $I_n = \int_0^\infty dx \frac{x^n}{e^x - 1} = n! \zeta(n+1)$, *e.g.* $I_1 = \pi^2/6 \simeq 1.645$, $I_2 = 2\zeta(3) \simeq 2.404$, $I_3 = \pi^4/15 \simeq 6.494$.

The number of photons in a Bose-Einstein distribution decreases with increasing chemical potential. In particular, a spectrum with $\mu < 0$ has more photons than a blackbody, $\mu = 0$; conversely, a spectrum with $\mu > 0$ has fewer photons. Parenthetically, note that with equation (3.40), we can express the double Compton scattering integral [equation (3.20)] as

$$I_{BE} = \int dx_p x_p^4 (1 + f_{BE}) f_{BE} = 4 I_3 \psi(\mu), \quad (3.45)$$

for the case of a Bose-Einstein distribution.

Now if we require energy and number conservation, equations (3.41) and (3.43) tell us:

$$\rho_{\gamma BE} = \frac{I_3}{\pi^2} T_e^4 \psi(\mu) = \rho_{\gamma P}(T_i)(1 + \delta\rho_{\gamma}/\rho_{\gamma}) = \frac{I_3}{\pi^2} T_i^4 (1 + \delta\rho_{\gamma}/\rho_{\gamma}), \quad (3.46)$$

and

$$n_{\gamma BE} = \frac{I_2}{\pi^2} T_e^3 \phi(\mu) = n_{\gamma P}(1 + \delta n_{\gamma}/n_{\gamma}) = \frac{I_2}{\pi^2} T_i^3 (1 + \delta n_{\gamma}/n_{\gamma}), \quad (3.47)$$

where T_i represents the temperature of the radiation before injection. For small chemical potentials, we may solve equations (3.46) and (3.47) simultaneously to obtain:

$$\mu_{pred}(z_h) \simeq \frac{1}{2.143} \left[3 \frac{\delta\rho_{\gamma}}{\rho_{\gamma}} - 4 \frac{\delta n_{\gamma}}{n_{\gamma}} \right] \quad \mu \ll 1, \quad (3.48)$$

to first order in the perturbations. The numerical factor comes from $8I_1/I_2 - 9I_2/I_3$. This is the chemical potential established near the epoch of heating z_h after a time $t > t_K$ but *before* photon-creating processes have taken effect.

The end state Bose-Einstein spectrum is independent of the precise form of the injection and is a function of the *total* number of photons and energy density of the photons injected. This is a very powerful result. For instance, direct heating of the electrons is equivalent to injecting a negligible number of high energy photons. Furthermore, an arbitrary distribution of injected photons can be parameterized by the single quantity $\mu(\delta n_{\gamma}/n_{\gamma}, \delta\rho_{\gamma}/\rho_{\gamma})$ alone. Given the independence of the evolution to the specifics of the injection for most cases, it is convenient to employ injections which may be represented as “delta functions” (*i.e.* peaked functions localized in frequency) located at some frequency x_h .

Let us examine the qualitative behavior of equation (3.48). Injection of energy even in the form of photons tends to heat the electrons and cause $T_e > T_i$ [see equation (3.38)]. Since the number of photons in a blackbody is proportional to T^3 , this would make the spectrum underpopulated with respect to the blackbody at T_e . However, this deficit of photons can be partially or wholly compensated by the number of photons involved in the injection. In fact, unlike the case of pure electron heating where $\delta n_{\gamma}/n_{\gamma} = 0$, the chemical potential can become negative if the energy is injected at a frequency $x_h \lesssim 3.6$. An even more curious effect happens if energy is injected either at, or symmetrically about, this critical value. In this case, the number of photons and the corresponding energy injected is just enough so that the electrons are heated to a temperature at which there are

exactly enough photons to create a blackbody spectrum. This implies that an arbitrarily large amount of energy may be injected at this critical frequency and, given sufficient time for the photons to redistribute, still leave $\mu = 0$, *i.e.* the spectrum will remain a perfect blackbody. This effect will be considered more carefully in §3.3.4. Presumably, however, any physically realistic process will inject photons over a wide range of frequencies and destroy this balance.

In the absence of number changing processes, negative chemical potential spectra become Bose-Einstein condensates from the downscattering of excess photons [87]. However, although it may be that double Compton scattering and bremsstrahlung are ineffective near the frequency of injection, their effect at low frequencies plays a crucial role in the evolution of the whole spectrum. Compton scattering will move excess photons downward in frequency only until they can be absorbed by double Compton scattering and/or bremsstrahlung. We therefore expect stability against condensation if $|\mu|$ is less than or equal to the frequency at which the photon absorbing processes are effective. This limits the range of accessible negative chemical potentials. To better quantify these considerations, we must examine the role of number changing processes in thermalization. It is to this subject we now turn.

3.2.3 Blackbody Formation

Blackbody formation must involve bremsstrahlung and/or double Compton scattering to create and destroy photons and reduce the chemical potential to zero. Let us examine the rates of these processes. The full kinetic equation (3.21) shows that at high redshifts, Compton and double Compton scattering will dominate over bremsstrahlung. Thus early on, double Compton scattering will be responsible for creating/absorbing photons at low frequencies, while Compton scattering will redistribute them in frequency. The net effect will be that a blackbody distribution is efficiently established. Notice that (3.16) and (3.19) imply that double Compton scattering and bremsstrahlung become increasingly efficient as the photon frequency decreases. Even at low redshifts, bremsstrahlung can return the spectrum to a blackbody form at low frequencies.

Now let us examine the rates quantitatively. It is useful to define an optical depth to absorption by the double Compton or bremsstrahlung processes.

$$\tau_{abs} = \int_{t_h}^t dt' (t_{br}^{-1} + t_{dc}^{-1})$$

$$\simeq \frac{1}{3} \frac{t_{exp}}{t_{br}} + 2 \frac{t_{exp}}{t_{br}}, \quad (3.49)$$

where the last line assumes radiation domination. For the double Compton process, we also assume the integral (3.20) $I(t) \simeq I_P$, as is appropriate if deviations from a Planck distribution in the high frequency regime are small. Note that if there were no photons to begin with, $I(t) = 0$ and double Compton scattering does not occur. This is because there must be an incoming photon for the scattering to take place. Double Compton scattering itself cannot create a Planck distribution *ex nihilo*. Bremsstrahlung can since it only needs electrons and ions in the initial state.

Thus above the redshift at which $t_{br} = t_{dc}$, double Compton should be the dominant photon-creating process. This occurs at

$$z_{dc,br} \simeq 8.69 \times 10^5 (x_e \Omega_b h^2)^{2/5} \Theta_{2.7}^{-11/5} [g(x_p)]^{2/5}, \quad x_p \ll 1, \quad (3.50)$$

which is roughly independent of frequency due to similar scaling of their rates. For estimation purposes, we assume that $T_e \simeq T$ here and below.

Ignoring Compton scattering for the moment, we can write down the kinetic equation as a trivial ordinary differential equation

$$\frac{\partial f}{\partial \tau_{abs}} = \frac{1}{e^{x_p} - 1} - f, \quad (3.51)$$

where we hold the frequency x_p fixed. This has the immediate solution

$$f(\tau_{abs}, x_p) = (e^{x_p} - 1)^{-1} \{1 - [1 - f(0, x_p)] \exp(-\tau_{abs})\}. \quad (3.52)$$

The initial spectrum $f(0, x_p)$ is exponentially damped with optical depth leaving a blackbody in its place. This is natural since the fraction of photons which have not been affected by absorption decreases as $e^{-\tau_{abs}}$.

When the optical depth to absorption drops below unity, thermalization becomes inefficient. As equation (3.49) shows, this is approximately when the absorption time scales t_{br} and t_{dc} equal the expansion time scale t_{exp} . Since the absorption rate is frequency dependent, the photon absorbing processes are effective below a frequency

$$\begin{aligned} x_{exp,br} &\simeq 1.1 \times 10^{-2} (1 - Y_p/2)^{-1/2} [g(x_{exp,br})]^{1/2} x_e \Omega_b h^2 \Theta_{2.7}^{-11/4} z^{1/4}, \\ x_{exp,dc} &\simeq 4.3 \times 10^{-10} (1 - Y_p/2)^{-1/2} (x_e \Omega_b h^2)^{1/2} \Theta_{2.7}^{-1} z^{3/2}, \end{aligned} \quad (3.53)$$

where $t_{br}(x_{exp,br}) = t_{exp}$ and $t_{dc}(x_{exp,dc}) = t_{exp}$. Combining the two, we obtain

$$x_{exp}^2 = x_{exp,br}^2 + x_{exp,dc}^2, \quad (3.54)$$

as the frequency above which photon creation and absorption are ineffective.

Now let us include Compton scattering. The time-scale for establishing a Bose-Einstein distribution via Compton scattering t_K is independent of frequency. We therefore expect that the number-changing processes will dominate over Compton scattering below the frequency at which the rates are equal. For $x_p \ll 1$, we may approximate this as:

$$\begin{aligned} x_{c,br} &\simeq 8.0 \times 10^1 [g(x_{c,br})]^{1/2} (x_e \Omega_b h^2)^{1/2} \Theta_{2.7}^{-9/4} z^{-3/4}, \\ x_{c,dc} &\simeq 3.0 \times 10^{-6} \Theta_{2.7}^{1/2} z^{1/2}, \end{aligned} \quad (3.55)$$

where $t_{br}(x_{c,br}) = t_K(x_{c,br})$ and $t_{dc}(x_{c,dc}) = t_K(x_{c,dc})$. Note that $g(x_p)$ is only logarithmically dependent on frequency. Let us define,

$$x_c^2 = x_{c,br}^2 + x_{c,dc}^2. \quad (3.56)$$

Above the frequency x_c , the spectrum will be Bose-Einstein given sufficient time to establish equilibrium. This is true even if number changing processes are effective compared with the expansion because the created photons are rapidly carried away by Comptonization to higher frequencies. Below this frequency, the spectrum returns to a Planck distribution if either the bremsstrahlung or double Compton processes are effective compared with the expansion.

Figure 3.3 displays these critical frequencies and redshifts for the representative choices of $\Omega_b h^2 = 0.025$ and 0.0125 . Notice the transition to double Compton scattering dominance for $z > z_{dc,br}$ and small deviations from the simple power law approximations for $x_p \simeq 1$ and $z < z_{eq}$. Here $\Omega_0 h^2 = 0.25$, but the total matter content plays only a small role in the thermalization process, entering only through the expansion rate for $z < z_{eq}$.

3.3 Low Frequency Evolution

The quantitative study of thermalization involves the time evolution of the spectrum. Let us assume that it is distorted at a reheat redshift z_h by some non-equilibrium process that injects an arbitrary amount of energy and/or photons into the CMB. In this general case, thermalization must be studied numerically. However, we shall see that for

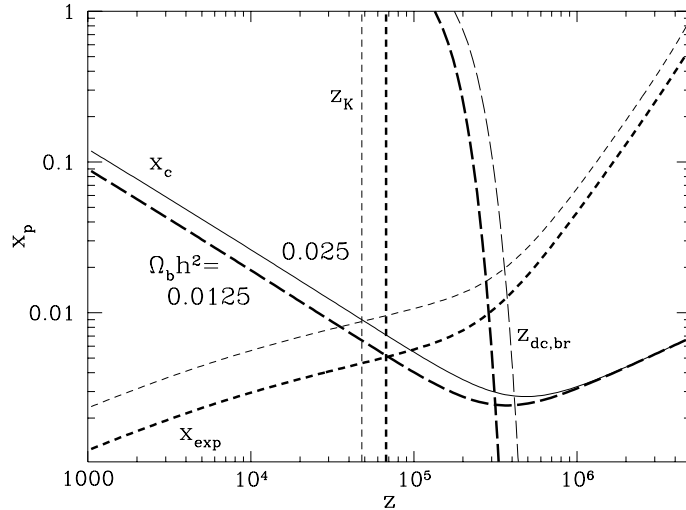


Figure 3.3: Critical Frequencies and Redshifts

Comparative rates for an $\Omega_b h^2 = 0.25$ universe and $\Omega_b h^2 = 0.0125$ (heavy) and 0.025 (light) Solid line is x_c , dashed line is x_{exp} , long dashed lines represent critical redshifts as labeled.

small distortions, analytic approximations are accurate and useful in understanding the thermalization process.

We shall see that thermalization to blackbody is determined at low frequencies where photons are most efficiently created and destroyed. Moreover, the low frequency regime carries the largest temperature distortions and is not yet well constrained by observation (see Fig. 1.1 and note that $x_p = 1$ is $\nu = 1.9\text{cm}^{-1}$).

At last scattering z_* , early spectral distortions are frozen in. However, Compton energy exchange is already ineffective at a higher redshift z_K . Up to $z = z_K$, Compton scattering moves the photons produced at low frequencies up or excesses at high frequencies down. It therefore plays a crucial role in the reduction of the chemical potential. After $z < z_K$, the high frequency chemical potential distortion is effectively frozen in, but the low frequency side can continue to evolve under bremsstrahlung.

An analytic approximation first employed by Zel'dovich and Sunyaev [185] and extended by Danese and De Zotti [41] to include double Compton scattering is quite useful for understanding the evolution. It assumes that one or more of the three processes are effective enough to establish quasi-static conditions:

$$\left(\frac{\partial f}{\partial t}\right) = \left(\frac{\partial f}{\partial t}\right)_K + \left(\frac{\partial f}{\partial t}\right)_{br} + \left(\frac{\partial f}{\partial t}\right)_{dc} \simeq 0, \quad (3.57)$$

i.e. the rate of change of the spectrum can be considered slow. Because of the frequency dependence of double Compton scattering and bremsstrahlung, equation (3.57) is valid for the entire spectrum only when $z \gg z_K$.

3.3.1 Chemical Potential Era

Let us first consider early evolution. We may always re-express the spectrum in terms of a frequency-dependent “chemical potential,”

$$f(x_p) = \frac{1}{\exp[x_p + \mu'(x_p)] - 1}, \quad (3.58)$$

without loss of generality. The complete kinetic equation in the quasi-static approximation, *i.e.* equation (3.57), then becomes

$$\begin{aligned} \frac{1}{x_p^2} \frac{d}{dx_p} \left[x_p^4 \frac{\exp[x_p + \mu'(x_p)]}{(\exp[x_p + \mu'(x_p)] - 1)^2} \frac{d\mu'}{dx_p} \right] = \\ \left(\frac{t_K}{t_{br}} + \frac{t_K}{t_{dc}} \frac{I_{BE}}{I_P} \right) \frac{e^{x_p}}{e^{x_p} - 1} \frac{\exp[\mu'(x_p)] - 1}{\exp[x_p + \mu'(x_p)] - 1}. \end{aligned} \quad (3.59)$$

If we make the further approximation that $g(x_p) \simeq g(x_{c,br})$, we may express this as

$$\frac{1}{x_p^2} \frac{d}{dx_p} \left[x_p^4 \frac{\exp[x_p + \mu'(x_p)]}{(\exp[x_p + \mu'(x_p)] - 1)^2} \frac{d\mu'}{dx_p} \right] = 4x_c^2 \frac{e^{x_p}}{x_p^3} \frac{\exp[\mu'(x_p)] - 1}{\exp[x_p + \mu'(x_p)] - 1}, \quad (3.60)$$

for $x_p \ll 1$. Here we have used the relations $t_K/t_{br} = (x_{c,br}/x_p)^2$ and $t_K/t_{dc} = (x_{c,dc}/x_p)^2$.

For $\mu'(x_p) \ll x_p$, equation (3.60) has the solution

$$\mu'(x_p) = C_1 \exp[-2x_c/x_p]. \quad (3.61)$$

We have taken the solution corresponding to $\mu'(0) = 0$, since at very low frequency the spectrum is a Planck distribution. At high frequencies $x_p \gg x_c$, we expect that the spectrum will be Bose-Einstein with chemical potential μ . Thus if $\mu < x_c$ as is relevant for small distortions, the two solutions must match at the junction, *i.e.* $C_1 = \mu$.

It is convenient to describe these distortions from a blackbody spectrum as a ratio of the frequency dependent effective temperature to the temperature of an equilibrium distribution at T_e before last scattering,

$$\frac{T}{T_e} = \frac{x_p}{\ln[(1+f)/f]}. \quad (3.62)$$

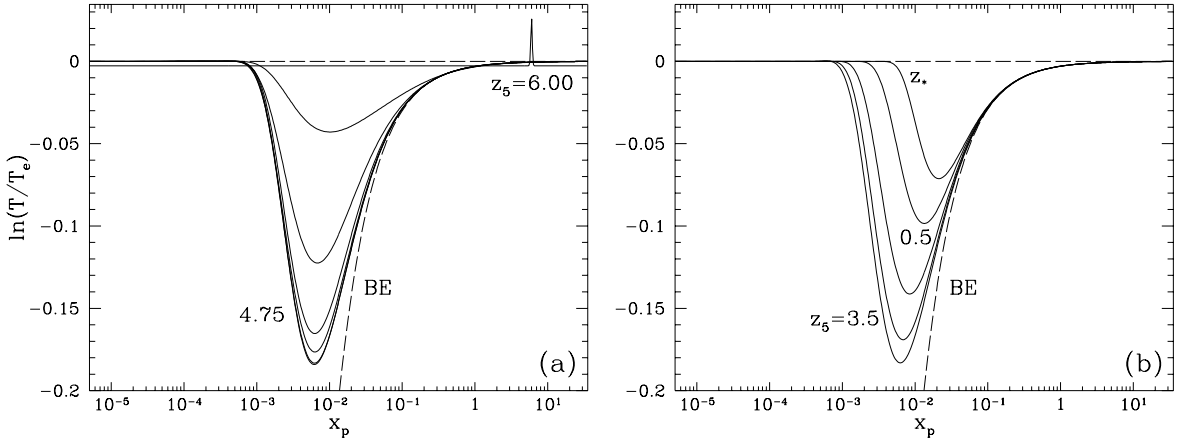


Figure 3.4: Low Frequency Evolution

Positive chemical potentials. Initial spectrum: injection at $x_h = 6$, $z_h = 6 \times 10^5$ with $\delta n_\gamma/n_\gamma = 2.5 \times 10^{-3}$, $\delta \rho_\gamma/\rho_\gamma = 5.5 \times 10^{-3}$, for $\Omega_0 h^2 = 0.25$, $\Omega_b h^2 = 0.025$. (a) Establishment of the Bose-Einstein spectrum, $4.75 \times 10^5 < z < 6.00 \times 10^5$ where $z_5 = z/10^5$ and curves are equally spaced in redshift. (b) Quasi-static evolution, $z_* < z < 3.5 \times 10^5$ and Bose-Einstein freeze out $z_K < z < z_*$. Long dashes represents best fit Bose-Einstein spectrum and the undistorted Planck distribution.

Notice that a spectrum of the form given by equation (3.61) obtains its peak distortions at

$$x_{peak} = 2x_c, \quad \mu < x_c(z) \quad (3.63)$$

at a value

$$\left(\ln \frac{T}{T_e} \right)_{max} = \ln \left(1 + \frac{C_1}{x_c e} \right) = \ln \left(1 + \frac{\mu}{2x_c e} \right). \quad (3.64)$$

Figure 3.4 shows the evolution of a spectrum, with $\mu(z_h) > 0$ ($\delta n_\gamma/n_\gamma = 2.5 \times 10^{-3}$, $\delta \rho_\gamma/\rho_\gamma = 5.5 \times 10^{-3}$) from the heating epoch $z_h = 6 \times 10^5$ to recombination. In Fig. 3.4a, the initial delta function injection is thermalized by Compton scattering and forms a Bose-Einstein distribution at high frequencies on a time scale comparable to t_K . Figure 3.4b displays the further quasi-static evolution of the spectrum and the gradual freeze-out of the processes for $z \lesssim z_K \simeq 5 \times 10^4$. Notice that significant evolution of the low frequency spectrum occurs between $z_* < z < z_K$, where quasi-static equilibrium cannot be maintained across the spectrum.

It is instructive to consider the evolution of this spectrum in some detail. Figure 3.4a displays the process of chemical potential formation via Compton scattering. At the epoch of heating z_h , the energy injected rapidly heats the electrons by Compton heating.

Initially, the temperature of the photons is thus lower than T_e across the spectrum. Therefore, there is a deficit of photons in comparison with a Planck distribution at temperature T_e . Scattering off hot electrons then comptonizes the spectrum, causing low frequency photons to gain energy. The high frequency deficit is consequently reduced at the expense of the low frequency until a Bose-Einstein distribution is attained at high frequencies. At this point, the spectrum ceases to evolve rapidly and comes into quasi-equilibrium. Bremsstrahlung and at the low redshifts considered here, to a lesser extent double Compton scattering, supplies photons at low frequencies. Thus the low frequency spectrum returns to a blackbody distribution at $x_p \ll x_c(z)$. The overall spectrum is described well by equation (3.61). For example, at $z = 4.75 \times 10^5$, $x_{peak} \simeq 6 \times 10^{-3}$ whereas $2x_c = 5.6 \times 10^{-3}$. The peak value is slightly underestimated by (3.64) due to the finite rate of Compton scattering. The peak amplitude of distortions is $(\log T/T_0) = 0.184$ whereas equation (3.64) predicts 0.183. The chemical potential is accurately predicted by equation (3.48): at $z = 4.75 \times 10^5$ has a high frequency tail with $\mu = 3.05 \times 10^{-3}$ whereas $\mu_{pred} = 3.06 \times 10^{-3}$.

Figure 3.4b displays the subsequent quasi-static evolution of the spectrum. At $x_c(z) < x_p < x_{exp}(z)$, photons are effectively produced *and* can be scattered up to affect the high frequency spectrum (*i.e.* reduce the chemical potential). Low frequency photons produced at $x_p < x_c(z)$ are absorbed by inverse bremsstrahlung and inverse double Compton scattering before they can be scattered up in frequency. Under the joint action of Compton scattering and the photon-creating processes, the spectrum evolves under equation (3.61). The peak of the distortion moves to higher frequencies since photons created by bremsstrahlung and double Compton scattering reduce the low frequency distortions. Higher frequency distortions are also affected as the newly created photons are scattered to higher and higher frequencies. However at these low redshifts, there is insufficient time to alter the chemical potential significantly. We will return to consider these effects in §3.4.

3.3.2 Chemical Potential Freeze Out

Compton upscattering ceases to be effective when the fractional energy shift drops below unity. Numerical results [24, 79] show that at $\tau_K = 16$ or after

$$\begin{aligned} z_{freeze} &= 4\sqrt{2}z_K \\ &= 4.01 \times 10^4 (1 - Y_p/2)^{-1/2} (x_e \Omega_b h^2)^{-1/2} \Theta_{2.7}^{1/2}, \end{aligned} \quad (3.65)$$

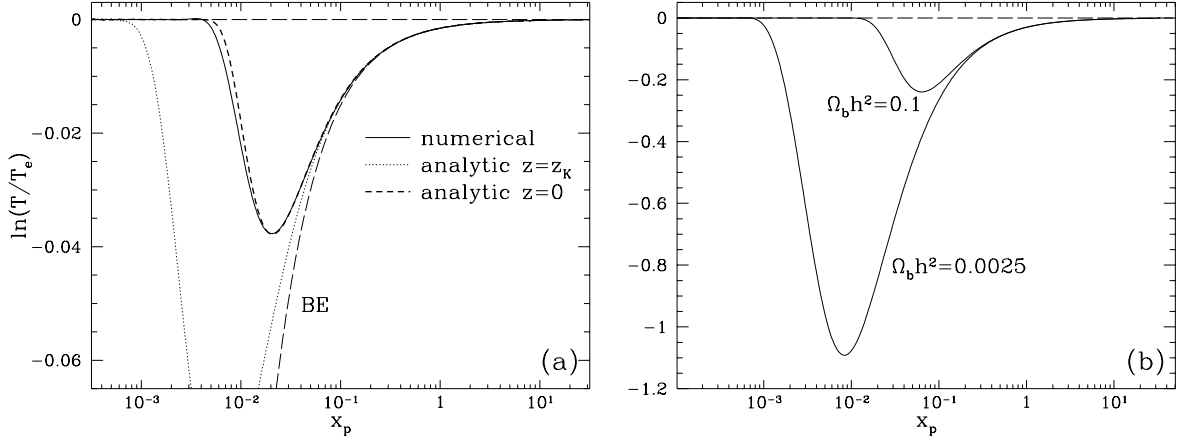


Figure 3.5: Low Frequency Spectrum

Positive chemical potentials (a) Comparison with analytic results. Initial spectrum: injection with $\delta n_\gamma/n_\gamma = 1.2 \times 10^{-3}$, $\delta \rho_\gamma/\rho_\gamma = 2.7 \times 10^{-3}$ at $x_h = 6$, $z_h = 4 \times 10^5$ for $\Omega_0 h^2 = 0.25$, $\Omega_b h^2 = 0.025$. The spectrum evolves significantly from Bose-Einstein freeze out at $z_c = 4\sqrt{2}z_K$ due to bremsstrahlung at low frequencies. The analytic estimation of the absorption optical depth provides an accurate description of the spectrum. (b) Baryon dependence of bremsstrahlung absorption. Initial spectrum: injection with $\delta n_\gamma/n_\gamma = 1.2 \times 10^{-2}$, $\delta \rho_\gamma/\rho_\gamma = 2.7 \times 10^{-2}$ at $x_h = 6$, for $\Omega_0 h^2 = 0.25$, $\Omega_b h^2 = 0.0025$, $z_h = 1.2 \times 10^6$ and $\Omega_b h^2 = 0.10$, $z_h = 1.5 \times 10^5$. The peak distortion measures the baryon content.

assuming radiation domination, the spectrum begins to deviate from Compton quasi-equilibrium equation (3.58),

$$f(z_{\text{freeze}}, x_p) = [\exp(x_p + \mu e^{-2x_c(z_{\text{freeze}})/x_p}) - 1]^{-1}. \quad (3.66)$$

However number changing processes are still effective at low frequencies (see Fig. 3.4b) and continue to return the spectrum to blackbody at higher and higher frequencies.

Let us see how to characterize the distribution [40, 24]. The kinetic equation in the absence of Compton upscattering can be described by the quasistatic condition

$$\frac{\partial f}{\partial t} \simeq \left(\frac{\partial f}{\partial t}\right)_{br} + \left(\frac{\partial f}{\partial t}\right)_{dc} \simeq 0. \quad (3.67)$$

We have already shown in equation (3.52) that its solution given an initial spectrum $f(z_{\text{freeze}}, x_p)$ is

$$f(z, x_p) = (e^{x_p} - 1)^{-1} \{1 - [1 - f(z_{\text{freeze}}, x_p)] \exp(-\tau_{abs}(z_{abs}, x_p))\}, \quad (3.68)$$

where z_{abs} is the redshift at which photon creating processes can act independently of Compton scattering. If bremsstrahlung dominates over double Compton scattering and

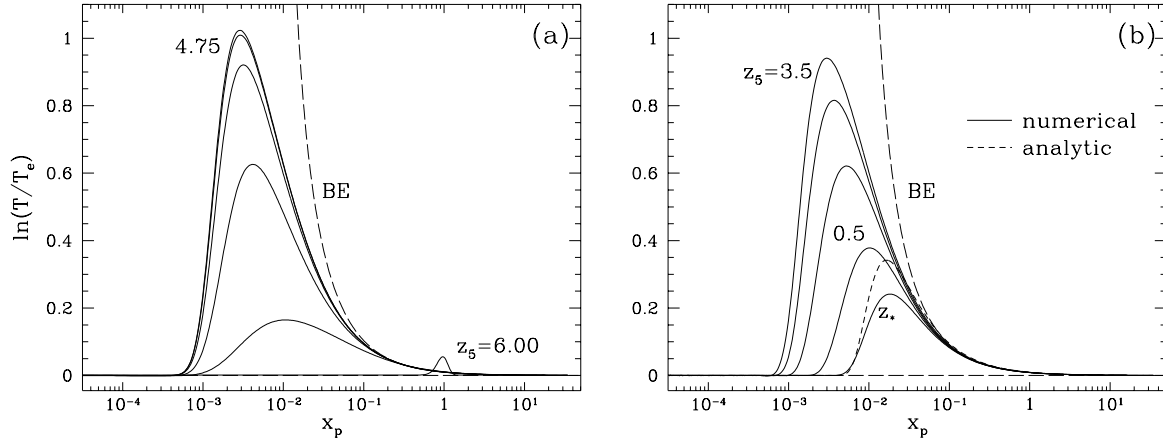


Figure 3.6: Negative Chemical Potentials

Initial spectrum: injection at $x_h = 1$, $z_h = 6 \times 10^5$ with $\delta n_\gamma/n_\gamma = 7.5 \times 10^{-3}$, $\delta \rho_\gamma/\rho_\gamma = 2.7 \times 10^{-3}$, for $\Omega_0 h^2 = 0.25$, $\Omega_b h^2 = 0.025$. (a) Establishment of the Bose-Einstein spectrum $4.75 \times 10^5 < z < 6.00 \times 10^5$ where $z_5 = z/10^5$ (equally spaced in redshift). (b) Quasi-static evolution and freeze out $z_* < z < 3.5 \times 10^5$. The analytic approximation for bremsstrahlung absorption is adequate but less accurate than for positive chemical potentials.

radiation over matter,

$$\tau_{abs}(z_{abs}, x_p) = 2 \frac{t_{exp}(z_{abs})}{t_{br}(z_{abs}, x_p)} = 1, \quad (3.69)$$

but bremsstrahlung only returns the spectrum to a blackbody after

$$\frac{t_K(z_{abs})}{t_{br}(z_{abs}, x_p)} = 1. \quad (3.70)$$

Thus the optical depth reaches unity *and* can create a blackbody only after

$$2 \frac{t_{exp}(z_{abs})}{t_K(z_{abs})} = 1. \quad (3.71)$$

Employing equation (3.34), we obtain the absorption redshift for equation (3.68)

$$z_{abs} = \sqrt{2} z_K \quad (3.72)$$

$$\simeq 1.00 \times 10^4 (1 - Y_p/2)^{-1/2} (x_e \Omega_b h^2)^{-1/2} \Theta_{2.7}^{1/2}, \quad (3.73)$$

which is of course close to but not exactly equal to z_K . As Fig. 3.5a shows, the agreement between this approximation and the numerical results is excellent. Notice that the final low frequency spectrum is quite sensitive to the baryon content $\Omega_b h^2$ since it is bremsstrahlung that returns the spectrum to blackbody (see Fig. 3.5b).

3.3.3 Negative Chemical Potentials

The simple analysis of energy and number balance of equation (3.48) shows us that negative chemical potentials are possible if the injection involves substantial photon number. Unlike positive chemical potentials however, at $x_p \leq |\mu|$, the spectrum becomes unphysical and *requires* the presence of photon absorbing processes to insure stability. If the predicted $\mu \lesssim x_{exp}(z)$, absorption is rapid enough to stabilize the spectrum. If not, down scattering will continue until μ is reduced to this level. Let us therefore first consider small negative chemical potentials where the stability criterion is satisfied.

Figure 3.6 displays the time evolution of a small $\mu < 0$ injection ($\delta n_\gamma/n_\gamma = 7.5 \times 10^{-3}$, $\delta \rho_\gamma/\rho_\gamma = 2.7 \times 10^{-3}$, $z_h = 4 \times 10^5$) for $\Omega_0 h^2 = 0.25$, $\Omega_b h^2 = 0.025$. Thermalization progresses in Fig. 3.6a as excess photons are downscattered until quasi-equilibrium is established with a $\mu < 0$ high frequency tail. In this case, number changing processes are effective at the $x_p = |\mu|$ instability and equation (3.48) gives a reasonable approximation to the chemical potential: $\mu = -9.8 \times 10^{-3}$, $\mu_{pred} = -1.0 \times 10^{-2}$. Quasi-static evolution is shown in Fig. 3.6b. During this stage, a small negative chemical potential behaves very much like a small positive chemical potential and obeys the form given by equation (3.61). After z_K , bremsstrahlung and double Compton scattering no longer have to compete with Compton scattering and sharply reduce the low frequency distortions, leaving the high frequency spectrum untouched. Again, the evolution of the spectrum between z_K and z_{rec} moves the peak of the distortion slightly upward in frequency. The analytic prediction of equation (3.68) accurately locates the frequency of the peak distortion but somewhat overestimates its magnitude due to the instability at $x_p \leq |\mu|$. For larger negative chemical potentials, this instability leads to rapid evolution as we shall show in §3.4.

3.3.4 Balanced Injection

One exceptional case is worth considering. When energy and number balance predicts $\mu \simeq 0$ by equation (3.48), a more careful analysis is necessary. For injection at the critical frequency, $x_h \simeq 3.6$, μ vanishes to first order in the perturbations. However, there is a difference between a $\mu \simeq 0$ case in which $\delta n_\gamma/n_\gamma$ and $\delta \rho_\gamma/\rho_\gamma$ are balanced so as to in effect cancel, and a case in which $\mu \simeq 0$ purely due to the intrinsic smallness of perturbations. Given sufficient time, the two *will* evolve toward the same final spectrum. However, the spectrum may not reach equilibrium by recombination since in the balanced case we can

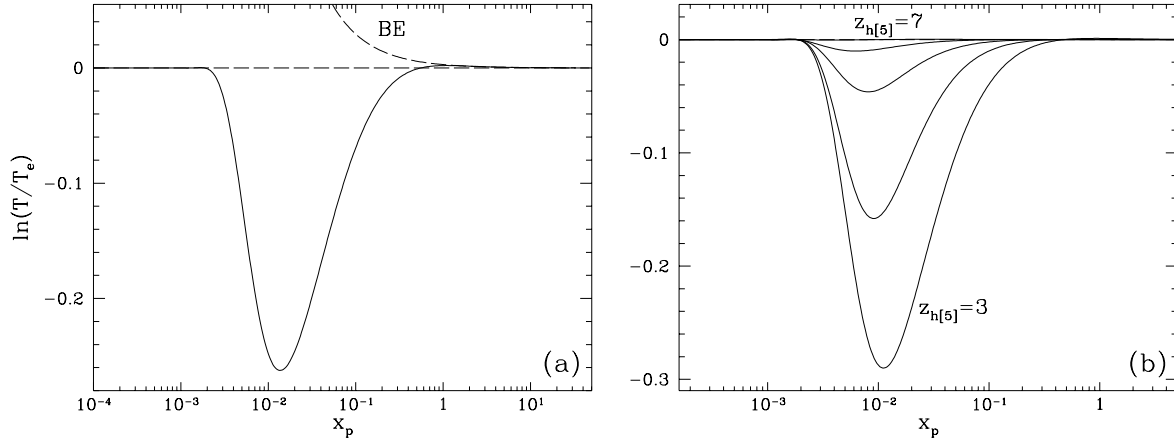


Figure 3.7: Balanced Injection

The number and energy injection are balanced to give $\mu = 0$ after reshuffling by Compton scattering. (a) Initial spectrum: injection at $x_h = 3.7$, $z_h = 2.5 \times 10^5$ with $\delta n_\gamma/n_\gamma = 0.16$, $\delta \rho_\gamma/\rho_\gamma = 0.22$ for $\Omega_0 h^2 = 0.25$, $\Omega_b h^2 = 0.025$. Dashed lines are best analytic fit for high frequencies (Bose-Einstein with negative chemical potential) and low frequencies (exponentially suppressed positive chemical potential). Note that low frequency distortions can be much larger than high frequency distortions would imply. (b) Time evolution of the spectrum for the same parameters as (a) save that $z_h = 3.0 \times 10^5$, 4.0×10^5 , 5.0×10^5 , 6.0×10^5 , 7.0×10^5 in order of decreasing distortions.

inject an arbitrarily large amount of energy. Large distortions take longer to thermalize even under Compton scattering. Specifically, the spectrum does not relax down to the final equilibrium configuration implied by equation (3.48) on a time-scale t_K . Instead, another type of quasi-equilibrium spectrum is established which in turn relaxes toward the actual equilibrium at a slower rate.

At injection, the electrons are heated as in the case of a positive chemical potential. Photons are then scattered up from low frequencies leaving a low frequency deficit of photons. However, just as in the case of the negative chemical potential, there is also an excess of photons at high frequencies. In fact, there is exactly the number needed to fill in the deficit at low frequencies. A quasi-equilibrium spectrum forms in which the high frequency spectrum behaves like a Bose-Einstein distribution with negative chemical potential, whereas the low frequency spectrum mimics one of a positive chemical potential. Given sufficient time, redistribution in frequency will reduce both the high frequency excess and the low frequency deficit. However, it is quite possible that the Comptonization process will freeze out before this has occurred.

Figure 3.7a displays an example. A large injection, $\delta n_\gamma/n_\gamma = 0.16$, $\delta \rho_\gamma/\rho_\gamma = 0.22$,

is introduced at $x_h = 3.7$ and $z_h = 2.5 \times 10^5$ in a universe with $\Omega_0 h^2 = 0.25$, $\Omega_b h^2 = 0.015$. The small shift in the critical frequency is due to the finite width of our so called “delta function” injection and second order effects. The high frequency spectrum fits well to $\mu = -2.89 \times 10^{-3}$, whereas the low frequency spectrum behaves as if $\mu \simeq 10^{-2}$ – almost an order of magnitude greater than the actual chemical potential at high frequencies.

If the injection occurs at earlier times, we expect that distortions will be reduced by the mechanism described above. Figure 3.7b displays the dependence on z_h for the same initial spectrum described for Fig. 3.7a. In order of decreasing distortions, the curves represent $z_h = 3.0 \times 10^5$, 4.0×10^5 , 5.0×10^5 , 6.0×10^5 , 7.0×10^5 . The high frequency regions can be fit to a Bose-Einstein spectrum of $\mu = -1.35 \times 10^{-3}$, -3.22×10^{-4} , -8.02×10^{-5} , -2.87×10^{-5} and $\mu \simeq 0$ respectively. For a redshift of $z_h = 7.0 \times 10^5$, the spectrum is fully thermalized under Compton scattering, leaving essentially no distortions from blackbody.

Notice also that even these curious spectra retain the same structure for the peak temperature distortion. This is because the analysis above for the location of the peak depends only on the balance between the number-changing processes and Compton scattering. This balance, in turn, depends on $\Omega_b h^2$ alone not the details of the positive, negative, or “zero” chemical potential injection. Equivalently, a measurement of the peak frequency yields information on the baryon density $\Omega_b h^2$ of the universe.

3.4 High Frequency Evolution

In §3.3.4, we have seen a special case in which the chemical potential can evolve purely under Compton scattering. However in the general case, the chemical potential only evolves if photons can be produced or absorbed at low frequencies. Furthermore, significant evolution of the high frequency spectrum, $x_p \gg x_c$, can only occur at $z > z_K$ since Compton scattering must be effective to redistribute these photons.

3.4.1 Analytic Approximations

The low frequency behavior governs the rate at which photons may be produced or absorbed and thus is critical in determining the evolution of the chemical potential. If there is no energy release after the epoch of heating z_h , the rate of change of the chemical potential can be derived in a fashion similar to equation (3.48) for a static chemical potential.

If we consider the number and energy density in the spectrum to be dominated by the high frequency Bose-Einstein form, equations (3.43) and (3.41) tell us

$$\begin{aligned}\frac{1}{a^3 n_{\gamma BE}} \frac{da^3 n_{\gamma BE}}{dt} &= \frac{1}{n_{\gamma P}} \frac{dn_{\gamma P}}{dT_e} \frac{dT_e}{dt} + 3 \frac{1}{a} \frac{da}{dt} + \frac{1}{\phi} \frac{d\phi}{d\mu} \frac{d\mu}{dt}, \\ \frac{1}{a^4 \rho_{\gamma BE}} \frac{da^4 \rho_{\gamma BE}}{dt} &= \frac{1}{\rho_{\gamma P}} \frac{d\rho_{\gamma P}}{dT_e} \frac{dT_e}{dt} + 4 \frac{1}{a} \frac{da}{dt} + \frac{1}{\psi} \frac{d\psi}{d\mu} \frac{d\mu}{dt} = 0.\end{aligned}\quad (3.74)$$

We may solve these two equations simultaneously to obtain:

$$\frac{d\mu}{dt} = - \left(\frac{4}{a^3 n_{\gamma BE}} \frac{da^3 n_{\gamma BE}}{dt} \right) / B(\mu), \quad (3.75)$$

where

$$B(\mu) = 3 \frac{d \ln \psi(\mu)}{d\mu} - 4 \frac{d \ln \phi(\mu)}{d\mu}. \quad (3.76)$$

Equation (3.75) was first derived by Sunyaev and Zel'dovich [162].

The rate of change of the number density is given by integrating the kinetic equation (3.21):

$$\begin{aligned}\frac{1}{a^3 n_{\gamma BE}} \frac{da^3 n_{\gamma BE}}{dt} &= \frac{1}{I_2 \phi(\mu)} \int dx_p x_p^2 \frac{\partial f_{BE}}{\partial t} \\ &= \frac{1}{I_2 \phi(\mu)} \left(\frac{I_{BE}}{I_P} J_{dc} + J_{br} \right),\end{aligned}\quad (3.77)$$

where I_{BE} is defined in equation (3.45) and

$$\begin{aligned}J_{dc} &= \int_0^{x_M} dx_p x_p^2 \frac{1}{t_{dc}} \left[\frac{1}{e^{x_p} - 1} - f \right], \\ J_{br} &= \int_0^{\infty} dx_p x_p^2 \frac{1}{t_{br}} \left[\frac{1}{e^{x_p} - 1} - f \right].\end{aligned}\quad (3.78)$$

We have introduced a cutoff $x_M \simeq 1$ in the integration for the double Compton scattering source term since the kinetic equation (3.17) is not valid for high frequencies. However, since double Compton scattering is extremely inefficient at high frequencies, we expect that the error involved in truncating the integral is negligible.

As we can see from equation (3.78), the change in the number of photons depends on the integral of the low frequency spectrum. From equation (3.61), we employ

$$f(t, x_p) = \frac{1}{\exp[x_p + \mu(t)] \exp(-2x_c/x_p) - 1}, \quad (3.79)$$

which is valid for small chemical potentials, $\mu(t) < x_c$. In the limit that only double Compton scattering is effective, we obtain

$$\frac{d\mu}{dt} = - \frac{\mu}{t_{\mu, dc}(z)}, \quad (3.80)$$

by employing equation (3.75). Here,

$$\begin{aligned} t_{\mu,dc}(z) &= \frac{1}{2}BI_2 \frac{t_K}{x_{c,dc}} \\ &= 2.09 \times 10^{33} (1 - Y_p/2)^{-1} (x_e \Omega_b h^2)^{-1} \Theta_{2.7}^{-3/2} z^{-9/2} \text{s}. \end{aligned} \quad (3.81)$$

As one might have guessed, the time scale is on order the Compton upscattering time t_K weighted by the portion of the spectrum where photons can be created and efficiently upscattered. The solution at the present time is

$$\mu(z=0) = \mu(z_h) \exp[-(z_h/z_{\mu,dc})^{5/2}], \quad (3.82)$$

with

$$z_{\mu,dc} = 4.09 \times 10^5 (1 - Y_p/2)^{-2/5} \Theta_{2.7}^{1/5} (x_e \Omega_b h^2)^{-2/5}. \quad (3.83)$$

This solution was first obtained by Danese and De Zotti [41].

For the case that bremsstrahlung dominates, a very similar equation holds:

$$\frac{d\mu}{dt} = -\frac{\mu}{t_{\mu,br}(z)}, \quad (3.84)$$

where

$$\begin{aligned} t_{\mu,br}(z) &= \frac{1}{2}BI_2 \frac{t_K}{x_{c,br}}, \\ &\simeq 3.4 \times 10^{25} (1 - Y_p/2)^{-1} (x_e \Omega_b h^2)^{-3/2} \Theta_{2.7}^{5/4} z^{-13/4} \text{s}, \end{aligned} \quad (3.85)$$

and we have approximated $g(x_{c,br}) \simeq 5.4$. These equations yield the solution

$$\mu(z=0) = \mu(z_h) \exp[-(z_h/z_{\mu,br})^{5/4}], \quad (3.86)$$

where

$$z_{\mu,br} \simeq 5.6 \times 10^4 (1 - Y_p/2)^{-4/5} (x_e \Omega_b h^2)^{-6/5} \Theta_{2.7}^{13/5}. \quad (3.87)$$

Let us call the smaller of these two redshifts z_μ . The characteristic redshifts for double Compton scattering and bremsstrahlung are equal for a universe with

$$\Omega_b h_{dc,br}^2 \simeq 0.084 (1 - Y_p/2)^{-1/2} x_e^{-1} \Theta_{2.7}^3. \quad (3.88)$$

For a universe with a higher baryon density, bremsstrahlung should dominate the evolution of the chemical potential.

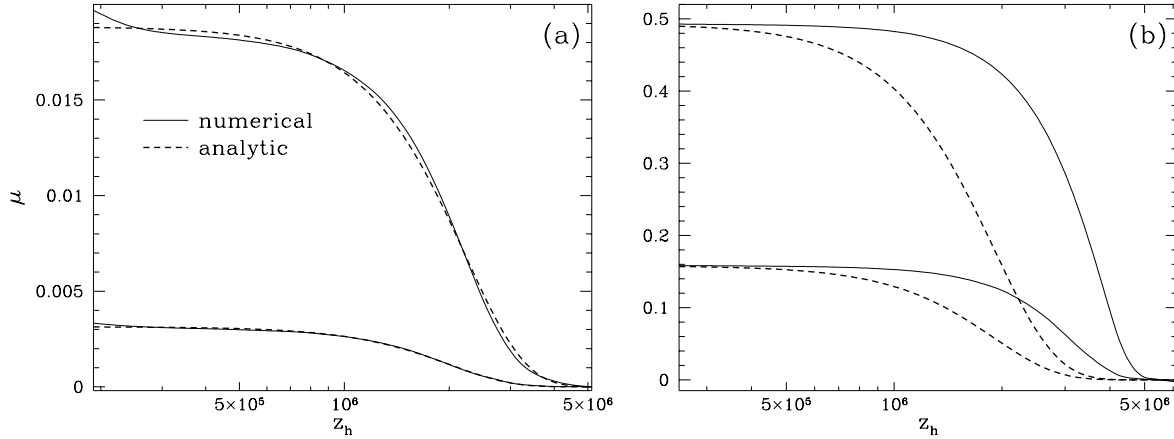


Figure 3.8: Positive Chemical Potential Evolution

(a) Small μ . Initial spectrum: injection of $\delta n_\gamma/n_\gamma = 5.4 \times 10^{-3}$, $\delta \rho_\gamma/\rho_\gamma = 2.0 \times 10^{-2}$ (top) and of $\delta n_\gamma/n_\gamma = 2.5 \times 10^{-3}$, $\delta \rho_\gamma/\rho_\gamma = 5.5 \times 10^{-3}$ (bottom) (b) Large μ . Initial spectrum: injection of $\delta n_\gamma/n_\gamma = 1.5 \times 10^{-1}$, $\delta \rho_\gamma/\rho_\gamma = 5.5 \times 10^{-1}$ (top) and of $\delta n_\gamma/n_\gamma = 4.4 \times 10^{-2}$, $\delta \rho_\gamma/\rho_\gamma = 1.6 \times 10^{-1}$ (bottom). All injections at $x_h = 6$ with $\Omega_0 h^2 = 0.25$, $\Omega_b h^2 = 0.025$.

3.4.2 Numerical Results

The analytic solutions are only valid in the case $\mu(z) < x_c(z) \ll 1$, for all z . In many cases, $\mu(z) < x_c(z)$ during some but not all epochs of interest $z < z_h$. Furthermore, a small chemical potential today could have originated from a large distortion $\mu \gtrsim 1$ at high redshifts. Thus we must examine the behavior numerically and look for deviations from the forms of equations (3.82) and (3.86).

Let us now examine the evolution of the chemical potential in a low $\Omega_b h^2$ universe as implied by nucleosynthesis. Numerical solutions suggest that equation (3.82) is indeed a good approximation for sufficiently small chemical potentials. The bottom curve of Fig. 3.8a shows such a case (the solid line is the numerical result, the dotted line is the best fit) for a initial spectrum $\mu(z_h) = 3.15 \times 10^{-3}$ with $\Omega_0 h^2 = 0.25$, $\Omega_b h^2 = 0.025$. For comparison, $z_{\mu, pred} = 1.9 \times 10^6$ whereas $z_{\mu, fit} = 2.0 \times 10^6$. For very low redshifts, there has been insufficient time to scatter photons upwards in frequency to establish a perfect Bose-Einstein spectrum. Thus the effective chemical potential deviates toward larger distortions that equation (3.48) predicts. The top curve of Fig. 3.8a shows an intermediate case: $\mu(z_h) = 1.84 \times 10^{-2}$ for $\Omega_0 h^2 = 0.25$, $\Omega_b h^2 = 0.025$. We see that equation (3.82) still describes the evolution adequately but not entirely. The best fit value of the critical redshift has shifted

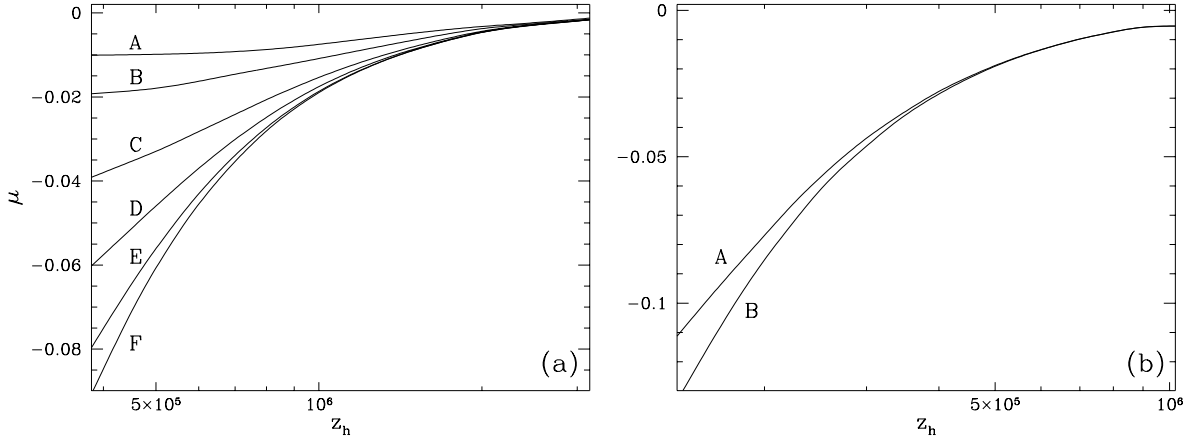


Figure 3.9: Negative Chemical Potential Evolution

(a) Time evolution and instability: (A) $\delta n_\gamma/n_\gamma = 7.5 \times 10^{-3}$, $\delta \rho_\gamma/\rho_\gamma = 2.7 \times 10^{-3}$; (B) $\delta n_\gamma/n_\gamma = 1.5 \times 10^{-2}$, $\delta \rho_\gamma/\rho_\gamma = 5.5 \times 10^{-3}$; (C) $\delta n_\gamma/n_\gamma = 3.8 \times 10^{-2}$, $\delta \rho_\gamma/\rho_\gamma = 1.4 \times 10^{-2}$; (D) $\delta n_\gamma/n_\gamma = 7.5 \times 10^{-2}$, $\delta \rho_\gamma/\rho_\gamma = 2.7 \times 10^{-2}$; (E) $\delta n_\gamma/n_\gamma = 1.5 \times 10^{-1}$, $\delta \rho_\gamma/\rho_\gamma = 5.5 \times 10^{-2}$; (F) $\delta n_\gamma/n_\gamma = 3.0 \times 10^{-1}$, $\delta \rho_\gamma/\rho_\gamma = 1.1 \times 10^{-1}$. All for injection at $x_h = 1$ with $\Omega_0 h^2 = 0.25$, $\Omega_b h^2 = 0.025$. (b) High baryon case. (A) $\delta n_\gamma/n_\gamma = 1.5 \times 10^{-1}$, $\delta \rho_\gamma/\rho_\gamma = 5.5 \times 10^{-2}$; (B) $\delta n_\gamma/n_\gamma = 3.0 \times 10^{-1}$, $\delta \rho_\gamma/\rho_\gamma = 1.1 \times 10^{-1}$, for injections at $x_h = 1$ with $\Omega_0 h^2 = 0.25$, $\Omega_b h^2 = 0.10$.

upwards however, $z_{\mu,fit} = 2.2 \times 10^6$. This is because $\mu > x_c(z)$ for a significant portion of the evolution and the spectrum evolves more slowly than the exponential suppression given in equation (3.82) suggests.

We can see this effect quite clearly for larger chemical potentials. Figure 3.8b shows such an evolution again for $\Omega_0 h^2 = 0.25$, $\Omega_b h^2 = 0.025$. The top curve has an initial spectrum with $\mu(z_h) = 4.9 \times 10^{-1}$ and the bottom $\mu(z_h) = 1.6 \times 10^{-1}$. Dashed lines represent the predictions of equation (3.82). For redshifts much less than z_μ , the chemical potential stays roughly constant, evolving more slowly than predictions. However, the fall off at high redshifts is correspondingly much more precipitous than equation (3.82) would imply. The effective redshift at which a substantial suppression of the chemical potential occurs is increased but only by a factor of order unity. Attempts to fit the curves to the form of equation (3.82) yield $z_{\mu,fit} = 3.5 \times 10^6$, 3.0×10^6 for (A) and (B) respectively. Note that in these cases, unlike Fig. 3.8a, the form of equation (3.82), even leaving z_μ arbitrary, does not accurately trace the evolution. In general then, a large positive chemical potential will exhibit stability up to a redshift $z \simeq z_\mu$ and then fall dramatically.

For negative chemical potentials, the spectrum can only establish such a quasi-static equilibrium as required for the analytic form if $|\mu| < x_{exp}(z_\mu)$. For larger negative

chemical potentials and $z > z_\mu$, inverse double Compton scattering absorbs excess photons and returns the distribution to $|\mu| \simeq x_{exp}(z_\mu)$ nearly instantaneously. Thus *regardless of initial input of photons* the evolution for $z > z_\mu$ will be approximately the same. Figure 3.9 displays this effect for $\Omega_0 h^2 = 0.25$, $\Omega_b h^2 = 0.025$. Here, we inject successively larger numbers of photons and energies at the same frequency $x_h = 1$ (see figure captions for details). At high redshifts, we see that $\mu(z)$ saturates at some maximum value regardless of the initial input. For lower redshifts $z < z_\mu$, double Compton scattering is not sufficiently efficient and must wait for Compton scattering to bring photons down to low enough frequencies to be absorbed. As can be seen in Fig. 3.9, large negative chemical potentials are rapidly evolved away under such a process. Quasi-equilibrium is never established and deviations from equation (3.82) are large. Small negative chemical potentials (A) exhibit the same stability as positive chemical potentials at redshifts $z < z_\mu$. Note also that this effect is only weakly dependent on $\Omega_b h^2$ (assuming double Compton scattering dominance):

$$x_{exp,dc}(z_\mu) \simeq 0.1(x_e \Omega_b h^2)^{-1/10} \Theta_{2.7}^{-7/10}, \quad (3.89)$$

and so the critical chemical potential $\mu_c \sim -x_{exp}(z_\mu)$ is roughly independent of both energy injection and $\Omega_b h^2$. Fig. 13 (curves A, B) shows the evolution of the same initial spectra as Fig. 12 (curves E, F) for $\Omega_b h^2 = 0.10$. Notice that μ_c is roughly the same in both cases. Of course, we expect the estimate of the numerical constant above to be extremely crude, since z_μ itself is only an order of magnitude estimate of the epoch of effectiveness of double Compton scattering. Figures 12 and 13 show that the actual value is $\mu_c \simeq -0.02$ and is reasonably independent of $\Omega_b h^2$. Thus, elastic and double Compton scattering conspire to eliminate negative chemical potentials greater than a few percent. This result is approximately independent of the details of injection given reasonable choices of the cosmological parameters.

In summary, the analytic formulae equations (3.82) and (3.86) describe the evolution adequately (to order of magnitude) within the range $-10^{-2} \lesssim \mu \lesssim 1$. The existence of a small positive chemical potential would place tight constraints on the energy injection mechanism. If the injection took place at $z_K < z < z_\mu$, the energy injected would have to be correspondingly small. Only if it took place in the narrow region, $z_\mu < z < \text{few} \times z_\mu$, would a large energy injection and a small chemical potential be consistent. Any earlier, and an arbitrarily large injection would be thermalized. On the other hand, the existence of a small negative chemical potential is not *a priori* as restrictive, since a large amount of energy can

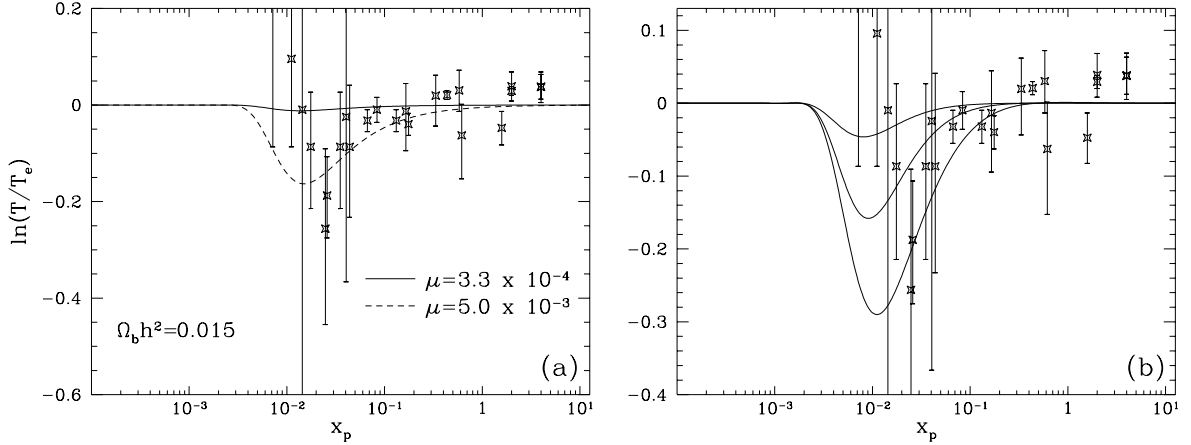


Figure 3.10: Comparison with Observational Data

Observational low frequency data compared with (a) numerical results for $\mu = 0.005$ (dotted) and $\mu = 3.3 \times 10^{-4}$ (solid line) with $\Omega_b h^2 = 0.015$ and $\Omega_0 h^2 = 0.25$. Only the latter satisfies the high frequency FIRAS data [116]. (b) Balanced injection $\mu = -1.3 \times 10^{-3}$, -3.2×10^{-4} , -8.0×10^{-5} in the Wien tail. Notice that this special case has large low frequency and small high frequency distortions.

be injected and still lead to a small value for $|\mu|$. However, for an extremely small negative chemical potential, $\mu \lesssim -3.3 \times 10^{-4}$ as required by observation, these considerations do not apply since we have determined numerically that the critical chemical potential for stability is $\mu \simeq -10^{-2}$. Extremely small negative chemical potentials are stable and equally as restrictive as small positive chemical potentials.

The *non-existence* of μ -distortions of course would rule out non-standard cosmologies with energy injection in the range $z_K < z < z_\mu$ but say very little about the physics for $z > z_\mu$. The one case that escapes these consideration is the balanced injection scenario. The chemical potential is driven to zero not by photon-creating processes but by Compton scattering itself and thus z_μ is not the critical redshift for this process. Furthermore, an arbitrary amount of energy can be injected and still maintain a small chemical potential even at comparatively low redshifts. However, even this case is likely to leave a low frequency signature which is potentially observable (§3.3.4). Thus the lack of low frequency distortions would set tight bounds on all possible injections in this redshift range. Let us now consider the observational status of spectral distortions.

3.5 Comparisons and Constraints

3.5.1 Observational Data

The *COBE* FIRAS experiment [116] places tight constraints on the presence of a Bose-Einstein distortion in the Wien tail, $|\mu| < 3.3 \times 10^{-4}$. However, as we have shown in §3.3, the Rayleigh-Jeans regime is also interesting. It is there that we expect to see the largest temperature distortions, specifically at the frequency $x_{peak} \simeq 2x_c(z_K)$. For a positive chemical potential, the effective temperature of the Rayleigh-Jeans part of the spectrum is lower than that of the Wien tail. Figure 3.10 plots the observational results. As is immediately obvious, the average effective temperature of the CMB in the Rayleigh-Jeans region *is* apparently lower than that of the Wien tail. Note we normalize the distortions so that “ T_e ” is the temperature of the Wien tail which is fixed by FIRAS to be 2.726K [116]. We have also plotted the results of our numerical integration for comparison. This marginally significant distortion implies a quite large chemical potential in the Wien tail (dotted line, $\mu = 0.005$) that is inconsistent with the FIRAS results. If we were to require that the Wien distortions be consistent with FIRAS (solid line, $\mu = 3.3 \times 10^{-4}$), the predicted distortions in the Rayleigh-Jeans region are far too small to explain the effect of the systematically low effective temperature.

There exists one loophole: the case of balanced injection (see §3.3.4). Although, $\mu \rightarrow 0$ given sufficient Comptonization, the distortions will typically freeze in before this occurs. Particularly interesting is the fact that Rayleigh-Jeans distortions can be significant while Wien distortions remain minimal (see Fig. 3.10b). Note that the distortions on the low frequency side are consistent with large deviations, implied by the low effective temperature of the measurements, even when high frequency distortions are consistent with the already restrictive $|\mu| < 3.3 \times 10^{-4}$. Alternatively, we can say that the injection of a large amount of energy even for this exceptional case in which high frequency distortions vanish will lead to significant low frequency distortions in many cases.

Low frequency distortions of this type may eventually be confirmed, and it is therefore interesting to see what information can be gained from them. As described in §3.3, their behavior is governed by the balance between bremsstrahlung and Compton scattering which is in turn sensitive to $\Omega_b h^2$ [see equation (3.55)]. At low frequencies, bremsstrahlung returns the spectrum to a Planck distribution. Thus, the critical frequency at which distortions peak is a *measure* of $\Omega_b h^2$. For illustrative purposes, Fig. 3.11 displays the

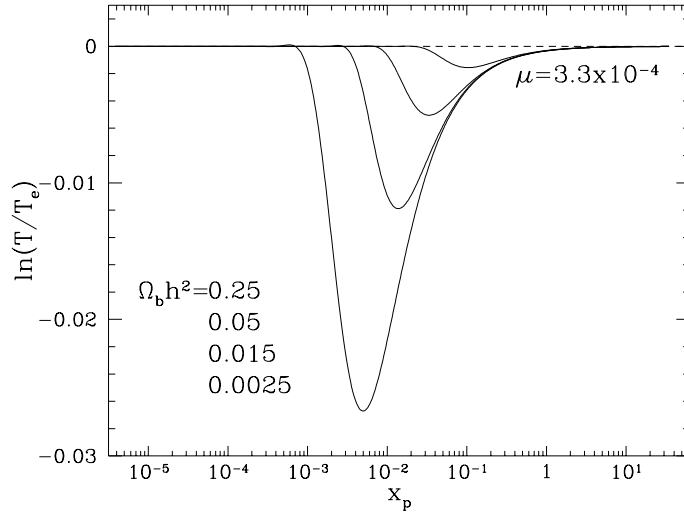


Figure 3.11: Rayleigh-Jeans Baryon Dependence

Predicted spectral distortions with $\mu = 3.3 \times 10^{-4}$ for $\Omega_b h^2 = 0.0025, 0.015, 0.050, 0.25$ in order of decreasing distortions for $\Omega_0 h^2 = 0.25$.

spectra obtained numerically for $\Omega_b h^2 = 0.0025, 0.015, 0.050, 0.25$ respectively, for a fixed Bose-Einstein Wien tail with $\mu = 3.3 \times 10^{-4}$. Note that the distortions are independent of the heating epoch, z_h , and the details of injection as long as the Wien tail is fixed in this manner. On the other hand, the location of the peak distortions is measurably different for various choices of $\Omega_b h^2$. Even in the balanced case, the dependence of the peak distortion on $\Omega_b h^2$ is essentially unchanged. Thus improved measurements in the Rayleigh-Jeans regime are desirable for a twofold purpose. If distortions are seen, they will give an interesting constraint on $\Omega_b h^2$ in all possible cases. If they are not seen, it will close the last loophole in the regime $z_{rec} < z < z_\mu$ for significant injection of energy. Let us now consider two specific examples of energy injection constraints implied by the FIRAS measurement.

3.5.2 Constraints on Decaying Particles

If the energy injection arises from the decay of a massive particle, we may translate the constraint on μ into one on the mass m_X , lifetime t_X and branching ratio f_X for decay to photons of such a species [142, 53, 78]. For this case, the number density of photons injected is negligible compared with that in the background. Therefore, the spectral distortions are determined by the integral of the fractional contributions to the CMB energy per comoving volume during the decay. Assuming that the comoving number density of species X decays

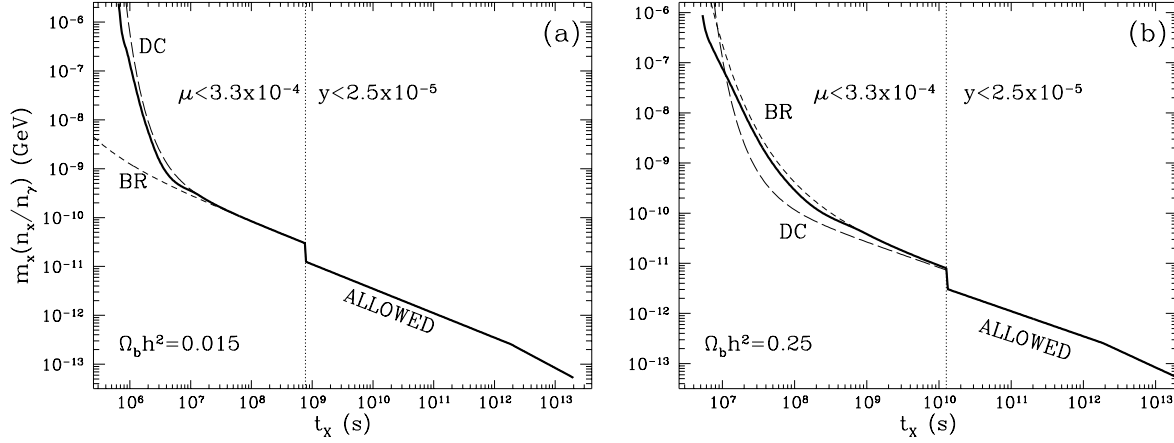


Figure 3.12: Particle Decay Constraints

FIRAS constraints on μ and y limit the energy injection from massive unstable particles. Dashed lines are the analytic approximation. Dotted vertical lines mark the approximate transition between μ and y distortions. In reality the constraint curve makes a smooth transition between the two. For low $\Omega_b h^2$, double Compton dominates the thermalization, whereas for high $\Omega_b h^2$ bremsstrahlung is most efficient.

exponentially in time with lifetime t_X , we obtain

$$\frac{\delta\epsilon_\gamma}{\epsilon_\gamma} = \frac{m_X}{T(t_{eff})} \left(\frac{n_X}{n_\gamma} \right) f_X, \quad (3.90)$$

where $T(t)$ is the CMB temperature and (n_X/n_γ) is the ratio of the number densities before decay. The functional form of equation (3.90) is identical to the case in which all particles decayed at a time $t_{eff} = [\Gamma(1 + \beta)]^{1/\beta} t_X$ for a time temperature relation of $T \propto t^{-\beta}$. Here Γ is the usual gamma function.

Let us first consider the case of a low $\Omega_b h^2$ universe as implied by nucleosynthesis where double Compton scattering dominates the thermalization process. For small energy injection, the analytic considerations of §3.4.1 yield

$$\begin{aligned} \mu_0 &\simeq 4.0 \times 10^2 \left(\frac{t_X}{s} \right)^{1/2} \exp \left[- (t_{\mu,dc}/t_X)^{5/4} \right] \left(\frac{m_X}{1\text{GeV}} \right) f_X n_X/n_\gamma \\ &< 3.3 \times 10^{-4}, \end{aligned} \quad (3.91)$$

where

$$t_{\mu,dc} = 1.46 \times 10^8 \Theta_{2.7}^{-12/5} (x_e \Omega_b h^2)^{4/5} (1 - Y_p/2)^{4/5} \text{s}. \quad (3.92)$$

We have assumed here that we are in the radiation-dominated epoch where $T \propto t^{-1/2}$.

If $\Omega_b h^2 \gtrsim 0.1$, bremsstrahlung dominates and this constraint becomes

$$\begin{aligned} \mu_0 &= 4.0 \times 10^2 \left(\frac{t_X}{\text{s}}\right)^{1/2} \exp\left[-(t_{\mu,br}/t_X)^{5/8}\right] \left(\frac{m_X}{1\text{GeV}}\right) f_X n_X / n_\gamma \\ &< 3.3 \times 10^{-4} \end{aligned} \quad (3.93)$$

where

$$t_{\mu,br} \simeq 7.7 \times 10^9 \Theta_{2.7}^{-36/5} (x_e \Omega_b h^2)^{12/5} (1 - Y_p/2)^{8/5} \text{s}. \quad (3.94)$$

The *weaker* of the two constraints, equations (3.91) and (3.93), is the relevant one to consider for intermediate cases.

Since the analytic formulae are only valid for small injections of energy $\delta\rho_\gamma/\rho_\gamma \ll 1$, we expect deviations from these predictions when particles decay near the thermalization epoch. Large distortions are thermalized less rapidly than the analytic approximations above would imply. Figure 3.12 displays the results of numerical integration for (a) $\Omega_b h^2 = 0.015$ and (b) $\Omega_b h^2 = 0.25$. In both cases, particles with a short lifetime that decay during the critical epoch for thermalization are more stringently constrained than analytic predictions, also plotted, would suggest. For late decays, Compton scattering can no longer establish a Bose-Einstein spectrum. Instead, the spectrum can be described by the Compton- y parameter which is related to the energy release by $\delta\rho_\gamma/\rho_\gamma = 4y$. We also plot the constraints implied by the most current value of $y < 2.5 \times 10^{-5}$ [116].

3.5.3 Dissipation of Acoustic Waves

Energy injection into the CMB occurs even in standard models for structure formation through the dissipation of acoustic waves by photon diffusion (see §5.2.3). The energy stored in the perturbations of the spatial distribution of the photons is transferred to distortions in the spectrum. The lack of observable spectral distortions can be used to limit the amount of power in acoustic waves before dissipation. By comparing this with the amount of power measured at large scales by the *COBE* DMR experiment, we can constrain the slope of the primordial power spectrum [163, 38, 179, 76].

By employing the relation between energy injection and chemical potential distortions equation (3.48), we can generalize equation (3.80) for the evolution of chemical potential distortions to the case where energy is being continuously injected into the CMB,

$$\frac{d\mu}{dt} \simeq -\frac{\mu}{t_{\mu,dc}} + 1.4 \frac{Q}{\rho_\gamma}, \quad (3.95)$$

where Q/ρ_γ is the rate of fractional energy injection. This equation can immediately be solved as

$$\mu \simeq 1.4 \int_0^{t(z_{\text{freeze}})} dt \frac{Q(t)}{\rho_\gamma} \exp[-(z/z_{\mu,dc})^{5/2}], \quad (3.96)$$

where $z_{\mu,dc}$ is given in (3.83) and $t(z_{\text{freeze}})$ is the time of Bose-Einstein freeze out when energy injection can no longer be thermalized [see equation (3.65)].

The average energy density in a plane acoustic wave in the photon-baryon fluid is given by $\rho_s \simeq \rho_{\gamma b} c_s^2 \langle \Delta_{\gamma b}^2 \rangle$, where $\rho_{\gamma b} = \rho_\gamma + \rho_b$ and $\Delta_{\gamma b}$ are the density and density perturbation in the photon-baryon fluid, and the brackets denote an average over an oscillation of the acoustic wave. Since μ distortions arise at $z > z_{\text{freeze}} > z_{\text{eq}}$, we can take the radiation-dominated limit, where the sound speed is $c_s^2 = 1/3$, and

$$\langle \delta_{\gamma b}^2 \rangle \simeq \langle |\Delta_\gamma(t, k)|^2 \rangle = \frac{1}{2} |\Delta_\gamma(\eta, k)|^2. \quad (3.97)$$

Therefore, the rate of fractional energy injection

$$\frac{Q(t)}{\rho_\gamma} = - \sum_k \frac{1}{3} \frac{d \langle |\Delta_\gamma(k, t)|^2 \rangle}{dt}. \quad (3.98)$$

The energy density perturbation in the photons Δ_γ in the acoustic phase is discussed in §5.2.3 and found to be related to the initial potential perturbation $\Phi(0, k)$ by

$$\Delta_\gamma(t, k) = 6\Phi(0, k) \exp[-(k/k_D)^2], \quad (3.99)$$

for adiabatic perturbations, where the diffusion scale is $k_D(z) = 2.34 \times 10^{-5} \Theta_{2.7} (1 - Y_p/2)^{1/2} (\Omega_B h^2)^{1/2} z^{3/2}$ Mpc⁻¹.

To perform the sum over k modes, we must make an assumption about the form of the initial power spectrum. The simplest and most often employed assumption is a pure power law $k^3 |\Phi(0, k)|^2 = B k^{n-1}$, where $n = 1$ is the scale-invariant Harrison-Zel'dovich spectrum. Inserting these expressions into equation (3.96), both the sum over k and the integral over time can be performed analytically for leading to,

$$\mu = 1.4 F(n) \frac{V_x}{2\pi^2} 36 k_D^3 |\Phi(0, k_D)|^2 \Big|_{z=z_\mu}, \quad (3.100)$$

where

$$F(n) = \frac{1}{10} \Gamma[(n+1)/2] \Gamma[3(n-1)/5, (z_{\text{freeze}}/z_\mu)^{5/2}]. \quad (3.101)$$

with $\Gamma(m, x)$ as the incomplete gamma function. If n is significantly greater than unity, the incomplete gamma function $\Gamma(m, x) \rightarrow \Gamma(m)$ since $z_{\text{freeze}}/z_\mu \ll 1$ and $F(n)$ is roughly of order unity.

It is easy to interpret this result. If $n > 1$, the smallest waves carry the most energy, and the distortion comes almost entirely from the waves that damped at the thermalization epoch. Prior to thermalization, no distortion survives due to the rapidity of the double Compton process. On the other hand if $n < 1$, the fractional energy injection from dissipation will be a maximum at the latest relevant time, *i.e.* recombination. This implies that the constraint from spectral distortions will come from the upper limit on Compton- y distortions. However if the spectrum is normalized at large scales, for $n < 1$ the power decreases at small scales leaving no useful constraint.

Let us see how perturbations on the damping scale are related to the large scale temperature fluctuations seen by the *COBE* satellite. In adiabatic models, these arise mainly from the Sachs-Wolfe effect,

$$C_\ell \simeq \frac{9}{200\sqrt{\pi}} BV \eta_0^{1-n} \frac{\Gamma[(3-n)/2]\Gamma[\ell+(n-1)/2]}{\Gamma[(4-n)/2]\Gamma[\ell+(5-n)/2]} \quad (3.102)$$

from equation (6.10), where the observed rms anisotropy is

$$\left(\frac{\Delta T}{T}\right)_{rms}^2 = \frac{1}{4\pi} \sum_{\ell=2}^{\infty} (2\ell+1) W_\ell C_\ell, \quad (3.103)$$

and is measured to be $(\Delta T/T)_{rms} = 1.12 \pm 0.10 \times 10^{-5}$ [10]. The COBE window function is approximately $W_\ell = \exp[-\ell(\ell+1)\sigma^2]$, with $\sigma = 0.0742$ being the gaussian width of the 10° FWHM beam. This relation sets the normalization B for the initial conditions $k^3|\Phi(0,k)|^2 = Bk^{n-1}$ as a function of the spectral index n . Substitution back into equation (3.100) yields the amplitude of the chemical potential distortion.

Note that the dependence on the cosmological parameters Ω_0 , Ω_b , h is quite weak: approximately $\mu \propto (\Omega_b^{1/10} h^{6/5})^{1-n} \Omega_0^{(2-n)/2}$. Hence for $n \simeq 1$, μ is completely independent of h and Ω_b . Moreover, μ is nearly independent of Ω_b for *all* n , since raising Ω_b makes both the damping length shorter and the thermalization redshift smaller.

It is also useful to provide an approximate inversion of equation (3.100):

$$n \simeq 1 + \frac{\ln[C_1 \Omega_0^{-0.46} \mu / (\Delta T/T)_{10^\circ}^2]}{\ln[C_2 (\Omega_b h^2)^{-1/10} (\Omega_0 h^2)^{-1/2} I(\Omega_0)]} \quad (3.104)$$

where we find the constants $C_1 = 5.6 \times 10^{-3}$ and $C_2 = 8.9 \times 10^5$ and the small logarithmic correction $I(\Omega_0) \simeq 1 - 0.085 \ln \Omega_0$. One can verify that this is an excellent approximation within the range $1.0 < n < 2.0$ and the allowable cosmological parameters. Note that the dependence of $n - 1$ on μ and the normalization is only logarithmic, and its dependence on

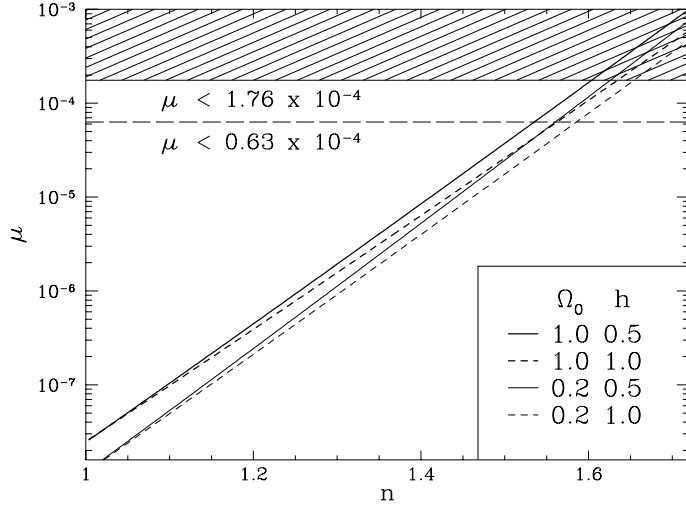


Figure 3.13: Diffusion Dissipation and Limits on n

Spectral distortions from the dissipation of acoustic waves for an initial adiabatic density perturbation spectrum of $k^3|\Psi(0, k)|^2 = Bk^{n-1}$ in an $\Omega_0 + \Omega_\Lambda = 1$ flat universe, normalized to give the *COBE* DMR rms of $(\Delta T/T)_{10^\circ} = 1.12 \times 10^{-5}$. With the uncertainties on both the DMR and FIRAS measurements, the conservative 95% upper limit is effectively $\mu < 1.76 \times 10^{-4}$. The constraint on n is weakly dependent on cosmological parameters. We have also plotted the optimistic limit of $\mu < 0.63 \times 10^{-4}$ discussed in the text.

the cosmological parameters is almost entirely negligible. Even relatively large changes in μ or the normalization will not greatly affect the constraint on n .

The best fit value of μ to the spectral data from the FIRAS experiment is $\mu = -1.2 \pm 1.1 \times 10^{-4}$ (68% CL) [116]. Naively speaking, this provides an upper limit on *positive* $\mu < 0.6 \times 10^{-4}$ (95% CL). However since $\mu \geq 0$ for damping distortions, a more conservative bound is obtained by renormalizing the quoted probability distribution, assumed to be Gaussian, under the condition that μ is positive. This is clearly the most reasonable approach if $\mu < 0$ were unphysical, which is not necessarily the case. Nonetheless, since this method provides a *conservative* limit, we employ it for the main result of our analysis. Taking into account the *COBE* DMR measurement errors and adopting a $4\mu\text{K}$ cosmic variance, $(\Delta T/T)_{rms}(10^\circ) = 1.12 \pm 0.18 \times 10^{-5}$ [10], we find

$$\frac{\mu}{(\Delta T/T)_{10^\circ}^2} < 1.4 \times 10^4 \quad (95\% \text{CL}). \quad (3.105)$$

This would be equivalent to an upper limit of $\mu < 1.76 \times 10^{-4}$ for a fixed normalization at the mean value of the DMR detection. Using equation (3.105), we set a limit on the slope $n < 1.60$ for $h = 0.5$ and $n < 1.63$ for $h = 1.0$ (see Fig. 3.13) for $\Omega_0 = 1$ with

similar but slightly less stringent limits for Λ -dominated universes ($\Omega_0 < 1$). If we were even more conservative, using $|\mu| < 3.3 \times 10^{-4}$ to imply $\mu < 3.3 \times 10^{-4}$, the constraints shift negligibly: $n < 1.65$ ($h = 0.5$) and $n < 1.68$ ($h = 1.0$). On the other hand, employing the more optimistic bound and taking into account the COBE DMR measurement, we obtain $\mu < 0.63 \times 10^{-4}$ which implies $n < 1.54$ ($h = 0.5$) and $n < 1.56$ ($h = 1.0$). These limits are nearly independent of Ω_B and do not change within the nucleosynthesis bounds of $0.011 < \Omega_B h^2 < 0.016$ [171, 151].

Chapter 4

Multifluid Perturbation Theory

It is the nature of things that they are ties to each other.

—Chuang-tzu, 20

In the standard scenario, small perturbations in the early universe grow by gravitational instability to form the wealth of structure observable today. At the early stages of this process, relevant for CMB work, fluctuations are still small and can be described in linear perturbation theory. What makes the problem non-trivial is the fact that different components such as the photons, baryons, neutrinos, and collisionless dark matter, have different equations of state and interactions. It is therefore necessary to employ a fully relativistic multifluid treatment to describe the coupled evolution of the individual particle species.

In this chapter, we discuss the framework for the evolution of fluctuations. Since in linear theory, each normal mode evolves independently we undertake a mode by mode analysis. In open universes, this decomposition implies a lack of structure above the curvature scale for random-field perturbations. We show why this arises and how it might be avoided by generalizing the random field condition [111]. The evolution itself is governed by the energy momentum conservation equations in the perturbed space-time and feeds back into the metric fluctuations through the Einstein equations. In Newtonian gauge, they generalize the Poisson equation familiar from the non-relativistic theory.

It is often useful to express the evolution in other gauges, *e.g.* the popular synchronous gauge and the total matter gauge. We discuss the general issue of gauge transformations and their effect on the interpretation of perturbations. Various aspects of the evolution appear simplest for different choices of gauge. Those that involve the photons are most straightforward to analyze in Newtonian form where redshift and infall correspond

to classical intuition. On the other hand, the evolution of the matter and consequently the metric perturbations themselves becomes simpler on its own rest frame. We therefore advocate a hybrid representation for perturbations based on the so-called ‘‘gauge invariant’’ formalism.

4.1 Normal Mode Decomposition

4.1.1 Laplacian Eigenfunctions

Any scalar fluctuation may be decomposed in eigenmodes of the Laplacian

$$\nabla^2 Q \equiv \gamma^{ij} Q_{|ij} = -k^2 Q, \quad (4.1)$$

where ‘|’ represents a covariant derivative with respect to the three metric γ_{ij} of constant curvature $K = -H_0^2(1 - \Omega_0 - \Omega_\Lambda)$. In flat space $\gamma_{ij} = \delta_{ij}$, and Q is a plane wave $\exp(i\mathbf{k}\cdot\mathbf{x})$. As we shall discuss further in §4.1.3, the eigenfunctions are complete for $k \geq \sqrt{-K}$. Therefore we define the transform of an arbitrary square integrable function $F(\mathbf{x})$ as [110, 111]

$$F(\mathbf{x}) = \sum_{|\mathbf{k}| \geq \sqrt{-K}} F(\mathbf{k}) Q(\mathbf{x}, \mathbf{k}) = \frac{V}{(2\pi)^3} \int_{|\mathbf{k}| \geq \sqrt{-K}}^\infty d^3 k F(\mathbf{k}) Q(\mathbf{x}, \mathbf{k}). \quad (4.2)$$

In the literature, an alternate convention is often employed in order to make the form appear more like the flat space convention [175, 83],

$$F(\mathbf{x}) = \sum_{\tilde{k}} \tilde{F}(\tilde{\mathbf{k}}) Q(\mathbf{x}, \tilde{\mathbf{k}}) = \frac{V}{(2\pi)^3} \int_0^\infty d^3 \tilde{k} \tilde{F}(\tilde{\mathbf{k}}) Q(\mathbf{x}, \tilde{\mathbf{k}}), \quad (4.3)$$

where the auxiliary variable $\tilde{k}^2 = k^2 + K$. The relation between the two conventions is

$$\begin{aligned} \tilde{k} |\tilde{F}(\tilde{k})|^2 &= k |F(k)|^2 \\ &= (\tilde{k}^2 - K)^{1/2} |F([\tilde{k}^2 - K]^{1/2})|^2 \end{aligned} \quad (4.4)$$

and should be kept in mind when comparing predictions. In particular, note that power law conditions in \tilde{k} for \tilde{F} are not the same as in k for F .

Vectors and tensors needed in the description of the velocity and stress perturbation can be constructed from the covariant derivatives of Q and the metric tensor,

$$\begin{aligned} Q_i &\equiv -k^{-1} Q_{|i}, \\ Q_{ij} &\equiv k^{-2} Q_{|ij} + \frac{1}{3} \gamma_{ij} Q, \end{aligned} \quad (4.5)$$

where the indices are to be raised and lowered by the three metric γ_{ij} and γ^{ij} . The following identities can be derived from these definitions and the commutation relation for covariant derivatives (see *e.g.* [173] eqn. 8.5.1) [99]

$$\begin{aligned} Q_i^{|i} &= kQ, \\ \nabla^2 Q_i &= -(k^2 - 3K)Q_i, \\ Q_{i|j} &= -k(Q_{ij} - \frac{1}{3}\gamma_{ij}Q), \\ Q^i_i &= 0, \\ Q_{ij}^{|j} &= \frac{2}{3}k^{-1}(k^2 - 3K)Q_i, \end{aligned} \tag{4.6}$$

and will be useful in simplifying the evolution equations.

4.1.2 Radial Representation

To gain intuition about these functions, let us examine an explicit representation. In radial coordinates, the 3-metric becomes

$$\gamma_{ij}dx^i dx^j = -K^{-1}[d\chi^2 + \sinh^2 \chi(d\theta^2 + \sin^2 \theta d\phi^2)], \tag{4.7}$$

where the distance is scaled to the curvature radius $\chi = \sqrt{-K}\eta$. Notice that the (comoving) angular diameter distance is $\sinh \chi$, leading to an exponential increase in the surface area of a shell with radial distance $\chi \gg 1$. The Laplacian can now be written as

$$\gamma^{ij}Q_{|ij} = -K \sinh^{-2} \chi \left[\frac{\partial}{\partial \chi} \left(\sinh^2 \chi \frac{\partial Q}{\partial \chi} \right) + \sin^{-1} \theta \frac{\partial}{\partial \theta} \left(\sin \theta \frac{\partial Q}{\partial \theta} \right) + \sin^{-2} \theta \frac{\partial^2 Q}{\partial \phi^2} \right]. \tag{4.8}$$

Since the angular part is independent of curvature, we may separate variables such that $Q = X_\nu^\ell(\chi)Y_\ell^m(\theta, \phi)$, where $\nu^2 = \tilde{k}^2/(-K) = -(k^2/K + 1)$. From equation (4.8), it is obvious that the spherically symmetric $\ell = 0$ function is

$$X_\nu^0(\chi) = \frac{\sin(\nu\chi)}{\nu \sinh \chi}. \tag{4.9}$$

As expected, the change in the area element from a flat to curved geometry causes $\chi \rightarrow \sinh \chi$ in the denominator. The higher modes are explicitly given by [106, 71]

$$X_\nu^\ell(\chi) = (-1)^{\ell+1} M_\ell^{-1/2} \nu^{-2} (\nu^2 + 1)^{-\ell/2} \sinh^\ell \chi \frac{d^{\ell+1}(\cos \nu \chi)}{d(\cosh \chi)^{\ell+1}}, \tag{4.10}$$

and become $j_\ell(k\eta)$ in the flat space limit, where

$$\begin{aligned} M_\ell &\equiv \prod_{\ell'=0}^{\ell} K_{\ell'}, \\ K_0 &= 1, \\ K_\ell &= 1 - (\ell^2 - 1)K/k^2, \quad \ell \geq 1, \end{aligned} \tag{4.11}$$

which all reduce to unity as $K \rightarrow 0$. This factor represents our convention for the normalization of the open universe functions,

$$\int X_\nu^\ell(\chi) X_{\nu'}^{\ell'}(\chi) \sinh^2 \chi d\chi = \frac{\pi}{2\nu^2} \delta(\nu - \nu') \delta(\ell - \ell'), \tag{4.12}$$

and is chosen to be similar to the flat space case. In the literature, the normalization is often chosen such that $\tilde{X}_\nu^\ell = X_\nu^\ell M_\ell^{-1/2}$ is employed as the radial eigenfunction [175, 83].

It is often more convenient to generate these functions from their recursion relations. One particularly useful relation is [3]

$$\frac{d}{d\eta} X_\nu^\ell = \frac{\ell}{2\ell + 1} k K_\ell^{1/2} X_\nu^{\ell-1} - \frac{\ell + 1}{2\ell + 1} k K_{\ell+1}^{1/2} X_\nu^{\ell+1}. \tag{4.13}$$

Since radiation free streams on radial null geodesics, we shall see that the collisionless Boltzmann equation takes on the same form as equation (4.13).

4.1.3 Completeness and Super Curvature Modes

Open universe eigenfunctions possess the curious property that they are complete for $k \geq \sqrt{-K}$. Mathematically, this is easier to see with a choice of three metric such that $\gamma_{ij} = \delta_{ij}/(-Kz^2)$, the so-called flat-surface representation [175, 111]. In this system $-\infty < x < \infty$, $-\infty < y < \infty$, $0 \leq z < \infty$ and surfaces of constant z are flat. The Laplacian

$$\nabla^2 Q = -Kz^2 \left(\frac{\partial^2 Q}{\partial x^2} + \frac{\partial^2 Q}{\partial y^2} + \frac{\partial^2 Q}{\partial z^2} \right) + Kz \frac{\partial Q}{\partial z}, \tag{4.14}$$

has eigenfunctions

$$Q = z \exp(ik_1 x + ik_2 y) K_{i\nu}(k_\perp z), \tag{4.15}$$

where $K_{i\nu}$ is the modified Bessel function and $k_\perp^2 = k_1^2 + k_2^2$. Since the x and y dependences are just those of plane waves, which we know are complete, we need only concern ourselves with the z coordinate. As pointed out by Wilson [175], it reduces to a Kontorovich-Lebedev

transform,

$$\begin{aligned} g(y) &= \int_0^\infty f(x)K_{ix}(y)dx, \\ f(x) &= 2\pi^{-2}x \sinh(x\pi) \int_0^\infty g(y)K_{ix}(y)y^{-1}dy, \end{aligned} \quad (4.16)$$

i.e. there exists a completeness relation,

$$\int_0^\infty d\nu \nu \sinh(\pi\nu)K_{i\nu}(k_\perp z)K_{i\nu}(k_\perp z') = \frac{\pi^2}{2}z\delta(z - z'). \quad (4.17)$$

Therefore an arbitrary square integrable function $F(\mathbf{x})$ can be decomposed into a sum of eigenmodes of $\nu \geq 0$,

$$\begin{aligned} F(\mathbf{x}) &= \int_0^\infty \nu \sinh(\pi\nu)d\nu \int_{-\infty}^\infty dk_1 \int_{-\infty}^\infty dk_2 F(\mathbf{k})Q(\mathbf{x}, \mathbf{k}), \\ F(\mathbf{k}) &= \frac{1}{2\pi^4} \int_0^\infty \frac{dz}{z^3} \int_0^\infty dx \int_0^\infty dy F(\mathbf{x})Q(\mathbf{x}, \mathbf{k}), \end{aligned} \quad (4.18)$$

where Q is given by equation (4.15) and $\mathbf{x} = (x, y, z)$ and $\mathbf{k} = (k_1, k_2, \nu)$. Since $\nu \geq 0$ implies $k \geq \sqrt{-K}$, this establishes the claimed completeness.

This completeness property leads to a seemingly bizarre consequence if we consider random fields, *i.e.* randomly phased superpositions of these eigenfunctions. To see this, return to the radial representation. In Fig. 4.1, we plot the spherically symmetric $\ell = 0$ mode given by equation (4.9). Notice that its first zero is at $\chi = \pi/\nu$. This is related to the completeness property: as $\nu \rightarrow 0$, we can obtain arbitrarily large structures. For this reason, ν or more specifically $\tilde{k} = \nu\sqrt{-K}$ is often thought of as the wavenumber [175, 95]. However, the *amplitude* of the structure above the curvature scale is suppressed as $e^{-\chi}$. Prominent structure lies only at the curvature scale as $\nu \rightarrow 0$. In this sense, k should be regarded as the effective wavelength. This is important to bear in mind when considering the meaning of “scale invariant” fluctuations. In fact, the $e^{-\chi}$ behavior is *independent* of the wavenumber and ℓ , if $\chi \gg 1$.

This peculiarity in the eigenmodes has significant consequences. Any random phase superposition of the eigenmodes X_ν^ℓ will have exponentially suppressed structure larger than the curvature radius. Even though completeness tells us that arbitrarily large structure can be built out of the X_ν^ℓ functions, it *cannot* be done without correlating the modes. This is true even if the function is square integrable, *i.e.* has support only to a finite radius possibly above the curvature scale.

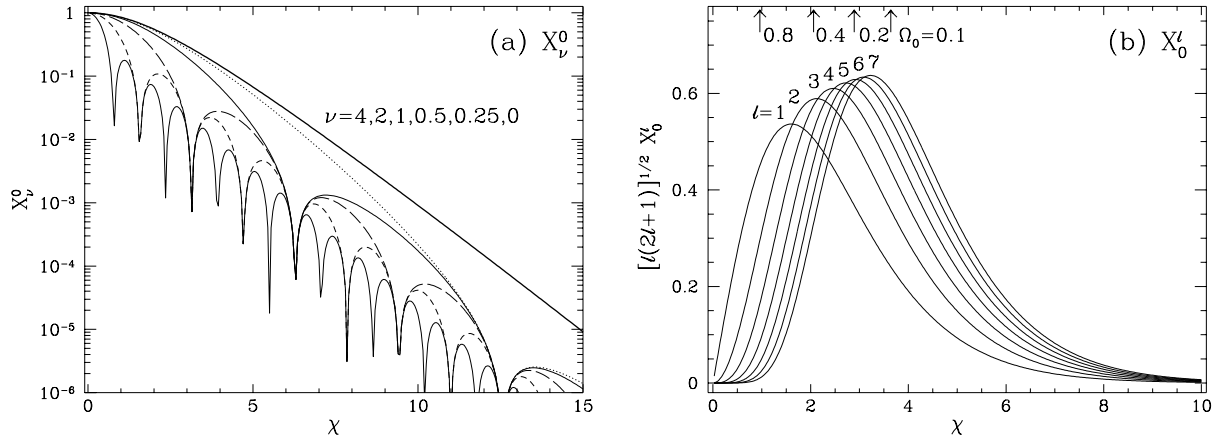


Figure 4.1: Open Radial Eigenfunctions

(a) The isotropic $\ell = 0$ function for several values of the wavenumber ν . The zero crossing moves out to arbitrarily large scales as $\nu \rightarrow 0$, reflecting completeness. However, the function retains prominent structure only near the curvature scale $\chi \simeq 1$. A random superposition of these low ν modes cannot produce more than exponentially decaying structure larger than the curvature scale. (b) Low order multipoles in the asymptotic limit $\nu \rightarrow 0$. If most power lies on the curvature scale, the ℓ -mode corresponding to the angle that the curvature radius subtends will dominate the anisotropy. The normalization is appropriate for comparing contributions to the anisotropy $\ell(2\ell + 1)C_\ell/4\pi$. Also shown is the location of the horizon $\chi = \eta_0\sqrt{-K}$ for several values of Ω_0 . If contributions to the anisotropy come from a sufficiently early epoch, the dominant ℓ -mode for the curvature scale will peak at this value (see *e.g.* Fig. 6.10).

Is the lack of structure above the curvature scale reasonable? The fundamental difference between open and flat universes is that the volume increases exponentially with the radial coordinate above the curvature scale $V(\chi_c) \sim [\sinh(2\chi_c) - 2\chi_c]$. Structure above the curvature scale implies correlations over vast volumes [95]. It is in fact difficult to conceive of a model where correlations do not die exponentially above the curvature radius. The random phase hypothesis has been proven to be valid for inflationary perturbations in a pre-existing open geometry [110] and only mildly violated for bubble nucleated open universes [180].

Lyth and Woszcynza [111] show that the simplest way to generalize random fields to include supercurvature scale structure is to employ an overcomplete set of eigenfunctions extended by analytic continuation of the modes to $k \rightarrow 0$. Of course, random phase conditions in the overcomplete set can alternatively be expressed as initially phase correlated modes of the complete set. In linear theory, the evolution of each mode is independent and thus there is no distinction between the two. Including supercurvature perturbations merely

amounts to extending the treatment to the full range of k : $0 \leq k < \infty$. All of the equations presented here may be extended in this manner with the understanding that $\nu \rightarrow |\nu|$.

4.1.4 Higher Angular Functions

We will often need to represent a general function of position \mathbf{x} and angular direction $\boldsymbol{\gamma}$, *e.g.* for the radiation distribution. As we have seen, vector and tensors constructed from Q and its covariant derivatives can be used to represent dipoles and quadrupoles, $G_1 = \gamma^i Q_i$ and $G_2 = \frac{3}{2} \gamma^i \gamma^j Q_{ij}$. We can generalize these considerations and form the full multipole decomposition [175]

$$F(\mathbf{x}, \boldsymbol{\gamma}) = \sum_{\mathbf{k}} \sum_{\ell=0}^{\infty} \tilde{F}_{\ell}(\mathbf{k}) G_{\ell}(\mathbf{x}, \boldsymbol{\gamma}, \mathbf{k}), \quad (4.19)$$

where

$$G_{\ell}(\mathbf{x}, \boldsymbol{\gamma}, \mathbf{k}) = (-k)^{-\ell} Q_{|i_1 \dots i_{\ell}}(\mathbf{x}, \mathbf{k}) P_{\ell}^{i_1 \dots i_{\ell}}(\mathbf{x}, \boldsymbol{\gamma}), \quad (4.20)$$

and

$$\begin{aligned} P_0 &= 1, & P_1^i &= \gamma^i, \\ P_2^{ij} &= \frac{1}{2}(3\gamma^i \gamma^j - \gamma^{ij}), \\ P_{\ell+1}^{i_1 \dots i_{\ell+1}} &= \frac{2\ell+1}{\ell+1} \gamma^{(i_1} P_{\ell}^{i_2 \dots i_{\ell+1})} - \frac{\ell}{\ell+1} \gamma^{(i_1 i_2} P_{\ell-1}^{i_3 \dots i_{\ell+1})}, \end{aligned} \quad (4.21)$$

with parentheses denoting symmetrization about the indices. For flat space, this becomes $G_{\ell} = (-i)^{\ell} \exp(i\mathbf{k} \cdot \mathbf{x}) P_{\ell}(\mathbf{k} \cdot \boldsymbol{\gamma})$, where P_{ℓ} is an ordinary Legendre polynomial. Notice that along a path defined by fixed $\boldsymbol{\gamma}$, the flat G_{ℓ} becomes $j_{\ell}(k\eta)$ after averaging over k -directions. Traveling on a fixed direction away from a point is the same as following a radial path outwards. Thus fluctuations *along* this path can be decomposed in the radial eigenfunction. It is therefore no surprise that G_{ℓ} obeys a recursion relation similar to X_{ν}^{ℓ} ,

$$\begin{aligned} \gamma^i G_{\ell|i} &= \frac{d}{d\eta} G[\mathbf{x}(\eta), \boldsymbol{\gamma}(\eta)] = \dot{x}^i \frac{\partial}{\partial x^i} G_{\ell} + \dot{\gamma}^i \frac{\partial}{\partial \gamma^i} G_{\ell} \\ &= k \left\{ \frac{\ell}{2\ell+1} K_{\ell} G_{\ell-1} - \frac{\ell+1}{2\ell+1} G_{\ell+1} \right\}, \end{aligned} \quad (4.22)$$

which follows from equation (4.20) and (4.21) via an exercise in combinatorics involving commutations of covariant derivatives [64]. Here we take $\mathbf{x}(\eta)$ to be the integral path

along γ . By comparing equations (4.13) and (4.22), the open universe generalization of the relation between G_ℓ and the radial eigenfunction is now apparent:

$$G_\ell[\mathbf{x}(\eta), \gamma(\eta)] = M_\ell^{1/2} X_\nu^\ell(\eta). \quad (4.23)$$

The only conceptual difference is that for the radial path that we decompose fluctuations on, γ is not constant. The normalization also suggests that to maintain close similarity to the flat space case, the multipole moments should be redefined as

$$F(\mathbf{x}, \gamma) = \sum_{|\mathbf{k}| \geq \sqrt{-K}} \sum_{\ell=0}^{\infty} F_\ell(\mathbf{k}) M_\ell^{-1/2} G_\ell(\mathbf{x}, \gamma, \mathbf{k}), \quad (4.24)$$

which again differ from the conventions of [175, 83] by a factor $M_\ell^{1/2}$.

4.2 Newtonian Gauge Evolution

4.2.1 Metric Fluctuations

In linear theory, the evolution of each k mode is independent. We can therefore assume without loss of generality that the equation of motion for the k th mode can be obtained by taking a metric of the form,

$$\begin{aligned} g_{00} &= -(a/a_0)^2(1 + 2\Psi Q), \\ g_{0i} &= 0, \\ g_{ij} &= (a/a_0)^2(1 + 2\Phi Q)\gamma_{ij}, \end{aligned} \quad (4.25)$$

assuming the Newtonian representation, and correspondingly

$$\begin{aligned} g^{00} &= -(a_0/a)^2(1 - 2\Psi Q), \\ g^{0i} &= 0, \\ g^{ij} &= (a_0/a)^2(1 - 2\Phi Q)\gamma^{ij}, \end{aligned} \quad (4.26)$$

where employ the notation $\Psi(\eta, \mathbf{x}) = \Psi(\eta)Q(\mathbf{x})$, *etc.* and drop the k index where no confusion will arise. Note that we have switched from time to conformal time as the zero component. The Christoffel symbols can now be written as

$$\Gamma_{00}^0 = \frac{\dot{a}}{a} + \dot{\Psi}Q,$$

$$\begin{aligned}
\Gamma_{0i}^0 &= -k\Psi Q_i, \\
\Gamma_{00}^i &= -k\Psi Q^i, \\
\Gamma_{0j}^i &= \left(\frac{\dot{a}}{a} + \dot{\Phi}Q\right)\delta_j^i, \\
\Gamma_{ij}^0 &= \left[\frac{\dot{a}}{a} + \left(-2\frac{\dot{a}}{a}\Psi + 2\frac{\dot{a}}{a}\Phi + \dot{\Phi}\right)Q\right]\gamma_{ij}, \\
\Gamma_{jk}^i &= {}^{(s)}\Gamma_{jk}^i - k\Phi(\delta_j^i Q_k + \delta_k^i Q_j - \gamma_{jk}Q^i),
\end{aligned} \tag{4.27}$$

where ${}^{(s)}\Gamma_{jk}^i$ is the Christoffel symbol on the unperturbed 3-surface γ_{ij} .

Finally we can write the Einstein tensor as $G_{\mu\nu} = \bar{G}_{\mu\nu} + \delta G_{\mu\nu}$, where

$$\begin{aligned}
\bar{G}^0_0 &= -3\left(\frac{a_0}{a}\right)^2 \left[\left(\frac{\dot{a}}{a}\right)^2 + K \right], \\
\bar{G}^i_j &= -\left(\frac{a_0}{a^2}\right)^2 \left[2\frac{\ddot{a}}{a} - \left(\frac{\dot{a}}{a}\right)^2 + K \right] \delta^i_j, \\
\bar{G}^0_i &= \bar{G}^i_0 = 0
\end{aligned} \tag{4.28}$$

are the background contributions and

$$\begin{aligned}
\delta G^0_0 &= 2\left(\frac{a_0}{a}\right)^2 \left[3\left(\frac{\dot{a}}{a}\right)^2 \Psi - 3\frac{\dot{a}}{a}\dot{\Phi} - (k^2 - 3K)\Phi \right] Q, \\
\delta G^0_i &= 2\left(\frac{a_0}{a}\right)^2 \left[\frac{\dot{a}}{a}k\Psi - k\dot{\Phi} \right] Q_i, \\
\delta G^i_0 &= -2\left(\frac{a_0}{a}\right)^2 \left[\frac{\dot{a}}{a}k\Psi - k\dot{\Phi} \right] Q^i, \\
\delta G^i_j &= 2\left(\frac{a_0}{a}\right)^2 \left\{ \left[2\frac{\ddot{a}}{a} - \left(\frac{\dot{a}}{a}\right)^2 \right] \Psi + \frac{\dot{a}}{a}[\dot{\Psi} - \dot{\Phi}] \right. \\
&\quad \left. - \frac{k^2}{3}\Psi - \dot{\Phi} - \frac{\dot{a}}{a}\dot{\Phi} - \frac{1}{3}(k^2 - 3K)\Phi \right\} \delta^i_j Q \\
&\quad - \left(\frac{a_0}{a}\right)^2 k^2(\Psi + \Phi)Q^i_j,
\end{aligned} \tag{4.29}$$

are the first order contributions from the metric fluctuations.

4.2.2 Conservation Equations

The equations of motion under gravitational interactions are most easily obtained by employing the conservation equations. The stress-energy tensor of a non-interacting fluid is covariantly conserved $T^{\mu\nu}_{;\mu} = 0$. The $\nu = 0$ equation gives energy density conservation, *i.e.* the continuity equation; the $\nu = i$ equations give momentum conservation, *i.e.* the Euler

equation. To first order, the stress energy tensor of a fluid x , possibly itself a composite of different particle species, is

$$\begin{aligned}
T_0^0 &= -(1 + \delta_x Q)\rho_x, \\
T_i^0 &= (\rho_x + p_x)V_x Q_i, \\
T_0^j &= -(\rho_x + p_x)V_x Q^j, \\
T_j^i &= p_x(\delta_j^i + \frac{\delta p_x}{p_x}\delta_j^i Q + \Pi_x Q_j^i),
\end{aligned} \tag{4.30}$$

where ρ_x is the energy density, p_x is the pressure, $\delta_x = \delta\rho_x/\rho_x$ and Π_x is the anisotropic stress of the fluid.

Continuity Equation

The zeroth component of the conservation equation becomes

$$\begin{aligned}
-\partial_0 T^{00} &= \partial_i T^{i0} + \Gamma_{\alpha\beta}^0 T^{\alpha\beta} + \Gamma_{\alpha\beta}^\alpha T^{0\beta} \\
&= T^{i0}|_i + 2\Gamma_{00}^0 T^{00} + \Gamma_{ij}^0 T^{ij} + \Gamma_{i0}^i T^{00},
\end{aligned} \tag{4.31}$$

where we have dropped second order terms. For pedagogical reasons, let us evaluate each term explicitly

$$\begin{aligned}
T^{00} &= (1 + \delta_x Q - 2\Psi Q)(a_0/a)^2 \rho_x, \\
\partial_0 T^{00} &= [(1 + \delta_x Q - 2\Psi Q)(\frac{\dot{\rho}_x}{\rho_x} - 2\frac{\dot{a}}{a}) + (\dot{\delta}_x - 2\dot{\Psi}Q)](a_0/a)^2 \rho_x, \\
T^{i0}|_i &= (1 + w_x)kV_x Q(a_0/a)^2 \rho_x, \\
\Gamma_{00}^0 T^{00} &= [\frac{\dot{a}}{a}(1 + \delta_x Q - 2\Psi Q) + \dot{\Psi}Q](a_0/a)^2 \rho_x, \\
\Gamma_{ij}^0 T^{ij} &= 3w_x[\frac{\dot{a}}{a}(1 + \frac{\delta p_x}{p_x}Q - 2\Psi Q) + \dot{\Phi}Q](a_0/a)^2 \rho_x, \\
\Gamma_{i0}^i T^{00} &= 3[\frac{\dot{a}}{a}(1 + \delta_x Q - 2\Psi Q) + \dot{\Phi}Q](a_0/a)^2 \rho_x,
\end{aligned} \tag{4.32}$$

where $w_x \equiv p_x/\rho_x$ gives the equation of state of the fluid.

The zeroth order equation becomes

$$\frac{\dot{\rho}_x}{\rho_x} = -3(1 + w_x)\frac{\dot{a}}{a}. \tag{4.33}$$

For a constant w_x , $\rho_x \propto a^{-3(1+w_x)}$, *i.e.* $w_r = \frac{1}{3}$ and $\rho_r \propto a^{-4}$ for the radiation, $w_m \simeq 0$ and $\rho_m \propto a^{-3}$ for the matter, and $w_v = -1$ and $\rho_v = \text{constant}$ for the vacuum or cosmological

constant contribution. The first order equation is the continuity equation for perturbations,

$$\dot{\delta}_x = -(1 + w_x)(kV_x + 3\dot{\Phi}) - 3\frac{\dot{a}}{a}\delta w_x, \quad (4.34)$$

where the fluctuation in the equation of state

$$\begin{aligned} \delta w_x &= \frac{p_x + \delta p_x}{\rho_x + \delta \rho_x} - w_x \\ &= \left(\frac{\delta p_x}{\delta \rho_x} - w_x \right) \delta_x. \end{aligned} \quad (4.35)$$

This may occur for example if the temperature of a non-relativistic fluid is spatially varying and can be important at late times when astrophysical processes can inject energy in local regions.

We can recast equation (4.34) into the form

$$\frac{d}{d\eta} \left(\frac{\delta_x}{1 + w_x} \right) = -(kV_x + 3\dot{\Phi}) - 3\frac{\dot{a}}{a} \frac{w_x}{1 + w_x} \Gamma_x, \quad (4.36)$$

where the entropy fluctuation is

$$w_x \Gamma_x = (\delta p_x / \delta \rho_x - c_x^2) \delta_x, \quad (4.37)$$

with the sound speed $c_x^2 \equiv \dot{p}_x / \dot{\rho}_x$. Here we have used the relation

$$\begin{aligned} \dot{w}_x &= \frac{\dot{\rho}_x}{\rho_x} \left(\frac{\dot{p}_x}{\dot{\rho}_x} - w_x \right) \\ &= -3(1 + w_x)(c_x^2 - w_x) \frac{\dot{a}}{a}, \end{aligned} \quad (4.38)$$

which follows from equation (4.33). Entropy fluctuations are generated if the fluid is composed of species for which both the equation of state and the number density fluctuations differ. For a single particle fluid, this term vanishes.

Let us interpret equation (4.36). In the limit of an ultra-relativistic or non-relativistic single particle fluid, the quantity

$$\frac{\delta_x}{1 + w_x} = \frac{\delta n_x}{n_x} \quad (4.39)$$

is the number density fluctuation in the fluid. Equation (4.36) thus reduces to the ordinary continuity equation for the number density of particles in the absence of creation and annihilation processes. Aside from the usual kV_x term, there is a $3\dot{\Phi}$ term. We have shown in §2.1.2 that this term represents the stretching of space due to the presence of space

curvature, *i.e.* the spatial metric has a factor $a(1 + \Phi)$. Just as the expansion term a causes an a^{-3} dilution of number density, there is a corresponding perturbative effect of 3Φ from the fluctuation. For the radiation energy density, there is also an effect on the wavelength which brings the total to 4Φ as equation (4.34) requires.

Euler Equation

Similarly, the conservation of momentum equation is obtained from the space component of the conservation equation,

$$\begin{aligned} -\partial_0 T^{0i} &= \partial_j T^{ji} + \Gamma^i_{\alpha\beta} T^{\alpha\beta} + \Gamma^{\alpha}_{\alpha\beta} T^{i\beta} \\ &= T^{ji}_{|j} + \Gamma^i_{00} T^{00} + 2\Gamma^i_{0j} T^{0j} + \Gamma^0_{00} T^{i0} + \Gamma^0_{0j} T^{ij} + \Gamma^j_{j0} T^{i0}. \end{aligned} \quad (4.40)$$

Explicitly, the contributions are

$$\begin{aligned} \partial_0 T^{0i} &= \left\{ [(1 + w_x) \left(\frac{\dot{\rho}_x}{\rho_x} - 2\frac{\dot{a}}{a} \right) + \dot{w}_x] V_x + (1 + w_x) \dot{V}_x \right\} Q^i (a_0/a)^2 \rho_x, \\ T^{ij}_{|j} &= \left[-\frac{\delta p_x}{p_x} + \frac{2}{3} (1 - 3K/k^2) \Pi_x \right] k w_x Q^i (a_0/a)^2 \rho_x, \\ \Gamma^i_{00} T^{00} &= -k \Psi Q^i (a_0/a)^2 \rho_x, \\ \Gamma^0_{0j} T^{ij} &= -k \Psi Q^i (a_0/a)^2 p_x, \\ \Gamma^i_{0j} T^{0j} &= \frac{\dot{a}}{a} (1 + w_x) V_x Q^i (a_0/a)^2 \rho_x, \\ &= \Gamma^0_{00} T^{i0} \\ &= \frac{1}{3} \Gamma^j_{j0} T^{i0}. \end{aligned} \quad (4.41)$$

These terms are all first order in the perturbation and form the Euler equation

$$\dot{V}_x = -\frac{\dot{a}}{a} (1 - 3w_x) V_x - \frac{\dot{w}_x}{1 + w_x} V_x + \frac{\delta p_x / \delta \rho_x}{1 + w_x} k \delta_x - \frac{2}{3} \frac{w_x}{1 + w_x} (1 - 3K/k^2) k \Pi_x + k \Psi. \quad (4.42)$$

Employing equation (4.38) for the time variation of the equation of state and equation (4.37) for the entropy, we can rewrite this as

$$\dot{V}_x + \frac{\dot{a}}{a} (1 - 3c_x^2) V_x = \frac{c_x^2}{1 + w_x} k \delta_x + \frac{w_x}{1 + w_x} k \Gamma_x - \frac{2}{3} \frac{w_x}{1 + w_x} (1 - 3K/k^2) k \Pi_x + k \Psi. \quad (4.43)$$

The gradient of the gravitational potential provides a source to velocities from infall. The expansion causes a drag term on the matter but not the radiation. This is because the expansion redshifts particle momenta as a^{-1} . For massive particles, the velocity consequently

decays as $V_m \propto a^{-1}$. For radiation, the particle energy or equivalently the temperature of the distribution redshifts. The bulk velocity V_r represents a *fractional* temperature fluctuation with a dipole signature. Therefore, the decay scales out. Stress in the fluid, both isotropic (pressure) and anisotropic, prevents gravitational infall. The pressure contribution is separated into an acoustic part proportional to the sound speed c_x^2 and an entropy part which contributes if the fluid is composed of more than one particle species.

4.2.3 Total Matter and Its Components

If the fluid x in the last section is taken to be the total matter T , equations (4.34) and (4.43) describe the evolution of the whole system. However, even considering the metric fluctuations Ψ and Φ as external fields, the system of equations is not closed since the anisotropic stress Π_T and the entropy Γ_T remain to be defined. The fluid must therefore be broken into particle components for which these quantities are known.

We can reconstruct the total matter variables from the components via the relations,

$$\rho_T \delta_T = \sum_i \rho_i \delta_i, \quad (4.44)$$

$$\delta p_T = \sum_i \delta p_i, \quad (4.45)$$

$$(\rho_T + p_T) V_T = \sum_i (\rho_i + p_i) V_i, \quad (4.46)$$

$$p_T \Pi_T = \sum_i p_i \Pi_i, \quad (4.47)$$

$$\dot{\rho}_T c_T^2 = \sum_i \dot{\rho}_i c_i^2, \quad (4.48)$$

which follow from the form of the stress-energy tensor. Vacuum contributions are usually not included in the total matter. Similarly, the entropy fluctuation can be written

$$\begin{aligned} p_T \Gamma_T &= \delta p_T - \frac{\dot{p}_T}{\dot{\rho}_T} \delta \rho_T \\ &= \sum_i \delta p_i - \frac{\dot{p}_i}{\dot{\rho}_i} \delta \rho_i + \left(\frac{\dot{p}_i}{\dot{\rho}_i} - \frac{\dot{p}_T}{\dot{\rho}_T} \right) \delta \rho_i \\ &= \sum_i p_i \Gamma_i + (c_i^2 - c_T^2) \delta \rho_i. \end{aligned} \quad (4.49)$$

Even supposing the entropy of the individual fluids vanishes, there can be a non-zero Γ_T due to differing density contrasts between the components which have different equations

of state w_i . If the universe consists of non-relativistic matter and fully-relativistic radiation only, there are only two relevant equations of state $w_r = 1/3$ for the radiation and $w_m \simeq 0$ for the matter. The relative entropy contribution then becomes,

$$\Gamma_T = -\frac{4}{3} \frac{1 - 3w_T}{1 + w_T} S, \quad (4.50)$$

where the S is the fluctuation in the matter to radiation number density

$$S = \delta(n_m/n_r) = \delta_m - \frac{3}{4}\delta_r, \quad (4.51)$$

and is itself commonly referred to as the entropy fluctuation for obvious reasons.

Although covariant conservation applies equally well to particle constituents as to the total fluid, we have assumed in the last section that the species were non-interacting. To generalize the conservation equations, we must consider momentum transfer between components. Let us see how this is done.

4.2.4 Radiation

In the standard model for particle physics, the universe contains photons and three flavors of massless neutrinos as its radiation components. For the photons, we must consider the momentum transfer with the baryons through Compton scattering. We have in fact already obtained the full evolution equation for the photon component through the derivation of the Boltzmann equation in Chapter 2. In real space, the temperature fluctuation is given by [see equation (2.63)]

$$\begin{aligned} \frac{d}{d\eta}(\Theta + \Psi) &\equiv \dot{\Theta} + \dot{\Psi} + \dot{x}^i \frac{\partial}{\partial x^i}(\Theta + \Psi) + \dot{\gamma}^i \frac{\partial}{\partial \gamma^i}(\Theta + \Psi) \\ &= \dot{\Psi} - \dot{\Phi} + \dot{\tau}(\Theta_0 - \Theta + \gamma_i v_b^i + \frac{1}{16} \gamma_i \gamma_j \Pi_\gamma^{ij}), \end{aligned} \quad (4.52)$$

recall that τ is the Compton optical depth, $\Theta_0 = \delta_\gamma/4$ is the isotropic component of Θ , and Π_γ^{ij} the quadrupole moments of the photon energy density are given by equation (2.64).

The angular fluctuations in a given spatial mode Q can be expressed by the multipole decomposition of equation (4.24)

$$\Theta(\eta, \mathbf{x}, \boldsymbol{\gamma}) = \sum_{\ell=0}^{\infty} \Theta_\ell(\eta) M_\ell^{-1/2} G_\ell(\mathbf{x}, \boldsymbol{\gamma}). \quad (4.53)$$

By employing the recursion relations (4.22), we can break equation (4.52) into the standard hierarchy of coupled equations for the ℓ -modes:

$$\begin{aligned}
\dot{\Theta}_0 &= -\frac{k}{3}\Theta_1 - \dot{\Phi}, \\
\dot{\Theta}_1 &= k \left[\Theta_0 + \Psi - \frac{2}{5}K_2^{1/2}\Theta_2 \right] - \dot{\tau}(\Theta_1 - V_b), \\
\dot{\Theta}_2 &= k \left[\frac{2}{3}K_2^{1/2}\Theta_1 - \frac{3}{7}K_3^{1/2}\Theta_3 \right] - \frac{9}{10}\dot{\tau}\Theta_2, \\
\dot{\Theta}_\ell &= k \left[\frac{\ell}{2\ell-1}K_\ell^{1/2}\Theta_{\ell-1} - \frac{\ell+1}{2\ell+3}K_{\ell+1}^{1/2}\Theta_{\ell+1} \right] - \dot{\tau}\Theta_\ell, \quad (\ell > 2)
\end{aligned} \tag{4.54}$$

where $\gamma_i v_b^i(\mathbf{x}) = V_b G_1(\mathbf{x}, \boldsymbol{\gamma})$ and recall $K_\ell = 1 - (\ell^2 - 1)K/k^2$. Since $V_\gamma = \Theta_1$, comparison with equation (4.43) gives the relation between the anisotropic stress perturbation of the photons and the quadrupole moment

$$\Pi_\gamma = \frac{12}{5}(1 - 3K/k^2)^{-1/2}\Theta_2. \tag{4.55}$$

Thus anisotropic stress is generated by the streaming of radiation from equation (4.54) once the mode enters the horizon $k\eta \gtrsim 1$. The appearance of the curvature term is simply an artifact of our convention for the multipole moment normalization. For supercurvature modes, it is also a convenient rescaling of the anisotropic stress since in the Euler equation (4.43), the term $(1 - 3K/k^2)k\Pi_\gamma = 12(k^2 - 3K)^{1/2}\Theta_2/5$ is manifestly finite as $k \rightarrow 0$.

By analogy to equation (4.54), we can immediately write down the corresponding Boltzmann equation for (massless) neutrino temperature perturbations $N(\eta, \mathbf{x}, \boldsymbol{\gamma})$ with the replacements

$$\Theta_\ell \rightarrow N_\ell, \dot{\tau} \rightarrow 0, \tag{4.56}$$

in equation (4.54). This is sufficient since neutrino decoupling occurs before any scale of interest enters the horizon.

4.2.5 Matter

There are two non-relativistic components of dynamical importance to consider: the baryons and collisionless cold dark matter. The collisionless evolution equations for the baryons are given by (4.34) and (4.43) with $w_b \simeq 0$ if $T_e/m_e \ll 1$. However, before recombination, Compton scattering transfers momentum between the photons and baryons. It is unnecessary to derive the baryon transport equation from first principles since the

momentum of the total photon-baryon fluid is still conserved. Conservation of momentum yields

$$(\rho_\gamma + p_\gamma)\delta V_\gamma = \frac{4}{3}\rho_\gamma\delta V_\gamma = \rho_b\delta V_b. \quad (4.57)$$

Thus equations (4.34), (4.43) and (4.54) imply

$$\begin{aligned} \dot{\delta}_b &= -kV_b - 3\dot{\Phi}, \\ \dot{V}_b &= -\frac{\dot{a}}{a}V_b + k\Psi + \dot{\tau}(V_\gamma - V_b)/R, \end{aligned} \quad (4.58)$$

where $R = 3\rho_b/4\rho_\gamma$. The baryon continuity equation can also be combined with the photon continuity equation [$\ell = 0$ in (4.54)] to obtain

$$\dot{\delta}_b = -k(V_b - V_\gamma) + \frac{3}{4}\dot{\delta}_\gamma. \quad (4.59)$$

As we shall see, this is useful since it has a gauge invariant interpretation: it represents the evolution of the number density or entropy fluctuation [see equation (4.51)]. Finally, any collisionless non-relativistic component can be described with equation (4.58) by dropping the interaction term $\dot{\tau}$. The equations can also be obtained from (4.34) and (4.43) by noting that for a collisionless massive particle, the pressure, sound speed and entropy fluctuation may be ignored.

4.2.6 Einstein Equations

The Einstein equations close the system by expressing the time evolution of the metric in terms of the matter sources,

$$G_{\mu\nu} = 8\pi GT_{\mu\nu}, \quad (4.60)$$

where $T_{\mu\nu}$ is now the total stress-energy tensor (including any vacuum contributions). The background equations give matter conservation for the space-space equation. This is already contained in equation (4.33). The time-space component vanishes leaving only the time-time component

$$\left(\frac{\dot{a}}{a}\right)^2 + K = \frac{8\pi G}{3}\left(\frac{a}{a_0}\right)^2(\rho_T + \rho_v), \quad (4.61)$$

where ρ_v is the vacuum contribution and we have used equation (4.28). This evolution equation for the scale factor is often written in terms of the Hubble parameter,

$$\begin{aligned} H^2 &\equiv \left(\frac{1}{a}\frac{da}{dt}\right)^2 = \left(\frac{\dot{a}}{a}\frac{a_0}{a}\right)^2 \\ &= \left(\frac{a_0}{a}\right)^4 \frac{a_{eq} + a}{a_{eq} + a_0} \Omega_0 H_0^2 - \left(\frac{a_0}{a}\right)^2 K + \Omega_\Lambda H_0^2, \end{aligned} \quad (4.62)$$

where recall $\Omega_0 = \rho_T/\rho_{crit}$ and $\Omega_\Lambda = \rho_v/\rho_{crit}$ with $\rho_{crit} = 3H_0^2/8\pi G$. Here a_{eq} is the epoch of matter-radiation equality. Notice that as a function of a , the expansion will be dominated successively by radiation, matter, curvature, and Λ . Of course, either or both of the latter terms may be absent in the real universe.

The first order equations govern the evolution of Ψ and Φ . They are the time-time term,

$$3\left(\frac{\dot{a}}{a}\right)^2\Psi - 3\frac{\dot{a}}{a}\dot{\Phi} - (k^2 - 3K)\Phi = -4\pi G\left(\frac{a}{a_0}\right)^2\rho_T\delta_T, \quad (4.63)$$

the time-space term,

$$\frac{\dot{a}}{a}\Psi - \dot{\Phi} = 4\pi G\left(\frac{a}{a_0}\right)^2(1 + w_T)\rho_TV_T/k, \quad (4.64)$$

and the traceless space-space term

$$k^2(\Psi + \Phi) = -8\pi G\left(\frac{a}{a_0}\right)^2 p_T\Pi_T. \quad (4.65)$$

The other equations express the conservation laws which we have already found. Equations (4.63) and (4.64) can be combined to form the generalized Poisson equation

$$(k^2 - 3K)\Phi = 4\pi G\left(\frac{a}{a_0}\right)^2\rho_T[\delta_T + 3\frac{\dot{a}}{a}(1 + w_T)V_T/k]. \quad (4.66)$$

Equations (4.65) and (4.66) form the two fundamental evolution equations for metric perturbations in Newtonian gauge.

Notice that the form of (4.66) reduces to the ordinary Poisson equation of Newtonian mechanics if the last term in the brackets is negligible. Employing the matter continuity equation (4.34), this occurs when $k\eta \gg 1$, *i.e.* when the fluctuation is well inside the horizon as one would expect. This extra piece represents a relativistic effect and depends on the frame of reference in which the perturbation is defined. This suggests that we can simplify the form and interpretation of the evolution equations by a clever choice of gauge.

4.3 Gauge

Sayings from a perspective work nine times out of ten, wise sayings work seven times out of ten. Adaptive sayings are new every day, smooth them out on the whetstone of Heaven.

—Chuang-tzu, 27

Fluctuations are defined on hypersurfaces of constant time. Since in general relativity, we can choose the coordinate system arbitrarily, this leads to an ambiguity in the

definition of fluctuations referred to as *gauge freedom*. There is *no* gauge invariant meaning to density fluctuations. For example, even a completely homogeneous and isotropic Friedmann-Robertson-Walker space can be expressed with an inhomogeneous metric by choosing an alternate time slicing that is warped (see Fig. 4.2). Conversely, a fluctuation can be thought of as existing in a homogeneous and isotropic universe where the initial time slicing is altered (see §5.1.2). Two principles are worthwhile to keep in mind when considering the gauge:

1. Choose a gauge whose coordinates are completely fixed.
2. Choose a gauge where the physical interpretation and/or form of the evolution is simplest.

The first condition is the most important. Historically, much confusion has arisen from the use of a particular gauge choice, the synchronous gauge, which *alone* does not fix the coordinates entirely [133]. An ambiguity in the mapping onto this gauge appears, for example, at the initial conditions. Usually this problem is solved by completely specifying the initial hypersurface. Improper mapping can lead to artificial “gauge modes” in the solution. The second point is that given gauge freedom exists, we may as well exploit it by choosing one which simplifies either the calculation or the interpretation. It turns out that the two often conflict. For this reason, we advocate a hybrid choice of representation for fluctuations.

How is a hybrid choice implemented? This is the realm of the so-called “gauge invariant” formalism. Let us consider for a moment the meaning of the term gauge invariant. If the coordinates are completely specified, the fluctuations are real geometric objects and may be represented in any coordinate system. They are therefore manifestly gauge invariant. However, in the new frame they may take on a different *interpretation*, *e.g.* density fluctuations in general will not remain density fluctuations. The “gauge invariant” program reduces to the task of writing down fluctuations in a given gauge in terms of quantities in an arbitrary gauge. It is therefore a problem in mapping. The only quantities that are not “gauge invariant” in this sense are those that are ill defined, *i.e.* represent fluctuations in a gauge whose coordinates have not been completely fixed. This should be distinguished from objects that actually have a gauge invariant interpretation. As we shall see, quantities such as anisotropies of $\ell \geq 2$ are the same in any frame. This is because the coordinate

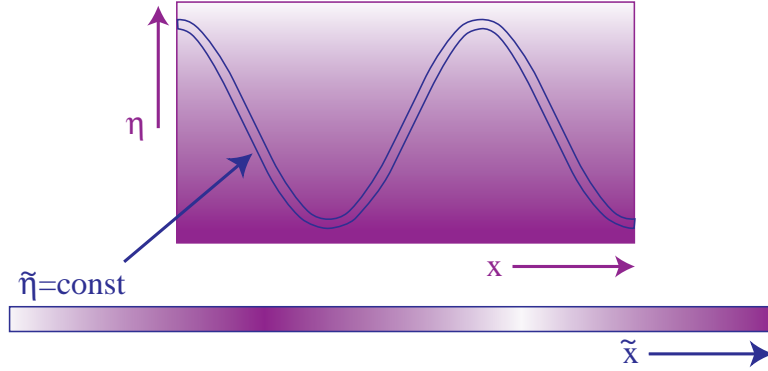


Figure 4.2: Gauge Ambiguity

Gauge ambiguity refers to the freedom to choose the time slicing on which perturbations are defined. In this simple example, a homogeneous FRW universe appears to have density perturbations for a warped choice of time slicing. One usually employs a set of standard “observers” to define the coordinate slicing. The Newtonian gauge boosts observers into a frame where the expansion rate looks isotropic (shear free). The synchronous gauge can be implemented to follow the collisionless non-relativistic particles. The total matter gauge employs the rest frame of the total energy density fluctuations.

system is defined by a scalar function in space to describe the “warping” of the time slicing and a vector to define the “boost,” leaving higher order quantities invariant.

4.3.1 Gauge Transformations

The most general form of a metric perturbed by scalar fluctuations is [99]

$$\begin{aligned} g_{00} &= -(a/a_0)^2[1 + 2A^G Q], \\ g_{0j} &= -(a/a_0)^2 B^G Q_j, \\ g_{ij} &= (a/a_0)^2[\gamma_{ij} + 2H_L^G Q \gamma_{ij} + 2H_T^G Q_{ij}], \end{aligned} \quad (4.67)$$

where the superscript G is employed to remind the reader that the actual values vary from gauge to gauge. A gauge transformation is a change in the correspondence between the perturbation and the background represented by the coordinate shift

$$\begin{aligned} \tilde{\eta} &= \eta + TQ, \\ \tilde{x}^i &= x^i + LQ^i. \end{aligned} \quad (4.68)$$

T corresponds to a choice in time slicing and L the choice of the spatial coordinate grid. They transform the metric as

$$\begin{aligned} \tilde{g}_{\mu\nu}(\eta, x^i) &= \frac{\partial x^\alpha}{\partial \tilde{x}^\mu} \frac{\partial x^\beta}{\partial \tilde{x}^\nu} g_{\alpha\beta}(\eta - TQ, x^i - LQ^i) \\ &\simeq g_{\mu\nu}(\eta, x^i) + g_{\alpha\nu} \delta x^\alpha_{,\mu} + g_{\alpha\mu} \delta x^\alpha_{,\nu} - g_{\mu\nu,\lambda} \delta x^\lambda. \end{aligned} \quad (4.69)$$

From this, we obtain the relations for the metric fluctuations

$$\begin{aligned}
A^{\tilde{G}} &= A^G - \dot{T} - \frac{\dot{a}}{a}T, \\
B^{\tilde{G}} &= B^G + \dot{L} + kT, \\
H_L^{\tilde{G}} &= H_L^G - \frac{k}{3}L - \frac{\dot{a}}{a}T, \\
H_T^{\tilde{G}} &= H_T^G + kL.
\end{aligned} \tag{4.70}$$

An analogous treatment of the stress energy tensor shows that

$$\begin{aligned}
v_x^{\tilde{G}} &= v_x^G + \dot{L}, \\
\delta_x^{\tilde{G}} &= \delta_x^G + 3(1 + w_x)\frac{\dot{a}}{a}T, \\
\delta p_x^{\tilde{G}} &= \delta p_x^G + 3c_x^2\rho_x(1 + w_x)\frac{\dot{a}}{a}T, \\
\Pi_x^{\tilde{G}} &= \Pi_x^G.
\end{aligned} \tag{4.71}$$

Therefore any ambiguity in the time slicing T leads to freedom in defining the density contrast δ_x . Notice that the anisotropic stress Π_x has a truly gauge invariant meaning as does any higher order tensor contribution. Furthermore, relative quantities do as well, *e.g.*

$$\begin{aligned}
\frac{\delta_x^{\tilde{G}}}{1 + w_x} - \frac{\delta_y^{\tilde{G}}}{1 + w_y} &= \frac{\delta_x^G}{1 + w_x} - \frac{\delta_y^G}{1 + w_y}, \\
v_x^{\tilde{G}} - v_y^{\tilde{G}} &= v_x^G - v_y^G, \\
\Gamma_x^{\tilde{G}} &= \Gamma_x^G,
\end{aligned} \tag{4.72}$$

the relative number density, velocity, and entropy fluctuation. We hereafter drop the superscript from such quantities.

4.3.2 Newtonian Gauge

In the Newtonian gauge, $B^N = H_T^N = 0$. Physically, it is a time slicing in which the expansion is isotropic. This considerably simplifies the interpretation of effects such as gravitational infall and redshift. From an arbitrary coordinate system G , the Newtonian gauge is reached by employing [see equation (4.70)]

$$\begin{aligned}
T &= -B^G/k + \dot{H}_T^G/k^2, \\
L &= -H_T^G/k.
\end{aligned} \tag{4.73}$$

From equations (4.70) and (4.71), the fundamental perturbations on this choice of hypersurface slicing are

$$\begin{aligned}
\Psi \equiv A^N &= A^G + \frac{1}{a} \frac{d}{d\eta} [aB^G/k - a\dot{H}_T^G/k^2], \\
\Phi \equiv H_L^N &= H_L^G + \frac{1}{3} H_T^G + \frac{\dot{a}}{a} (B^G/k - \dot{H}_T^G/k^2), \\
\delta_x^N &= \delta_x^G + 3(1+w_x) \frac{\dot{a}}{a} (-B^G/k + \dot{H}_T^G/k^2), \\
\delta p_x^N &= \delta p_x^G + 3c_x^2 \rho_x (1+w_x) \frac{\dot{a}}{a} (-B^G/k + \dot{H}_T^G/k^2), \\
V_x \equiv v_x^N &= v_x^G - \dot{H}_T^G/k.
\end{aligned} \tag{4.74}$$

This is commonly referred to as the ‘‘gauge invariant’’ definition of Newtonian perturbations. Note that the general form of the Poisson equation becomes

$$\Phi = 4\pi G \left(\frac{a}{a_0} \right)^2 \rho_T \left(\delta_T^G + 3 \frac{\dot{a}}{a} (1+w_T) (v_T^G - B^G)/k \right). \tag{4.75}$$

As we have seen, density perturbations in this gauge grow due to infall into the potential Ψ and metric stretching effects from Φ . In the absence of changes in Φ , they will therefore not grow outside the horizon since causality prevents infall growth.

4.3.3 Synchronous Gauge

The synchronous gauge, defined by $A^S = B^S = 0$ is a popular and in many cases computationally useful choice. The condition $A^S = 0$ implies that proper time corresponds with coordinate time, and $B^S = 0$ that constant space coordinates are orthogonal to constant time hypersurfaces. This is the natural coordinate system for freely falling observers.

From an arbitrary coordinate choice, the synchronous condition is satisfied by the transformation

$$\begin{aligned}
T &= a^{-1} \int d\eta a A^G + c_1 a^{-1}, \\
L &= - \int d\eta (B^G + kT) + c_2,
\end{aligned} \tag{4.76}$$

where c_1 and c_2 are integration constants. There is therefore residual gauge freedom in synchronous gauge. It manifests itself as a degeneracy in the mapping of fluctuations onto the synchronous gauge and appears, for example as an ambiguity in δ_x^S of $3(1+w_x)c_1\dot{a}/a^2$. This represents an unphysical gauge mode. To eliminate it, one must carefully define the initial conditions.

It is a simple exercise in algebra to transform the evolution equations from Newtonian to synchronous representation. The metric perturbations are commonly written as

$$\begin{aligned} h_L &\equiv 6H_L^S, \\ \eta_T &\equiv -H_L^S - \frac{1}{3}H_T^S. \end{aligned} \quad (4.77)$$

Equation (4.76) tells us that

$$\begin{aligned} T &= -\dot{L}/k = (v_x^N - v_x^S)/k \\ &= \frac{1}{2}(\dot{h}_L + 6\dot{\eta}_T)/k^2, \end{aligned} \quad (4.78)$$

from which it follows

$$\dot{\Phi} = \frac{1}{6}\dot{h}_L - k(v_x^N - v_x^S)/3 + \frac{d}{d\eta}\left[\frac{\dot{a}}{a}(v_x^N - v_x^S)/k\right]. \quad (4.79)$$

Furthermore, the density and pressure relations

$$\begin{aligned} \delta_x^N &= \delta_x^S - 3(1 + w_x)\frac{\dot{a}}{a}(v_x^N - v_x^S)/k, \\ \delta p_x^N &= \delta p_x^S - 3(1 + w_x)c_x^2\rho_x\frac{\dot{a}}{a}(v_x^N - v_x^S)/k, \end{aligned} \quad (4.80)$$

and equation (4.38) yields

$$\delta_x^N = \delta_x^S - (1 + w_x) \left\{ 3\left(\dot{\Phi} - \frac{1}{6}\dot{h}_L\right) + \left[k^2 - 9(c_x^2 - w_x) \left(\frac{\dot{a}}{a}\right)^2 \right] (v_x^N - v_x^S)/k \right\}, \quad (4.81)$$

and

$$3\frac{\dot{a}}{a}\left(\frac{\delta p_x^N}{\delta\rho_x^N} - w_x\right)\delta_x^N = 3\frac{\dot{a}}{a}\left(\frac{\delta p_x^S}{\delta\rho_x^S} - w_x\right)\delta_x^S + 9(1 + w_x)(c_x^2 - w_x)\left(\frac{\dot{a}}{a}\right)^2(v_x^N - v_x^S)/k. \quad (4.82)$$

Thus the continuity equation of (4.34) becomes

$$\dot{\delta}_x^S = -(1 + w_x)(kv_x^S + \dot{h}_L/2) - 3\frac{\dot{a}}{a}\left(\frac{\delta p_x^S}{\delta\rho_x^S} - w_x\right)\delta_x^S. \quad (4.83)$$

Likewise with the relation

$$\dot{v}_x^S + \frac{\dot{a}}{a}v_x^S = \dot{v}_x^N + \frac{\dot{a}}{a}v_x^N - k\Psi, \quad (4.84)$$

and equation (4.38), the transformed Euler equation immediately follows:

$$\dot{v}_x^S = -\frac{\dot{a}}{a}(1 - 3w_x)v_x^S - \frac{\dot{w}_x}{1 + w_x}v_x^S + \frac{\delta p_x^S/\delta\rho_x^S}{1 + w_x}k\delta_x^S - \frac{2}{3}\frac{w_x}{1 + w_x}(1 - 3K/k^2)k\Pi_x. \quad (4.85)$$

Finally, one can also work in the reverse direction and obtain the Newtonian variables in terms of the synchronous gauge perturbations. Given the residual gauge freedom, this is a many to one mapping. The Newtonian metric perturbation follows from equation (4.75), $B^S = 0$, and the gauge invariance of Π_T :

$$\begin{aligned} (k^2 - 3K)\Phi &= 4\pi G \left(\frac{a}{a_0}\right)^2 \rho_T [\delta_T^S + 3\frac{\dot{a}}{a}(1 + w_T)v_T^S/k], \\ k^2(\Psi + \Phi) &= -8\pi G \left(\frac{a}{a_0}\right)^2 p_T \Pi_T. \end{aligned} \quad (4.86)$$

They can also be written in terms of the synchronous gauge metric perturbations as

$$\begin{aligned} \Psi &= \frac{1}{2k^2} \left[\ddot{h}_L + 6\ddot{\eta}_T + \frac{\dot{a}}{a}(\dot{h}_L + 6\dot{\eta}_T) \right], \\ \Phi &= -\eta_T + \frac{1}{2k^2} \frac{\dot{a}}{a}(\dot{h}_L + 6\dot{\eta}_T). \end{aligned} \quad (4.87)$$

In fact, equations (4.86) and (4.87) close the system by expressing the time evolution of the metric variables η_T and h_L in terms of the matter sources.

Now let us return to the gauge mode problem. The time slicing freedom can be fixed by a choice of the initial hypersurface. The natural choice is one in which the velocity vanishes $v_x^S(\eta_i) = 0$ for some set of “observer” particle species x . This condition fixes c_1 and removes the gauge ambiguity in the density perturbations. Notice also that the synchronous gauge has an elegant property. Since it is the coordinate system of freely falling observers, if the velocity of a *non-interacting* pressureless species is set to zero initially it will remain so. In the Euler equation (4.85), the infall term that sources velocities has been transformed away by equation (4.84). Thus in the absence of pressure and entropy terms, there are no sources to the velocity.

The synchronous gauge therefore represents a “Lagrangian” coordinate system as opposed to the more “Eulerian” choice of a Newtonian coordinate system. In this gauge, the coordinate grid follows freely falling particles so that density growth due to infall is transformed into dilation effects from the stretching of the grid. Although the coordinate grid must be redefined when particle trajectories cross, this does not occur in linear perturbation theory if the defining particles are non-relativistic. Thus in synchronous gauge, the dynamics are simpler since we employ the rest frame of the collisionless matter. The only drawback to this gauge choice is that physical intuition is more difficult to obtain since we have swept dynamical effects into the behavior of the coordinate grid.

4.3.4 Total Matter Gauge

As an obvious extension of the ideas which make the synchronous gauge appealing, it is convenient to employ the rest frame of the total rather than collisionless matter. The total matter velocity is thus set to be orthogonal to the constant time hypersurfaces $v_T^T = B^T$. With the additional constraint $H_T^T = 0$, the transformation is obtained by

$$\begin{aligned} T &= (v_T^G - B^G)/k, \\ L &= -H_T^G/k, \end{aligned} \quad (4.88)$$

which fixes the coordinates completely. The matter perturbation quantities become

$$\begin{aligned} \Delta_x &\equiv \delta_x^T = \delta_x^G + 3(1 + w_x) \frac{\dot{a}}{a} (v_T^G - B^G)/k, \\ \delta p_x^T &= \delta p_x^G + 3(1 + w_x) c_x^2 \rho_x \frac{\dot{a}}{a} (v_T^G - B^G)/k, \\ V_x &\equiv V_x^T = v_x^G - \dot{H}_T^G/k. \end{aligned} \quad (4.89)$$

Notice that the Newtonian gauge $B^N = H_N^T = 0$ and $v_x^T = v_x^N = V_x$. In synchronous gauge, $B^S = 0$ as well. If the rest frame of the total matter is the same as the collisionless non-relativistic matter, as is the case for adiabatic conditions, $\delta_x^S \simeq \Delta_x^T$ if $v_x^S(0) = 0$.

The evolution equations are easily obtained from Newtonian gauge with the help of the following relations,

$$\frac{d}{d\eta} \left(\frac{\dot{a}}{a} \right) = -\frac{1}{2} \left[\left(\frac{\dot{a}}{a} \right)^2 + K \right] (1 + 3w_T) + \frac{3}{2} (1 + w_T) \left(\frac{a}{a_0} \right)^2 \Omega_\Lambda H_0^2, \quad (4.90)$$

which follows from equation (4.61) and

$$\frac{\dot{a}}{a} \Psi - \dot{\Phi} = \frac{3}{2} \left[\left(\frac{\dot{a}}{a} \right)^2 + K - \left(\frac{a}{a_0} \right)^2 \Omega_\Lambda H_0^2 \right] (1 + w_T) V_T/k \quad (4.91)$$

from equation (4.64). The Newtonian Euler equation can also be rewritten as

$$\begin{aligned} \frac{d}{d\eta} \left(\frac{\dot{a}}{a} (1 + w_T) V_T \right) &= - \left(\frac{\dot{a}}{a} \right)^2 (1 - 3w_T) (1 + w_T) V_T + \frac{\dot{a}}{a} \frac{\delta p_T^N}{\delta \rho_T^N} k \delta_T^N \\ &\quad - \frac{2}{3} \frac{\dot{a}}{a} w_T (1 - 3K/k^2) k \Pi_T + (1 + w_T) \frac{\dot{a}}{a} k \Psi \\ &\quad - \frac{1}{2} (1 + 3w_T) (1 + w_T) \left[\left(\frac{\dot{a}}{a} \right)^2 + K \right] V_T \\ &\quad + \frac{3}{2} (1 + w_T)^2 \left(\frac{a}{a_0} \right)^2 \Omega_\Lambda H_0^2 V_T. \end{aligned} \quad (4.92)$$

With this relation, the total matter continuity and Euler equations readily follow,

$$\dot{\Delta}_T - 3w_T \frac{\dot{a}}{a} \Delta_T = -(1 - 3K/k^2)(1 + w_T)kV_T - 2(1 - 3K/k^2) \frac{\dot{a}}{a} w_T \Pi_T, \quad (4.93)$$

$$\dot{V}_T + \frac{\dot{a}}{a} V_T = \frac{c_T^2}{1 + w_T} k \Delta_T + k \Psi + \frac{w_T}{1 + w_T} k \Gamma_T - \frac{2}{3} (1 - 3K/k^2) \frac{w_T}{1 + w_T} k \Pi_T. \quad (4.94)$$

The virtue of this representation is that the evolution of the total matter is simple. This is reflected by the form of the Poisson equation,

$$(k^2 - 3K)\Phi = 4\pi G \left(\frac{a}{a_0}\right)^2 \rho_T \Delta_T, \quad (4.95)$$

$$k^2(\Psi + \Phi) = -8\pi G \left(\frac{a}{a_0}\right)^2 p_T \Pi_T. \quad (4.96)$$

In the total matter rest frame, there are no relativistic effects from the velocity and hence the Poisson equation takes its non-relativistic form. Again the drawback is that the interpretation is muddled.

4.3.5 Hybrid Formulation

We have seen that the Newtonian gauge equations correspond closely with classical intuition and thus provide a simple representation for relativistic perturbation theory. However, since density perturbations grow by the causal mechanism of potential infall, we have build a fundamental scale, the particle horizon, into the evolution. Frames that co-move with the matter, *i.e.* in which the particle velocity vanishes, have no fundamental scale. This simplifies the perturbation equations and in many cases admit scale invariant, *i.e.* power law solutions (see §5). Two such frames are commonly employed: the rest frame of the collisionless non-relativistic mater and that of the total matter. The former is implemented under a special choice of the synchronous gauge condition and the latter by the total matter gauge. For the case of adiabatic fluctuations, where non-relativistic and relativistic matter behave similarly, they are essentially identical. For entropy fluctuations, the total matter gauge is more ideal.

Since we can express fluctuations on any given frame by combination of variables on any other, we can mix and match quantities to suit the purpose at hand. To be explicit, we will hereafter employ total matter gauge density fluctuations $\Delta_x \equiv \delta_x^T$, but Newtonian temperature $\Theta \equiv \delta_\gamma^N/4$ and metric perturbations Ψ and Φ . The velocity perturbation is the same in both these frames, which we denote $V_x = v_x^N = v_x^T$. To avoid confusion, we will

hereafter employ *only* this choice. We now turn to the solution of these equations and their implications for the CMB.

Chapter 5

Perturbation Evolution

*Although heaven and earth are great, their evolution is uniform.
Although the myriad things are numerous, their governance is unitary.*

—Chuang-tzu, 12

Superhorizon and subhorizon perturbation evolution take on simple asymptotic forms and interpretations under the hybrid gauge representation developed in §4.3. All component fluctuations *evolve* similarly above the horizon and assume differing forms only due to the initial conditions. We discuss the general solution to the perturbation equations valid for an arbitrary mixture of initial curvature and entropy fluctuations in a universe that passes from radiation to matter to curvature and/or cosmological constant domination. These two initial conditions distinguish the adiabatic and isocurvature growing modes. Evolution during and after horizon crossing exhibits more complicated behavior. Well under the horizon but before recombination, photon pressure in the Compton coupled photon-baryon fluid resists gravitational compression and sets up acoustic waves. In the intermediate case, gravity *drives* the acoustic oscillations. The presence of baryons and radiation feedback on the potentials alter the simple oscillatory form of the acoustic wave. These effects leave distinct signatures on CMB anisotropies in the degree to arcminute range. After recombination, the baryons are released from Compton drag and their density fluctuations can again grow by gravitational instability. The discussion here of the evolutionary properties of perturbations sets the stage for the analysis of anisotropy formation in §6 and §7.

5.1 Superhorizon Evolution

5.1.1 Total Matter Equation

Only gravity affects the evolution of the matter and radiation above the horizon scale in the total matter representation. This greatly simplifies the evolution equations since we can treat all the particle species as a combined total matter fluid without loss of information. Let us prove this assertion. Specifically, we need to show that all particle velocities are equal [84]. Ignoring particle interactions which play no role above the horizon, the Euler equations for pressureless matter and radiation components are given by

$$\dot{V}_m = -\frac{\dot{a}}{a}V_m + k\Psi, \quad (5.1)$$

$$\dot{V}_r = -\frac{\dot{a}}{a}V_r + k\Psi + \frac{1}{4}k\Delta_r, \quad (5.2)$$

where we have transformed the Newtonian Euler equation (4.43) into the total matter representation with equation (4.89). We have also neglected the small contribution from anisotropic stress.

Infall into potential wells sources the matter and radiation velocities alike. Although it attains its maximum effect near horizon crossing $k\eta \gtrsim 1$ due to causality, the fact that a given eigenmode k does not represent one physical scale alone allows infall to generate a small velocity contribution of $\mathcal{O}(k\eta)$ when $k\eta \lesssim 1$. Expansion drag on the matter causes V_m to decay as a^{-1} . However, the Euler equation for the radiation contains not only a different expansion drag term but also pressure contributions which prevent infall. Let us determine when pressure is important. The Poisson equation (4.95) requires

$$(k^2 - 3K)\Phi = \frac{3}{2} \left[\left(\frac{\dot{a}}{a} \right)^2 + K - \left(\frac{a}{a_0} \right)^2 \Omega_\Lambda H_0^2 \right] \Delta_T, \quad (5.3)$$

where we have employed the Hubble equation (4.61). Since

$$\frac{\dot{a}}{a} = \begin{cases} 1/\eta & \text{RD} \\ 2/\eta, & \text{MD} \end{cases} \quad (5.4)$$

in the radiation-dominated (RD) and matter-dominated (MD) epochs, to order of magnitude

$$\Delta_T \sim (k\eta)^2 \Phi, \quad (5.5)$$

before curvature or Λ domination. Since $\Psi \simeq -\Phi$, pressure may be neglected compared with infall outside the horizon where $k\eta \ll 1$. This seemingly obvious statement is actually

not true for the Newtonian gauge density perturbation since $\delta_T^N = \mathcal{O}(\Psi)$ if $k\eta \ll 1$. The appearance of the expansion drag term V_T in equation (5.2) is in fact due to the pressure contributions in the Newtonian frame. Starting from arbitrary initial conditions and in the absence of infall, the expansion will damp away velocities until $V_T = V_m = V_r = 0$. The infall source gives rise to equal velocities for all components.

We can thus describe the coupled multi-component system as a single fluid, defined by the total matter variables whose behavior does not depend on the microphysics of the components. Assuming the various species are all either fully relativistic or non-relativistic, *i.e.* employing equations (4.54) and (4.58) with their decoupled variants, we obtain

$$\dot{\Delta}_T - 3w_T \frac{\dot{a}}{a} \Delta_T = - \left(1 - \frac{3K}{k^2}\right) (1 + w_T) k V_T - 2 \left(1 - \frac{3K}{k^2}\right) \frac{\dot{a}}{a} w \Pi_T, \quad (5.6)$$

$$\begin{aligned} \dot{V}_T + \frac{\dot{a}}{a} V_T &= \frac{4}{3} \frac{w_T}{(1 + w_T)^2} k [\Delta_T - (1 - 3w_T) S] + k \Psi \\ &\quad - \frac{2}{3} k \left(1 - \frac{3K}{k^2}\right) \frac{w_T}{1 + w_T} \Pi_T, \end{aligned} \quad (5.7)$$

where we have used the entropy relation (4.50) and recall $S \equiv \Delta_m - \frac{3}{4} \Delta_r$. The difference in how V_m and V_r is damped by the expansion appears as an entropy term in the total Euler equation. Again for superhorizon scales, we can ignore the pressure term $\propto \Delta_T$ in the total Euler equation above.

The evolution of the entropy is given by the continuity equation for the number density (4.59), *i.e.* $\dot{S} = k(V_r - V_m)$, where the matter and radiation velocities are defined in a manner analogous to V_T [see equation (4.46)]. Since all components have the same velocity, S is a constant before the mode enters the horizon and, if it is present, must have been established at the initial conditions.

5.1.2 General Solution

From Radiation to Matter Domination

Before horizon crossing, radiation pressure may be neglected. Specifically this occurs at $\dot{a}/a = k$ or

$$a_H = \frac{1 + \sqrt{1 + 8(k/k_{eq})^2}}{4(k/k_{eq})^2}, \quad \text{RD/MD} \quad (5.8)$$

where $k_{eq} = (2\Omega_0 H_0^2 a_0)^{1/2}$ is the scale that passes the horizon at equality and $a_{eq} = 1$. Dropping the curvature and Λ contribution to the expansion and combining the total continuity

(5.6) and Euler equations (5.7) yields the second order evolution equation

$$\left\{ \frac{d^2}{da^2} - \frac{f}{a} \frac{d}{da} + \frac{1}{a^2} \left[\left(\frac{k}{k_{eq}} \right)^2 \left(1 - \frac{3K}{k^2} \right) h - g \right] \right\} \Delta_T = \left(\frac{k}{k_{eq}} \right)^2 \left(1 - \frac{3K}{k^2} \right) jS, \quad (5.9)$$

where

$$\begin{aligned} f &= \frac{3a}{4+3a} - \frac{5}{2} \frac{a}{1+a}, \\ g &= 2 + \frac{9a}{4+3a} - \frac{a}{2} \frac{6+7a}{(1+a)^2}, \\ h &= \frac{8}{3} \frac{a^2}{(4+3a)(1+a)}, \\ j &= \frac{8}{3} \frac{a}{(4+3a)(1+a)^2}. \end{aligned} \quad (5.10)$$

Here we have used $3w_T = (1+a)^{-1}$ and have dropped the anisotropic stress correction Π_T (see Appendix A.1.1). The solutions to the homogeneous equation with $S = 0$ are given by

$$\begin{aligned} U_G &= \left[a^3 + \frac{2}{9}a^2 - \frac{8}{9}a - \frac{16}{9} + \frac{16}{9}\sqrt{a+1} \right] \frac{1}{a(a+1)}, \\ U_D &= \frac{1}{a\sqrt{a+1}}, \end{aligned} \quad (5.11)$$

and represent the growing and decaying mode of adiabatic perturbations respectively. Using Green's method, the particular solution in the presence of a *constant* entropy fluctuation S becomes $\Delta_T = C_G U_G + C_D U_D + S U_I$, where U_I is given by [100]

$$U_I = \frac{4}{15} \left(\frac{k}{k_{eq}} \right)^2 \left(1 - \frac{3K}{k^2} \right) \frac{3a^2 + 22a + 24 + 4(4+3a)(1+a)^{1/2}}{(1+a)(3a+4)[1+(1+a)^{1/2}]^4} a^3. \quad (5.12)$$

From Matter to Curvature or Λ domination

After radiation becomes negligible, both the isocurvature and adiabatic modes evolve in the same manner

$$\ddot{\Delta}_T + \frac{\dot{a}}{a} \dot{\Delta}_T = 4\pi G \rho_T \left(\frac{a}{a_0} \right)^2 \Delta_T. \quad (5.13)$$

For pressureless perturbations, each mass shell evolves as a separate homogeneous universe. Since a density perturbation can be viewed as merely a different choice of the initial time surface, the evolution of the fractional shift in the scale factor $a^{-1}\delta a/\delta t$, *i.e.* the Hubble parameter H , must coincide with Δ_T . This is an example of how a clever choice of gauge

simplifies the analysis. It is straightforward to check that the Friedman equations (4.61) and (4.33) do indeed imply

$$\ddot{H} + \frac{\dot{a}}{a}\dot{H} = 4\pi G\rho_T \left(\frac{a}{a_0}\right)^2 H, \quad (5.14)$$

so that one solution, the decaying mode, of equation (5.13) is $\Delta_T \propto H$ [124]. The growing mode $\Delta_T \propto D$ can easily be determined by writing its form as $D \propto HG$ and by substitution into equation (5.13)

$$\ddot{G} + \left(\frac{\dot{a}}{a} + 2\frac{\dot{H}}{H}\right)\dot{G} = 0. \quad (5.15)$$

This can be immediately solved as [124]

$$D(a) \propto H \int \frac{da}{(aH)^3}. \quad (5.16)$$

Note that we ignore pressure contributions in H . If the cosmological constant $\Lambda = 0$, this integral can be performed analytically

$$D(a) \propto 1 + \frac{3}{x} + \frac{3(1+x)^{1/2}}{x^{3/2}} \ln[(1+x)^{1/2} - x^{1/2}], \quad (5.17)$$

where $x = (\Omega_0^{-1} - 1)(a/a_0)$. In the more general case, a numerical solution to this integral must be employed. Notice that $D \propto a$ in the matter-dominated epoch and goes to a constant in the curvature or Λ -dominated epoch.

General Solution

Before curvature or Λ domination, $D \propto a$. The full solution for Δ_T , where the universe is allowed to pass through radiation, matter and curvature or Λ domination, can be simply obtained from equation (5.11) and (5.12), by replacing a with D normalized so that $D = a$ early on, *i.e.*

$$a \rightarrow D = \frac{5}{2}a_0\Omega_0g(a) \int \frac{da}{a} \frac{1}{g^3(a)} \left(\frac{a_0}{a}\right)^2, \quad (5.18)$$

where

$$g^2(a) = \left(\frac{a_0}{a}\right)^3 \Omega_0 + \left(\frac{a_0}{a}\right)^2 (1 - \Omega_0 - \Omega_\Lambda) + \Omega_\Lambda. \quad (5.19)$$

For convenience, we parameterize the initial amplitude of the homogeneous growing mode with the initial curvature fluctuation $\Phi(0)$. The general growing solution then becomes

$$\Delta_T = \Phi(0)U_A + S(0)U_I, \quad (5.20)$$

The evolutionary factors U_A and U_I are given by equations (5.18), (5.11), (5.12) to be

$$\begin{aligned} U_A &= \frac{6}{5} \left(\frac{k}{k_{eq}} \right)^2 \left(1 - \frac{3K}{k^2} \right) \left[D^3 + \frac{2}{9} D^2 - \frac{8}{9} D - \frac{16}{9} + \frac{16}{9} \sqrt{D+1} \right] \frac{1}{D(D+1)}, \\ U_I &= \frac{4}{15} \left(\frac{k}{k_{eq}} \right)^2 \left(1 - \frac{3K}{k^2} \right) \frac{3D^2 + 22D + 24 + 4(4+3D)(1+D)^{1/2}}{(1+D)(4+3D)[1+(1+D)^{1/2}]^4} D^3 \end{aligned} \quad (5.21)$$

respectively. We have implicitly assumed that curvature and Λ dynamical contributions are only important well after equality $a \gg 1$. Curvature dominates over matter at $a/a_0 > \Omega_0/(1-\Omega_0-\Omega_\Lambda)$, whereas Λ dominates over matter at $a/a_0 > (\Omega_0/\Omega_\Lambda)^{1/3}$ and over curvature at $a/a_0 > [(1-\Omega_0-\Omega_\Lambda)/\Omega_\Lambda]^{1/2}$. Although we will usually only consider Λ models which are flat, these solutions are applicable to the general case.

5.1.3 Initial Conditions

Two quantities, the initial curvature perturbation and entropy fluctuation serve to entirely specify the growing solution. Adiabatic models begin with no entropy fluctuations, *i.e.* $S(0) = 0$. Isocurvature models on the other hand have no curvature perturbations initially, *i.e.* $\Phi(0) = 0$. Note that any arbitrary mixture of adiabatic and isocurvature modes is also covered by equation (5.20).

For a universe with photons, 3 families of massless neutrinos, baryons and cold collisionless matter, the entropy becomes,

$$\begin{aligned} S &= \Delta_m - \frac{3}{4} \Delta_r \\ &= \left(1 - \frac{\Omega_b}{\Omega_0} \right) \Delta_c + \frac{\Omega_b}{\Omega_0} \Delta_b - \frac{3}{4} (1 - f_\nu) \Delta_\gamma - \frac{3}{4} f_\nu \Delta_\nu \\ &= \left(1 - \frac{\Omega_b}{\Omega_0} \right) [(1 - f_\nu) S_{c\gamma} + f_\nu S_{c\nu}] + \frac{\Omega_b}{\Omega_0} [(1 - f_\nu) S_{b\gamma} + f_\nu S_{b\nu}], \end{aligned} \quad (5.22)$$

where c represents the cold collisionless component. The neutrino fraction $f_\nu = \rho_\nu/(\rho_\nu + \rho_\gamma)$ is time independent after electron-positron annihilation, implying $f_\nu = 0.405$ for three massless neutrinos and the standard thermal history. S_{ab} is the entropy or number density fluctuation between the a and b components,

$$S_{ab} = \delta(n_a/n_b) = \frac{\Delta_a}{1+w_a} - \frac{\Delta_b}{1+w_b}. \quad (5.23)$$

Entropy conservation $\dot{S}_{ab} = 0 = \dot{S}$ then has an obvious interpretation: since the components cannot separate above the horizon, the particle number ratios must remain constant.

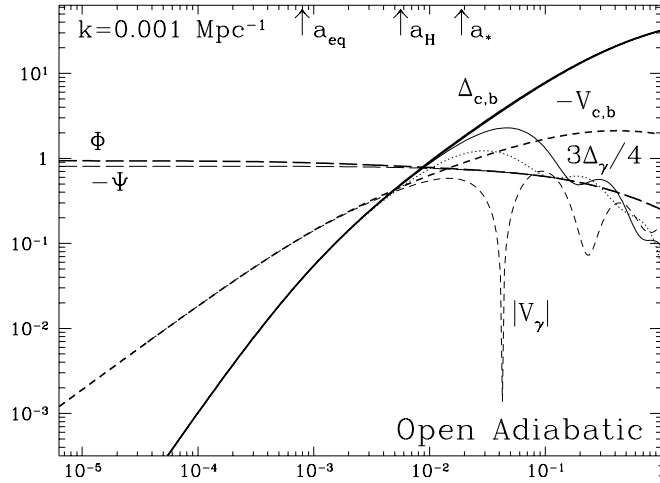


Figure 5.1: Large Scale Adiabatic Evolution

All density fluctuations evolve adiabatically $\Delta_c = \Delta_b = \frac{3}{4}\Delta_\gamma = \frac{3}{4}\Delta_\nu$ for the cold dark matter, baryons, photons and neutrinos respectively above the horizon $a < a_H$. Unlabeled dotted line is $\frac{3}{4}\Delta_\nu$. The potentials remain nearly constant until curvature domination with a 10% change at equality. The small difference between Φ and $-\Psi$ is due to the neutrino anisotropic stress (see Appendix A.1.1). After horizon crossing, the neutrinos free stream as do the photons after last scattering a_* . The model here is a fully ionized adiabatic $\Omega_0 = 0.2$, $h = 0.5$, $\Omega_b = 0.06$ universe.

The axion isocurvature model introduces density perturbations Δ_c in the cold collisionless axions in the radiation-dominated epoch without generating curvature. This implies that $S_{c\gamma} = S_{c\nu} = \Delta_c(0) = \text{constant}$ and $S_{b\gamma} = S_{b\nu} = 0$. However, the scale invariant model does not succeed in forming large scale structure and tilted models overproduce CMB anisotropies. The most promising isocurvature model is the baryon-dominated model of Peebles [125, 126] where ρ_c is assumed absent. By the same argument as above, $S_{b\gamma} = S_{b\nu} = \Delta_b(0)$ initially. Of course, since there is no cold collisionless component $S_{c\gamma} = S_{c\nu} = 0$ and $S_{b\gamma} = S_{b\nu} = S$. We shall see that some versions of this model can succeed since baryon fluctuations can lead to early structure formation and reionization damping of CMB anisotropies (see §7.1.2). When displaying isocurvature models, we implicitly assume the baryonic case.

5.1.4 Component Evolution

With the definition of S [equation (5.22)], all component perturbations can be written in terms of Δ_T . The velocity and potentials are constructed as

$$\begin{aligned} V_T &= -\frac{3}{k} \frac{\dot{a}}{a} \left(1 - \frac{3K}{k^2}\right)^{-1} \frac{1+a}{4+3a} \left[a \frac{d\Delta_T}{da} - \frac{1}{1+a} \Delta_T \right], \\ \Psi &= -\frac{3}{4} \left(\frac{k_{eq}}{k}\right)^2 \left(1 - \frac{3K}{k^2}\right)^{-1} \frac{1+a}{a^2} \Delta_T, \end{aligned} \quad (5.24)$$

where note that constant entropy assumption requires that all the velocities $V_i = V_T$. The relation for the velocity may be simplified by noting that

$$\begin{aligned} \eta &\simeq \frac{2\sqrt{2}}{k_{eq}} \left[\sqrt{1+a} - 1 \right] \quad \text{RD/MD} \\ &\simeq \frac{1}{\sqrt{-K}} \cosh^{-1} \left[1 + \frac{2(1-\Omega_0)}{\Omega_0} \frac{a}{a_0} \right], \quad \text{MD/CD} \end{aligned} \quad (5.25)$$

where CD denotes curvature domination with $\Lambda = 0$. For $\Lambda \neq 0$, it must be evaluated by numerical integration. Before curvature or Λ domination

$$\frac{\dot{a}}{a} = \frac{(1+a)^{1/2}}{\sqrt{2}a} k_{eq}, \quad (5.26)$$

which can be used to explicitly evaluate (5.24).

Now let us consider the implications of the general solution (5.20). The results for the adiabatic mode are extremely simple. When the universe is dominated by radiation (RD), matter (MD), curvature (CD) or the cosmological constant (Λ D), the total density fluctuation takes the form

$$\Delta_T/\Phi(0) = \begin{cases} \frac{4}{3}(k/k_{eq})^2(1-3K/k^2)a^2 & \text{RD} \\ \frac{6}{5}(k/k_{eq})^2(1-3K/k^2)a & \text{MD} \\ \frac{6}{5}(k/k_{eq})^2(1-3K/k^2)D. & \text{CD}/\Lambda\text{D} \end{cases} \quad (5.27)$$

Moreover since $S = 0$, the components evolve together $\Delta_b = \Delta_c = \frac{3}{4}\Delta_\gamma = \frac{3}{4}\Delta_\nu$ where Δ_c is any decoupled non-relativistic component (*e.g.* CDM). The velocity and potential are given by

$$V_T/\Phi(0) = \begin{cases} -\frac{\sqrt{2}}{2}(k/k_{eq})a & \text{RD} \\ -\frac{3\sqrt{2}}{5}(k/k_{eq})a^{1/2} & \text{MD} \\ -\frac{6}{5}(k/k_{eq})\dot{D}/k_{eq}, & \text{CD}/\Lambda\text{D} \end{cases} \quad (5.28)$$

$$\Psi/\Phi(0) = -\Phi/\Phi(0) = \begin{cases} -1 & \text{RD} \\ -\frac{9}{10} & \text{MD} \\ -\frac{9}{10}D/a. & \text{CD}/\Lambda\text{D} \end{cases} \quad (5.29)$$

An example of the evolution is plotted in Fig. 5.1.

We can also generate the Newtonian temperature perturbation from the gauge transformation

$$\Theta_0 = \frac{\Delta_\gamma}{4} - \frac{\dot{a}}{a} \frac{V_T}{k}, \quad (5.30)$$

which yields

$$\Theta_0/\Phi(0) = \begin{cases} \frac{1}{2} & \text{RD} \\ \frac{3}{5} & \text{MD} \\ \frac{3}{2} - \frac{9}{10}D/a. & \text{CD}/\Lambda\text{D} \end{cases} \quad (5.31)$$

In fact, these relations are far easier to derive in the Newtonian gauge itself where $\dot{\Theta}_0 = \dot{\Phi}$. Note that in the matter-dominated epoch, $\Theta_0 = -\frac{2}{3}\Psi$ which will be important for the Sachs-Wolfe effect (see §6.2).

Contrast this with the isocurvature evolution,

$$\Delta_T/S(0) = \begin{cases} \frac{1}{6} (k/k_{eq})^2 (1 - 3K/k^2) a^3 & \text{RD} \\ \frac{4}{15} (k/k_{eq})^2 (1 - 3K/k^2) a & \text{MD} \\ \frac{4}{15} (k/k_{eq})^2 (1 - 3K/k^2) D. & \text{CD}/\Lambda\text{D} \end{cases} \quad (5.32)$$

In baryonic models

$$\Delta_b = \frac{1}{4 + 3a} [4S + 3(1 + a)\Delta_T], \quad (5.33)$$

and

$$\begin{aligned} \Delta_\nu &= \frac{4}{3} (\Delta_b - S_{b\nu}), \\ \Delta_\gamma &= \frac{4}{3} (\Delta_b - S_{b\gamma}). \end{aligned} \quad (5.34)$$

Recall that since the curvature perturbation vanishes initially $S_{b\nu} = S_{b\gamma} = S$. From these relations, we obtain

$$\Delta_b/S(0) = \begin{cases} 1 - \frac{3}{4}a & \text{RD} \\ \frac{4}{3} \left[a^{-1} + \frac{1}{5} (k/k_{eq})^2 (1 - 3K/k^2) a \right] & \text{MD} \\ \frac{4}{3} \left[a^{-1} + \frac{1}{5} (k/k_{eq})^2 (1 - 3K/k^2) D \right], & \text{CD}/\Lambda\text{D} \end{cases} \quad (5.35)$$

and

$$\Delta_\gamma/S(0) = \Delta_\nu/S(0) = \begin{cases} -a & \text{RD} \\ \frac{4}{3} \left[-1 + \frac{4}{15} (k/k_{eq})^2 (1 - 3K/k^2) a \right] & \text{MD} \\ \frac{4}{3} \left[-1 + \frac{4}{15} (k/k_{eq})^2 (1 - 3K/k^2) D \right], & \text{CD}/\Lambda\text{D} \end{cases} \quad (5.36)$$

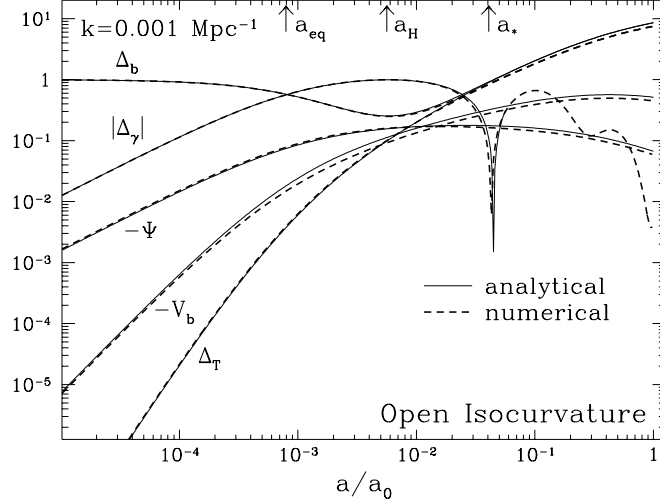


Figure 5.2: Large Scale Isocurvature Evolution

Perturbations, which originate in the baryons, are transferred to the radiation as the universe becomes more matter dominated to avoid a significant curvature perturbation. Nonetheless, radiation fluctuations create total density fluctuations from feedback. These adiabatic fluctuations in Δ_T dominate over the original entropy perturbation near horizon crossing a_H in the matter dominated epoch. The single fluid approximation cannot extend after last scattering for the photons a_* , since free streaming will damp Δ_γ away. After curvature domination, the total density is prevented from growing and thus leads to decay in the gravitational potential Ψ .

for the baryon and radiation components. Lastly, the velocity, potential, and photon temperature also have simple asymptotic forms,

$$V_T/S(0) = \begin{cases} -\frac{\sqrt{2}}{8}(k/k_{eq})a^2 & \text{RD} \\ -\frac{2\sqrt{2}}{15}(k/k_{eq})a^{1/2} & \text{MD} \\ -\frac{4}{15}(k/k_{eq})\dot{D}/k_{eq}, & \text{CD}/\Lambda\text{D} \end{cases} \quad (5.37)$$

$$\Psi/S(0) = -\Phi/S(0) = \begin{cases} -\frac{1}{8}a & \text{RD} \\ -\frac{1}{5} & \text{MD} \\ -\frac{1}{5}D/a, & \text{CD}/\Lambda\text{D} \end{cases} \quad (5.38)$$

$$\Theta_0/S(0) = \begin{cases} -\frac{1}{8}a & \text{RD} \\ -\frac{1}{5} & \text{MD} \\ -\frac{1}{5}D/a. & \text{CD}/\Lambda\text{D} \end{cases} \quad (5.39)$$

The equality of Θ and Ψ is easy to understand in the Newtonian gauge where $\dot{\Theta}_0 = -\dot{\Phi}$. In Fig. 5.2, we display an example of the isocurvature component evolution.

5.1.5 Discussion

Let us try to interpret these results physically. The isocurvature condition is satisfied by initially placing the fluctuations in the baryons $\Delta_b = S(0)$ with $\Delta_\gamma = 0$, so that $\Delta_T = 0$. As the universe evolves however, the relative significance of the baryon fluctuation $\Delta_b \rho_b / \rho_T$ for the total density fluctuation Δ_T grows as a . To compensate, the photon and neutrino fluctuations grow to be equal and opposite $\Delta_\gamma = \Delta_\nu = -aS(0)$. The tight-coupling condition $\dot{\Delta}_b = \frac{3}{4}\dot{\Delta}_\gamma$ implies then that the baryon fluctuation must also decrease so that $\Delta_b = (1 - 3a/4)S(0)$. The presence of Δ_γ means that there is a gradient in the photon energy density. This gradient gives rise to a dipole V_γ as the regions come into causal contact [see equation (4.54)], *i.e.* $V_\gamma \propto k\eta\Delta_\gamma \propto -ka^2S(0)$. The same argument holds for the neutrinos. Constant entropy requires that the total fluid move with the photons and neutrinos $V_T = V_\gamma$, and thus infall, produced by the gradient in the velocity, yields a total density perturbation $\Delta_T \propto -k\eta(1 - 3K/k^2)V_T \propto k^2(1 - 3K/k^2)a^3S(0)$ [see equation (5.6)]. This is one way of interpreting equation (5.21) and the fact that the entropy provides a source of total density fluctuations in the radiation-dominated epoch [73]

A similar analysis applies for adiabatic fluctuations, which begin instead with finite potential Ψ . Infall implies $V_T \propto k\eta\Psi(0) \simeq -k\eta\Phi(0)$, which then yields $\Delta_T \propto -k\eta V_T \propto k^2(1 - 3K/k^2)a^2\Phi(0)$, thereby also keeping the potential constant. Compared to the adiabatic case, the isocurvature scenario predicts total density perturbations which are smaller by one factor of a in the radiation-dominated epoch as might be expected from cancellation.

After radiation domination, both modes grow in pressureless linear theory $\Delta_T \propto D$ [*c.f.* equations (5.27) and (5.32)]. Whereas in the radiation-dominated limit, the entropy term S and the gravitational infall term Ψ are comparable in equation (5.6), the entropy source is thereafter suppressed by $w_T = p_T/\rho_T$, making the isocurvature and adiabatic evolutions identical. Furthermore, since the growth of Δ_T is suppressed in open and Λ -dominated universes, the potential Ψ decays which has interesting consequences for anisotropies as we shall see in §6.2.

5.2 Subhorizon Evolution before Recombination

As the perturbation enters the horizon, we can no longer view the system as a single fluid. Decoupled components such as the neutrinos free stream and change the

number density, *i.e.* entropy, fluctuation. However, above the photon diffusion scale, the photons and baryons are still tightly coupled by Compton scattering until recombination. Since even then the diffusion length is much smaller than the horizon η_* , it is appropriate to combine the photon and baryon fluids for study [92, 147]. In this section, we show that photon pressure resists the gravitational compression of the photon-baryon fluid, leading to *driven* acoustic oscillations [82] which are then damped by photon diffusion.

5.2.1 Analytic Acoustic Solutions

At intermediate scales, neither radiation pressure nor gravity can be ignored. Fortunately, their effects can be analytically separated and analyzed [82]. Since photon-baryon tight coupling still holds, it is appropriate to expand the Boltzmann equation (4.54) and the Euler equation (4.58) for the baryons in the Compton scattering time $\dot{\tau}^{-1}$ [127]. To zeroth order, we regain the tight-coupling identities,

$$\begin{aligned}\dot{\Delta}_\gamma &= \frac{4}{3}\dot{\Delta}_b, & (\text{or } \dot{\Theta}_0 &= \frac{1}{3}\dot{\delta}_b^N) \\ \Theta_1 &\equiv V_\gamma = V_b, \\ \Theta_\ell &= 0. & \ell \geq 2\end{aligned}\tag{5.40}$$

These equations merely express the fact that the radiation is isotropic in the baryon rest frame and the density fluctuations in the photons grow adiabatically with the baryons. Substituting the zeroth order solutions back into equations (4.54) and (4.58), we obtain the iterative first order solution,

$$\begin{aligned}\dot{\Theta}_0 &= -\frac{k}{3}\Theta_1 - \dot{\Phi}, \\ \dot{\Theta}_1 &= -\frac{\dot{R}}{1+R}\Theta_1 + \frac{1}{1+R}k\Theta_0 + k\Psi,\end{aligned}\tag{5.41}$$

where we have used the relation $\dot{R} = (\dot{a}/a)R$. The tight-coupling approximation eliminates the multiple time scales and the infinite hierarchy of coupled equations of the full problem. In fact, this simple set of equations can readily be solved numerically [147]. To solve them analytically, let us rewrite it as a single second order equation,

$$\ddot{\Theta}_0 + \frac{\dot{R}}{1+R}\dot{\Theta}_0 + k^2c_s^2\Theta_0 = F,\tag{5.42}$$

where the photon-baryon sound speed is

$$c_s^2 \equiv \frac{\dot{p}_\gamma}{\dot{\rho}_\gamma + \dot{\rho}_b} = \frac{1}{3} \frac{1}{1+R},\tag{5.43}$$

assuming $p_b \simeq 0$ and

$$F = -\ddot{\Phi} - \frac{\dot{R}}{1+R}\dot{\Phi} - \frac{k^2}{3}\Psi, \quad (5.44)$$

is the forcing function. Here $\ddot{\Phi}$ represents the dilation effect, $\dot{\Phi}$ the modification to expansion damping, and Ψ the gravitational infall. The homogeneous $F = 0$ equation yields the two fundamental solutions under the adiabatic approximation,

$$\begin{aligned} \theta_a &= (1+R)^{-1/4} \cos kr_s, \\ \theta_b &= (1+R)^{-1/4} \sin kr_s, \end{aligned} \quad (5.45)$$

where the sound horizon is

$$r_s = \int_0^\eta c_s d\eta' = \frac{2}{3} \frac{1}{k_{eq}} \sqrt{\frac{6}{R_{eq}}} \ln \frac{\sqrt{1+R} + \sqrt{R+R_{eq}}}{1 + \sqrt{R_{eq}}}. \quad (5.46)$$

The phase relation $\phi = kr_s$ just reflects the nature of acoustic oscillations. If the sound speed were constant, it would yield the expected dispersion relation $\omega = kc_s$.

The adiabatic or WKB approximation assumes that the time scale for the variation in the sound speed is much longer than the period of the oscillation. More specifically, the mixed $\dot{R}\dot{\Theta}_0$ is included in this first order treatment, but second order terms are dropped under the assumption that

$$(kc_s)^2 \gg (1+R)^{1/4} \frac{d^2}{d\eta^2} (1+R)^{-1/4}, \quad (5.47)$$

or

$$\begin{aligned} (kc_s)^2 &\gg \frac{\dot{R}^2}{(1+R)^2} \\ &\gg \frac{\ddot{R}}{1+R}. \end{aligned} \quad (5.48)$$

It is therefore satisfied at early times and on small scales. Even at last scattering the approximation holds well for $k > 0.08h^3 \text{ Mpc}^{-1}$ if $R < 1$ and $a > 1$, as is the case for the standard CDM model.

Now we need to take into account the forcing function $F(\eta)$ due to the gravitational potentials Ψ and Φ . Employing the Green's method, we construct the particular solution,

$$\hat{\Theta}_0(\eta) = C_1\theta_a(\eta) + C_2\theta_b(\eta) + \int_0^\eta \frac{\theta_a(\eta')\dot{\theta}_b(\eta) - \theta_a(\eta)\dot{\theta}_b(\eta')}{\theta_a(\eta')\dot{\theta}_b(\eta') - \dot{\theta}_a(\eta')\theta_b(\eta')} F(\eta') d\eta'. \quad (5.49)$$

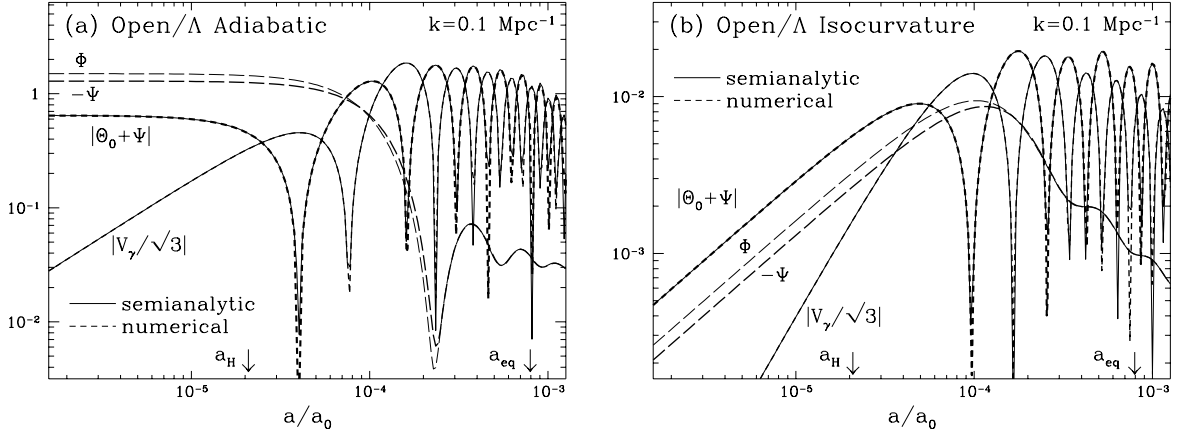


Figure 5.3: Acoustic Oscillations

Pressure resists the gravitational forces of compression (adiabatic) and rarefaction (isocurvature) leading to acoustic oscillations. Baryons increase the gravitating mass leading to higher compressional peaks, which dominate over the rarefaction peaks and the Doppler line of sight velocity contribution $V_\gamma/\sqrt{3}$ as R is increased. Whereas the isocurvature case has $\Omega_0 = \Omega_b$, the adiabatic model has $\Omega_b = 0.06$ and a consequently smaller R . Also displayed here is the semianalytic approximation described in the text, which is essentially exact. The small difference in the numerical amplitudes of Φ and Ψ is due to the anisotropic stress of the neutrinos (see §A.1.1). Here $\Omega_0 = 0.2$ and $h = 0.5$.

Equation (5.45) implies

$$\theta_a(\eta')\theta_b(\eta) - \theta_a(\eta)\theta_b(\eta') = [1 + R(\eta)]^{-1/4}[1 + R(\eta')]^{-1/4}\sin[kr_s(\eta) - kr_s(\eta')], \quad (5.50)$$

and

$$\theta_a(\eta')\dot{\theta}_b(\eta') - \dot{\theta}_a(\eta')\theta_b(\eta') = \frac{k}{\sqrt{3}}[1 + R(\eta')]^{-1}. \quad (5.51)$$

With C_1 and C_2 fixed by the initial conditions, the solution in the presence of the source F then becomes [82]

$$\begin{aligned} [1 + R(\eta)]^{1/4}\hat{\Theta}_0(\eta) &= \Theta_0(0)\cos kr_s(\eta) + \frac{\sqrt{3}}{k}[\dot{\Theta}_0(0) + \frac{1}{4}\dot{R}(0)\Theta_0(0)]\sin kr_s(\eta) \\ &\quad + \frac{\sqrt{3}}{k}\int_0^\eta d\eta'[1 + R(\eta')]^{3/4}\sin[kr_s(\eta) - kr_s(\eta')]F(\eta'), \end{aligned} \quad (5.52)$$

and $k\Theta_1 = -3(\dot{\Theta}_0 + \dot{\Phi})$. The potentials in F can be approximated from their large (§5.1.4) and small (§5.2.3) scale solutions. As we shall show in Appendix A.2.2, this can lead to extremely accurate solutions. To show the true power of this technique here, we instead employ their numerical values in Fig. 5.3. The excellent agreement with the full solution indicates that our technique is limited only by our knowledge of the potentials.

5.2.2 Driven Acoustic Oscillations

Baryon Drag

Some basic features of the acoustic oscillations are worthwhile to note. Let us start with a toy model in which the potential is constant $\dot{\Psi} = 0 = \dot{\Phi}$. This corresponds to a universe which was always matter dominated. Let us also assume that the baryon-photon ratio R is constant. Of course neither of these assumptions are valid for the real universe, but as we shall see the generalization to realistic cases is qualitatively simple. Under these assumption, the solution of equation (5.42) is obvious,

$$\hat{\Theta}_0(\eta) = [\Theta_0(0) + (1 + R)\Psi]\cos(kr_s) + \frac{1}{kc_s}\dot{\Theta}_0(0)\sin(kr_s) - (1 + R)\Psi, \quad (5.53)$$

where the sound horizon reduces to $r_s = c_s\eta$. Several basic features are worth noting:

1. The zero point of the oscillation $\Theta_0 = -(1 + R)\Psi$ is increasingly shifted with the baryon content.
2. The amplitude of the oscillation increases with the baryon content R .
3. The redshift Ψ from climbing out of potential wells cancels the $R = 0$ zero point shift.
4. Adiabatic initial conditions where $\Theta_0(0) = \text{constant}$ and isocurvature initial conditions where $\dot{\Theta}_0(0) = \text{constant}$ stimulate the cosine and sine harmonic respectively.

Of course here $\dot{\Theta}_0(0)$ does not really describe the isocurvature case since here $\Phi \neq 0$ in the initial conditions. We will see in the next section what difference this makes.

The zero point of the oscillation is the state at which the forces of gravity and pressure are in balance. If the photons dominate, $R \rightarrow 0$ and this balance occurs at $\Theta_0 = -\Psi$ reflecting the fact that in equilibrium, the photons are compressed and hotter inside the potential well. Infall not only increases the number density of photons but also their energy through gravitational blueshifts. It is evident however that when the photons climb back out of the well, they suffer an equal and opposite effect. Thus the effective temperature is $\Theta_0 + \Psi$. It is this quantity that oscillates around zero if the baryons can be neglected.

Baryons add gravitational and inertial mass to the fluid without raising the pressure. We can rewrite the oscillator equation (5.42) as

$$(1 + R)\ddot{\Theta}_0 + \frac{k^2}{3}\Theta_0 = -(1 + R)\frac{k^2}{3}\Psi, \quad (5.54)$$

neglecting changes in R and Φ . Note that $m_{\text{eff}} = 1 + R$ represents the effective mass of the oscillator. Baryonic infall drags the photons into potential wells and consequently leads to greater compression shifting the effective temperature to $-R\Psi$. All compressional phases will be enhanced over rarefaction phases. This explains the alternating series of peak amplitudes in Fig. 5.3b where the ratio R is significant at late times. In the lower R case of Fig. 5.3a, the effect is less apparent. Furthermore, a shift in the zero point implies larger amplitude oscillations since the initial displacement from the zero point becomes larger.

Adiabatic and isocurvature conditions also have different phase relations. Peak fluctuations occur for $kr_s = m\pi$ and $kr_s = (m - 1/2)\pi$ for adiabatic and isocurvature modes respectively. Unlike their adiabatic counterpart, isocurvature conditions are set up to resist gravitational attraction. Thus the compression phase is reached for odd m adiabatic peaks and even m isocurvature peaks.

Doppler Effect

The bulk velocity of the fluid along the line of sight $V_\gamma/\sqrt{3}$ causes the observed temperature to be Doppler shifted. From the continuity equation (5.41), the acoustic velocity becomes

$$\frac{V_\gamma(\eta)}{\sqrt{3}} = -\frac{\sqrt{3}}{k}\dot{\Theta}_0 = \sqrt{3}[\Theta_0(0) + (1 + R)\Psi]c_s \sin(kr_s) - \frac{\sqrt{3}}{k}\dot{\Theta}_0(0)\cos(kr_s), \quad (5.55)$$

assuming $\dot{\Phi} = 0$, which yields the following interesting facts:

1. The velocity is $\pi/2$ out of phase with the temperature.
2. The zero point of the oscillation is not displaced.
3. The amplitude of the oscillation is reduced by a factor of $\sqrt{3}c_s = (1 + R)^{-1/2}$ compared with the temperature.

Because of its phase relation, the velocity contribution will fill in the zeros of the temperature oscillation. Velocity oscillations, unlike their temperature counterparts are symmetric around zero. The *relative* amplitude of the velocity compared with the temperature oscillations also decreases with the baryon content R . For the same initial displacement, conservation of energy requires a smaller velocity as the mass increases. Together the zero point shift and the increased amplitude of temperature perturbations is sufficient to make

compressional temperature peaks significantly more prominent than velocity or rarefaction peaks (see Fig. 5.3b).

Effective Mass Evolution

In the real universe however, R must grow from zero at the initial conditions and adiabatically changes the effective mass of the oscillator $m_{\text{eff}} = (1 + R)$. While the statements above for constant R are qualitatively correct, they overestimate the effect. The exact solution given in equation (5.52) must be used for quantitative work.

Notice that the full first order relation (5.41) is exactly an oscillator with time-varying mass:

$$\frac{d}{d\eta}(1+R)\dot{\Theta}_0 + \frac{k^2}{3}\Theta_0 = -(1+R)\frac{k^2}{3}\Psi - \frac{d}{d\eta}(1+R)\dot{\Phi}, \quad (5.56)$$

where the last term on the rhs is the dilation effect from $\dot{\Theta}_0 = -\dot{\Phi}$. This form exposes a new feature due to a time varying effective mass. Treating the effective mass as an oscillator parameter, we can solve the homogeneous part of equation (5.56) under the adiabatic approximation. In classical mechanics, the ratio of the energy $E = \frac{1}{2}m_{\text{eff}}\omega^2 A^2$ to the frequency ω of an oscillator is an adiabatic invariant. Thus the amplitude scales as $A \propto \omega^{1/2} \propto (1+R)^{-1/4}$, which explains the appearance of this factor in equation (5.45).

Driving Force and Radiation Feedback

Now let us consider a time varying potential. In any situation where the matter does not fully describe the dynamics, feedback from the radiation into the potential through the Poisson equation can cause time variation. For isocurvature conditions, we have seen that radiation feedback causes potentials to grow from zero outside the horizon (see §5.1 and Fig. 5.2). The net effect for the isocurvature mode is that outside the sound horizon, fluctuations behave as $\Theta = -\Phi \simeq \Psi$ [see equation (5.39)]. After sound horizon crossing, radiation density perturbations cease to grow, leading to a decay in the gravitational potential in the radiation-dominated epoch. Thus scales that cross during matter domination experience more growth and are enhanced over their small scale counterparts. Furthermore, morphologically $-\ddot{\Phi} - k^2\Psi/3 \propto \sin(kr_s)$ leading to near resonant driving of the sine mode of the oscillation until sound horizon crossing. This supports our claim above that $\sin(kr_s)$ represents the isocurvature mode.

The adiabatic mode exhibits contrasting behavior. Here the potential is constant outside the sound horizon and then decays like the isocurvature case. However, it is the decay itself that drives the oscillation since the form of the forcing function becomes approximately $-\ddot{\Phi} - k^2\Psi/3 \propto \cos(kc_s\eta)$ until $kc_s\eta \sim 1$ and then dies away. In other words, the gravitational force drives the first compression without a counterbalancing effect on the subsequent rarefaction phase. Therefore, for the adiabatic mode, the oscillation amplitude is boosted at sound horizon crossing in the radiation-dominated universe which explains the prominence of the oscillations with respect to the superhorizon tail in Fig. 5.3a. One might expect from the dilation effect $\dot{\Theta} = -\dot{\Phi}$ that the temperature is boosted up to $\Theta(\eta) \simeq \Theta(0) - \Phi(\eta) + \Phi(0) \simeq \frac{3}{2}\Phi(0)$. We shall see in the next section that a more detailed analysis supports this conclusion. Therefore, unlike the isocurvature case, adiabatic modes experience an enhancement for scales smaller than the horizon at equality.

5.2.3 Damped Acoustic Oscillations

Well below the sound horizon in the radiation-dominated epoch, the gravitational potentials have decayed to insignificance and the photon-baryon fluctuations behave as simple oscillatory functions. However photon-baryon tight coupling breaks down at the photon diffusion scale. At this point, photon fluctuations are exponentially damped due to diffusive mixing and rescattering. We can account for this by expanding the Boltzmann and Euler equations for the photons and baryons respectively to second order in $\dot{\tau}^{-1}$ (see [124] and Appendix A.3.1). This gives the dispersion relation an imaginary part, making the general solution

$$\Theta_0 = C_A(1+R)^{-1/4}\mathcal{D}(\eta, k)\cos kr_s + C_I(1+R)^{-1/4}\mathcal{D}(\eta, k)\sin kr_s, \quad (5.57)$$

where C_A and C_I are constants and the damping factor is

$$\mathcal{D}(\eta, k) = e^{-(k/k_D)^2}, \quad (5.58)$$

with the damping scale

$$k_D^{-2} = \frac{1}{6} \int d\eta \frac{1}{\dot{\tau}} \frac{R^2 + 4(1+R)/5}{(1+R)^2}. \quad (5.59)$$

For small corrections to this relation due to the angular dependence of Compton scattering and polarization, see [93] and Appendix A.3.1. Since the R factors in equation (5.59) go to $\frac{4}{5}$ for $R \ll 1$ and 1 for $R \gg 1$, the damping length is approximately $\lambda_D^2 \sim k_D^{-2} \sim \int d\eta/\dot{\tau}$.

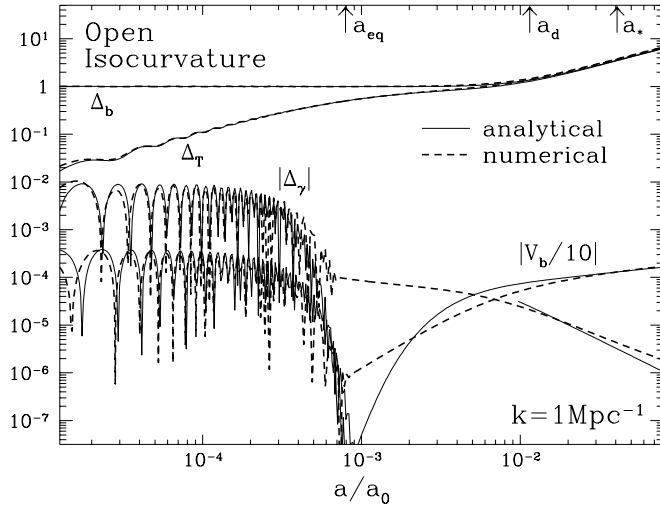


Figure 5.4: Small Scale Isocurvature Evolution

At small scales gravity may be ignored, yielding pure adiabatic oscillations. Perturbations in the photons damp once the diffusion length grows larger than the wavelength $k_D < k$. Likewise the adiabatic component of the baryon fluctuations also damps leaving them with the original entropy perturbation. After diffusion, the photons and baryons behave as separate fluids, allowing the baryons to grow once Compton drag becomes negligible $a > a_d$. Photon fluctuations are then regenerated by the Doppler effect as they diffuse across infalling baryons. The analytic approach for the photons in this limit apply between the drag epoch and last scattering $a_d < a < a_*$ (see §7.1.3). The model here is $\Omega_0 = 0.2$, $h = 0.5$, and no recombination.

This relation is easy to understand qualitatively. The Compton mean free path of the photons is $\lambda_C = \dot{\tau}^{-1}$. The scale on which a photon can diffuse is given by a random walk process $\sqrt{N}\lambda_C$ where the number of steps is $N = \eta/\lambda_C$. Therefore the diffusion scale is approximately $\lambda_D \simeq \sqrt{\lambda_C\eta} = \sqrt{\eta/\dot{\tau}}$.

The amplitudes of these oscillations, *i.e.* the constants C_A and C_I , are determined by the total effect of the gravitational driving force in equation (5.44). However, a simpler argument suffices for showing its general behavior. As shown in §5.1.4, isocurvature fluctuations grow like $\Delta_\gamma \simeq -aS(0)$ until sound horizon crossing. Since the sound horizon crossing is near $a_H \sim k_{eq}/k$ (see equation (5.8)), the isocurvature amplitude will be suppressed by k_{eq}/k . On the other hand, adiabatic fluctuations which grow as a^2 will have a $(k_{eq}/k)^2$ suppression factor which just cancels the factor $(k/k_{eq})^2$ from the Poisson equation [see (5.27)] when expressed in terms of the initial potential. This simple argument fixes the amplitude up to a factor of order unity.

We obtain the specific amplitude by solving equation (5.6) under the constant en-

tropy assumption $\dot{S} = 0$. The latter approximation is not strictly valid since free streaming of the neutrinos will change the entropy fluctuation. However, since the amplitude is fixed after sound horizon crossing, which is only slightly after horizon crossing, it suffices. Under this assumption, the equation can again be solved in the small scale limit. Kodama & Sasaki [100] find that for adiabatic perturbations,

$$C_A = \frac{3}{2}\Phi(0), \quad C_I = 0, \quad (\text{adi}) \quad (5.60)$$

from which the isocurvature solution follows via Greens method,

$$C_A = 0, \quad C_I = -\frac{\sqrt{6} k_{eq}}{4 k} S(0), \quad (\text{iso}) \quad (5.61)$$

if $k \gg k_{eq}$, $k\eta \gg 1$ and $k \gg \sqrt{-K}$. As expected, the isocurvature mode stimulates the $\text{sink}r_s$ harmonic, as opposed to $\text{cos}kr_s$ for the adiabatic mode.

We can also construct the evolution of density perturbations at small scales. Well inside the horizon $\Delta_\gamma = 4\Theta_0$, since total matter and Newtonian fluctuations are equivalent. The isocurvature mode solution therefore satisfies (RD/MD)

$$\Delta_\gamma/S(0) = -\sqrt{6} \left(\frac{k_{eq}}{k} \right) (1+R)^{-1/4} \mathcal{D}(a, k) \text{sink}r_s. \quad (5.62)$$

The tight-coupling limit implies $\dot{\Delta}_b = \frac{3}{4}\dot{\Delta}_\gamma$ which requires (RD/MD),

$$\Delta_b/S(0) = 1 - \frac{3\sqrt{6}}{4} \left(\frac{k_{eq}}{k} \right) (1+R)^{-1/4} \mathcal{D}(a, k) \text{sink}r_s. \quad (5.63)$$

This diffusive suppression of the adiabatic component for the baryon fluctuation is known as Silk damping [150]. After damping, the baryons are left with the original entropy perturbation $S(0)$. Since they are surrounded by a homogeneous and isotropic sea of photons, the baryons are unaffected by further photon diffusion. From the photon or baryon continuity equations at small scales, we obtain (RD/MD)

$$V_b/S(0) = V_\gamma/C_I \simeq \frac{3\sqrt{2}}{4} \left(\frac{k_{eq}}{k} \right) (1+R)^{-3/4} \mathcal{D}(a, k) \text{cos}kr_s. \quad (5.64)$$

As one would expect, the velocity oscillates $\pi/2$ out of phase with, and increasingly suppressed compared to, the density perturbations. Employing equations (5.62) and (5.63), we construct the total density perturbation by assuming that free streaming has damped out the neutrino contribution (RD/MD),

$$\Delta_T/S(0) = \frac{a}{1+a} \left[1 - \frac{3\sqrt{6} k_{eq}}{4 k} R^{-1} (1+R)^{3/4} \mathcal{D}(a, k) \text{sink}r_s \right]. \quad (5.65)$$

From this equation, we may derive the potential (RD/MD),

$$\Psi/S(0) = -\frac{3}{4} \left(\frac{k_{eq}}{k} \right)^2 \frac{1}{a} \left[1 - \frac{3\sqrt{6}}{4} \frac{k_{eq}}{k} R^{-1} (1+R)^{3/4} \mathcal{D}(a, k) \text{sinc}kr_s \right], \quad (5.66)$$

which decays with the expansion since Δ_T goes to a constant. In Fig. 5.4, we compare these analytic approximations with the numerical results. After damping eliminates the adiabatic oscillations, the evolution of perturbations is governed by diffusive processes. A similar analysis for adiabatic perturbations shows that diffusion damping almost completely eliminates small scale baryonic fluctuations.¹ Unlike the isocurvature case, unless CDM wells are present to reseed fluctuations, adiabatic models consequently fail to form galaxies.

5.3 Matter Evolution after Recombination

At $z_* \simeq 1000$, the CMB can no longer keep hydrogen ionized and the free electron density drops precipitously. The photons thereafter free stream until a possible epoch of reionization. The subsequent evolution of the photon fluctuations will be intensely studied in §6 and §7. Essentially, they preserve the fluctuations they possess at last scattering in the form of anisotropies. Here we will concentrate on the evolution of the matter as it is important for structure formation and feeds back into the CMB through reionization.

5.3.1 Compton Drag

Baryon fluctuations in diffusion damped scales can be regenerated after Compton scattering has become ineffective. The critical epoch is that at which the photon pressure or “Compton drag” can no longer prevent gravitational instability in the baryons. The drag on an individual baryon does not depend on the total number of baryons but rather the number of photons and its ionization state. From the baryon Euler equation (4.58) and the Poisson equation (5.24), the drag term $\propto V_b$ comes to dominate over the gravitational infall term $\propto k\Psi$ at redshifts above $z \sim 200(\Omega_0 h^2)^{1/5} x_e^{-2/5}$. Thus all modes are released from Compton drag at the same time, which we take to be

$$z_d = 160(\Omega_0 h^2)^{1/5} x_e^{-2/5}, \quad (5.67)$$

defined as the epoch when fluctuations effectively join the growing mode of pressureless linear theory.

¹Residual fluctuations are on the order $R\Psi$ as discussed in Appendix A.3.1.

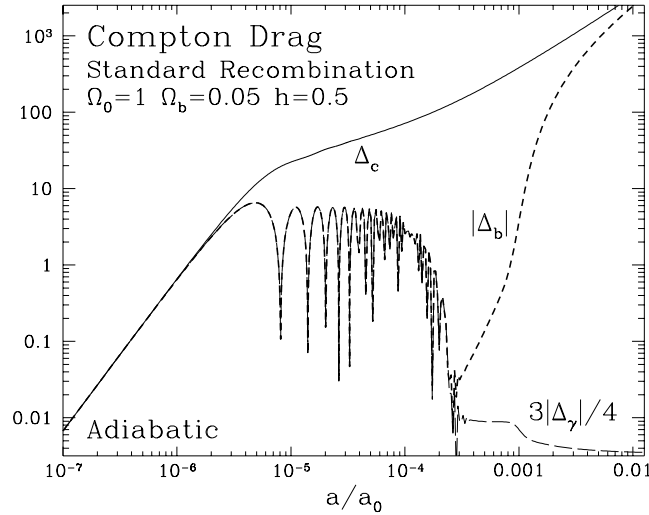


Figure 5.5: Compton Drag and Standard Recombination

After recombination, the Compton drag on the baryons decreases sharply. The residual ionization after recombination however is sufficient to slow baryon infall into dark matter wells. The baryon and cold dark matter fluctuation Δ_c only converge at $z \lesssim 100$.

It is important to realize that the drag and the last scattering redshift are generally not equal. Following the drag epoch, baryons can be treated as freely falling. If cold dark matter exists in the model, potential wells though suppressed at small scales will still exist. In adiabatic CDM models, the Silk damped baryon fluctuations under the photon diffusion scale can be regenerated as the baryons fall into the dark matter potentials (see Fig. 5.5). For isocurvature models, the entropy fluctuations remaining after Silk damping are released at rest to grow in linear theory.

One complication arises though. The collapse of baryon fluctuations after recombination can lead to small scale non-linearities. Astrophysical processes associated with compact object formation can inject enough energy to reionize the universe (see §7 and *e.g.* [58]). Ionization again couples the baryons and photons. Yet even in a reionized universe, the Compton drag epoch eventually ends due to the decreasing number density of electrons. In CDM-dominated adiabatic models, the baryons subsequently fall into the dark matter wells leaving no trace of this extra epoch of Compton coupling. The CMB also retains no memory since last scattering occurs after the drag epoch in reionized scenarios. This is not the case for baryon isocurvature models since there are no dark matter wells into which baryons might fall. Evolution in the intermediate regime therefore has a direct effect on the

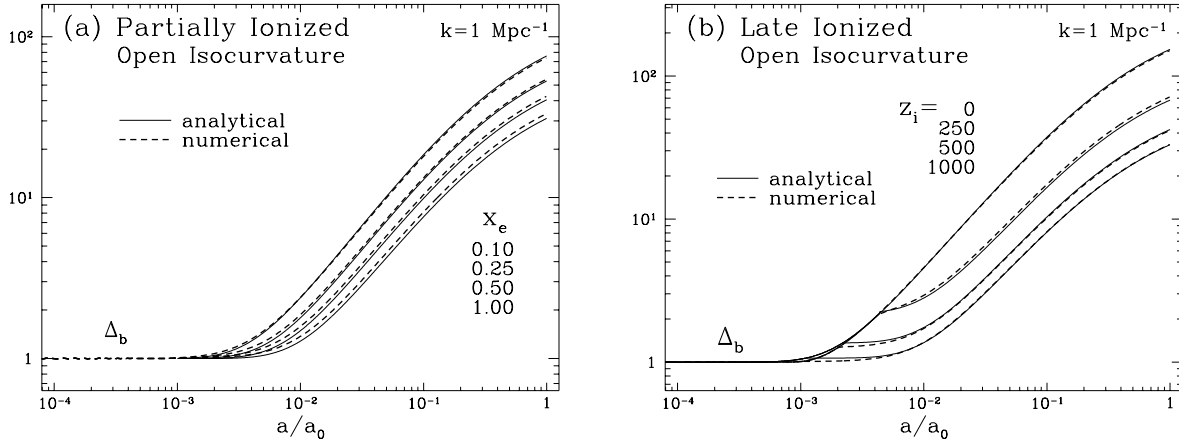


Figure 5.6: Compton Drag and Reionization

(a) The baryons are released to grow in pressureless linear theory after Compton drag becomes negligible. Raising the ionization fraction x_e delays the end of the drag epoch and makes fluctuations larger. (b) A transparent period between recombination and reionization at z_i leads to enhanced growth. After reionization, fluctuations are again suppressed until the end of the drag epoch. The model here an open baryon isocurvature one with $\Omega_0 = \Omega_b = 0.2$ $h = 0.5$.

amplitude of fluctuations in the matter and CMB today.

Reionization is also more likely in models where the initial power spectrum is tilted toward small scales. In the baryon isocurvature case, entropy fluctuations at small scales can be made quite large since they are essentially unprocessed by the pre-recombination evolution. For these reasons, we will concentrate on baryon isocurvature models in discussing Compton drag in reionized models.

5.3.2 Reionization in Isocurvature Models

Let us first consider the case where the universe was reionized immediately following standard recombination. Well before the end of the drag epoch z_d , the initial entropy fluctuations are frozen into the baryons. Well afterwards, the baryon fluctuations grow as in pressureless linear theory. An excellent empirical approximation to the behavior at intermediate times is given by

$$\Delta_b/S(0) = \mathcal{G}(a, a_d), \quad (5.68)$$

with the interpolation function

$$\mathcal{G}(a_1, a_2) = 1 + \frac{D(a_1)}{D(a_2)} \exp(-a_2/a_1), \quad (5.69)$$

where if $a_1 \gg a_2$, $\mathcal{G}(a_1, a_2) \rightarrow D(a_1)/D(a_2)$. The velocity V_T is given by the continuity equation (5.6). Notice that growth in an open and/or Λ universe is properly accounted for. This approximation is depicted in Fig. 5.6a.

Now let us consider more complicated thermal histories. Standard recombination may be followed by a significant transparent period before reionization at z_i , due to some later round of structure formation. There are two effects to consider here: fluctuation behavior in the transparent regime and after reionization. Let us begin with the first question. Near recombination, the baryons are released from drag essentially at rest and thereafter can grow in pressureless linear theory. The joining conditions then imply that $\frac{3}{5}$ of the perturbation enters the growing mode D [124], yielding present fluctuations of $\sim \frac{3}{5}C_I D(z=0)/D(z_d)$. This expression overestimates the effect for low $\Omega_0 h^2$ models due to the slower growth rate in a radiation-dominated universe. We introduce a phenomenological correction² by taking the effective drag epoch to be $z_d \simeq 750$ for $\Omega_0 h^2 \simeq 0.05$. The evolution is again well described by the interpolation function (5.69) so that $\Delta_b(a) = \mathcal{G}(a, a_t)C_I$. By this argument, the effective redshift to employ is $z_t \sim \frac{3}{5}z_d$.

Now let us consider the effects of reionization at z_i . After z_i , Compton drag again prevents the baryon perturbations from growing. Therefore the final perturbations will be $\Delta_b(a_0) \simeq \Delta_b(a_i)D(a_0)/D(a_d)$. Joining the transparent and ionized solutions, we obtain

$$\Delta_b/C_I = \begin{cases} \mathcal{G}(a, a_t) & a < a_g \\ \mathcal{G}(a_i, a_t)\mathcal{G}(a, a_d), & a > a_g \end{cases} \quad (5.70)$$

which is plotted in Fig. 5.6b. Since perturbations do not stop growing immediately after reionization and ionization after the drag epoch does not affect the perturbations, we take $a_g = \min(1.1a_i, a_d)$.

For the photons, the continued ionization causes the diffusion length to grow ever larger. As the electron density decreases due to the expansion, the diffusion length reaches the horizon scale and the photons effectively last scatter. As we have seen, diffusion destroys the intrinsic fluctuations in the CMB. Any residual fluctuations below the horizon must therefore be due to the coupling with the electrons. Since last scattering follows the drag epoch, the electrons can have a significant velocity at last scattering. Thus we expect the Compton coupling to imprint a Doppler effect on the photons at last scattering. We will discuss this process in greater detail in §7.

²A deeper and more complete analysis of this case is given in [84].

Chapter 6

Primary Anisotropies

*Trees in the mountains plunder themselves,
Grease in the flame sizzles itself,
Cinnamon has a taste, so they hack it down,
Lacquer has a use, so they strip it off.
All men know the uses of the useful,
No man knows the uses of the useless.*

—Chuang-tzu, 4

6.1 Overview

What can the study of anisotropy tell us about cosmology in general? When the *COBE* DMR team first reported the detection of anisotropies on the 10° scale and larger [153] at the 10^{-5} level, they were widely hailed as the panacea for all cosmological ills and uncertainties. It was quickly realized however that that which makes the discovery so important also makes it less than ideal for pinning down cosmological models: anisotropies at this level are a generic prediction of the gravitational instability picture for structure formation. The *COBE* DMR data *alone* lacks the dynamic range to distinguish between closely related instability scenarios. However, combined with the smaller scale measurements of large scale structure and the CMB itself, its true potential can be tapped.

The CMB suffers from fewer problems of interpretation than large scale structure since fluctuations are likely to be still in the linear regime at last scattering. It therefore has the potential to offer clean tests of the underlying cosmology. The current generation of anisotropy experiments extends the angular scale coverage an order of magnitude down to the degree scale. The next generation of space based experiments will probe yet another

order of magnitude down to the several arcminute scale. It is important to realistically assess what cosmological information lies in the spectrum of anisotropies from arcminute scales on up. The general study of anisotropy formation will be the focus of the remaining portion of this work. In this chapter, we consider primary anisotropy formation. Specifically, we assume that the photons free stream since recombination suffering only gravitational interactions between $z_* \simeq 1000$ and today. In the next chapter, we will consider processes in the intermediate regime which may alter the anisotropy.

6.1.1 Anisotropy Sources

At the most abstract level, there are only two factors relevant to the formation of anisotropies: gravitational interactions and Compton scattering. Nevertheless, their influence encodes a great wealth of cosmological information in the CMB. At the next level of detail, primary anisotropies are characterized by four quantities:

1. $\Theta_0(\eta_*, \mathbf{x})$: the intrinsic temperature at last scattering.
2. $\boldsymbol{\gamma} \cdot [\mathbf{v}_\gamma(\eta_*, \mathbf{x}) - v_{obs}]$: the line of sight velocity at η_* relative to the observer.
3. $\partial_x \Psi(\eta, \mathbf{x}(\eta))$: the gradient of the gravitational potential along the line of sight.
4. $\partial_\eta \Phi(\eta, \mathbf{x}(\eta))$: the time derivative of the space curvature along the line of sight.

Obviously intrinsic hot and cold spots on the last scattering surface appear as anisotropies today. The observed temperature of the background is also Doppler shifted due to the line of sight bulk motion (dipole moment) of the photons at last scattering relative to the observer. Our own peculiar velocity will just yield a dipole anisotropy pattern on the sky. The measured dipole in the CMB is almost certainly due to this effect and implies that the local group is moving at 627 ± 22 km/s with respect to the CMB frame [152]. A spatial variation in the photon bulk velocity at last scattering can result in an anisotropy at smaller angles. Gradients in the gravitational potential cause redshifts and blueshifts as the photons climb in and out of potential wells. Changes in the space curvature cause dilation effects due to the implied stretching of space. This effect therefore has the the same origin as the cosmological redshift (see §2.1.2).

Even this description is not very useful unless we specify how the four quantities Θ_0 , v_γ , Ψ and Φ arise. Linear perturbation theory, developed in the last two chapters,

supplies these quantities. Let us summarize those results. The initial conditions and the subsequent evolution of the total matter determines the metric fluctuations Ψ and Φ by the Poisson equation (4.95). These in turn feedback on the matter and radiation through gravitational infall and dilation. For scales outside the horizon, gravitational interactions alone determine the fluctuations and make all particle components in the universe evolve similarly.

Inside the horizon, physical interactions must be taken into account. Before recombination, Compton scattering couples the photons to the baryons. From the Boltzmann equation (4.54) for the multipole moments, this has two significant effects:

1. $\mathbf{v}_b = \mathbf{v}_\gamma$: photons and baryons track each other during their evolution.
2. $\Theta_\ell \propto e^{-\tau}, \ell \geq 2$: except for the dipole, anisotropies are strongly damped.

Together they imply that the photons are isotropic in the baryon rest frame. This also explains why the photons may be characterized by their temperature and bulk velocity alone.

Since the two velocities are equal, photons and baryons cannot stream away from each other. This means that number density fluctuations are frozen in, *i.e.* the entropy fluctuation is constant [see equation (4.51)]. The photons and baryons therefore evolve adiabatically and may be thought of as a single photon-baryon fluid. Photon pressure resists the gravitational compression of the fluid and sets up acoustic waves. The oscillations are frozen in at last scattering leading to intrinsic temperature fluctuations Θ_0 from compression and rarefaction as well as bulk motion of the fluid v_γ . At the smallest scales, photon diffusion amongst the baryons and subsequent rescattering collisionally damps fluctuations as $e^{-\tau}$ leading to a small scale cut off in the spectrum at last scattering.

6.1.2 Projection and Free Streaming

After last scattering, photons free stream toward the observer on radial null geodesics and suffer only the gravitational interactions of redshift and dilation. Spatial fluctuations on the last scattering surface are observed as anisotropies in the sky. Free streaming thus transfers $\ell = 0$ inhomogeneities and $\ell = 1$ bulk velocities to high multipoles as the ℓ -mode coupling of the Boltzmann equation (4.54) suggests. Microphysically, this occurs because the paths of photons coming from hot and cold regions on the last scattering

surface cross. Isotropic $\ell = 0$ density perturbations are thus averaged away collisionlessly. It is also evident that this conversion does not occur for superhorizon scales $k\eta \ll 1$ since the photons can travel only a small fraction of a wavelength.

The background curvature also affects the photons in the free streaming limit. Due to the more rapid deviation of geodesics, a given length scale will correspond to a smaller angle in an open universe than a flat one. Thus the *only* effect of negative spatial curvature during free streaming is to speed the transfer of power to higher multipoles [see equation (4.54)]. Its effect is noticeable if the angular scale $\theta \sim \ell^{-1}$ is less than the ratio of the physical scale to the curvature radius $\sqrt{-K}/k$. Notice that even the lowest eigenmode, $k = \sqrt{-K}$ possesses ℓ -mode coupling and hence free streaming damping of low-order multipoles, once the horizon becomes larger than the curvature radius $\eta\sqrt{-K} \gtrsim 1$. As discussed in §4.1.3, this is simply because the $k = \sqrt{-K}$ eigenmode has structure only as large as the curvature scale. After the curvature scale passes inside the horizon, structure at this scale is seen as an anisotropy on the sky as opposed to the featureless lowest flat eigenmode $k = 0$. If a truly scale invariant spectrum is desired, the modes must be “over-completed” by taking $k \rightarrow 0$ in the open case as well.

6.1.3 Mathematical Description

A full description of the photon temperature must be two dimensional to account for both the spatial and angular distribution $\Theta(\eta, \mathbf{x}, \boldsymbol{\gamma})$. However, we can only observe the CMB from one location and hence have information on the angular distribution alone. The ensemble average of the angular temperature correlation function can be decomposed into the moments of the normal modes as

$$\langle \Theta^*(\eta, \mathbf{x}, \boldsymbol{\gamma}) \Theta(\eta, \mathbf{x}, \boldsymbol{\gamma}') \rangle = \frac{V}{2\pi^2} \int_{k \geq \sqrt{-K}}^{\infty} \sum_{\ell} \frac{1}{2\ell + 1} k^3 |\Theta_{\ell}(\eta, k)|^2 P_{\ell}(\boldsymbol{\gamma}' \cdot \boldsymbol{\gamma}), \quad (6.1)$$

where P_{ℓ} is a Legendre polynomial. Orthogonality of the P_{ℓ} 's insures that ℓ modes do not couple and the random phase assumption does the same for the k modes. For models which predict supercurvature fluctuations, the lower limit of the integral should be taken to zero. The power in the ℓ th multipole is usually denoted C_{ℓ} , where

$$\frac{2\ell + 1}{4\pi} C_{\ell} = \frac{V}{2\pi^2} \int_{k \geq \sqrt{-K}}^{\infty} \frac{dk}{k} k^3 \frac{|\Theta_{\ell}(\eta, k)|^2}{2\ell + 1}. \quad (6.2)$$

Note that the ensemble average anisotropy predicted for an experiment with window function W_ℓ is $(\Delta T/T)^2 = \sum (2\ell + 1)W_\ell C_\ell / 4\pi$ with C_ℓ evaluated at the present.¹ We can also sum in ℓ to obtain

$$|\Theta + \Psi|_{rms}^2 \equiv |\Theta_0 + \Psi|^2 + \sum_{\ell=1}^{\infty} \frac{|\Theta_\ell|^2}{2\ell + 1}, \quad (6.3)$$

which measures the total power in a single k -mode. Since fluctuations are merely transferred to high multipoles by free streaming, the rms is conserved if $\dot{\Phi} = \dot{\Psi} = \dot{\tau} = 0$, as is evident from equation (4.52). This merely indicates that the blueshift from falling into a static potential is exactly cancelled by the redshift climbing out.

Up until this point, the initial spectrum in k has been left arbitrary since k modes evolve independently. It is always possible to incorporate the evolution as a transfer function in k . However, each multipole ℓ of C_ℓ contains a sum over modes and does not evolve independently. We will often employ as examples simple power law initial spectra for which $\mathcal{P}(k) = k^3 |\Phi(0, k)|^2 \propto k^{n-1}$ and $k^3 |S(0, k)|^2 \propto k^{m+3}$ for adiabatic and isocurvature modes respectively. Thus $n = 1$ and $m = -3$ are the scale invariant choices for the spectrum. Here scale invariance represents equal power per logarithmic k interval and is not equivalent to the commonly employed choice of equal power per logarithmic $\tilde{k} = (k^2 + K)^{1/2}$ interval (see §4.1.1 and Appendix B.4).

It is often instructive to consider the full angular and spatial information contained in the two dimensional transfer function

$$T_\ell^2(k) \mathcal{P}(k) \equiv \frac{V}{2\pi^2} \frac{1}{2\ell + 1} k^3 |\Theta_\ell|^2. \quad (6.4)$$

which satisfies $(2\ell + 1)C_\ell / 4\pi = \int T_\ell^2(k) \mathcal{P}(k) d \ln k$ for any initial spectra. Note that ℓT_ℓ^2 also represents the power per logarithmic interval in k and ℓ of anisotropies in the scale invariant model.

6.2 Sachs-Wolfe Effect

On large scales, gravity dominates the anisotropy through redshift and dilation [138]. Its effects are usually broken up into two parts. Contributions at or before last scattering combine to form the ordinary Sachs-Wolfe (SW) effect. Those occurring after last

¹We only observe one realization of the ensemble and thus C_ℓ must be estimated with $2\ell + 1$ measurements. Reversing this statement, there is a ‘‘cosmic variance,’’ associated with a χ^2 distribution of $2\ell + 1$ degrees of freedom, in the theoretical predictions for even an ideal measurement.

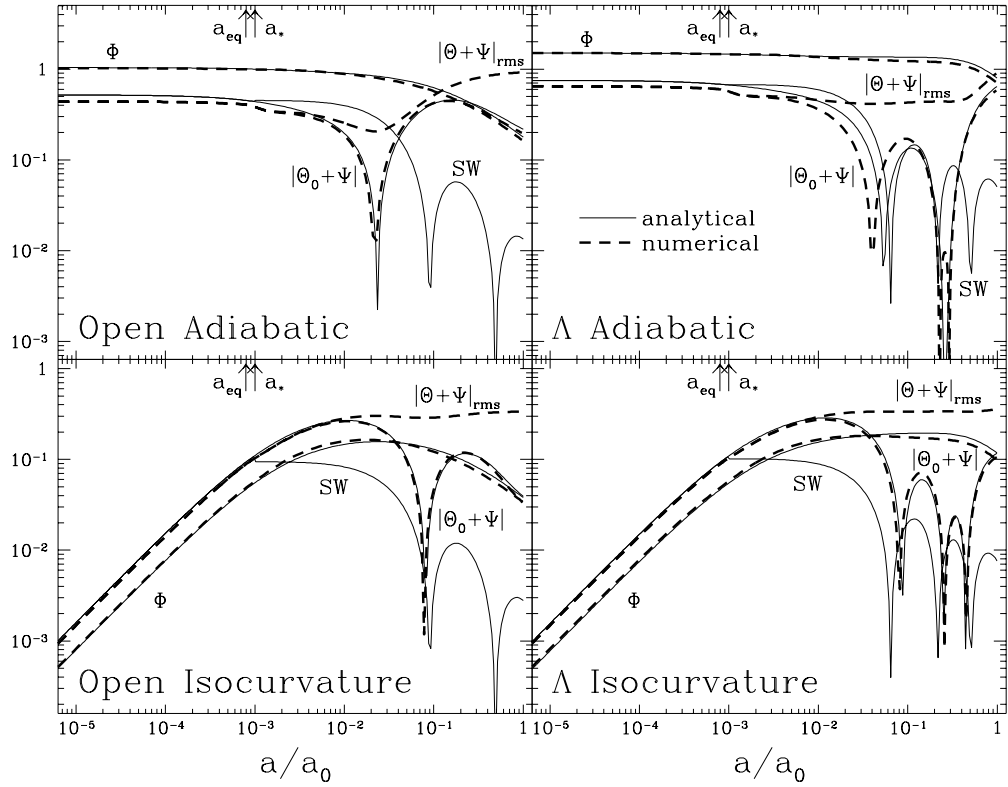


Figure 6.1: Sachs-Wolfe Evolution

In the adiabatic case, temperature fluctuations are enhanced in gravitational wells such that Θ_0 and Ψ cancel, yielding $\Theta_0 + \Psi = \Psi/3$ in the matter dominated epoch. For the isocurvature case, the dilation effect creates a net total of $\Theta_0 + \Psi = 2\Psi$ reflecting the anticorrelated nature of radiation and total density fluctuations. After last scattering at a_* , this SW contribution (analytic only) collisionlessly damps from the monopole and transfers power to anisotropies. The rms temperature fluctuations (numerical only) acquires contributions after a_* from the ISW effect due to the radiation (early) and curvature or Λ (late) contributions. The scale here is chosen to be $k = 4 \times 10^{-4} \text{Mpc}^{-1}$ in an $\Omega_0 = 0.1$ $h = 0.5$ universe.

scattering are referred to as the integrated Sachs-Wolfe (ISW) effect. After first describing their general nature, we will examine in detail their manifestation in a critical, open and Λ -dominated, adiabatic or isocurvature model.

6.2.1 Ordinary Sachs-Wolfe Effect

As the photons climb out of potential wells at last scattering, gravity redshifts the temperature to $\Theta_0 \rightarrow \Theta_0 + \Psi$, where $|\Psi| < 0$ in a potential well. The effective perturbation at last scattering is thus $[\Theta + \Psi](\eta_*)$. The combination of intrinsic temperature fluctuations and gravitational redshift is called the ordinary Sachs-Wolfe (SW) effect [138]. For a gauge choice other than Newtonian, the two may be divided up in different ways.

The intrinsic fluctuations at η_* are in turn determined by gravitational effects *before* last scattering. If $k\eta \ll 1$, the Boltzmann equation (4.54) reduces to the dilation effect

$$\dot{\Theta}_0 = -\dot{\Phi} \simeq \dot{\Psi}, \quad (6.5)$$

or

$$[\Theta_0 + \Psi](\eta) \simeq \Theta_0(0) + 2\Psi(\eta_*) - \Psi(0). \quad (6.6)$$

Here we have again assumed $\Pi_T = 0$, which causes a $\sim 10\%$ error (see §A.1.1).

Isocurvature and Adiabatic Cases

Since the isocurvature initial conditions satisfy $\Psi(0) = 0 = \Theta_0(0)$, equation (6.5) implies $\Theta_0(\eta) = \Psi(\eta)$. The effective superhorizon scale temperature perturbation for isocurvature fluctuations is therefore

$$\Theta_0 + \Psi = 2\Psi. \quad (\text{iso}) \quad (6.7)$$

The growing potential stretches space so as to dilute the photon density in the well. Gravitational redshift out of the well subsequently doubles the effect. Note however that in a low $\Omega_0 h^2$ model with standard recombination, the potential may not reach its full matter-dominated value of $\Psi = -\frac{1}{5}S(0)$ from equation (5.38) by last scattering (see Fig. 6.1).

For adiabatic perturbations, the initial conditions require $\Theta_0(0) = -\frac{1}{2}\Psi(0)$ [see equation (5.21)], reflecting the fact that the photons are overdense inside the potential well [see equation (5.31)]. Although the potential is constant in both the matter- and radiation-dominated epoch, it changes to $\Psi(a) = \frac{9}{10}\Psi(0)$ through equality. The dilation

effect then brings the photon temperature perturbation in the matter-dominated epoch to $\Theta(\eta) = -\frac{2}{3}\Psi(\eta)$. Thus the effective perturbation is

$$[\Theta_0 + \Psi] = \begin{cases} \frac{1}{2}\Psi & \text{RD} \\ \frac{1}{3}\Psi, & \text{MD} \end{cases} \quad (\text{adi}) \quad (6.8)$$

where the latter is the familiar Sachs-Wolfe result. Again since last scattering may occur before full matter domination, one should employ the full form of equation (6.6) instead of the asymptotic form from equations (5.38) and (6.8). After a_* , the photons climb out of the potential wells, leaving the quantity $[\Theta_0 + \Psi](\eta_*)$ to be viewed as temperature fluctuations on the sky today.

Free Streaming Solution

To determine the exact nature of the resultant anisotropies, one must follow the photons from last scattering to the present. The collisionless Boltzmann equation for $(\Theta + \Psi)/(2\ell + 1)$ takes the same form as the recursion relation for the radial eigenfunctions of the Laplacian [*c.f.* equations (4.13) and (4.54)]. This is natural since the radiation free streams on null geodesics. Thus the spatial fluctuation represented by $[\Theta + \Psi](\eta_*, k)$ is seen by the distant observer as an anisotropy of

$$\frac{\Theta_\ell(\eta, k)}{2\ell + 1} = [\Theta_0 + \Psi](\eta_*, k) X_\nu^\ell(\chi - \chi_*), \quad (6.9)$$

where recall that $\chi = \sqrt{-K}\eta$. In the flat case, $X_\nu^\ell \rightarrow j_\ell$ which peaks at $\ell \simeq k(\eta - \eta_*)$. If the distance traveled by the photon is under a wavelength, *i.e.* $k(\eta - \eta_*) \ll 1$, then only j_0 has weight and fluctuations remain in the monopole. As time progresses, power is transferred from the monopole to high ℓ as one would expect from the projection effect (see Fig. 6.1).

In the adiabatic flat case, power law models for the initial conditions $k^3|\Phi(0)|^2 = Bk^{n-1}$ have a simple form for the Sachs-Wolfe contribution to C_ℓ . If we assume that the universe was matter dominated at last scattering, $\Theta_0 + \Psi = \frac{1}{3}\Psi$. From equation (6.2),

$$\begin{aligned} C_\ell^{SW} &\simeq \left(\frac{1}{3} \frac{\Psi(\eta_*)}{\Phi(0)}\right)^2 \frac{2}{\pi} BV \int \frac{dk}{k} k^{n-1} j_\ell^2(k\eta_0) \\ &\simeq \frac{9}{200\sqrt{\pi}} BV \eta_0^{1-n} \frac{\Gamma[(3-n)/2]\Gamma[\ell + (n-1)/2]}{\Gamma[(4-n)/2]\Gamma[\ell + (5-n)/2]}, \end{aligned} \quad (6.10)$$

where we have employed the relation $\Psi(\eta_*)/\Phi(0) = -9/10$ of equation (5.29). In this flat model,

$$\eta_0 \simeq 2(\Omega_0 H_0^2)^{-1/2} (1 + \ln \Omega_0^{0.085}), \quad (6.11)$$

where the small logarithmic correction is from the rapid expansion at the present in a Λ universe. Notice that for scale invariant spectra, the projection factor η_0^{n-1} vanishes. With equal power at all scales, it does not matter which physical scale gets mapped onto a given angular scale.

Equation (6.10) is more commonly expressed in terms of the amplitude of the matter power spectrum today $|\Delta_T(\eta_0, k)|^2 = Ak^n$. From equation (5.27), the relation between the two normalizations is

$$\begin{aligned} B &= \frac{25}{36} k_{eq}^4 D^{-2} A \\ &= \frac{25}{9} (\Omega_0 H_0^2)^2 (a_0/D_0)^2 A, \end{aligned} \quad (6.12)$$

where $D_0 = D(\eta_0)$ and recall that D is the pressureless growth factor normalized at equality. Since in a Λ universe, growth is suppressed and $a_0/D_0 < 1$, the same matter power spectrum normalization A implies a greater Sachs-Wolfe anisotropy since it was generated when the potentials were larger. The final expression becomes

$$C_\ell^{SW} \simeq \frac{1}{8\sqrt{\pi}} AV H_0^4 \Omega_0^2 (a_0/D_0)^2 \eta_0^{1-n} \frac{\Gamma[(3-n)/2]\Gamma[\ell+(n-1)/2]}{\Gamma[(4-n)/2]\Gamma[\ell+(5-n)/2]}. \quad (6.13)$$

The factor $\Omega_0^2 (a_0/D_0)^2 \simeq \Omega_0^{1.54}$ for Λ models [52]. Since $\Gamma(\ell+2)/\Gamma(\ell) = \ell(\ell+1)$, the Sachs-Wolfe contribution for a scale invariant $n=1$ spectrum is flat in $\ell(\ell+1)C_\ell$. We will therefore occasionally plot $\ell(\ell+1)C_\ell/2\pi$ instead of the logarithmic power $\ell(2\ell+1)C_\ell/4\pi$ as has become standard convention. For $\ell \gg 1$, the two conventions yield identical results. Note that this formula describes only the Sachs-Wolfe contributions and does not account for the early ISW and acoustic contributions, which push the high ℓ tail up, and the late ISW effect, which enhances the low ℓ multipoles.

6.2.2 Integrated Sachs-Wolfe Effect

If the potentials vary with time, the photon will experience differential redshifts due to the gradient of Ψ , which no longer yield equal and opposite contributions as the photons enter and exit the potential well, and time dilation from Φ . They act like an impulse $(\dot{\Psi} - \dot{\Phi})\delta\eta$ at some intermediate time η which then free streams to the present. The sum of these contributions along the line of sight is called the integrated Sachs-Wolfe (ISW) effect. By the same reasoning that lead to the solution for the Sachs-Wolfe effect, one can

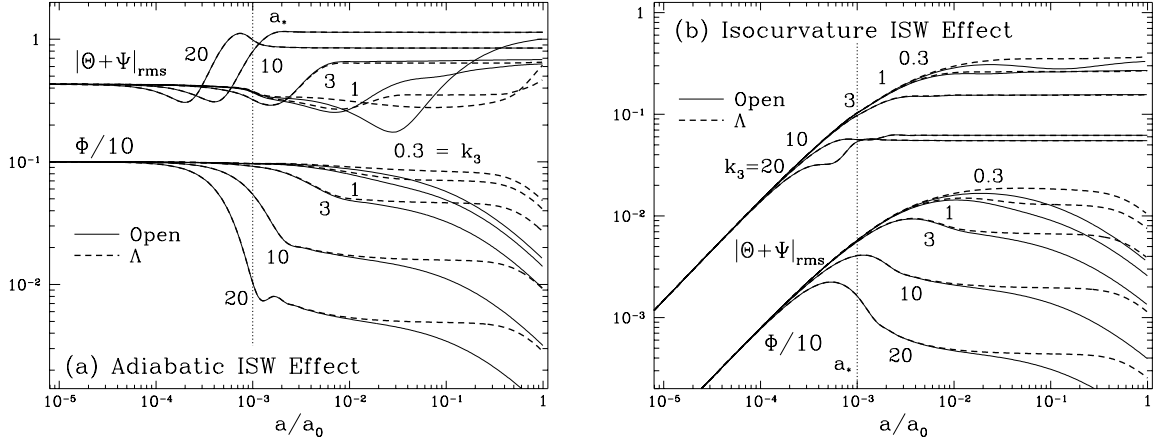


Figure 6.2: ISW Effect

(a) Adiabatic models. Potential decay at horizon crossing during radiation domination boosts scales approaching the first acoustic oscillation through the early ISW effect. Larger scales suffer only the late ISW effects due to the rapid expansion in open and Λ models, leaving a deficit at intermediate scales. (b) Isocurvature models. For small scales, potential growth halts after horizon crossing in the radiation dominated epoch leading to a relative boost for large scale fluctuations. Since this early ISW effect dominates, there is little distinction between open and Λ models. All models have $\Omega_0 = 0.1, h = 0.5$ with standard recombination and $k = k_3 \times 10^{-3} \text{Mpc}^{-1}$.

immediately write down the solution for the combined effect:

$$\frac{\Theta_\ell(\eta, k)}{2\ell + 1} = [\Theta_0 + \Psi](\eta_*, k) X_\nu^\ell(\chi - \chi_*) + \int_{\eta_*}^{\eta} [\dot{\Psi} - \dot{\Phi}](\eta', k) X_\nu^\ell(\chi - \chi') d\eta'. \quad (6.14)$$

Since the potentials for both the adiabatic and isocurvature modes are constant in the matter-dominated epoch, the ISW contribution is separated into two parts:

1. The early ISW effect from radiation domination: (a) isocurvature growth before horizon crossing and (b) pressure growth suppression after horizon crossing for either mode.
2. The late ISW effect due to expansion growth suppression in the Λ - or curvature-dominated epoch.

In adiabatic models, scales which cross the sound horizon in the radiation-dominated epoch experience a boost from the decay of the potential (see Fig. 6.2a). Since the effect is due to radiation pressure and depends only on the epoch of equality, open and Λ models predict identical contributions. These scales will furthermore not experience significant late ISW effects since the potential has already decayed by Λ or curvature domination. On the other

hand, larger scales are unaffected by the early ISW effect and suffer only the consequences of the late ISW effect. Because Λ domination occurs only recently if $\Omega_0 \gtrsim 0.1$, the potential will not have had a chance to fully decay and the net effect is smaller than in the corresponding open case.

For isocurvature models, potential growth outside the sound horizon in the radiation-dominated epoch forces the temperature fluctuation to grow with it through the dilation effect (see Fig. 6.2b). Modes which cross only after matter domination experience the full effect of growth. For scales that cross during radiation domination, radiation pressure suppresses further growth. Thus large scale modes are enhanced over small scale modes. Since isocurvature models are dominated by this early ISW effect, the difference between open and Λ models is smaller than in adiabatic models.

The total Sachs-Wolfe effect predicts rich structure in the anisotropy spectra. To understand the full Sachs-Wolfe spectrum, it is necessary to examine simultaneously the spatial and angular information in the radiation. It will therefore be instructive to consider the radiation transfer function $T_\ell(k)$, rather than C_ℓ for any one model. Note that $\ell T_\ell^2(k)$ is equivalent to the logarithmic contribution in k and ℓ to the anisotropy of a scale invariant model [see equation (6.4)]. Summing in k produces $\ell(2\ell + 1)C_\ell/4\pi$ and in ℓ yields $k^3|\Theta + \Psi|_{rms}^2$ for this model.

6.2.3 Adiabatic $\Omega_0 = 1$ models

To build intuition for equation (6.14), let us first consider the familiar adiabatic $\Omega_0 = 1$ model in which the ISW term represents only a small correction. A given k -mode contributes maximally to the angle that scale subtends on the sky at last scattering. The transfer function therefore displays a sharp ridge corresponding to this correlation (see Fig. 6.3a),

$$\ell_{main} + \frac{1}{2} \simeq kr_\theta(\eta_*), \quad (6.15)$$

where the comoving angular diameter distance is

$$r_\theta(\eta) = (-K)^{-1/2} \sinh(\chi_0 - \chi), \quad (6.16)$$

and reduces to $r_\theta = \eta_0 - \eta_*$ as $K \rightarrow 0$. It is evident from Fig. 6.3a that the full result contains more than just this main correlation ridge. The conversion of fluctuations in a spatial eigenmode k on the last scattering surface into anisotropies on the sky is basically a

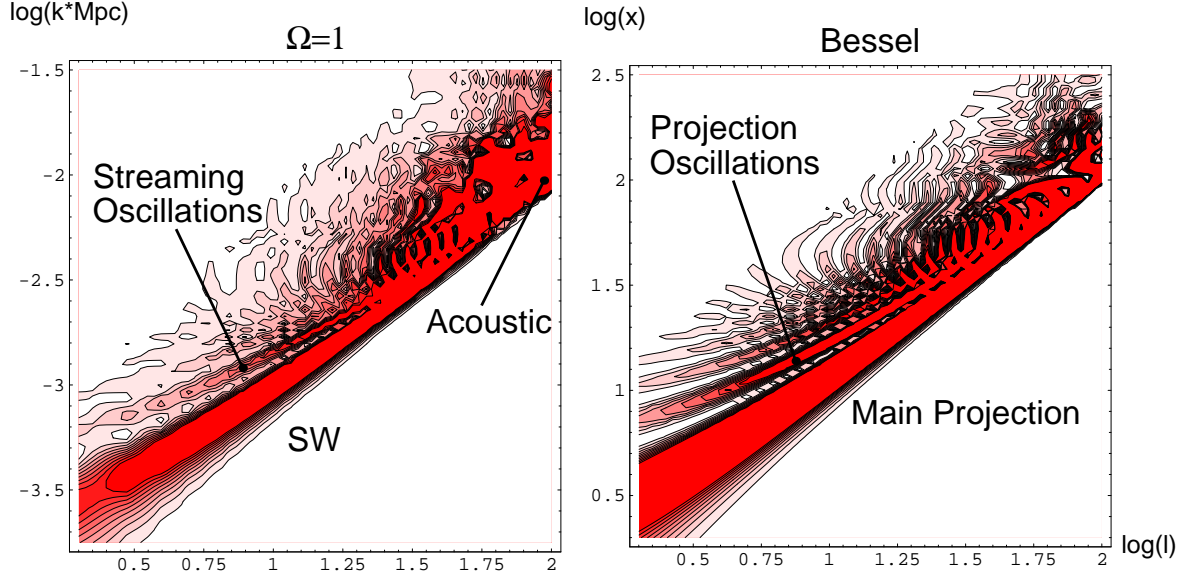


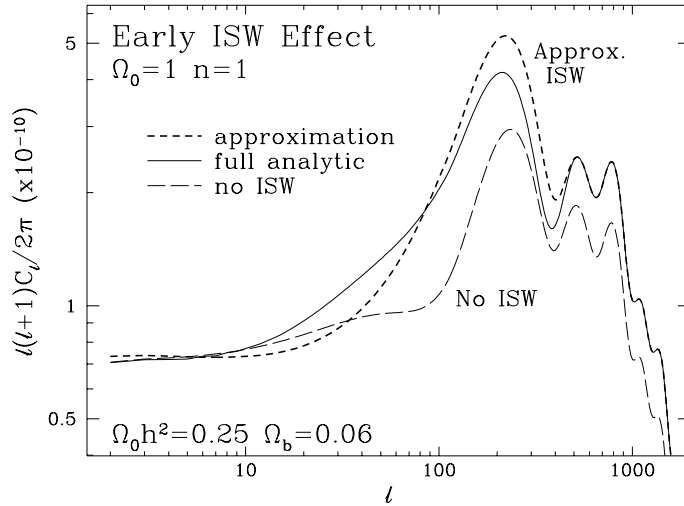
Figure 6.3: $\Omega_0 = 1$ Radiation Transfer Function

Shown here and in Figs. 6.5, 6.8, and 6.10 is the weighted squared transfer function $\ell T_\ell^2(k)$ which also represents the anisotropy contribution per logarithmic k and ℓ interval in a scale invariant model. Contours are equally spaced up to a cut off set to best display the features. The strong correlation between ℓ and k merely reflects the projection of a scale on the last scattering surface to an angle on the sky. At $\log \ell \gtrsim 2$, SW contributions fall off and are replaced by the acoustic peaks (saturated here). The detailed structure can be traced to the radial eigenfunction $X_\nu^\ell(\chi) = j_\ell(x)$ which governs the projection and free streaming oscillations.

projection of the eigenmode in the spherical geometry. For example, a plane wave $\exp(ik\Delta\eta)$ can be written as a sum over $j_\ell(k\Delta\eta)Y_\ell^m$. Since the projection is not precisely one-to-one, a given mode will project onto a range of angles. In fact, it will alias angles equal to and larger than what the main face on $\mathbf{k} \perp \boldsymbol{\gamma}$ projection of equation (6.15) predicts, *i.e.* $\ell \leq \ell_{\text{main}}$, as is clear from Fig. 1.7. This is expressed by the oscillatory structure of the radial eigenfunction. Comparing panels in Fig. 6.3, we see that the structure in the transfer function is indeed due to this effect.

Even with $\Omega_0 = 1$, a low $h \simeq 0.5$ model has additional contributions after last scattering. The early ISW effect affects modes that cross the sound horizon between last scattering and full matter domination. Since these contributions come from near last scattering, the ISW integral (6.14) may be approximated as

$$\int_{\eta_*}^{\eta_0} [\dot{\Psi} - \dot{\Phi}] j_\ell(k(\eta_0 - \eta)) d\eta \simeq \int_{\eta_*}^{\eta_0} [\dot{\Psi} - \dot{\Phi}] j_\ell(k\eta_0) d\eta$$

Figure 6.4: $\Omega_0 = 1$ Early ISW Spectrum

Even in an $\Omega_0 = 1$ $\Omega_0 h^2 = 0.25$ high matter content universe, early ISW contributions from radiation pressure are non-negligible. Ignoring the ISW effect entirely leads to a significant error in both the large scale normalization and shape of the anisotropies. Approximating *all* of the ISW contribution to occur near recombination through equation (6.17) leads to 10–15% errors in temperature since it comes from more recent times where the fluctuation subtends a larger angle on the sky. The full integration therefore has more power at larger angular scales and makes the rise to the first Doppler peak more gradual. These are analytic results from Appendix A.2.2.

$$= [\Delta\Psi - \Delta\Phi]j_\ell(k\eta_0), \quad (6.17)$$

which is strictly only valid for contributions from $k\eta \ll 1$. Contributions to the k th mode in fact occur near horizon crossing where $k\eta \simeq 1$. Nevertheless this approximation is instructive.

The early ISW effect adds nearly coherently with the SW effect and in fact cancels it by removing the redshift that the photon would otherwise suffer. At large scales, this brings the total effect down to the matter-dominated $\frac{1}{3}\Psi(\eta_0)$ value and thus changes the large scale normalization. At scales approaching the sound horizon at last scattering, it increases the effective temperature from the acoustic compression again by removing the cancelling redshift. In Fig. 6.4, we compare the approximation of equation (6.17) to the the full integral and the effect of dropping the contribution entirely. Notice that, aside from its affect on the normalization, the early ISW contribution fills in scales somewhat larger than the sound horizon at last scattering. The approximation underestimates the angular scale somewhat by assuming that the contribution comes from the further distance η_0 as

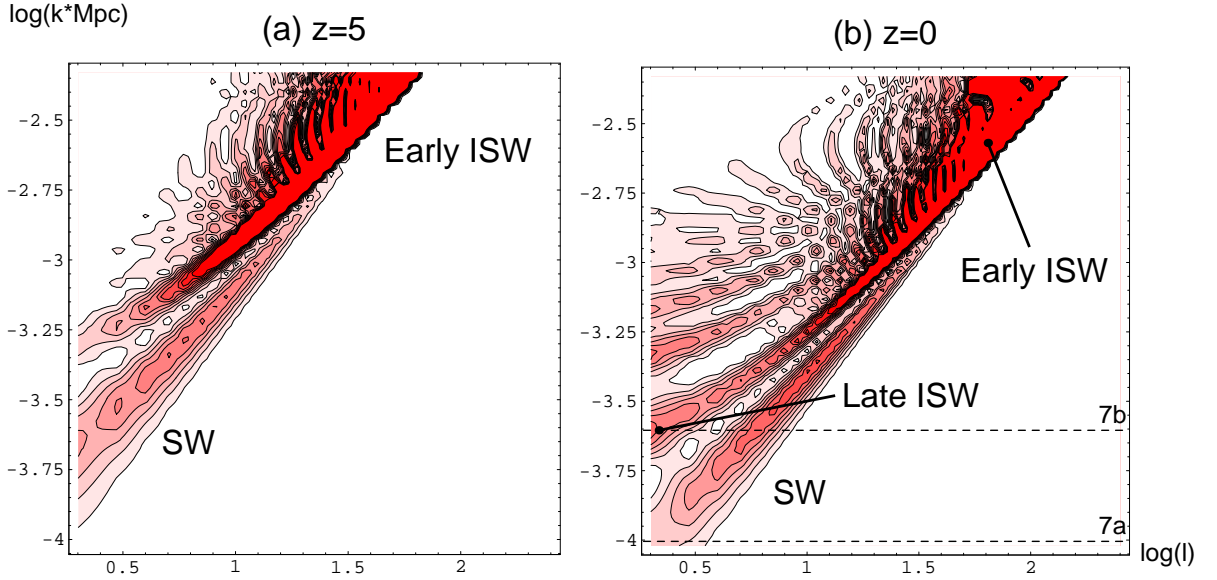


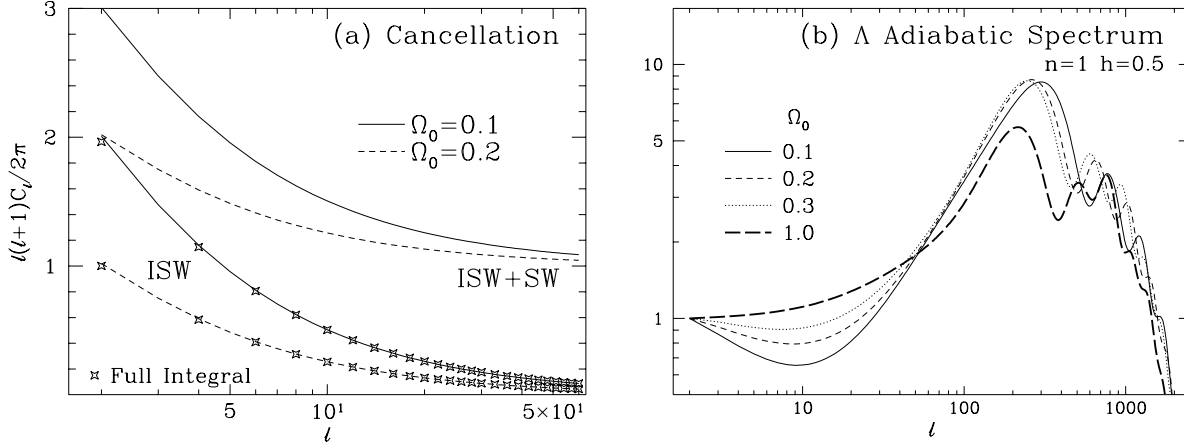
Figure 6.5: Λ Adiabatic Radiation Transfer Function

Unlike the $\Omega_0 = 1$ case, this scenario has strong contributions after last scattering from the early and late ISW effect. (a) The early ISW effect projects onto a second ridge which is more prominent than the SW ridge at intermediate but not large angles. (b) After Λ domination, the late ISW contributions come free streaming in from the monopole yielding a boost in the low order multipoles for a small range in k , due to cancellation with SW contributions at the largest scales and crest-trough cancellation at smaller scales. Scales depicted in Fig. 6.7 are marked here by dashed lines. The model here is $\Omega_0 = 0.1$, $h = 0.5$ with standard recombination.

opposed to the true distance $\eta_0 - \eta$.

6.2.4 Adiabatic Λ Models

Now let us move onto the more complicated Λ case. For Λ models, the ISW term in equation (6.14) yields both early and late type contributions. The boost on intermediate scales from the early ISW effect is much more dramatic than for the high $\Omega_0 h^2$ models. In the transfer function, this appears as a high ridge crossing larger angles for the same k as the SW effect, due to its origin closer to the observer. The maximum contribution the early ISW effect can make is if the potential decayed to zero between last scattering and the present. From the relation $\dot{\Theta}_0 = -\dot{\Phi}$, this would yield $\Theta_0(\eta) = \Theta_0(0) + \Phi(0) = \frac{3}{2}\Phi(0)$. Compared with the matter-dominated SW tail of $\frac{1}{3}\Psi = -\frac{3}{10}\Phi(0)$, the early ISW effect can approach a height 5 times greater than the SW tail. Note that the same decay drives the acoustic oscillation to a similar height so that this effect will join smoothly onto the acoustic

Figure 6.6: Λ Late ISW Spectrum

(a) Analytic Separation. The late ISW effect is cancelled as photons stream through many wavelengths of the perturbation during the decay. The comparison here of the full late ISW integral to the cancellation approximation shows that even at the largest angles, the late ISW contributions are well inside the cancellation regime. The SW effect on the other hand is flat in this representation. As Λ increases, the contribution of the late ISW effect relative to the SW effect increases at low multipoles and appears as a boost. (b) Numerical results. The early ISW effect contributes significantly at scales not much smaller than the cancellation tail of the late ISW effect bending the spectrum back up.

peaks as we shall see below. The lack of potential decay for scales that enter the horizon during matter domination makes the early ISW ridge drop off at large scales (see Fig. 6.5).

After Λ domination $a_\Lambda/a_0 = (\Omega_0/\Omega_\Lambda)^{1/3}$, the potential once again decays. For typical values of $\Omega_0 \gtrsim 0.1$, this occurs only recently. Furthermore, the potential at all scales decays at the same rate. The expansion time scale at Λ domination $\eta_\Lambda = \eta(a_\Lambda)$ sets a critical wavelength corresponding to $k\eta_\Lambda = 1$. The ISW integral takes on different form in the two regimes separated by this division

$$\int_{\eta_*}^{\eta_0} [\dot{\Psi} - \dot{\Phi}] j_\ell[k(\eta_0 - \eta)] d\eta \simeq \begin{cases} [\Delta\Psi - \Delta\Phi] j_\ell[(k\eta_0 - k\eta_\Lambda)] & k\eta_\Lambda \ll 1 \\ [\dot{\Psi} - \dot{\Phi}](\eta_k) I_\ell/k, & k\eta_\Lambda \gg 1 \end{cases} \quad (6.18)$$

where $\Delta\Phi$ and $\Delta\Psi$ are the changes in the potential from the matter-dominated form of (5.29) to the present. We have used the angle-distance relation (6.15) to find the peak of j_ℓ at $\eta_k = \eta_0 - (\ell + 1/2)/k$. The integral I_ℓ is given by

$$I_\ell \equiv \int_0^\infty dx j_\ell(x) = \frac{\sqrt{\pi}}{2} \frac{\Gamma[\frac{1}{2}(\ell + 1)]}{\Gamma[\frac{1}{2}(\ell + 2)]}. \quad (6.19)$$

The limits correspond physically to two cases:

1. If the wavelength is much longer than distance a photon can travel during the decay, photons essentially receive an instantaneous kick. The result is similar to the SW and early ISW effects.
2. In the opposite limit, the photon traverses many wavelengths during the decay and suffers alternating red and blueshifts from crests and troughs. The result is a cancellation of contributions.

Since Λ domination occurs near the present, the critical wavelength is approximately the horizon size at present and yields $\ell = 0$ monopole contributions along the projection ridge. Thus most contributions will come from the cancellation regime if the k modes are weighted equally. We can verify this by comparing the cancellation approximation with the full integral for the scale invariant model. Fig. 6.6 shows that in this case the cancellation approximation is excellent. Compared with the SW effect which predicts a flat spectrum, the late ISW Λ contributions fall with ℓ due to cancellation. For the more general case of power law initial spectra $k^3|\Phi(0, k)|^2 = Bk^{n-1}$, the total contribution becomes

$$C_\ell^{ISW} \simeq 2 \left(\frac{9}{10}\right)^2 BV \left(\frac{\Gamma[(\ell+1)/2]}{\Gamma[(\ell+2)/2]}\right)^2 \int_0^\infty \frac{dk}{k} k^{n-3} \left[\frac{D}{a} \left(\frac{\dot{D}}{D} - \frac{\dot{a}}{a}\right)\right]_{\eta=\eta_k}^2, \quad (6.20)$$

where we have employed equation (5.29) for the potentials and recall that the growth factor D is normalized such that $D(a_{eq}) = a_{eq} = 1$.

Let us take a closer look at the transfer function in Fig. 6.5. For $k\eta_\Lambda \ll 1$, cancellation is ineffective and like its early counterpart, the late ISW effect opposes the SW effect. In Fig. 6.7a, we plot the analytic decomposition of contributions to a k -mode slice corresponding to these large scales. As one can see from equation (6.18), these modes contribute little to $\ell \geq 2$, since $k(\eta_0 - \eta_\Lambda) \ll 1$. For intermediate scales, the late ISW effect itself is partially cancelled. The ridge structure of Fig. 6.5 at the low multipoles is due to the late ISW effect adding with every other ridge in the SW free streaming oscillation (see Fig. 6.7b). At the smallest scales, those which would ordinarily contribute to higher order multipoles, the late ISW effect is entirely cancelled. Again this implies that typical adiabatic Λ spectra have a small boost in anisotropies from the late ISW effect only at the lowest multipoles (see Fig. 6.6b).

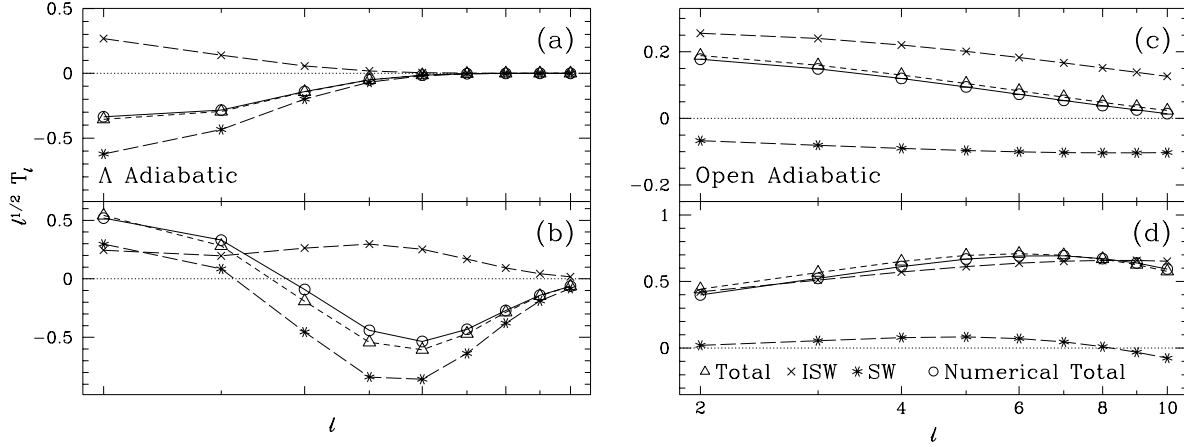


Figure 6.7: Analytic Decomposition: Adiabatic Models

Scales are chosen to match the features in Fig. 6.5 and 6.8. Λ models: (a) At the largest scales, *e.g.* here $k = 10^{-4} \text{Mpc}^{-1}$, the SW effect dominates over, but is partially cancelled by, the late ISW effect. (b) Intermediate scale peaks in Fig. 6.5 are due to the late ISW boost of the higher SW projection ridges. Open models: (c) The maximum scale corresponds to the curvature radius $k = \sqrt{-K}$. For the SW effect, this scale projects broadly in ℓ peaking near $\ell \sim 10$. For the late ISW effect, this scale projects onto the monopole and dipole near curvature domination thus leaving the ISW contributions to decrease smoothly with ℓ . (d) At smaller scales, corresponding to the large ridge in Fig. 6, the late ISW effect projects onto $\ell \simeq 2 - 10$ and completely dominates leading to a rising spectrum of anisotropies. The models are for $\Omega_0 = 0.1$ $h = 0.5$ with standard recombination and arbitrary normalization.

6.2.5 Adiabatic Open Models

Open adiabatic models follow similar physical principles. The early ISW effect depends only on the matter-radiation ratio near last scattering from $\Omega_0 h^2$ and thus is identical to the Λ case. However, photons curve on their geodesics so that the projection takes the same physical scale to a significantly smaller angular scale. This is quantified by the angle to distance relation (6.16). In the transfer function, one sees that the early ISW ridge is pushed to significantly higher ℓ (see Fig. 6.8).

Curvature dominates at $a/a_0 = \Omega_0/(1 - \Omega_0)$ leaving the potential more time to decay than in the Λ model. The late ISW effect will therefore be more significant in this model (see Fig. 6.2a). Moreover, the cancellation scale is smaller leading to a less sharp decline with k (or ℓ) of the effect. The net result is that the late ISW cancellation tail merges smoothly onto the early ISW rise for sufficiently low Ω_0 . For $\Omega_0 \simeq 0.1 - 0.3$, they overwhelm the SW effect on all scales.

Unlike the flat case, there is a lowest eigenmode corresponding to the curvature

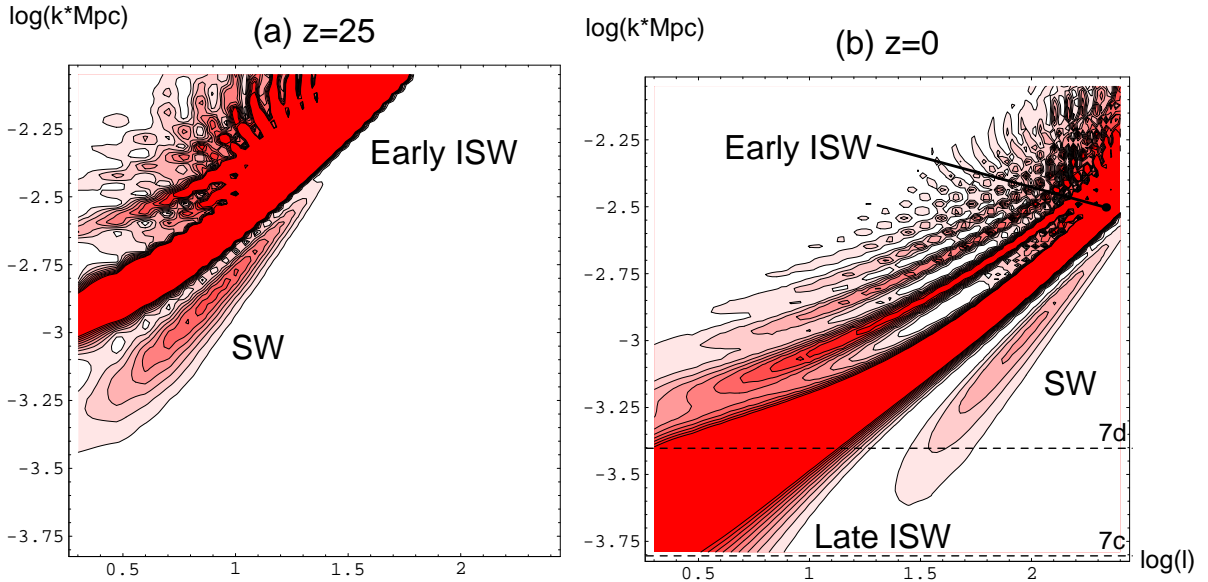


Figure 6.8: Open Adiabatic Radiation Transfer Function

(a) Like the Λ case, the radiation ISW effect contributes significantly to intermediate angle anisotropies. (b) The late ISW effect appearing at the left is much more significant than the corresponding Λ effect. Thus on all angular scales, the total ISW contribution dominates the SW effect. The curvature scale $\log(k*\text{Mpc}) = -3.8$ intersects the late ISW ridge near the lowest multipoles. Absence of supercurvature contributions can suppress these multipoles. Dashed lines represent scales in Fig. 6.7. The model is $\Omega_0 = 0.1$, $h = 0.5$, with standard recombination.

scale $k = \sqrt{-K}$. Supercurvature scales that would ordinarily contribute to low order multipoles are absent unless the modes are “overcompleted” (see §4.1.3). For the low $\Omega_0 = 0.1$ example displayed in Fig. 6.8, this cutoff at $\log(k*\text{Mpc}) \simeq 3.8$ chops off some of the main projection ridge of the late ISW effect for the lowest multipoles. Thus the absence of supercurvature modes in the sum over k can lead to a slight suppression of the lowest multipoles. With scale invariant weighting of the k -modes, the spectrum has the form shown in Fig. 6.9. Note that this is the typical [110, 134] but not unique [20] prediction of open inflationary models.

Due to its more recent origin, the late ISW effect projects onto a significantly larger angle than the SW effect for a given k . Examining the individual contributions in Fig. 6.7c, we see that indeed at the curvature scale, the late ISW effect affects the lowest multipoles, whereas the SW effect peaks around $\ell \simeq 10$. Thus the presence or lack of supercurvature modes is not as significant as one might naively expect from the fact that the curvature

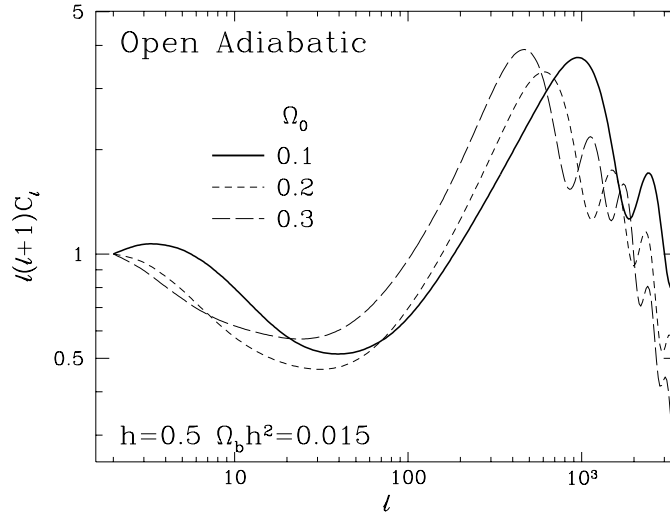


Figure 6.9: Open Adiabatic Spectrum

Scale invariant $n = 1$ model: equal power per logarithmic k interval to the curvature scale $k = \sqrt{-K}$. The early ISW effect merges with the cancellation tail of the late ISW effect completely dominating the SW contributions. The lack of supercurvature modes can lead to a suppression of low order multipoles as the curvature scale becomes significantly smaller than the horizon (see also Fig. 6.7d). Notice also that geodesic deviation shifts the acoustic contributions more than the early ISW contributions and broaden out the first peak.

scale subtends $\ell \simeq 10$ at the horizon distance in an $\Omega_0 = 0.1$ universe. For a smaller scale chosen to intersect the main late ISW projection ridge in Fig. 6.7d, we see that the late ISW effect completely dominates the SW effect as claimed.

6.2.6 Isocurvature Λ and Open Models

Isocurvature models differ significantly in that the potentials *grow* until full matter domination. Strong early ISW contributions which are qualitatively similar to the SW term will occur *directly* after recombination and continue until full matter domination (see Fig. 6.1). Thus the projection of scales onto angles will follow a continuous sequence which merges the SW and early ISW ridges (see Fig. 6.10).

For the Λ case, the early ISW effect completely dominates that of the late ISW effect. Thus the analytic separation shows that the ISW and SW effects make morphologically similar contributions and the boost in low order multipoles is not manifest. Moreover, the two add coherently creating a greater total effect unlike the adiabatic case (see Fig. 5a,b). Open isocurvature models behave similarly except that the late ISW contributions near its

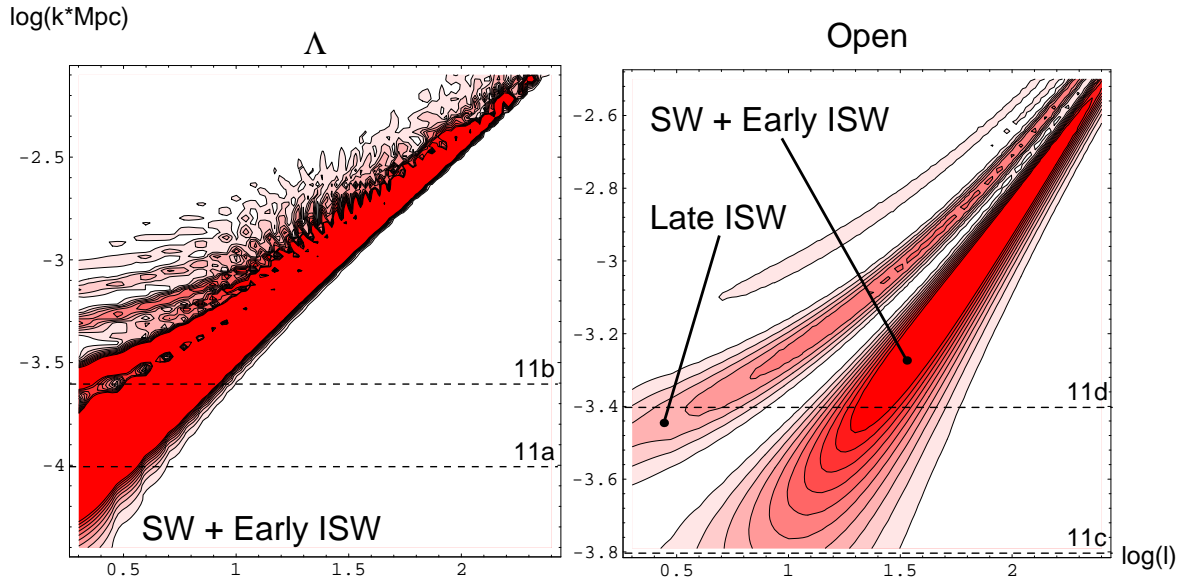


Figure 6.10: Isocurvature Radiation Transfer Function

Unlike their adiabatic counterparts, the potential *grows* in the radiation domination era only to turn over and decay in the curvature and Λ dominated era. The ISW contribution will thus smoothly match onto the SW contribution. This has the effect of merging the SW and ISW ridges to make a wide feature that contributes broadly in ℓ . For Λ models, the early ISW effect completely dominates over the late ISW effect. Scales depicted in Fig. 6.11 are marked here in dashed lines. The model here is $\Omega_0 = \Omega_b = 0.1$, $h = 0.5$ with standard recombination.

maximum (late ISW ridge) is not entirely negligible. It is thus similar to the adiabatic case (*c.f.* Fig. 6.7d and 6.11d) except that it does not usually dominate the *total* anisotropy. Note that the curvature cutoff can strongly affect the anisotropy spectrum since the curvature scale projects onto $\ell \simeq 10$ for the SW and early ISW contributions in the $\Omega_0 = 0.1$ model. There will be a deficit of power at $\ell \lesssim 10$ if no supercurvature contributions are considered.

On the other hand, the scale invariant model represented here does not present a viable model for structure formation. As discussed in §6.2.2, potential growth leads to an enhancement of large over small scale power. The initially scale invariant isocurvature $m = -3$ model has insufficient small scale power to form galaxies. The problem can be alleviated by increasing the spectral index to $m \simeq -1$. This has significant effects on the anisotropy. By heavily weighting the small physical scales, we enhance the projection aliasing contribution from the higher ridges of Fig. 6.10. This aliasing or power bleeding from small scales makes the anisotropy spectrum less steep (blue) than the spatial power

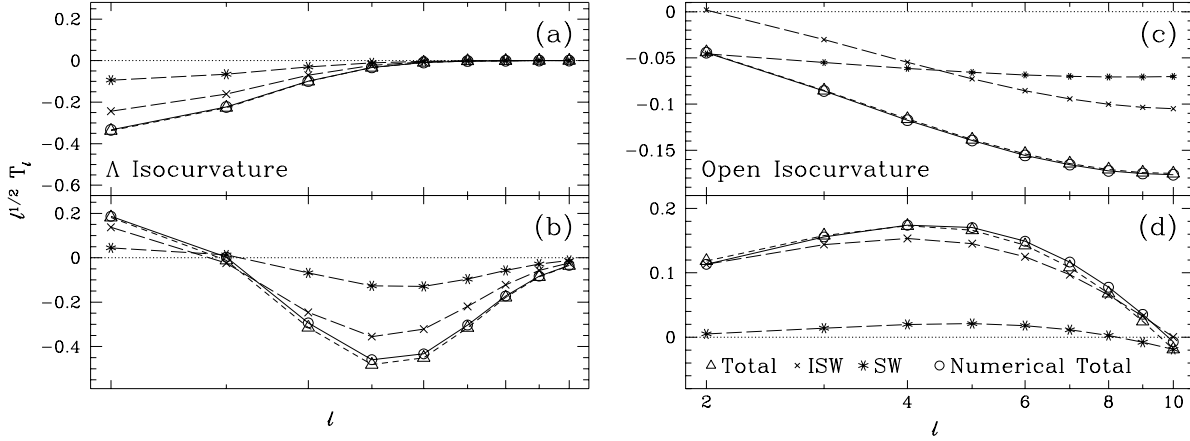


Figure 6.11: Analytic Decomposition: Isocurvature Models

In general, isocurvature models have strong early ISW contributions which mimic and coherently boost the SW effect. Scales are chosen to match the features in Fig. 6.10. Λ models: (a) Notice that the shape of the SW and ISW effects are identical at large scales. (b) Even at the late ISW peak, the early ISW contributions are so strong that the late contributions are never apparent unlike the adiabatic model. Open models: (c) As with Λ models, early ISW and SW contributions are similar in form at large scales. (d) Near the peak of the late ISW contribution however, the relative contributions are similar to the adiabatic case. The model here is $\Omega_0 = \Omega_b = 0.1$, $h = 0.5$ with standard recombination.

spectrum (see Fig. 6.12).

In fact, there is an upper limit as to how fast anisotropies can rise with ℓ . Suppose that the spectrum is so blue as to have all contributions come from the smallest physical scale in the problem k_{cut} , *e.g.* the photon diffusion scale at last scattering. In this case, $j_\ell(k_{cut}\Delta\eta)$ becomes independent of ℓ and thus $\Theta_\ell \propto 2\ell + 1$ from equation (6.2) or $C_\ell \simeq \text{constant}$. This corresponds to an effective large scale slope of $n_{\text{eff}} = 3$ as compared with the adiabatic SW prediction of equation (6.13). Isocurvature $m = -1$ models are an intermediate case with $n_{\text{eff}} \simeq 2$. Since the effect is from small scale power aliasing for $m \gtrsim -2$, the effective anisotropy slope will only weakly depend on the initial power spectrum slope m . In Fig. 6.13, we plot the dependence of isocurvature large scale anisotropies with m . Note that because the power comes from small scales, large scale anisotropies are not sensitive to the initial spectrum at large spatial scales. In particular, possible curvature scale ambiguities, such as the absence (or presence) of supercurvature modes which can suppress (enhance) the low order multipoles, have little effect on the result for $m \gtrsim -2$.

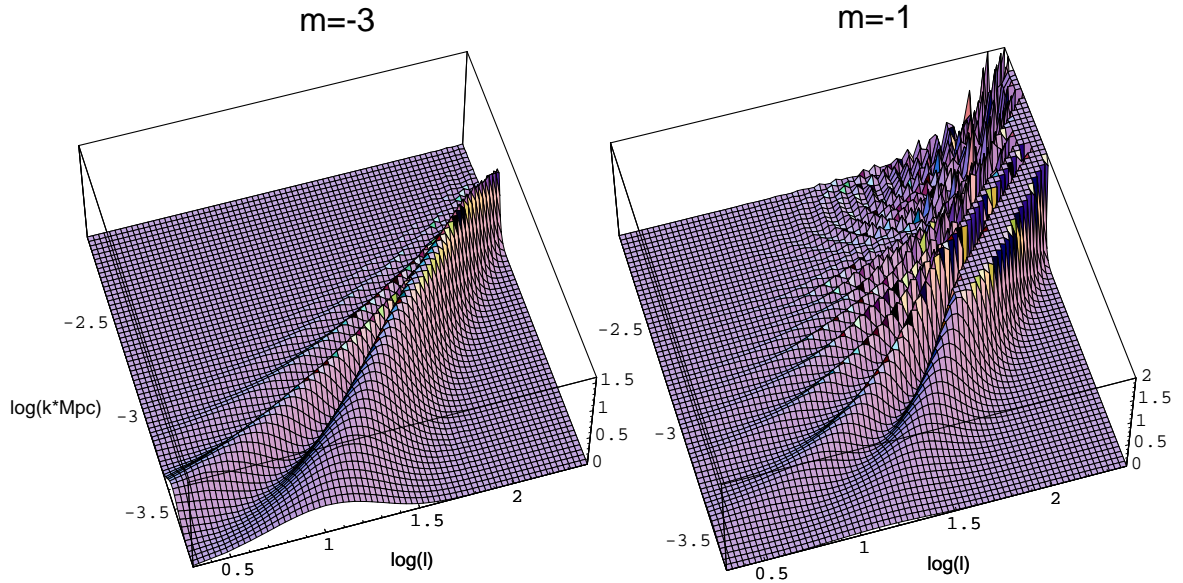


Figure 6.12: Aliasing Effect

The full open isocurvature photon power spectrum for $k^3|S(0)|^2 \propto k^{m+3}$. (a) Scale invariant $m = -3$. (b) Blue $m = -1$. The steeply blue spectrum required by large scale structure constraints suffers projection aliasing. Large scale anisotropies are dominated by small scale power leaking through the projection. The anisotropy spectrum is thus less blue than the spatial power spectrum and insensitive to the large scale power spectrum.

6.3 Acoustic Peaks

On scales below the sound horizon, acoustic oscillations imprint hot and cold spots from regions caught in compression and rarefaction at last scattering. Viewed today, these become peaks in the anisotropy power spectrum. Since acoustic oscillations are generic in the gravitational instability scenario for structure formation, these peaks contain valuable model-independent cosmological information.

6.3.1 Mathematical Description

Acoustic contributions are described by the phase and the amplitude of the sound waves at last scattering. Since different k modes are frozen at different phases of their oscillation, there will in general be a series of peaks in the temperature and velocity spectra at last scattering. The bulk velocity of the photon fluid contributes as a Doppler shift in the observed temperature. The fluctuations captured at last scattering for a scale invariant adiabatic model is displayed in Fig. 6.14.

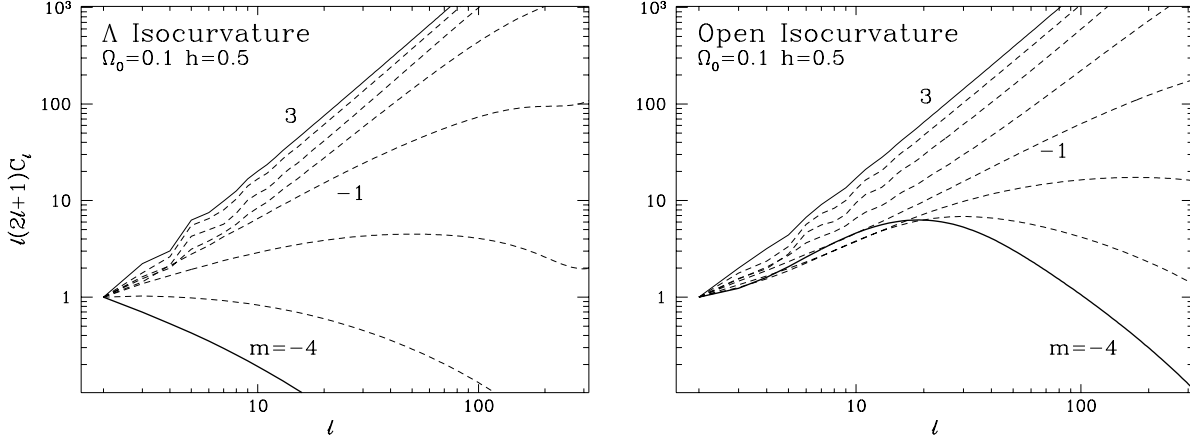


Figure 6.13: The m Dependence of Isocurvature Spectra

Blue spectra $m \gtrsim -2$ are dominated by small scale power aliased onto large angle anisotropies. The effective slope never exceeds $n_{\text{eff}} = 3$. In the $m \simeq 1$ regime $n_{\text{eff}} \simeq 2$ for both open and Λ models. Red spectra show different open and Λ models due to the lack of supercurvature modes in the open case which cuts off anisotropies. This is more severe in isocurvature models since the curvature scale at early ISW formation scales projects onto smaller angles than for their adiabatic late ISW counterparts.

These fluctuations are projected onto anisotropies as

$$\begin{aligned} \frac{\Theta_\ell(\eta)}{2\ell+1} &= [\Theta_0 + \Psi](\eta_*, k) X_\nu^\ell(\chi - \chi_*) + \Theta_1(\eta_*, k) \frac{1}{k} \frac{d}{d\eta} X_\nu^\ell(\chi - \chi_*) \\ &\quad + \int_{\eta_*}^{\eta} (\dot{\Psi} - \dot{\Phi}) X_\nu^\ell(\chi - \chi') d\eta', \end{aligned} \quad (6.21)$$

(see Appendix A.2.3 for a derivation). The dipole projects in a different manner than the monopole because of its angular dependence. The face on $\mathbf{k} \perp \boldsymbol{\gamma}$ mode of the “main projection” (see Fig. 6.3 and 1.7) vanishes for the Doppler effect which arises because of the line of sight velocity. This causes velocity contributions to be out of phase with the temperature as the derivative structure suggests and indicates that the two effects add in quadrature.

Due to the finite duration of last scattering, the effective fluctuations $[\Theta_0 + \Psi](\eta_*)$ and $\Theta_1(\eta_*)$ are more severely diffusion damped than one might naively expect. As the ionization fraction drops due to recombination, the mean free path and hence the diffusion length increases. We will see how this affects the amplitude of oscillations in §6.3.4. Once this is accounted for, the tight coupling description of the acoustic oscillations from §5.2 leads to an excellent description of the resultant anisotropy (see [82] and Appendix A.2.3). It is useful however to extract a few simple model-independent results.

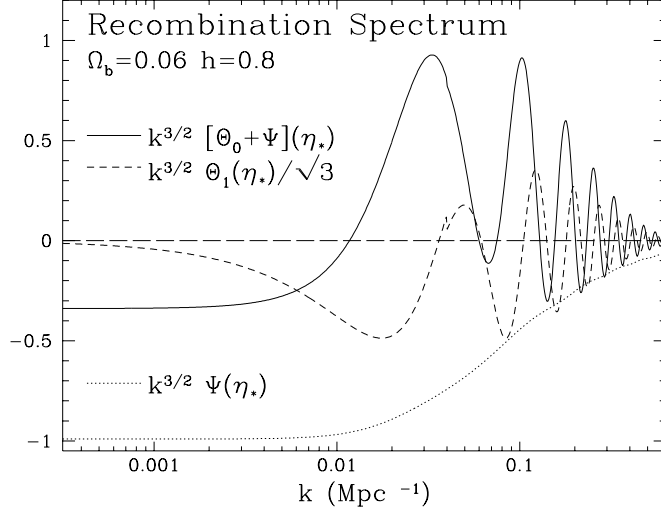


Figure 6.14: Fluctuations at Last Scattering

Analytic separation from Appendix A.2.3. Notice that the dipole is significantly smaller than the monopole as expected but is not negligible, especially near the zeros of the monopole oscillations. In particular, along with the early ISW effect, it fills in fluctuations *before* the first acoustic peak. Due to baryon contributions, gravity is able to shift the equilibrium position of the fluctuations, leading to a modulation of the monopole peaks (see §3.2). We have drawn in the zero level of the oscillations to guide the eye. The kink at $k = 0.04 \text{ Mpc}^{-1}$ is due to the joining of the large and small scale solutions.

6.3.2 Location of the Peaks

The most robust feature of the acoustic oscillations is the angular location of the peaks. Consider first, the spatial power spectrum at last scattering. Peaks will occur at extrema of the oscillations, *i.e.*

$$k_p r_s(\eta_*) = \begin{cases} p\pi & \text{adi} \\ (p - 1/2)\pi, & \text{iso} \end{cases} \quad (6.22)$$

where the sound horizon at last scattering is

$$r_s(\eta_*) = \int_0^{\eta_*} c_s d\eta' = \frac{2}{3} \frac{1}{k_{eq}} \sqrt{\frac{6}{R_{eq}}} \ln \frac{\sqrt{1 + R_*} + \sqrt{R_* + R_{eq}}}{1 + \sqrt{R_{eq}}}, \quad (6.23)$$

with $k_{eq} = (2\Omega_0 H_0^2 a_0/a_{eq})^{1/2}$, $a_{eq}/a_0 = 2.38 \times 10^{-5} \Theta_{2.7}^4 (\Omega_0 h^2)^{-1} (1 - f_\nu)^{-1}$ and recall $R = 3\rho_b/4\rho_\gamma$, *i.e.*

$$\begin{aligned} R_{eq} &= \frac{1}{1 - f_\nu} \frac{3\Omega_b}{4\Omega_0}, \\ R_* &= 31.5\Omega_b h^2 \Theta_{2.7}^{-4} (z_*/10^3)^{-1}, \end{aligned} \quad (6.24)$$

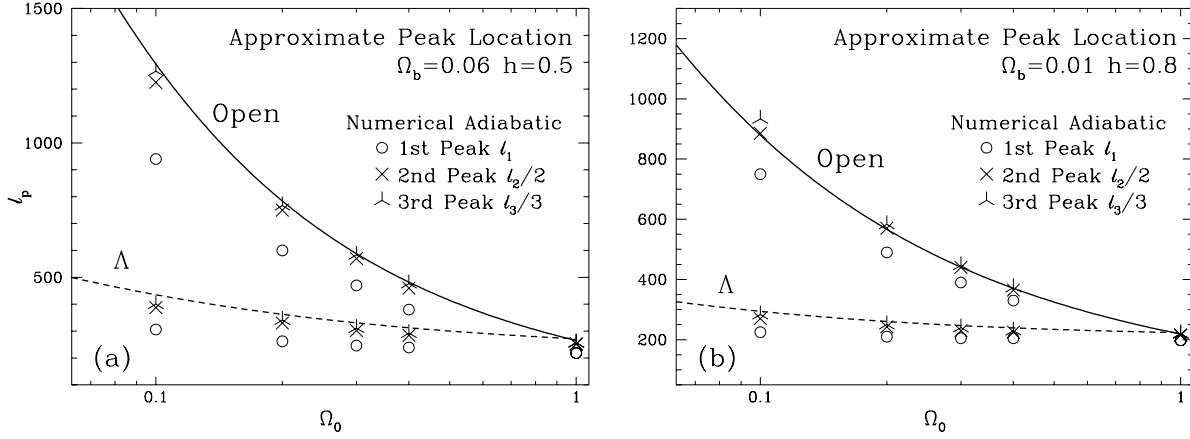


Figure 6.15: Acoustic Peak Location

The physical scale of the peaks is simply related to the sound horizon at last scattering and corresponds to multiples of the angle that this scale subtends on the sky $\ell_p = p\pi r_\theta / r_s$ for adiabatic models. Varying $\Omega_0 h^2$ changes both the sound horizon at η_* and the present horizon η_0 leaving little effect. For open models, a given scale will correspond to a smaller angle by geodesic deviation. This projection estimate for the peak location is valid for pure acoustic contributions and underestimates the scale of the first peak in low $\Omega_0 h^2$ models due to neglect of the early ISW effect.

$\Theta_{2.7} = T_0/2.7\text{K}$ and $(1 - f_\nu)^{-1} = 1.68$ for three massless neutrinos.

From equation (6.15), the scale k_p subtends an angle

$$\ell_p \simeq k_p r_\theta(\eta_*), \quad (6.25)$$

where

$$r_\theta(\eta_*) \simeq \begin{cases} 2(\Omega_0 H_0)^{-1} & \Omega_\Lambda = 0 \\ 2(\Omega_0 H_0^2)^{-1/2} (1 + \ln \Omega_0^{0.085}) & \Omega_\Lambda + \Omega_0 = 1 \end{cases} \quad (6.26)$$

For low $\Omega_b h^2$, $R_* \ll 1$ and the sound horizon at last scattering reduces to

$$r_s(\eta_*) \simeq \frac{1}{\sqrt{3}} \eta_* \simeq \frac{2}{\sqrt{3}} (\Omega_0 H_0^2)^{-1/2} [(1 + x_R)^{1/2} - x_R^{1/2}] z_*^{-1/2}, \quad (6.27)$$

where the radiation contribution at last scattering produces the modification factor in square brackets with $x_R = a_{eq}/a_*$. Note that the correction factor in equation (6.27) goes asymptotically to 1 and $\frac{1}{2} x_R^{-1/2} \propto (\Omega_0 h^2)^{1/2} (1 - f_\nu)^{1/2}$ in the high and low $\Omega_0 h^2$ limits respectively.

Let us summarize these results. Adiabatic models will possess peaks in ℓ that follow a series (1 : 2 : 3 : 4...), whereas isocurvature models obey the relation (1 : 3 : 5 : 7...) due to their phase difference (see §5.2.2). The fundamental angular scale on which these series are based is that which is subtended by the sound horizon at last scattering.

It is purely dependent on the background dynamics, matter content, and geometry and thus can be used as a robust probe of these fundamental cosmological parameters. The scale is only weakly sensitive to the baryon content if it is near the value required by nucleosynthesis $\Omega_b h^2 \simeq 10^{-2}$ but becomes increasingly sensitive as $\Omega_b h^2$ increases beyond the point at which the photon-baryon fluid is baryon dominated at last scattering $\Omega_b h^2 \gtrsim 0.03$. The radiation content at last scattering increases the expansion rate and thus decreases the horizon scale at last scattering. If $\Omega_0 h^2$ is sufficiently low, the location of the peaks can provide an interesting constraint on the matter-radiation ratio, including perhaps the number of relativistic (massless) neutrino species. Otherwise, changes in the age of the universe through $\Omega_0 h^2$ and Ω_Λ largely scale out of the ratio between the two scales but may provide some constraint on large Λ models.

The location of the peaks is by far the most sensitive to the presence of curvature in the universe. Curvature makes the sound horizon at last scattering subtend a much smaller angle in the sky than a flat universe. In Fig. 6.15, we compare open and Λ geometric effects. The corresponding spectra are plotted in Figs. 6.6b and 6.9. Notice that aside from the first peak, the numerical results agree quite well with the simple projection scaling. This is because the first peak also obtains contributions from the early ISW effect. Because of its later generation, those contributions subtend a larger angle on the sky. They also are generated when radiation is less important. Thus for example, in an open universe, the angular location scales close to $\Omega_0^{1/2}$ even in a low $\Omega_0 h^2$ model.

6.3.3 Heights of the Peaks

The heights of the peaks are somewhat more model dependent than their locations since they will be controlled by the initial spectrum of fluctuations. However, for initial conditions that are featureless (*e.g.* the commonly assumed power law models) in the decade or so of scales that yield observable peaks, the *relative* heights again contain nearly model independent information.

Aside from the initial spectrum, essentially two quantities control the heights of the peaks: the baryon-photon ratio $\Omega_b h^2$ and the matter-radiation ratio $\Omega_0 h^2 (1 - f_\nu)$ (see Fig. 6.16). The presence of baryons increases the gravitating mass of the fluid leading to more gravitational compression of the fluid from baryon drag. Thus every other peak will be enhanced by gravitational effects on the baryons. As discussed in §5.2.2, these are the

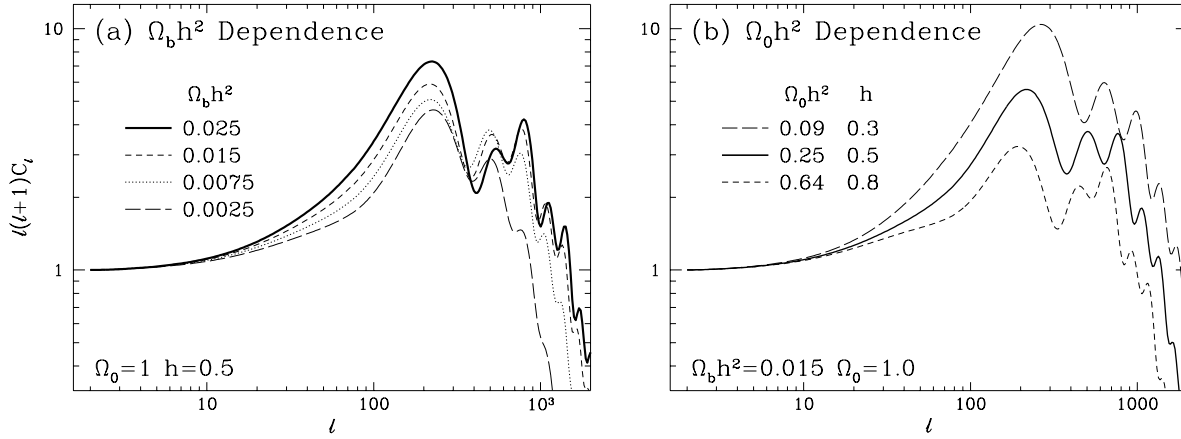


Figure 6.16: Acoustic Peak Heights

(a) The baryon-photon ratio $R \propto \Omega_b h^2$ determines the balance between pressure and gravity and thus the zero point of the oscillation. Gravitational enhancement of compression leads to higher odd peaks as $\Omega_b h^2$ increases. For sufficiently high $\Omega_b h^2$, the even peaks cannot be distinguished at all. (b) Decay of the potentials Ψ and Φ due to radiation pressure inside the horizon during radiation domination drives the oscillation to higher amplitude. If matter radiation equality is delayed by lowering $\Omega_0 h^2$, this enhancement can boost the first few peaks. The radiation also changes the expansion rate and shifts the location of the peaks.

odd peaks for the adiabatic mode and the even for the isocurvature. Enhancement only occurs if the gravitational potential is still significant. In the radiation-dominated epoch, the gravitational potential decays after sound horizon crossing. Thus the alternating series of peaks only occurs for scales that cross after radiation domination leading to a pattern that is dependent on the matter-radiation ratio.

In adiabatic models, the decay of the potentials Ψ and Φ lead to driving effects from infall and dilation. This boosts oscillations by a factor of ~ 5 in amplitude for modes that cross in radiation domination. By delaying equality through lowering $\Omega_0 h^2(1 - f_\nu)$, we can bring this effect to larger scales and thus boost more of the peaks. For isocurvature models, the opposite occurs. By delaying equality, we take away potential growth from larger and larger scales. This lowers the radiation fluctuation.

6.3.4 Diffusion Damping at Recombination

At small scales, the features described above for the heights of the peaks can be hidden by diffusion damping. We obtain the diffusion damped fluctuation at last scattering from the acoustic solutions of equation (5.52), denoted by an overhat, with the relations

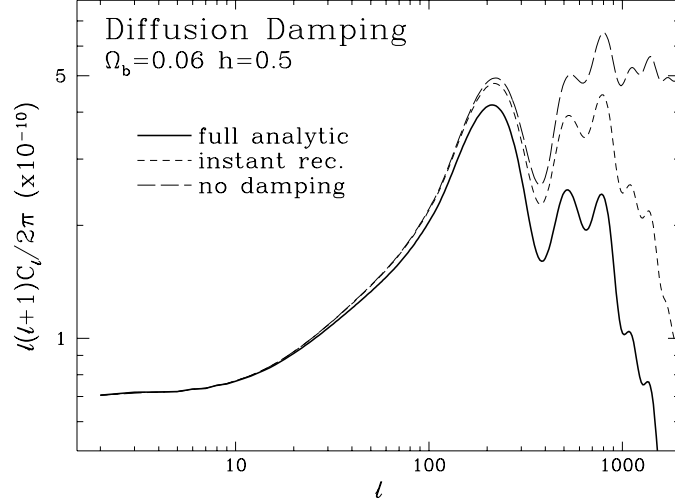


Figure 6.17: Diffusion Damping

The effect of the finite duration of last scattering from the results of Appendix A.2.3. Estimating the damping in the instantaneous recombination approximation leads to a significant underestimate of the damping scale. It is however far better than neglecting diffusion damping entirely.

(see Appendix A.3.1 [82])

$$\begin{aligned} [\Theta_0 + \Psi](\eta_*) &= [\hat{\Theta}_0 + \Psi](\eta_*)\mathcal{D}(\eta_*, k), \\ \Theta_1(\eta_*) &= \hat{\Theta}_1(\eta_*)\mathcal{D}(\eta_*, k), \end{aligned} \quad (6.28)$$

where we assume $R\Psi(\eta_*) \ll \Theta_0$ and the damping factor is weighted by the visibility function

$$\mathcal{D}(\eta_*, k) = \int_0^{\eta_*} d\eta \dot{\tau} e^{-\tau} e^{-(k/k_D)^2}. \quad (6.29)$$

with the damping scale $k_D(\eta)$ calculated from equation (5.59). Since the visibility function $\dot{\tau}e^{-\tau}$ goes to a delta function for large τ , this definition also coincides with its tight-coupling definition from equation (5.58). Note that the ionization history enters in two places: the increase in the diffusion length k_D^{-1} and the visibility function weighting. Since the visibility function peaks at $z \simeq 10^3$ nearly independent of cosmological parameters and is by definition normalized to have unit area, much of the qualitative behavior of the damping can be determined by examining k_D^{-1} .

Recall from §5.2.3 that the diffusion length is approximately the distance a photon can random walk by η_* , $k_D^{-1} \propto \sqrt{\eta_* \lambda_C}$, where the Compton mean free path is $\lambda_C \propto (x_e n_b)^{-1}$. The behavior of the diffusion length through last scattering will be determined by the

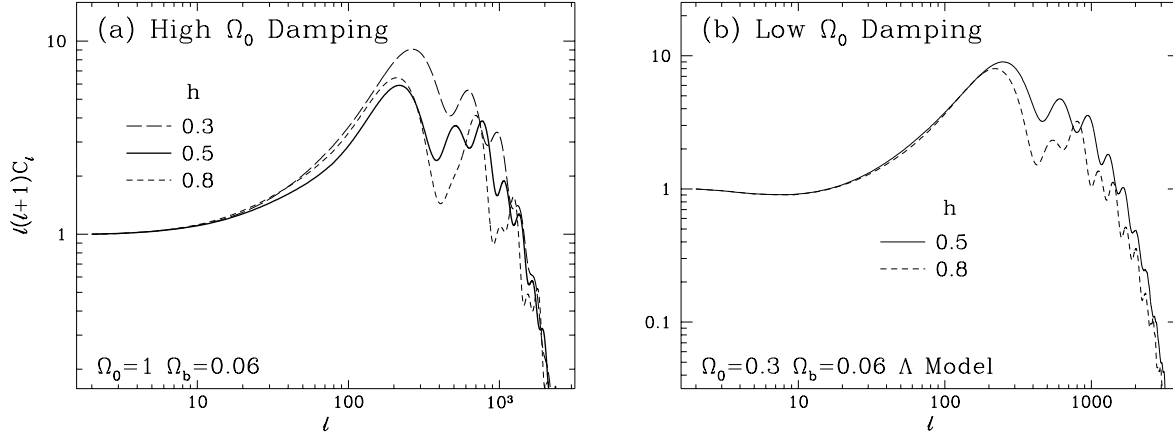


Figure 6.18: Damping Scale

The diffusion damping scale depends somewhat differently on cosmological parameters than the acoustic scale. It is more sensitive to Ω_b (see Fig. 6.16) and less sensitive to h . Its presence can also alter the pattern of heights expected from the acoustic peaks, *e.g.* the small scale boost from dilation and the alternating peak heights from infall.

evolution of the ionization fraction. In Appendix A.2.3, we will show how to construct the diffusion length from a realistic treatment of recombination. However, to obtain simple scaling results, the Saha approximation for the equilibrium ionization suffices.

The Saha equation assumes that photoionization and recombination of hydrogen $e + p \leftrightarrow H + \gamma$ are in equilibrium. If the photon chemical potential is vanishingly small as required by the FIRAS observation [116], the chemical potentials of the other species must satisfy $\mu_e + \mu_p = \mu_H$. The number density of a non-relativistic species x is given by

$$n_x = g_x \left(\frac{m_x T_x}{2\pi} \right)^{3/2} e^{(\mu_x - m_x)/T_x} \quad (6.30)$$

where g_x is the spin multiplicity. This chemical potential relation then implies the Saha equation

$$\frac{n_e n_p}{n_H n_b} = \frac{x_e^2}{1 - x_e} = \frac{1}{n_b} \left(\frac{m_e T}{2\pi} \right)^{3/2} e^{-(m_e + m_p - m_H)/T} \quad (6.31)$$

where we neglect the helium fraction, $n_b = n_p + n_H$ and the strong thermal coupling between photons, electrons, and baryons at last scattering has allowed us to set all the temperatures equal (see §3.1.2). Note that $m_e + m_p - m_H = 13.6\text{eV}$, the electron binding energy.

The interesting result here is that as the ionization drops to zero, its parameter dependence goes to $x_e \propto (\Omega_b h^2)^{-1/2}$ at fixed redshift (or temperature). The final damping length approximately scales as $k_D^{-1}(\eta_*) \propto \eta_*^{1/2} (\Omega_b h^2)^{-1/4}$. The damping angular scale

therefore becomes

$$\ell_D \propto \eta_*^{-1/2} (\Omega_b h^2)^{1/4} r_\theta(\eta_*) \quad (6.32)$$

At asymptotically high and low $\Omega_0 h^2$, this goes to $\Omega_0^{-3/4} \Omega_b^{1/4}$ and $\Omega_0^{-5/4} \Omega_b^{1/4} h^{-1/2}$ in an open universe and $\Omega_0^{-1/4} \Omega_b^{1/4}$ and $\Omega_0^{-1/2} \Omega_b^{1/4} h^{-1/2}$ in a Λ universe. The damping scale is thus somewhat more strongly dependent on Ω_b than the acoustic scale but even more weakly dependent on h alone (see Fig. 6.18). The Saha prediction requires modification for high $\Omega_b h^2$ models due to the increasing importance of the Lyman- α opacity at last scattering [84].

Chapter 7

Secondary Anisotropies

*Mingled and merged, densely sprouting,
In the primaeval mass, there is no shape.
Spreading and scattering, leaving no trail behind,
In the darkness of its depths, there is no sound.*

—Chuang-tzu, 14

Between recombination and the present, astrophysical processes can alter the anisotropy spectrum. In general, they may have two distinct effects:

1. Erasure or masking of primary anisotropies by rescattering and other filtering.
2. Generation of secondary fluctuations imprinting the mark of a much more evolved and complex universe.

Indeed from the null result of the Gunn-Peterson test [69], we know that the universe is almost completely ionized out to redshift 4-5 [144, 172]. Although this alone would only have a percent or so affect on primary anisotropies, it raises the possibility that reionization of the universe could have occurred at a much higher redshift. In models with sufficient small scale power, it is plausible that an early round of structure formation may have released the energy required to keep the universe ionized at high redshift (see *e.g.* [58, 165]).

Early reionization scenarios enjoyed a brief period of popularity following the detection of puzzlingly small anisotropies at the $\sim 2^\circ$ scale by the SP91 experiment [145], as the great number of papers that it generated bears witness to [61, 45, 31, 75, 160, 81, 46]. Although the status is far from clear at the present, their popularity has declined due to the steady stream of higher detections on roughly the same scale [174, 104]. Still, some filtering

of primary anisotropies must have occurred. Indeed, for typical (primordial) isocurvature baryon (PIB) models [125, 126] significant reionization is both necessary and natural due to their excessive amounts of small scale power.

Since secondary anisotropies depend on the astrophysical details of structure formation, they provide interesting constraints on models and clues to the process of structure formation. On the other hand, they do not have much power to measure background parameters in a model independent manner. In this sense, primary and secondary anisotropies complement each other. If reionization is not too substantial, both mechanisms may contribute. In this case, the information contained in the CMB increases and consequently so does the care needed to extract it. The problem of extraction alone would motivate the study of secondary anisotropy formation (see also Appendix A.3).

In this chapter, we first discuss the general principles that govern secondary anisotropy formation in linear theory. Since the results are quite model dependent, we will offer the CDM and PIB models to illustrate their effect. Linear contributions are generally cancelled at small scales. It is therefore necessary to include higher order effects. We discuss second order calculations in detail and find that the Vishniac, or second order Doppler contribution is the dominant source at small angles. We then briefly survey highly non-linear effects and their importance for secondary anisotropy formation. In this case, even the qualitative sense of the effects can be model dependent.

7.1 Linear Contributions

7.1.1 Reionization Damping

Secondary anisotropy formation in linear theory follows the same basic principles as primary anisotropy formation. The main difference is that the photons and baryons are no longer tightly coupled. As shown in §5.3, the baryons are released from Compton drag when the redshift falls below

$$z_d \simeq 160(\Omega_0 h^2)^{1/5} x_e^{-2/5}, \quad (7.1)$$

where recall that x_e is the ionization fraction. Fluctuations in the matter then are free to grow and follow the pressureless solution D to the evolution equations (see §5.1). Likewise, the photon diffusion length grows to be comparable to the horizon size. Last scattering effectively occurs when the Compton scattering time becomes greater than the expansion

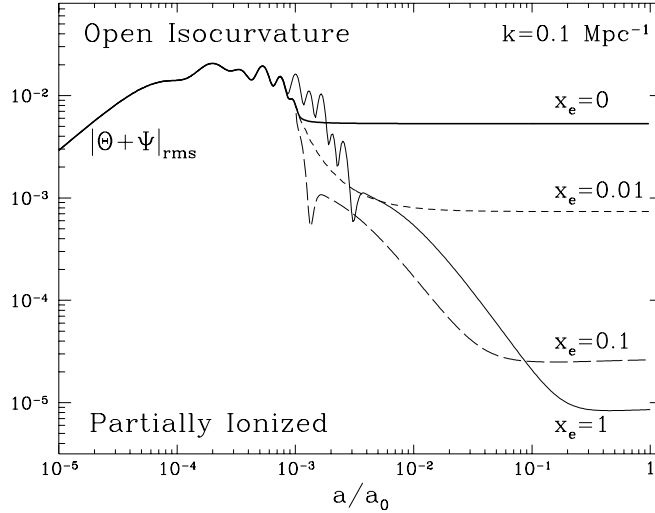


Figure 7.1: Reionization Damping Evolution

If the universe stays transparent after standard recombination at $z_* \simeq a_0/a_* \simeq 1000$, the acoustic oscillations in the photon-baryon fluid will be frozen into the rms temperature fluctuation. For partially reionized models, the diffusion length continues to grow and sharply damps the acoustic contributions. Fluctuations are regenerated by scattering induced Doppler shifts from the electrons. The model here is an open baryon isocurvature model with $\Omega_0 = \Omega_b = 0.2$, $h = 0.5$.

time. More specifically, we can define it as the epoch when optical depth reaches unity. Since the optical depth

$$\tau = 4.61 \times 10^{-2} (1 - Y_p/2) x_e \frac{\Omega_b h}{\Omega_0^2} \times \begin{cases} [2 - 3\Omega_0 + (1 + \Omega_0 z)^{1/2} (\Omega_0 z + 3\Omega_0 - 2)] & \Omega_\Lambda = 0 \\ \Omega_0 [1 - \Omega_0 + \Omega_0 (1 + z)^3]^{1/2} - \Omega_0 & \Omega_0 + \Omega_\Lambda = 1 \end{cases} \quad (7.2)$$

if x_e is constant, this occurs at

$$z_* \simeq 98 \left(\frac{\Omega_0 h^2}{0.25} \right)^{1/3} \left[\frac{(x_e \Omega_b h^2) (1 - Y_p/2)}{0.0125 \cdot 0.885} \right]^{-2/3}, \quad (7.3)$$

for both cases since last scattering occurs before curvature or Λ domination. Notice that last scattering occurs after the end of the drag epoch for sufficiently high ionization and baryon fraction.

In this limit, photons diffuse amongst the freely falling baryons inside the horizon. Recall that diffusion damps intrinsic photon fluctuations as $e^{-\tau}$ due to streaming conversion of inhomogeneities to anisotropies and subsequent rescattering isotropization. Thus

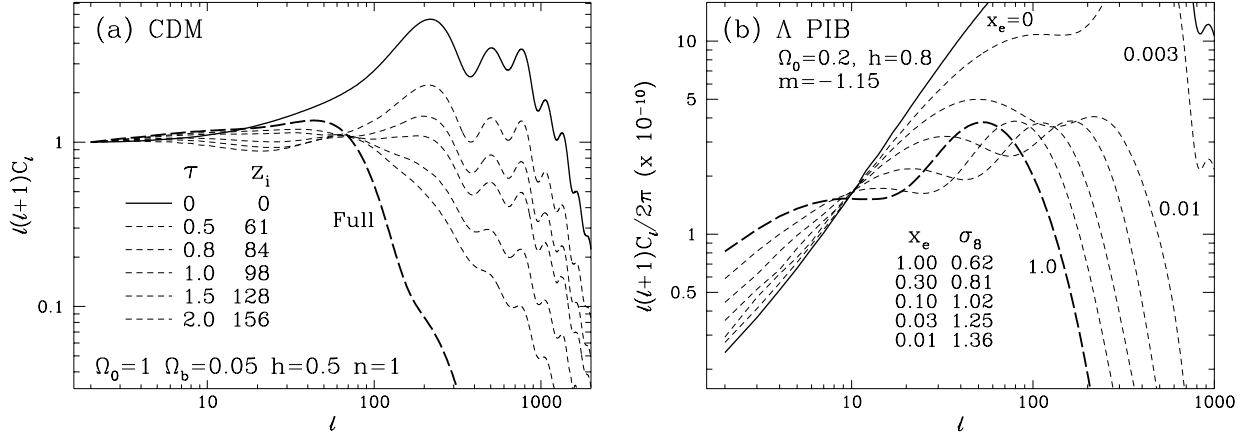


Figure 7.2: Reionization Damped Spectrum

(a) Standard CDM. Reionization damps anisotropy power as $e^{-2\tau}$ under the horizon (diffusion length) at last scattering. The models here are fully ionized $x_e = 1.0$ out to a reionization redshift z_i . Notice that with high optical depth, fluctuations at intermediate scales are regenerated as the fully ionized (long-dashed) model shows. (b) Λ PIB. PIB models have excess small scale power and require high optical depth to damp the corresponding anisotropy. In this case, both reionization damping and regeneration can be quite important and the spectrum is sensitive to the details of the ionization history not merely the optical depth. Models here have constant ionization from $z_i = 800$ and are normalized to the COBE detection [74]. Note that the amplitude of matter fluctuations σ_8 is also highly sensitive to the ionization.

primary anisotropies are sharply damped below the horizon scale implying that no acoustic oscillations will survive (see Fig. 7.1).

Features in the primary spectrum will be accordingly damped away as the optical depth between recombination and the present increases. For sufficiently high optical depth, the ability to measure fundamental cosmological parameters through the location of the peaks may be lost (see Fig. 7.2a). Notice that for $\tau \lesssim 1$, the oscillation amplitudes are still high enough to make measurements possible. Beyond this value, the primary signal is likely to be lost in the noise, foreground contamination, and non-linear source contributions. For the low $\Omega_b h^2 = 0.0125$ standard CDM model, this only occurs for an ionization redshift $z_i \gtrsim 100$. This possibility is highly unlikely since its $n = 1$ primordial spectrum does not have enough power for such early structure formation.

7.1.2 COBE Constraints on PIB Models

Reionization damping can on the other hand save models which would otherwise predict too high an amplitude for small scale anisotropies. Such is the case for standard PIB

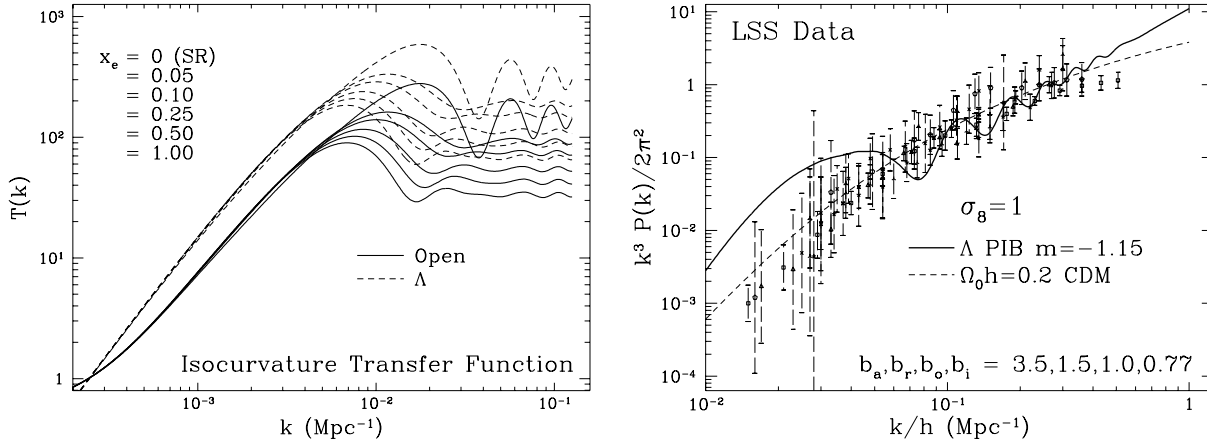


Figure 7.3: PIB Matter Power Spectrum

(a) Transfer function. Baryon perturbations $\Delta_b(\eta_0, k) = T(k)S(0, k)$ have a prominent peak at the maximal Jeans scale. Silk damping of acoustic oscillations increases with ionization leaving a constant small scale tail. The amplitude of the tail depends on the amount of time between the drag epoch and the present for fluctuations to grow as $D(a)$. The model here is $\Omega_0 = 0.2$, $h = 0.5$. (b) Large scale structure data with optical bias unity and relative biases chosen to best reconstruct the power spectrum [122] (see also Appendix B.4) require that the isocurvature index $m \simeq -1$. The model plotted is a $m = -1.15$ Λ PIB model with $\Omega_0 = 0.2$, $h = 0.8$ and $x_e = 0.1$ chosen to match $\sigma_8 = 1$ with a *COBE* normalization and not violate CMB constraints. A low $\Omega_0 h \sigma_8$ normalized CDM model is shown for comparison.

models which have initial isocurvature fluctuations $|S(0, k)|^2 \propto k^m$ in a baryon-dominated $\Omega_0 = \Omega_b$ universe [125, 126]. Although $\Omega_0 = 0.1 - 0.3$ models, designed to satisfy dynamical estimates of the mass, consequently fail to satisfy nucleosynthesis constraints on the baryon density, astrophysical processes could alter light element abundances [58, 59]. Moreover since there is no *ab initio* mechanism for generating the required entropy perturbations, the index m is fixed by measurements of large scale structure today. Recall from §5.2.3 that isocurvature perturbations evolve such that below the photon diffusion scale, the initial entropy fluctuations become the density perturbations that seed large scale structure (see Fig. 7.3). The observed power spectrum of approximately $P(k) \propto k^{-1}$ at large scale structure scales [122] then implies an $m \simeq -1$ initial power law in the model. Numerical simulations which take into account non-linearities confirm this result [157]. At the largest scales, however, isocurvature conditions prevent the formation of potential perturbations leaving $k^3 |\Phi|^2 \propto k^{3+m}$ which is steeply rising for $m = -1$. When normalized to the *COBE* DMR measurement, this leads to a steeply rising spectrum of anisotropies with effective slope $n_{\text{eff}} \simeq 2$. This model therefore has three difficulties to overcome

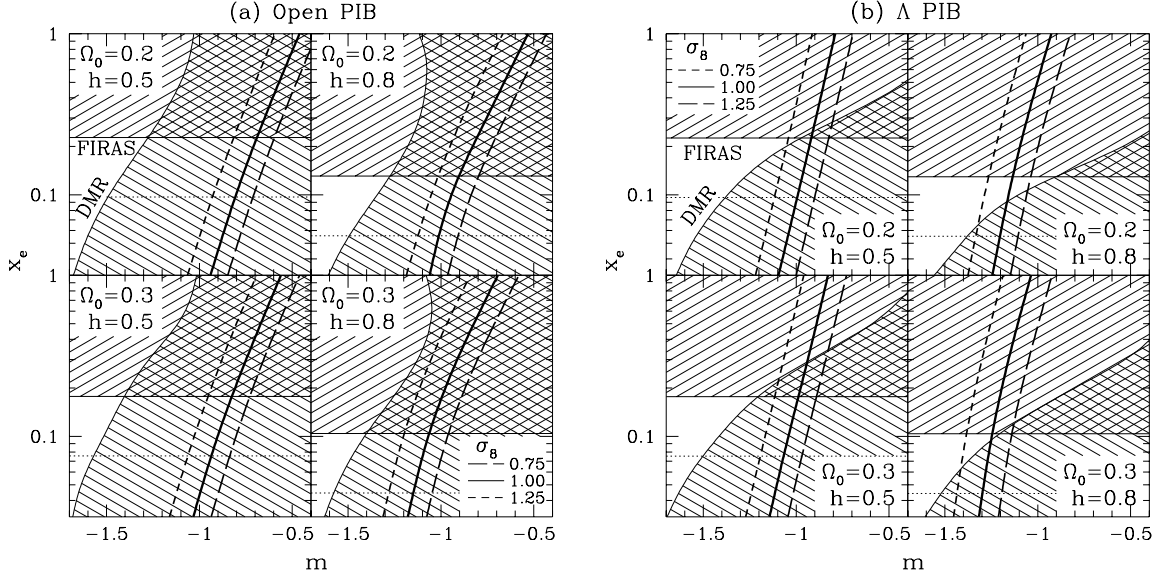


Figure 7.4: Constraints on PIB Models

The *COBE* DMR slope imposes an upper (95% confidence) limit on the initial spectral index m . The *COBE* FIRAS constraint on spectral distortions through the Compton- y parameter sets an upper limit on the ionization fraction. Here a conservative $T_e = 5000\text{K}$ is assumed with the more realistic $T_e = 10000\text{K}$ in dotted lines. The *COBE* DMR normalization also sets the level of matter fluctuations at the $8 h^{-1}\text{Mpc}$ scale σ_8 . (a) No open model simultaneously satisfies all the observational constraints. (b) For Λ models, a small region of parameter space is open for high h , low Ω_0 models.

1. Steeply rising *COBE* slope.
2. Large degree scale anisotropies.
3. High matter power spectrum normalization, σ_8 the amplitude at the $8h^{-1}\text{Mpc}$ scale.

They are all alleviated somewhat by reionization. Since Silk damping [150] does not destroy entropy fluctuations, the large amount of small scale power in the model allows for collapse of objects immediately following recombination (see §5.3.1). This could lead to sufficient energy input to reionize the universe as early as $z_i = 800$ [125, 126]. As we have noted, reionization damps the steeply rising primary signal (see Fig. 7.2b) and can help the first two problems. Furthermore, because Compton drag prevents the growth of structure, the ionization history can be tuned to provide the right ratio of matter to temperature fluctuations (see Figs. 5.6, 7.3).

Unfortunately, reionization can only damp fluctuations under the horizon scale at last scattering. Thus it is difficult to lower the effective slope n_{eff} at *COBE* scales $\ell \simeq 2 - 25$. Geodesic deviation carries the same physical scale onto smaller angles for open universes. Thus open models will thus be even less affected by reionization than Λ models. Smaller effects include raising the baryon content through $\Omega_b h^2$ which delays last scattering and increases the physical scale of the horizon. However even for flat models, the projection from the last scattering surface depends strongly on Ω_0 and counters the Ω_b dependence in these $\Omega_0 = \Omega_b$ baryonic models. Furthermore, the late ISW effect boosts the low order multipoles slightly as Ω_0 decreases (see §6.2.6). In the range of interest, decreasing Ω_0 leads to a shallower *COBE* slope. High x_e , high h , low Ω_0 , Λ models therefore offer the best prospects of bringing down the *COBE* slope.

The amount of reionization allowable is moreover constrained by the lack of spectral distortions in the CMB, $y \leq 2.5 \times 10^{-5}$ (95% CL) [116], where recall from §3.2.1 that $y = \int d\tau k(T_e - T)/m_e c^2$ measures the amount of upscattering in frequency from hot electrons. For collisional ionization, the electron temperatures must be quite high to overcome the Boltzmann suppression factor, typically $T_e \gtrsim 15000\text{K}$ [58, 28]. For photoionization, there is no firm lower limit on T_e since we can always fine tune the photoelectron energy to zero (*e.g.* with a decaying neutrino that produces 13.6 eV photons). Yet, given the ionization potential, we would generically expect electron energies of a few eV. Compton cooling from energy transfer to the CMB (see §3.1.2) then suppresses the equilibrium electron temperature to an average of $T_e \sim 5000\text{K}$ [165]. We will therefore adopt an electron temperature of $T_e = 5000\text{K}$. Since the collisionally ionized model is to date the only isocurvature scenario to successfully modify nucleosynthesis [58], this is a very conservative choice.

Bunn, Scott, & White [22] find that the observational constraints require $n_{\text{eff}} = 1.3_{-0.37}^{+0.24}$ (with quadrupole) which indicates that $n_{\text{eff}} = 2$ should be ruled out at greater than 95% confidence. Since PIB spectra are not pure power laws in the effective slope (see Fig. 7.2b), to quantify this constraint, we employ a full likelihood analysis of the two-year *COBE* DMR sky maps for open and Λ isocurvature baryon models fixed by Ω_0 , h , and x_e [74]. We expand the two-year DMR data in a set of basis functions which are optimized to have the maximum rejection power for incorrect models (see [21] for a full discussion). To set limits on m and the normalization Q , the rms quadrupole, we assume a prior distribution which is uniform for all Q and $m \leq 0$. Spectra with $m > 0$ are unphysical due to non-linear effects which regenerate an $m = 0$, $P(k) \propto k^4$ large scale tail to the fluctuations [124]. The

constraint in the crucial $m \simeq -1$ regime is not sensitive to the details of this cutoff. It is furthermore not very sensitive to ambiguities in the definition of power law initial conditions at the curvature scale (see §4.1.1 and §6.2.6 for a discussion). Shown in Fig. 7.4 are the 95% confidence upper limits imposed on m by integrating over the normalization Q to form the marginal likelihood in m . As expected, all open models with $m \simeq -1$ are ruled out regardless of ionization fraction, whereas highly ionized Λ models remain acceptable. Notice however that the constraint tightens for the highest ionization fractions. This is because fluctuations are in fact regenerated at the new last scattering surface if the optical depth is sufficiently high (see §7.1.3 below).

Since the PIB model is phenomenologically based, it is always possible to add free parameters to adjust the model to fit observations. Indeed an initial power spectrum with $m \simeq -1$ is required only in the large scale structure regime. Aside from simplicity arguments, we have no firm reason to believe that the power law behavior extends to *COBE* scales. It is therefore worthwhile to consider smaller scale anisotropy formation where CMB and large scale structure observations will overlap. This will eventually provide powerful consistency tests for *any* model since the two measure fluctuations at very different epochs in the evolution of structure (see *e.g.* [164]). In the case of early reionization, regeneration of small scale anisotropies can be significant. It is to this subject that we now turn.

7.1.3 Anisotropy Regeneration

Fluctuations are not entirely damped away by reionization (see Fig. 7.1). Since the baryons are in free fall after the drag epoch, they possess a non-negligible bulk velocity. Compton scattering still attempts to isotropize the photons in the electron rest frame and couples the photon and baryon bulk velocities V_γ and V_b . Thus at each scattering event, the photons are given a Doppler kick from the electrons. Subsequent diffusion over many wavelengths of the fluctuation damps away this contribution. Thus fluctuations will be on the order of $V_b \tau_k$ if the optical depth through a wavelength of the fluctuation, $\tau_k \simeq \dot{\tau}/k \ll 1$. In the opposite regime, the photons are still tightly coupled. Doppler fluctuations then go to V_b and add to the undamped temperature fluctuations.

We can employ analytic techniques to better understand these Doppler contributions. Ignoring curvature, as is appropriate for these small scales before last scattering, the

formal solution to the Boltzmann equation is

$$[\Theta + \Psi](\eta, k, \mu) = [\Theta + \Psi](\eta_d, k, \mu)e^{ik\mu(\eta_d - \eta)}e^{-\tau(\eta_d, \eta)} + [\Theta_D + \Theta_{ISW}](\eta, k, \mu), \quad (7.4)$$

where recall $k\mu = \mathbf{k} \cdot \boldsymbol{\gamma}$ and the optical depth $\tau(\eta_1, \eta_2) = \int_{\eta_1}^{\eta_2} \dot{\tau} d\eta$. Here Θ_D and Θ_{ISW} represent the Doppler and the ISW effect respectively. The initial conditions are taken at the drag epoch η_d so that we can consider the matter source V_b as evolving independently. As noted above, scattering rapidly damps out the contributions from before the drag epoch as $e^{-\tau}$, and we will hereafter ignore this term. Thus the photon temperature perturbation is a function of the matter perturbations alone. These source terms are explicitly given by

$$\begin{aligned} \Theta_D(\eta, k, \mu) &= \int_{\eta_d}^{\eta} (\Theta_0 + \Psi - i\mu V_b) \dot{\tau} e^{-\tau(\eta', \eta)} e^{ik\mu(\eta' - \eta)} d\eta', \\ \Theta_{ISW}(\eta, k, \mu) &= \int_{\eta_d}^{\eta} 2\dot{\Psi} e^{-\tau(\eta', \eta)} e^{ik\mu(\eta' - \eta)} d\eta', \end{aligned} \quad (7.5)$$

where we have neglected the small correction to the quadrupole from the angular dependence of Compton scattering (see [82] for the justification) and recall that the plane-wave decomposition is defined such that $\boldsymbol{\gamma} \cdot \mathbf{v}_b(\eta, \mathbf{x}) = -i\mu V_b(\eta, k)\exp(i\mathbf{k} \cdot \mathbf{x})$.

To solve equation (7.4) to the present, we must obtain an expression for the effective temperature $\Theta_0 + \Psi$ at last scattering. Taking the zeroth moment of equation (7.4), we obtain

$$[\Theta_0 + \Psi](\eta, k, \mu) = \int_{\eta_d}^{\eta} \dot{\tau} e^{-\tau(\eta', \eta)} \left\{ (\Theta_0 + \Psi + 2\dot{\Psi})j_0[k(\eta - \eta')] - V_b j_1[k(\eta - \eta')] \right\} d\eta', \quad (7.6)$$

where we have employed the identity

$$j_\ell(z) = \frac{i^\ell}{2} \int_{-1}^1 \exp(i\mu z) P_\ell(\mu) d\mu, \quad (7.7)$$

with P_ℓ as the Legendre polynomial. In the diffusion limit, the optical depth across a wavelength is small and the sources do not vary much over a time scale $\eta \sim 1/k$. Taking these quantities out of the integral and assuming $\eta \gg \eta_d$, we obtain

$$[\Theta_0 + \Psi](\eta, k, \mu) \simeq [\Theta_0 + \Psi] \frac{\dot{\tau} \pi}{k} - V_b \frac{\dot{\tau}}{k} + 2 \frac{\dot{\Psi} \pi}{k}, \quad (7.8)$$

where we have employed the relation

$$\int_0^\infty j_\ell(z) dz = \frac{\sqrt{\pi} \Gamma[(\ell + 1)/2]}{2 \Gamma[(\ell + 2)/2]}. \quad (7.9)$$

As advertised, the contribution from the electron velocity is of order $\dot{\tau}/k$ or the optical depth through a wavelength. It is thus suppressed at short wavelengths. Since last scattering occurs before curvature or Λ domination, the change in the potential across a wavelength is negligibly small and we can neglect the ISW contribution at last scattering. Therefore the effective temperature becomes

$$[\Theta_0 + \Psi](\eta, k, \mu) \simeq -V_b \frac{\dot{\tau}}{k} \quad (7.10)$$

through last scattering.

It may seem counterintuitive that a source to the dipole Θ_1 creates an isotropic temperature fluctuation Θ_0 . Mathematically, it is clear from the Boltzmann hierarchy (4.54) that the dipole indeed sources the monopole as photons travel across a wavelength, $k\delta\eta \sim 1$. Consider an observer at the origin of a sine wave baryon velocity fluctuation in real space $v_b(x) = V_b \sin(kx)$. The observer sees photons coming from both the crest at $kx = \pi/2$, where $v_b > 0$, and the trough at $kx = -\pi/2$, where $v_b < 0$. The scattered photon distribution at these sights will be oppositely aligned dipoles. Thus the scattered radiation observed at the origin will be *redshifted* in both directions. This leads to a net temperature fluctuation. Of course, the effect is not cumulative. Radiation from further crests and troughs have shifts that cancel leaving an effect only for the photons which scattered within a wavelength of the perturbation, $\Theta_0 = \mathcal{O}(V_b \dot{\tau}/k)$.

Although this contribution is suppressed at short wavelengths, it is comparatively important since the dipole source V_b itself is severely cancelled. Inserting the effective temperature (7.10) in equation (7.4) and integrating the dipole source by parts, we obtain

$$[\Theta + \Psi](\eta_0, k, \mu) = \int_{\eta_d}^{\eta_0} \frac{1}{k} (\dot{V}_b \dot{\tau} + V_b \ddot{\tau} + 2k \dot{\Psi}) e^{-\tau(\eta, \eta_0)} e^{ik\mu(\eta - \eta_0)} d\eta. \quad (7.11)$$

The multipole decomposition is then obtained from equation (7.7),

$$\frac{\Theta_\ell(\eta_0, k)}{2\ell + 1} = \int_{\eta_d}^{\eta_0} \frac{1}{k} [\dot{V}_b \dot{\tau} + V_b \ddot{\tau} + 2k \dot{\Psi}] e^{-\tau(\eta, \eta_0)} j_\ell[k(\eta_0 - \eta)] d\eta, \quad (7.12)$$

where we have employed equation (7.7) and recall that the multipole moments are defined such that $\Theta_\ell = i^\ell (2\ell + 1)^{\frac{1}{2}} \int_{-1}^1 P_\ell(\mu) \Theta d\mu$. For the open universe generalization, replace j_ℓ with X_ν^ℓ .

We can further simplify the result by noting that in the small scale limit the anisotropy is sourced over many wavelengths of the perturbation. Contributions from crests

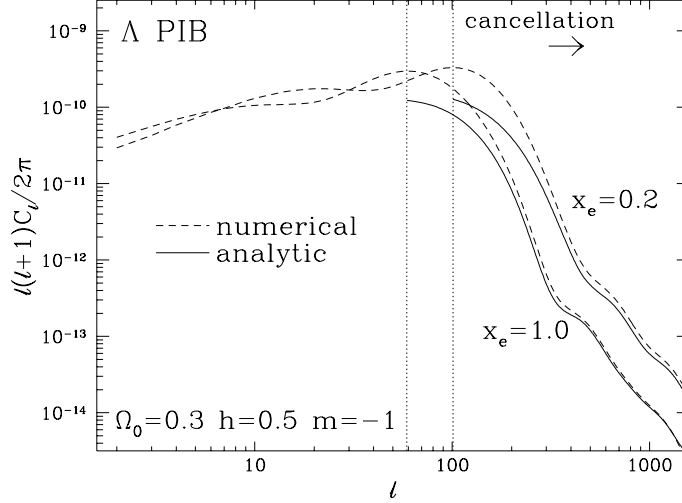


Figure 7.5: First Order Doppler Effect

Analytic calculations in the small scale cancellation regime show that first order anisotropies are dominated by the cancelled Doppler effect. Cancellation depends on the horizon scale at last scattering which increases with the ionization fraction x_e . As x_e or Ω_b is lowered, last scattering approaches the drag epoch where the analytic estimate breaks down.

and troughs of the perturbation cancel. In this case, $j_\ell(x)$ can be approximated as a δ -function at $x = \ell + 1/2$. In fact, we have already used this approximation for the late ISW effect of Λ models in §6.2.4. Employing equation (7.9) and the Stirling approximation of $\Gamma(x)/\Gamma(x + 1/2) \simeq x^{-1/2}$ for $x \gg 1$, we obtain

$$\frac{\Theta_\ell(\eta_0, k)}{2\ell + 1} \simeq \sqrt{\frac{\pi}{2\ell}} \frac{1}{k^2} \left[(\dot{V}_b \dot{\tau} + V_b \ddot{\tau} + 2k\dot{\Psi}) e^{-\tau(\eta, \eta_0)} \right] \Big|_{\eta=\eta_0-\ell/k}, \quad (7.13)$$

in a flat universe. With the relations

$$\begin{aligned} kV_b &= -\frac{\dot{D}}{D_0} \Delta_T(\eta_0, k), \\ k^2\Psi &= -\frac{3}{2} H_0^2 \Omega_0 \frac{D}{D_0} \frac{a_0}{a} \Delta_T(\eta_0, k), \end{aligned} \quad (7.14)$$

from the continuity and Poisson equations (5.24), the final expression for C_ℓ becomes

$$C_\ell^D = \frac{V}{\ell} \int \frac{dk}{k} \frac{1}{(k\eta_0)^6} S_L^2(\eta_0 - \ell/k) k^3 P(k), \quad (7.15)$$

where the matter power spectrum is $P(k) = |\Delta_T(\eta_0, k)|^2$ and the linear theory source is

$$S_L(\eta) = \left[\frac{\ddot{D}}{D_0} \dot{\tau} + \frac{\dot{D}}{D_0} \ddot{\tau} + 3H_0^2 \Omega_0 \frac{a_0}{a} \left(\frac{\dot{D}}{D_0} - \frac{D}{D_0} \frac{\dot{a}}{a} \right) \right] \eta_0^3 e^{-\tau(\eta, \eta_0)}. \quad (7.16)$$

This relation accurately describes the anisotropy on scales smaller than the horizon at last scattering if last scattering occurs *well* after the drag epoch (see Fig. 7.5). For low baryon fraction models such as CDM or partially ionized PIB models, these relations become less accurate. Notice that the amplitude of the Doppler effect depends strongly on the epoch of last scattering. This is due to the presence of a cancellation scale $k\eta_* \sim 1$ as we shall now see.

7.1.4 Cancellation Damping

It is instructive to consider the spatial power spectrum of the radiation $k^3|\Theta + \Psi|_{rms}^2$ as well as the anisotropy spectrum. With the projection deconvolved, the physical processes are easier to understand. In fact, historically the above analysis was originally presented in k -space [94]. The photons illuminate a surface of thickness $\delta\eta$ of the source field, *i.e.* the line of sight electron velocity for the Doppler effect and the decaying potential for the ISW effect. For perturbations with wavelength smaller than the thickness, the observer sees through many crests and troughs if the wavevector is aligned parallel to the line of sight. Thus contributions will be severely cancelled for these modes (see Figs. 1.7 and 1.9). A loophole occurs however if the wavevector is aligned perpendicular to the line of sight. In this case, all the contributions are additive along the line of sight and cancellation does not occur. For an isotropic source field, the net effect after summing over both components is a suppression of power by $(k\delta\eta)^{-1}$ or approximately the inverse number of wavelengths across the fluctuation.

For the Doppler effect, the source field is not isotropic. Indeed, it is only the line of sight component of the velocity that contributes at all. In linear theory, the potential gradient $\nabla\Psi$ generates an infall velocity. Thus gravitationally induced flows are irrotational $\nabla \times \mathbf{v}(\mathbf{x}) = 0$ or $\mathbf{k} \times \mathbf{v}(\mathbf{k}) = 0$ and the velocity is parallel to the wavevector. The line of sight component of the electron velocity vanishes for the perpendicular mode. In this case, cancellation is much more severe. Only if the electron velocity or the probability of scattering changes across a wavelength do the redshifts and blueshifts from crests and troughs not entirely cancel. The contributing sources are of order \dot{V}_b/k and $V_b\dot{\tau}/\dot{\tau}$, as we have seen, and suppress the net effect by an additional $(k\delta\eta)^{-2}$ in power.

We can formalize these considerations by noting that equation (7.11) is approximately a Fourier transform in η whose transform pair is $k\mu$ (with k fixed). This implies the

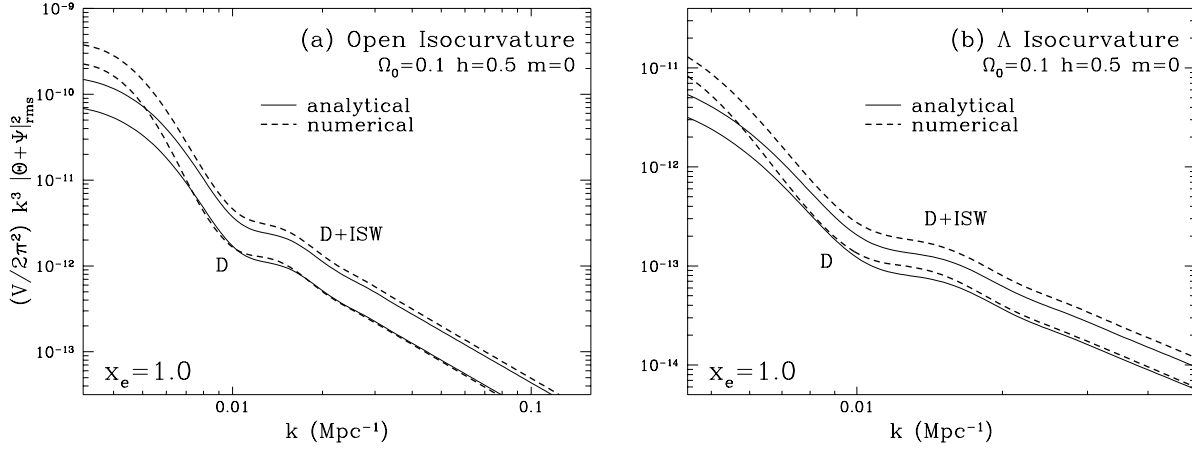


Figure 7.6: Cancellation Damping

If the wavelength is much smaller than the thickness of the surface upon which the anisotropy source lies, cancellation of contributions as the photon streams over many wavelengths of the perturbation will damp the effect. For the spatial power spectrum this implies mild cancellation of the late ISW effect and severe cancellation of the Doppler effect. The two can be comparable at small scales. For the Λ model however the projection carries the late ISW effect to larger angles where it is hidden by the Doppler effect in C_ℓ .

relation

$$k^2 \eta_0^3 \frac{[\Theta + \Psi](\eta_0, k, k\mu)}{\Delta_T(\eta_0, k)} \xrightarrow{\text{FT}} S_L(\eta), \quad (7.17)$$

where S_L is the linear theory source given by equation (7.16). Thus the two mean squares are related by Parseval's theorem,

$$\int_0^{\eta_0} S_L^2(\eta) d\eta \simeq \frac{1}{2\pi} k^4 \eta_0^6 P^{-1}(k) \int k d\mu |\Theta + \Psi|^2 \quad (7.18)$$

or rearranging the terms,

$$|\Theta + \Psi|_{rms}^2(\eta_0, k) \simeq \pi \frac{P(k)}{(k\eta_0)^5} \int_0^{\eta_0} S_L^2(\eta) d\eta / \eta_0. \quad (7.19)$$

where we have employed the relation $|\Theta + \Psi|_{rms}^2 = \frac{1}{2} \int_{-1}^1 d\mu |\Theta + \Psi|^2$.

All the terms in equation (7.19) are easy to understand. The velocity power spectrum is proportional to $P(k)/k^2$ and the potential power spectrum to $P(k)/k^4$. The Doppler term suffers cancellation in power by k^{-3} and the late ISW effect by k^{-1} . This brings the contribution to $P(k)/k^5$ for both effects and represents a significant small scale suppression compared with the matter fluctuations. In Fig. 7.6, we show an isocurvature baryon examples compared with the numerical results. Notice that the late ISW effect

can make a strong contribution to this *spatial* power spectrum even at small scales [80]. Equation (7.19) is slightly less accurate for the Λ late ISW effect since the potential is still decaying at the present and Parseval's theorem begins to break down because of the upper limit of the integral.

In fact, the radiation power spectrum can be approximated by taking a projection of real space onto angles

$$\frac{\ell(2\ell + 1)}{4\pi} C_\ell \simeq \frac{V}{2\pi^2} k_{\text{proj}}^3 |\Theta + \Psi|_{rms}^2(\eta_0, k_{\text{proj}}) \quad (7.20)$$

where $k_{\text{proj}} \simeq \ell/r_\theta(\eta_{\text{max}})$, η_{max} is the epoch when the source S_L peaks, and the angle-distance relation r_θ is given by equation (6.15). This is often useful for open universes where the radial eigenfunctions at high wavenumber are difficult to compute. However, one must be careful to separate component effects if S_L is bimodal. For example, since the Λ late ISW effect arises near the present time, spatial scales are carried to larger angles by the projection than for the Doppler contributions. In fact, even for the $\Omega_0 = 0.1$ Λ model, the late ISW effect is not visible in C_ℓ . This exhibits one of the dangers of naively working with spatial power spectra.

7.1.5 Minimal PIB Anisotropies

As an example of the regeneration of fluctuations through the Doppler effect, let us consider the open PIB model. It is particularly interesting to construct one with minimal anisotropies. We have seen that the steeply rising spectrum of anisotropies in this model can only be moderately mitigated by reionization because of the angle to distance relation in open universes. On the other hand, the lack of information about the initial spectrum near the curvature scale can be employed to evade the large angle constraint of §7.1.2. Degree scale anisotropies can alternately be employed to constrain the model. Since the observational state is still in flux, we shall limit ourselves to stating rules of thumb which may be useful to model builders in the future. For a concrete use of current data sets along these lines, see [81].

We might generalize the standard PIB model with a two dimensional parameterization of the ionization history involving both the ionization fraction x_e and the ionization redshift z_i . Since the fundamental scale for cancellation damping is the horizon at last scattering, anisotropies will depend sensitively on the epoch of last scattering. Raising the ionization fraction delays last scattering and makes the damping scale larger. By allowing

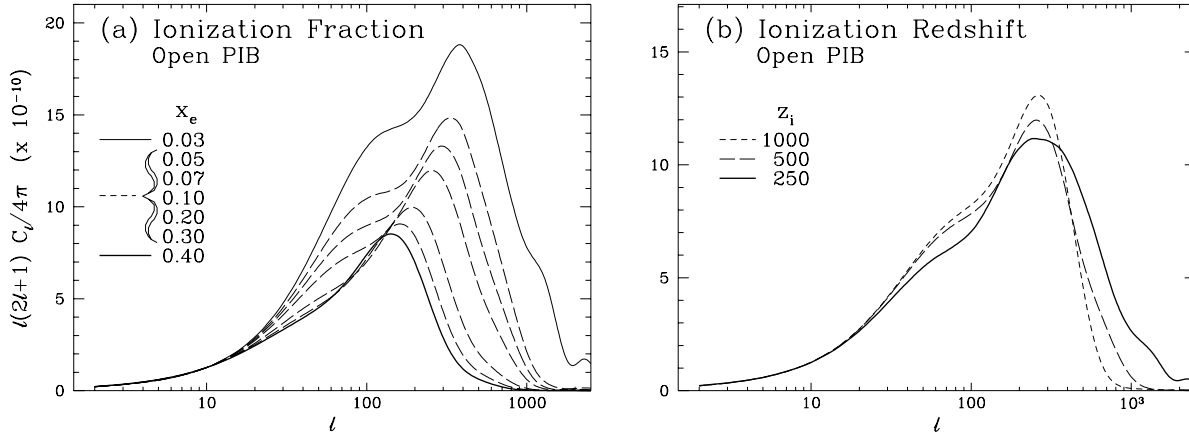


Figure 7.7: Minimal PIB Anisotropies

Two free parameters in the standard PIB model are the ionization fraction x_e and the ionization redshift z_i . (a) The ionization fraction, assumed to be constant after redshift $z_i = 500$, fixes the epoch of last scattering and the amount of cancellation damping. Aside from a small boost due to fluctuation growth, later last scattering always leads to smaller anisotropies. (b) The ionization redshift determines fluctuation growth before last scattering. Here $x_e = 0.1$. Adiabatic photon growth at large scales and baryon velocity growth at small scales yield opposite tendencies with z_i . The model here is open PIB with $\Omega_0 = 0.2$ $h = 0.5$ and $m = -0.5$. Ionization parameters are chosen to avoid Compton- y constraints.

more growth between the drag and last scattering epochs, it also increases the amplitude of velocity perturbations at last scattering. These two effects oppose each other but are not of equal magnitude: cancellation damping is more significant than growth (see Fig. 7.7). Thus minimal anisotropies will occur for maximal ionization fraction x_e .

The ionization redshift has a more complicated effect. Before reionization, fluctuations can grow in pressureless linear theory. Thus the baryon velocity and correspondingly the Doppler effect will be lowest for the latest reionization. However, at scales near to and above the horizon at last scattering, adiabatic growth of the temperature fluctuation dominates (see §5.1). For these scales, the latest reionization that still permits significant optical depth between recombination and the present minimizes fluctuations (see Fig. 7.7). Since PIB models must have high optical depth $\tau \gtrsim 3$ between recombination and the present to damp the large primary fluctuations [81], the ionization redshift must be significantly before last scattering. However, it must also be low enough to avoid Compton- y constraints. These constraints together with degree scale anisotropy and large scale structure observations will make PIB model building a real challenge in the future.

7.2 Second Order Contributions

The severe but in some sense “accidental” cancellation of the linear effect for reionized scenarios leads to the possibility that higher order effects may dominate sub-degree scale anisotropies. In this section, we will consider anisotropy generation to second order in perturbation theory [82, 46]. The fundamental equations and concepts necessary to understand these effects have already been discussed in §2.2.2. Applying them to the case of reionized models, we find that one source, the so-called Vishniac term [121, 169], dominates over all other contributions.

7.2.1 Generalized Doppler Effect

As we have seen, cancellation is a geometric effect and its severity for the Doppler effect is due irrotational nature of flows in linear theory. All modes except those for which \mathbf{k} is perpendicular to the line of sight are cancelled as the photon streams through many wavelengths of the perturbation to the observer. However for the Doppler effect, only the parallel component of the electron velocity yields an effect. Thus, for irrotational flows $\mathbf{v}_b \parallel \mathbf{k}$, Doppler contributions are severely suppressed. Note however that the full Doppler source is in fact $\dot{\tau} \mathbf{v}_b$, where recall $\dot{\tau} = x_e n_e \sigma_T a / a_0$, since the probability of scattering must be factored in. A photon is more likely to scatter in regions of high density or ionization. Thus perturbations in x_e and n_e will change the Doppler source. The effective velocity is therefore

$$\begin{aligned} \mathbf{q}(\mathbf{x}) &= [1 + \delta n_e(\mathbf{x})/n_e][1 + \delta x_e(\mathbf{x})/x_e] \mathbf{v}_b(\mathbf{x}) \\ &= [1 + \Delta_b(\mathbf{x})][1 + \delta x_e(\mathbf{x})/x_e] \mathbf{v}_b(\mathbf{x}). \end{aligned} \quad (7.21)$$

If fluctuations in the electron density or ionization are small, the additional contributions will be of second order. They can however escape the severe cancellation of the first order term. For example, there could be a large scale bulk flow $\mathbf{v}_b(k_1)$ with $\mathbf{k}_1 \parallel \boldsymbol{\gamma}$ and a small scale density fluctuation $\Delta_b(k_2)$ with $\mathbf{k}_2 \perp \boldsymbol{\gamma}$. In this case, scattering will induce a small scale temperature fluctuations perpendicular to the line of sight since more photons will have been scattered in the overdense regions (see Fig. 1.10). In the extreme limit of high density fluctuations, this is the kinetic Sunyaev-Zel’dovich effect for clusters (see §7.3 and [162]).

The solution of equation (7.4) can be generalized to

$$[\Theta + \Psi](\eta_0, \mathbf{k}, \boldsymbol{\gamma}) = \int_{\eta_a}^{\eta_0} \dot{\tau} e^{-\tau(\eta, \eta_0)} \boldsymbol{\gamma} \cdot \mathbf{q} e^{ik\mu(\eta - \eta_0)} d\eta. \quad (7.22)$$

We have neglected the feedback term into the temperature fluctuation at last scattering since it is suppressed by the optical depth through a wavelength. Following Vishniac [169], let us decompose the solution into multipole moments,

$$[\Theta + \Psi](\eta_0, \mathbf{k}, \boldsymbol{\gamma}) = \sum_{\ell, m} a_{\ell m}(\mathbf{k}) Y_{\ell m}(\Omega), \quad (7.23)$$

so that

$$|a_{\ell m}|^2 = \left| \int d\Omega Y_{\ell m}(\Omega) \int_0^{\eta_0} \dot{\tau} e^{-\tau(\eta, \eta_0)} (\boldsymbol{\gamma} \cdot \mathbf{q}) e^{ik\mu(\eta - \eta_0)} \right|^2. \quad (7.24)$$

Since the final result after summing over \mathbf{k} modes has no preferred direction, let us average over m such that $|a_\ell|^2 = \frac{1}{2\ell+1} \sum_m |a_{\ell m}|^2$, which corresponds to $|a_\ell|^2 = 4\pi |\Theta_\ell / (2\ell + 1)|^2$. Choosing $\hat{\mathbf{z}} \parallel \mathbf{k}$, we note that the azimuthal angle dependence separates out components of \mathbf{q} parallel and perpendicular to \mathbf{k} by employing the angular addition formula

$$\begin{aligned} \frac{4\pi}{2\ell + 1} \sum_m Y_{\ell m}^*(\theta, \phi) Y_{\ell m}(\theta', \phi') &= P_\ell(\cos\theta) P_\ell(\cos\theta') \\ &+ 2 \sum_m \frac{(\ell - m)!}{(\ell + m)!} P_\ell^m(\cos\theta) P_\ell^m(\cos\theta') \cos[m(\phi - \phi')]. \end{aligned} \quad (7.25)$$

Since $\boldsymbol{\gamma} \cdot \mathbf{q} = \cos\phi \sin\theta q_\perp + \cos\theta q_\parallel$, the cross terms between the two components vanish after integrating over azimuthal angles. The two contributions add in quadrature and may be considered as separate effects.

We have already noted that the $\mathbf{q} \parallel \mathbf{k}$ term is strongly suppressed by cancellation. Thus let us calculate the perpendicular component,

$$|a_\ell(k)|^2 = \frac{\pi}{2\ell(\ell + 1)} \left| \int_{-1}^1 d\mu P_\ell^1(1 - \mu^2)^{1/2} \int_0^{\eta_0} d\eta \dot{\tau} e^{-\tau(\eta, \eta_0)} q_\perp e^{ik\mu(\eta - \eta_0)} \right|^2. \quad (7.26)$$

The μ integral can be performed with the following identity

$$\int_{-1}^1 d\mu (1 - \mu^2)^{1/2} P_\ell^1(\mu) e^{iq\mu} = -2\ell(\ell + 1) (-i)^{-\ell+1} j_\ell(q)/q, \quad (7.27)$$

so that

$$|a_\ell(k)|^2 = 2\pi\ell(\ell + 1) \left| \int_0^{\eta_0} d\eta \dot{\tau} e^{-\tau(\eta, \eta_0)} q_\perp \frac{j_\ell(k\Delta\eta)}{k\Delta\eta} \right|^2, \quad (7.28)$$

where $\Delta\eta = \eta_0 - \eta$. Notice that this has a simple physical interpretation. We know from the spherical decomposition that a plane wave perturbation projects onto the shell at

distance $\Delta\eta$ as $j_\ell(k\Delta\eta)$. If the amplitude of the plane wave has an angular dependence, the projection is modified. In particular, the perpendicular component suffers less projection aliasing (see Fig. 1.7) and thus the higher oscillations are damped as $\eta/k\Delta\eta$.

7.2.2 Vishniac Effect

The Vishniac effect [121, 169] is the second order Doppler effect due to the density enhancement $n_e(\mathbf{x}) = \bar{n}_e[1 + \Delta_b(\mathbf{x})]$ in linear theory, *i.e.* $\mathbf{q}(\mathbf{x}) = [1 + \Delta(\mathbf{x})]\mathbf{v}_b(\mathbf{x})$ to second order. The convolution theorem tells us that

$$\mathbf{q}_\perp(\mathbf{k}) = \left(I - \frac{\mathbf{k}\mathbf{k}}{k^2}\right) \frac{1}{2} \sum_{\mathbf{k}'} \mathbf{v}_b(\mathbf{k}') \Delta_b(|\mathbf{k} - \mathbf{k}'|) + \mathbf{v}_b(\mathbf{k} - \mathbf{k}') \Delta_b(k'). \quad (7.29)$$

Taking the ensemble average of the fluctuation and assuming random phases for the underlying linear theory perturbations, we obtain

$$\langle q_\perp^*(k, \eta) q_\perp(k, \eta') \rangle = \frac{1}{2} \dot{D}(\eta) D(\eta) \dot{D}(\eta') D(\eta') \sum_{k'} d^2 P(k') P(|\mathbf{k} - \mathbf{k}'|), \quad (7.30)$$

where the projected vector

$$\mathbf{d} \equiv \left(I - \frac{\mathbf{k}\mathbf{k}}{k^2}\right) \left[\frac{\mathbf{k}'}{k^2} + \frac{\mathbf{k} - \mathbf{k}'}{|\mathbf{k} - \mathbf{k}'|^2}\right]. \quad (7.31)$$

A bit of straightforward but tedious algebra yields

$$\langle |a_\ell(k)|^2 \rangle = \frac{1}{4\pi} \frac{V}{\eta_0^3} \frac{\ell(\ell+1)}{k\eta_0} M_V(k) I_\ell^2(k) P^2(k), \quad (7.32)$$

where the mode-coupling integral is

$$M_V(k) = \int_0^\infty dy \int_{-1}^1 d(\cos\theta) \frac{(1 - \cos^2\theta)(1 - 2y\cos\theta)^2}{(1 + y^2 - 2y\cos\theta)^2} \frac{P[k(1 + y^2 - 2y\cos\theta)^{1/2}]}{P(k)} \frac{P(ky)}{P(k)}, \quad (7.33)$$

and the time integral is

$$\begin{aligned} I_\ell(k) &= \int_0^{\eta_0} \frac{d\eta}{\eta_0} S_V(\eta) j_\ell(k\Delta\eta) \\ &\simeq \sqrt{\frac{\pi}{2\ell}} \frac{1}{k\eta_0} S_V(\eta_0 - \ell/k), \end{aligned} \quad (7.34)$$

with

$$S_V(\eta) = \frac{\dot{D}}{D_0} \frac{D}{D_0} \frac{\eta_0^3}{\eta_0 - \eta} \dot{\tau} e^{-\tau}. \quad (7.35)$$

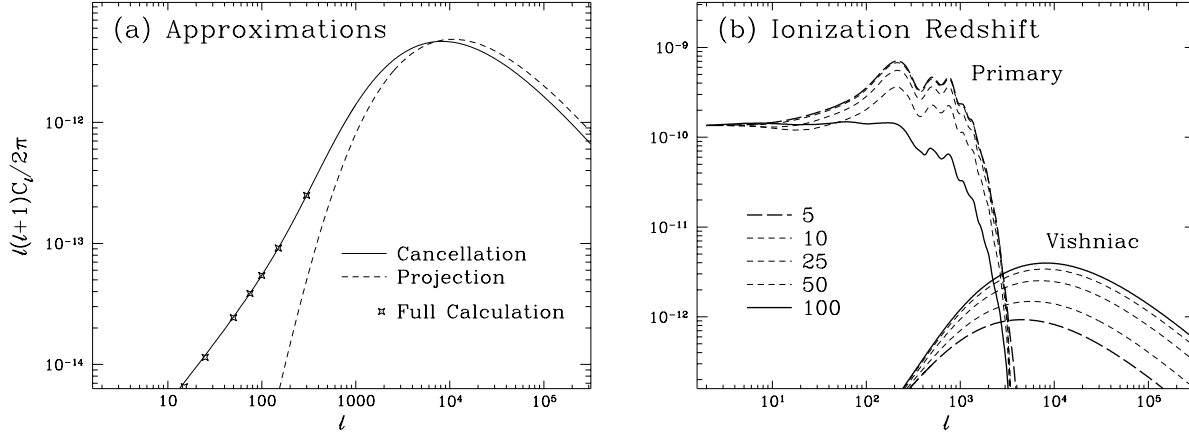


Figure 7.8: Vishniac Effect

The model is standard CDM $\Omega_0 = 1$, $\Omega_b = 0.05$, $h = 0.5$ with a quadrupole normalization to *COBE* of $20\mu\text{K}$. (a) The cancellation approximation to the Vishniac source is excellent. Calculations in k space projected onto angles underestimates the coherence angle of the Vishniac effect if fluctuations are all considered to come from last scattering $\eta_{max} = \eta_*$ in equation (7.20). (b) The Vishniac effect originates mainly after last scattering. Therefore even if the optical depth is as low as its Gunn-Peterson minimal value $z_i \simeq 5$, the Vishniac effect contributes a significant fraction of its total. Both primary anisotropies and the Vishniac effect may be present in the spectrum.

The random phase assumption for the underlying linear perturbations assures us that there are no cross terms between first and second order contributions or different k modes. Thus total anisotropy is obtained by integrating over all k modes [86],

$$\begin{aligned}
 C_\ell^V &= \frac{V}{2\pi^2} \int \frac{dk}{k} k^3 \langle |a_\ell(k)|^2 \rangle \\
 &= \frac{\ell(\ell+1)V^2}{(2\pi)^3 \eta_0^6} \int \frac{dk}{k} (k\eta_0)^2 M_V(k) I_\ell^2(k) P^2(k) \\
 &\simeq \frac{\ell}{(4\pi)^2} \frac{V^2}{\eta_0^6} \int \frac{dk}{k} M_V(k) S_V^2(\eta_0 - \ell/k) P^2(k).
 \end{aligned} \tag{7.36}$$

In Fig. 7.8, we plot the Vishniac effect for standard CDM. Notice that since S_V^2 depends on the amplitude of fluctuations to the fourth power, contributions are highly weighted toward late times and allows extremely small scales to contribute to observable anisotropies. Thus even with minimal ionization of $z_i = 5$, for which primary anisotropies are only damped at the percent level, the Vishniac effect can dominate the anisotropy at small scales.

Again it is useful to consider the k -space power spectrum. Employing the same

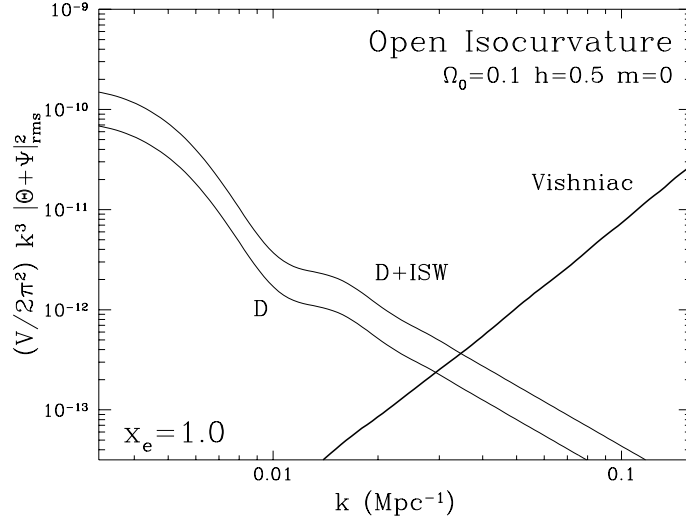


Figure 7.9: PIB Vishniac Power Spectrum

Analytic k space power spectrum calculation of the Vishniac effect in a PIB model. Vishniac contributions dominate over first order effects at small scales. For this steeply small scale weighted $m = 0$ spectrum, high k modes can contribute to lower ℓ modes that one would naively think. A full non-linear calculation is needed to account for these high k contributions.

Parseval approximation as for the first order contribution, we obtain

$$|\Theta + \Psi|^2 = \frac{V}{\eta_0^3} \frac{P^2(k)}{16\pi} M_V(k) \int_0^{\eta_0} (1 - \eta/\eta_0)^2 S_V^2(\eta) d\eta/\eta_0, \quad (7.37)$$

where the extra factor $1 - \eta/\eta_0$ in the integrand is due to the projection effect for the perpendicular mode. The k factors come from weak cancellation of $(k\delta\eta)^{-1}$, the continuity equation conversion of velocity to density $(k\eta)^{-2}$, and the volume in k available for mode coupling k^3 . Although the exact nature of the mode coupling integral can change the scaling, this simple power counting implies that the Vishniac effect will have more power at small scales than the cancelled first order contribution.

The k -space power spectrum has often been used in the past to estimate the anisotropy through a distance to angle conversion such as equation (7.20). The common assumption is that the Vishniac effect projects as if it all arises from the last scattering surface [50, 82, 46]. Given the strong weighting toward late times, this significantly underestimates its coherence scale (see Fig. 7.8a). The magnitude of this misestimation increases with the amount of small scale power in the model. Take for example, a PIB model with a steeply blue $m = 0$ spectrum (see Fig. 7.9). In this case, the k space power keeps on rising

to small scales. When this is projected onto ℓ space, it predicts a divergent anisotropy. Of course, second order theory breaks down as the fluctuation amplitude becomes comparable to unity so that the real spectrum would not continue to rise indefinitely. By inserting a cut-off at the non-linear scale, the anisotropy predicted by equation (7.36) or power projection is finite. However, to calculate the effect precisely, one needs to go to N -body simulations to accurately track the non-linear evolution.

7.2.3 Other Second Order Effects

It is by no means obvious that the Vishniac effect dominates over all other second order sources. It is therefore worthwhile to consider the general Boltzmann equation to second order [82]. Indeed spatial variations in the ionization fraction $\delta x_e(\mathbf{x})$ from patchy reionization can have an effect comparable to the Vishniac source. However because it is strongly dependent on the model for structure formation and reionization, it is beyond the scope of this discussion.

The second order Boltzmann equation is obtained by integrating the sources calculated in §2.2.2 over frequency and is given in real space by

$$\dot{\Theta} + \dot{\Psi} + \gamma^i \partial_i (\Theta + \Psi) = \dot{\tau} (1 + \Delta_b) \left[\Theta_0 + \Psi - \Theta + \gamma_i v_b^i - v_b^2 + 7(\gamma_i v_b^i)^2 \right] \quad (7.38)$$

$$+ 2\dot{\Psi} + \mathcal{O}([\Theta_0 - \Theta]v_b)], \quad (7.39)$$

where we have again neglected the small correction to the quadrupole [82]. We also assume that the ionization is uniform. Aside from the $\mathcal{O}(\Delta_b v_b)$ Vishniac contribution, there are several new terms to consider here.

$\mathcal{O}(v_b^2)$ Quadratic Doppler Effect

The kinetic energy of the electrons can be transferred to the photons in a manner identical to the thermal energy transfer of the Sunyaev-Zel'dovich effect (see §2.2.2 and §7.3). Spatial variations in the kinetic energy cause of order v_b^2 anisotropies in the CMB. Note that these anisotropies carry spectral distortions of the Compton- y just as their thermal counterpart.

These fluctuations do not suffer the drastic cancellation of the linear Doppler effect since the energy is direction independent. At small scales, the power is reduced by a factor $(k\delta\eta)^{-1}$ like the late ISW and Vishniac effect. Counting powers in k , we expect that aside

from a spectrum-dependent mode-coupling integral, the contribution will consist of $(k\delta\eta)^{-1}$ from cancellation, $(k\eta)^{-4}$ from the velocity to density conversion, and k^3 for the volume available to mode coupling. This gives a total of k^{-2} and implies that the Vishniac effect should be more important at small scales.

The Parseval approximation to the power spectrum confirms this scaling relation,

$$|\Theta + \Psi|_{rms}^2 = \frac{1}{32\pi} \frac{V}{\eta_0^3} \frac{1}{(k\eta_0)^2} M_Q(k) P^2(k) \int_0^{\eta_0} S_Q^2(\eta) d\eta / \eta_0, \quad (7.40)$$

where the mode-coupling integral is

$$M_Q(k) = \int_0^\infty dy \int_{-1}^{+1} d(\cos\theta) \frac{(y - \cos\theta)^2 - 7(1 - \cos^2\theta)(y - \cos\theta)y + \frac{147}{8}(1 - \cos^2\theta)^2 y^2}{(1 + y^2 - 2y \cos\theta)^2} \\ \times \frac{P[k(1 + y^2 - 2y \cos\theta)^{1/2}]}{P[k]} \frac{P[ky]}{P[k]}, \quad (7.41)$$

and the source is

$$S_Q(\eta) = \frac{\dot{D}}{D_0} \frac{\dot{D}}{D_0} \dot{\tau} e^{-\tau(\eta, \eta_0)} \eta_0^3. \quad (7.42)$$

Therefore, unless the mode-coupling integral behaves much differently than its Vishniac counterpart, this contribution will be small in comparison. In Fig. 7.10, we show a comparison for the CDM model. Note that since the quadratic Doppler effect carries a spectral distortion of $(\Delta T/T)_{RJ} = -2y$, we have multiplied the power by a factor of 4 to correspond to the case where the Raleigh-Jeans temperature is measured. The quadratic Doppler effect is never dominant in this model.

$\mathcal{O}([\Theta_0 - \Theta]v_b)$ Quadratic Doppler Suppression

As discussed in §2.2.2, the quadratic Doppler effect ceases to operate once the photons are isotropic in the baryon rest frame. If the optical depth within a coherence scale of the baryon velocity $\mathbf{v}_b(\mathbf{x})$ is high, then the CMB will possess a dipole $\Theta - \Theta_0$ of exactly $\mathbf{v}_b(\mathbf{x})$. This will cancel any further contributions from the quadratic Doppler effect. However, in the small scale diffusion limit, by definition the optical depth never reaches unity in a coherence scale. The critical division is the horizon scale at optical depth unity, *i.e.* last scattering. In the mode-coupling integral, if the source of the contributions arise from larger wavelengths than this, they will be cancelled by the $\mathcal{O}([\Theta_0 - \Theta]v_b)$ term. This can only make the small quadratic Doppler contribution even smaller.

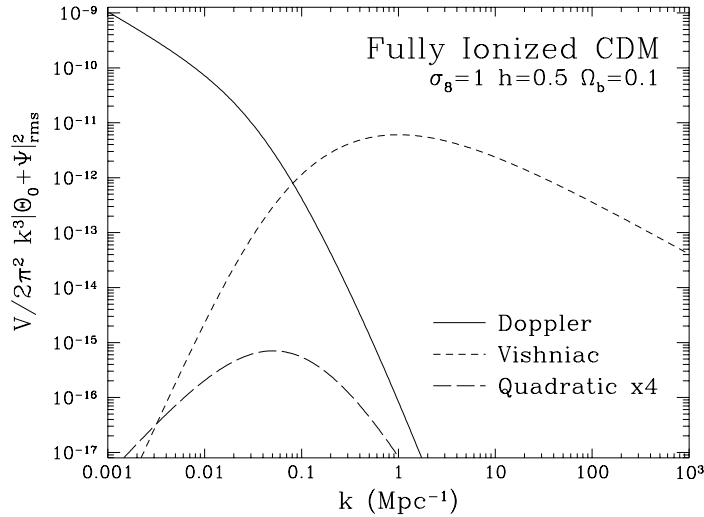


Figure 7.10: Quadratic Doppler Effect

Spatial power spectrum of the CMB for the first order Doppler, Vishniac and quadratic Doppler effects in a CDM model. The quadratic effect is multiplied by 4 to account for the spectral distortion in the Rayleigh-Jeans regime but never dominates.

$\mathcal{O}([\Theta_0 - \Theta]\Delta_b)$ Vishniac Suppression

The same suppression mechanism works for the Vishniac effect. Recall that the Vishniac effect arises since small scale overdensities can possess bulk velocities along the line of sight. The increased probability of scattering off overdense regions causes a small scale temperature variation from the Doppler shift. If the optical depth across the coherence scale of the bulk velocity is high, then all the photons will have scattered. Since further scattering does not affect the distribution, the increased probability of rescattering in overdense regions has no effect. In other words, a dipole $\Theta - \Theta_0$ has already been generated, such that the $\mathcal{O}([\Theta - \Theta_0]\Delta_b)$ term exactly cancels with the Vishniac $v_b\Delta_b$ term. Again one must check whether the Vishniac effect arises from bulk flows smaller or larger than the horizon at last scattering. By inserting cutoffs in the mode coupling integral equation (7.33), one can show that they arise from smaller scales for the range of power law spectra usually considered in the CDM and PIB models.

Mixed Order Terms

It is possible that first and third order terms couple in the rms. We have shown that the parallel and perpendicular components of the Doppler effect separate and add in

quadrature for C_ℓ (see [82] for the k -space proof). Since the first order contribution only possesses a parallel part, the mixed effect will only couple with the parallel third order term. However, this term is again severely suppressed by cancellation. The mixed order Doppler effect can therefore be entirely ignored.

7.3 Beyond Perturbation Theory: A Survey

To acknowledge, mark out, study, assess,

Divide, discriminate, compete, and dispute.

These are our eight powers.

What is outside the cosmos, acknowledge but do not study.

What is within the cosmos, study but do not assess

What is a matter of record, assess but do not dispute.

–Chuang-tzu, 2

Beyond the realm of linear calculations lies a plethora of higher order effects that are highly sensitive to assumptions about structure formation. Modeling and N-body simulations are needed to estimate their effects. Consequently, a full study of these individual effects is beyond the scope of this chapter. Instead, we survey the literature on these subjects and provide order of magnitude estimates where possible. Most of these effects are small in the degree to arcminute regime where one hopes that primary anisotropies will yield important cosmological information. Others such as the cluster Sunyaev-Zel'dovich effect and foreground sources in the galaxy may be filtered out by spectral information and object identification.

Cluster Sunyaev-Zel'dovich Effect

As pointed out by Sunyaev and Zel'dovich [162] clusters can induce anisotropies in the CMB from Compton scattering off electrons in the hot cluster medium. These hot electrons transfer energy to the CMB, leading to temperature anisotropies *and* spectral distortions in the CMB (see §3.2.1). The frequency dependence can be used to separate its signal from the primary anisotropy.

For a typical cluster of $T_e \simeq 1-10\text{keV}$ and a typical optical depth of $\tau \simeq 0.1-0.01$, the effect is of order $(\Delta T/T)_{RJ} = -2y \simeq 10^{-5} - 10^{-3}$. Of course, the rms fluctuation on a random patch of the sky will be much lower than this. Much effort has been expended to estimate the fluctuations caused by the SZ effect with varying results (e.g. [114, 112, 7, 33]).

Recently, empirical modelling of clusters has shown that the anisotropy at arcminutes is on the order of $(\Delta T/T)_{RJ} \lesssim 10^{-7}$ [27]. Moreover, the signal is in large part due to bright and easily identifiable clusters. If such known clusters are removed from the sample, the anisotropy drops to an entirely negligible level.

The peculiar velocity of a cluster also produces anisotropies via a Doppler shift of the scattered photons. This is the non-linear analogue of the Vishniac and patchy reionization effects. This process leads to no spectral distortions to first order and yields a true temperature fluctuation of $\Delta T/T = \mathcal{O}(\tau_c v_c)$ for an individual cluster, where the optical depth through the cluster is typically of order $\tau_c \simeq 0.1 - 0.01$ and its peculiar velocity $v_p \simeq \text{few} \times 10^{-3}$. Again there is hope that the signal can be removed by identifying bright clusters and perhaps even the thermal effect.

Rees-Sciama effect

Higher order corrections to the density evolution cause time dependence in the gravitational potentials from the Poisson equation. As pointed out by Rees & Sciama [136], this can cause a late ISW effect even in an $\Omega_0 = 1$ universe. The second order contribution has been shown to be negligibly small [115]. One can understand this by simple scaling arguments. Just as the first order late ISW contribution, this term suffers cancellation in power by $(k\delta\eta)^{-1}$ where $\delta\eta$ is now the time scale for change in the potential. The Poisson equation relates potentials to densities via a factor $(k\eta)^{-4}$ and the mode coupling volume factor yields k^3 . Thus the effect scales as $k^{-2}P(k)$ and will be small in comparison to even the minimal Vishniac effect if the mode coupling integrals behave similarly.

The fully non-linear case has been estimated using N-body simulations and power spectrum techniques [149]. In the standard CDM model, non-linear contributions dominate over the primary fluctuations only at $\ell \gtrsim 5000$ and are thus smaller than the minimal Vishniac effect. Ray tracing techniques corroborate these results by showing that fluctuations are at the 10^{-7} level at degree scales [167].

Gravitational Lensing

The presence of potential fluctuations gravitationally lenses the CMB and changes the projection of temperature inhomogeneities into anisotropies. Lensing neither generates or erases power but merely redistributes it in angles. The magnitude and sense of the effect

is somewhat dependent on the model for structure formation, including the assumptions for non-linear clustering. This has led to some seemingly inconsistent results in the literature (e.g. [14, 34, 143, 166, 108]). Recently Seljak [148] has shown that for CDM, and indeed most realistic scenarios of structure formation, the effect is small above the arcminute scales and above. At arcminute scales, it smooths out features such as the acoustic peaks at the few percent level in power.

Galactic Foreground Contamination

Though not a part of the cosmic microwave *background*, galactic foreground contamination contributes to anisotropies at microwave frequencies. This may make the extraction of information from the primary signal extremely difficult at small angular scales. Typical sources such as synchrotron, bremsstrahlung and dust emission can be identified by their spectral signature with multifrequency experiments (see *e.g.* [19, 9]). Near 100 GHz, one expects that synchrotron and bremsstrahlung will have already died away, whereas dust has not yet reached its peak. However, a sensitivity in the $\Delta T/T \lesssim 10^{-6}$ range will be necessary to extract some of the information encoded in the primary signal (see Appendix A.3). It may be however that even with full sky coverage from the next generation of satellite experiments only a small fraction containing the clean patches will be useful for observing the structure of primary anisotropies at this level. Clearly further work is needed on this important subject, but it may be that we will only know the full story once the next generation of CMB satellites have flown and taken data.

7.4 Final Thoughts

What goes on being hateful about analysis is that it implies that the analyzed is a completed set. The reason why completion goes on being hateful is that it implies everything can be a completed set.

–Chuang-tzu, 23

We have endeavored to cover all of the major sources of primary and secondary anisotropies in the CMB known to date. Still, there is no doubt that nature will continue to surprise us with the unexpected. In the end, despite the theory developed here, the ultimate answers can only be obtained through observations. Currently, several groups are testing long duration balloon flights in the hope that they will be able to measure anisotropies across a substantial fraction of the sky at degree resolutions. The experimental challenge to

eliminate atmospheric noise and sidelobe contamination is formidable (see *e.g.* [178]). Space based missions, for which these problems can be avoided, are now under consideration. A mission of this kind can essentially obtain cosmic variance limited measurements of the anisotropy spectrum down to ten arcminutes with a wide frequency coverage. With such data, one can realistically hope to measure all the classical cosmological parameters, the curvature K , the matter content $\Omega_0 h^2$, the cosmological constant Ω_Λ , the baryon content $\Omega_b h^2$ and possibly even the gravitational wave background and neutrino mass (see Appendix A.3.3 and A.3.4). The frequency coverage could allow measurements of the thermal SZ effect in a large number of clusters and yield a calibration of the distance scale and so measure the expansion rate h itself (see *e.g.* [13]). Combined with large scale structure measurements, the anisotropy data would provide important information on the model for structure formation as well as consistency tests for the gravitational instability scenario itself. Perhaps even more exciting is the chance that new phenomena, either cosmological or astrophysical, will be detected with all sky maps in the new frequency bands. Until such a mission flies, we can only guess at the possibilities.

Rather than go toward what suits you, laugh. Rather than acknowledge it with your laughter, shove it from you. Shove it from you and leave the transformation behind, then you will enter the unity of the featureless sky.

—Chuang-tzu, 6

Appendix A

Toward Higher Accuracy: A CDM Example

The scale invariant cold dark matter (CDM) model with $\Omega_0 = 1.0$ and $\Omega_b h^2$ near the nucleosynthesis value $\Omega_b h^2 \simeq 0.01 - 0.02$ is elegantly simple and succeeds in explaining the gross features of both anisotropies in the CMB and large scale structure formation. It is therefore of value to study this model more closely. We will here refine our understanding of primary anisotropy formation first to the 5% level down to a fraction of a degree. It is possible and instructive to carry out this task through analytic construction. We then embark on the quest of obtaining 1% accurate results through the arcminute scale by considering the numerical calculation of subtle effects. This treatment should serve as an example of the types of consideration necessary for accurate predictions in the general case.

Aside from the coupling to the baryons, photons only experience gravitational effects from the other matter components. Primary anisotropy formation therefore depends sensitively on two quantities

1. The evolution of the metric perturbations.
2. The decoupling of the photons from the baryons.

We must therefore refine our understanding of both. As for the metric perturbations Ψ and Φ , there are two modifications we must make to the analysis of §5.1 and §5.2. At large scales we must include the anisotropic stress contribution of the neutrinos. Anisotropic stress

serves to differentiate the Newtonian potential Ψ from the space curvature perturbation Φ . As we have seen in §6, they are both important in anisotropy formation. At small scales, we must be able to describe accurately the pressure feedback effects from the radiation onto the potentials. This in turn leads to some sensitivity to neutrino masses in the eV range. Finally, tensor metric perturbations, *i.e.* gravity waves, can also produce gravitational redshifts and dilation in the CMB. Depending on the exact inflationary model, they can perhaps be significant at large scales but are almost certainly small perturbations to the scalar spectrum near the acoustic peaks. We shall quantify this statement in section A.3.3.

We must also improve our understanding of recombination over the equilibrium Saha treatment presented in §6.3.4. Last scattering is delayed due to the high opacity to recombination photons which keep the plasma ionized [123, 183]. This delay increases the diffusion length and thus is responsible for further damping of anisotropies. Following the population of the first excited state of hydrogen allows analytic construction of the anisotropies to 5% through to the damping scale. Subtle effects can change the damping scale at the several percent level. Polarization feedback weakens photon-baryon coupling by generating viscosity, *i.e.* a quadrupole moment in the photons. Helium ionization decreases the diffusion length before helium recombination. It is quite possible that other subtle effects change the damping tail at a comparable or even greater level. We offer these two considerations only as examples of the care that is required to obtain 1% accurate primary anisotropies under the damping scale.

A.1 Refining the Gravitational Potentials

A.1.1 Neutrino Anisotropic Stress

The solution for the gravitational potentials given by equation (5.11) must be corrected for the anisotropic stress Π_T . Recall that the anisotropic stress is related to the quadrupole moments of the radiation via equation (4.55), *i.e.*

$$p_T \Pi_T = \frac{12}{5} (p_\gamma \Theta_2 + p_\nu N_2). \quad (\text{A.1})$$

Due to the isotropizing effects of scattering, the anisotropic stress of the photons is negligibly small before recombination. Hence the main contribution to Π_T comes from the neutrino quadrupole anisotropy N_2 .

We can take it into account perturbatively. Specifically, we use the exact zeroth order growing and decaying solutions (5.11) to obtain the anisotropic stress. We then take this solution to iteratively correct for anisotropic stress in the evolution equation (5.6). If we neglect higher order multipole components, which is reasonable for superhorizon sized modes, the second moment of the Boltzmann equation (4.54) for the neutrinos becomes

$$\dot{N}_2 = \frac{2}{3}kN_1 \simeq \frac{2}{3}kV_T, \quad (\text{A.2})$$

where recall from §5.1.1 that all fluid velocities are equal above the horizon *i.e.* $N_1 \equiv V_\nu \simeq V_T$.

The exact zeroth order solution for V_T is found by substituting the growing mode solution equation (5.11) into the continuity equation (5.24). If the zeroth order solution is denoted $\Delta_T = C_G U_G$, then the solution to equation (A.2) is

$$\bar{N}_2(a)/C_G \simeq 2 \int_0^a \frac{da'}{a'} \frac{1}{3a'+4} \left(U_G - (a'+1)a' \frac{dU_G}{da'} \right), \quad (\text{A.3})$$

where recall that $3w_T = 1/(1+a)$ with a normalized at equality. The overbar represents the superhorizon solution since pressure growth suppression inside the horizon must be taken into account (see §A.1.2). Although it is possible to analytically integrate equation (A.3), the expression is cumbersome. Instead, we can employ an approximate solution which is exact in the limit $a \ll 1$ and $a \gg 1$,

$$\bar{N}_2(a)/C_G = -\frac{1}{10} \frac{20a+19}{3a+4} U_G - \frac{8}{3} \frac{a}{3a+4} + \frac{8}{9} \ln \left(\frac{3a+4}{4} \right). \quad (\text{A.4})$$

We have checked that this approximation works quite well by comparing it to equation (A.3) and the full numerical solution.

Next, we employ the above solution for \bar{N}_2 in equations (5.6). These two first order equations may be rewritten as one second order equation for Δ_T . The particular solution including the source terms Π_T and $\dot{\Pi}_T$ can be obtained from the homogeneous solutions U_G and U_D by Green's method,

$$\bar{\Delta}_T(a)/C_G = \left(1 + \frac{2}{5}f_\nu \right) U_G(a) + \frac{2}{5}f_\nu [I_1(a)U_G(a) + I_2(a)U_D(a)], \quad (\text{A.5})$$

where $I_1(a) = \int_0^a da' F_\nu(a')U_D(a')$, $I_2(a) = \int_0^a da' F_\nu(a')U_G(a')$,

$$F_\nu(a) = \frac{24}{5} \frac{(a+1)^{5/2}}{a^2(3a+4)} \left\{ \frac{2a}{3a+4} \frac{d}{da} U_G(a) - \frac{2}{(3a+4)(a+1)} U_G(a) \right. \\ \left. + \left[\frac{1}{(a+1)^2} - \frac{2}{a+1} + \frac{12}{3a+4} \right] \bar{N}_2(a)/C_G \right\}, \quad (\text{A.6})$$

and recall f_ν is the ratio of neutrino to total radiation density $f_\nu \equiv \rho_\nu/(\rho_\nu + \rho_\gamma)$. If we assume three massless neutrinos and the standard thermal history, $\rho_\nu/\rho_\gamma = 3(7/4)(4/11)^{4/3}/2 = 0.68$, *i.e.* $f_\nu = 0.405$. The first term in equation (A.5) comes from the initial conditions for Δ_T which can be iteratively established by employing equation (A.2) in (5.6). All terms which are proportional to f_ν in the equation (A.5) come from equation (A.1) since the anisotropic stress $\Pi_T \simeq (12/5)f_\nu N_2$. The asymptotic behavior of equation (A.5) is

$$\bar{\Delta}_T(a) \rightarrow \begin{cases} \left(1 + \frac{2}{5}f_\nu\right) C_G U_G(a) & (a \ll 1) \\ \left(1 + \frac{4}{15}f_\nu\right) C_G U_G(a). & (a \gg 1) \end{cases} \quad (\text{A.7})$$

Here we have used the fact that if $a \gg 1$, the decaying term $I_2 U_D$ may be ignored and $I_1 \rightarrow -\frac{1}{3}$ approximately.

Therefore we may obtain a simple approximate expression for the large scale density fluctuations,

$$\bar{\Delta}_T(a) \simeq \left[1 + \frac{2}{5}f_\nu \left(1 - \frac{1}{3} \frac{a}{a+1}\right)\right] C_G U_G(a). \quad (\text{A.8})$$

Again we have checked that this approximation works reasonably well by comparing it to numerical calculations. The potentials $\bar{\Phi}$ and $\bar{\Psi}$ are therefore written as

$$\begin{aligned} \bar{\Phi}(a) &= \frac{3}{4} \left(\frac{k_{eq}}{k}\right)^2 \frac{a+1}{a^2} \bar{\Delta}_T(a), \\ \bar{\Psi}(a) &= -\frac{3}{4} \left(\frac{k_{eq}}{k}\right)^2 \frac{a+1}{a^2} \left(\bar{\Delta}_T(a) + \frac{8}{5}f_\nu \frac{\bar{N}_2(a)}{a+1}\right), \end{aligned} \quad (\text{A.9})$$

where recall $k_{eq} = \sqrt{2}(\Omega_0 H_0^2 a_0)^{1/2}$ is the scale that passes the horizon at matter-radiation equality. By using the asymptotic form of $\bar{\Delta}_T$ and \bar{N}_2 , we easily obtain the corresponding relation between $\bar{\Phi}$ and $\bar{\Psi}$,

$$\bar{\Phi}(a) = \begin{cases} -\bar{\Psi}(a) \left(1 + \frac{2}{5}f_\nu\right) & (a \ll 1) \\ -\bar{\Psi}(a). & (a \gg 1) \end{cases} \quad (\text{A.10})$$

Also of interest are the ratios of initial to final values of the gravitational potentials:

$$\begin{aligned} \bar{\Phi}(a_0) &= -\bar{\Psi}(a_0) = \frac{9}{10} \left(1 + \frac{4}{15}f_\nu\right) \left(1 + \frac{2}{5}f_\nu\right)^{-1} \bar{\Phi}(0), \\ \bar{\Psi}(a_0) &= \frac{9}{10} \left(1 + \frac{4}{15}f_\nu\right) \bar{\Psi}(0). \end{aligned} \quad (\text{A.11})$$

Thus we see that the correction for anisotropic stress makes a 10% difference in $\bar{\Psi}$ during radiation domination. If recombination occurs near equality, this results in a small correction to the standard Sachs-Wolfe formula due to anisotropic stress.

The initial conditions for the perturbations may now be expressed in terms of $\bar{\Phi}(0)$,

$$\begin{aligned}\Psi(0) &\equiv \bar{\Psi}(0) = -\left(1 + \frac{2}{5}f_\nu\right)^{-1} \bar{\Phi}(0), \\ \Theta(0) &\equiv \bar{\Theta}(0) = \frac{1}{2}\left(1 + \frac{2}{5}f_\nu\right)^{-1} \bar{\Phi}(0).\end{aligned}\tag{A.12}$$

Note that since all modes are superhorizon sized at the initial epoch, the overbar is superfluous. Moreover, even in the initial conditions, the anisotropic stress represents a small but important correction to the $\Pi_T = 0$ solutions of §5.1, $\bar{\Phi}(0) = -\bar{\Psi}(0) = 2\bar{\Theta}_0(0)$. Finally, we can relate these quantities to the initial power spectrum,

$$k^3|\Phi(0, k)|^2 \equiv k^3|\bar{\Phi}(0, k)|^2 = \left[\frac{5}{6}\left(1 + \frac{2}{5}f_\nu\right)\right]^2 \left(\frac{k_{eq}}{k}\right)^4 k^3 C_G^2(k) = Bk^{n-1},\tag{A.13}$$

where we have restored the implicit k index. Note that C_G is the normalization of the density fluctuations at equality. It is related to the matter power spectrum today $|\Delta(\eta_0, k)|^2 = Ak^n$ by

$$\begin{aligned}Ak^n &\simeq \left[\left(1 + \frac{4}{15}f_\nu\right) C_G a_0/a_{eq}\right]^2 \\ &\simeq \left(1 + \frac{4}{15}f_\nu\right)^2 \left(1 + \frac{2}{5}f_\nu\right)^{-2} \frac{36}{25} k_{eq}^{-4} (a_0/a_{eq})^2 Bk^n \\ &\simeq \left(1 + \frac{4}{15}f_\nu\right)^2 \left(1 + \frac{2}{5}f_\nu\right)^{-2} \frac{9}{25} (\Omega_0 H_0^2)^{-2} Bk^n,\end{aligned}\tag{A.14}$$

[*c.f.* equation (6.12)] where we have used equation (A.8).

A.1.2 Small Scale Radiation Feedback

Next we need to obtain solutions of Ψ and Φ in the small scale limit where pressure cannot be neglected. Qualitatively speaking, we know that the potentials decay inside the sound horizon in the radiation-dominated epoch since pressure prevents Δ_T from growing. However in general, it is impossible to obtain the exact solution valid through matter-radiation equality even if we neglect the anisotropic stress term. Only the asymptotic behavior in certain limits has been found [101]. For the CDM scenario, it is well known that the *final* value of the potential at small scales is obtained from the superhorizon solution (A.9) by the transfer function $\Phi(a_0) = -\Psi(a_0) = T(k)\bar{\Phi}(a_0)$, where

$$T(k) = \frac{\ln(1 + 2.34q)}{2.34q} [1 + 3.89q + (14.1q)^2 + (5.46q)^3 + (6.71q)^4]^{-1/4},\tag{A.15}$$

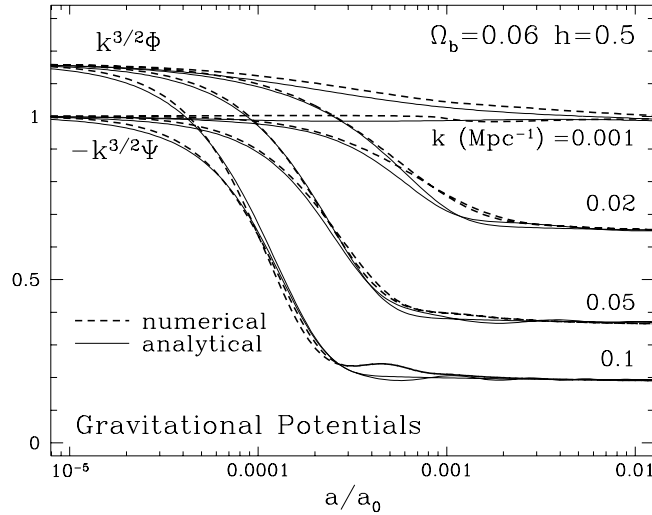


Figure A.1: Gravitational Potential Evolution

Gravitational potentials in the Harrison-Zel'dovich CDM model. The potential decays after crossing the sound horizon in the radiation dominated epoch and only flattens out *well* into the matter dominated epoch. Moreover $\Phi \neq -\Psi$ early on due to anisotropic stress. The analytic approximations trace the numerical potentials reasonably well.

with $q \equiv k/[\Omega_0 h^2 \exp(-2\Omega_b)]$ in units of Mpc^{-1} [122, 6]. Note that $q \propto k/k_{eq}$ approximately, reflecting the fact that only modes that cross the Jeans length before equality are suppressed. This implies that the potentials are larger in amplitude if equality occurs later, *i.e.* for high $\Omega_0 h^2$ models. Equation (A.15) therefore empirically accounts for the lack of growth in the radiation-dominated era. Now let us consider the time evolution of the potential. We know that in the matter-dominated epoch the potentials are constant on all scales. Therefore, we smoothly join the superhorizon scale solutions of equation (A.9) with a constant matter-dominated tail whose relative amplitude is given by the transfer function. Since the Jeans crossing epoch is approximately the same as the horizon crossing time in radiation-dominated era, we can take $(k/Ha) \sim ak/k_{eq} \sim 1$ as the matching epoch,

$$\begin{aligned} \Phi(a) &= \bar{\Phi}(a) \left\{ [1 - T(k)] \exp[-\alpha_1 (ak/k_{eq})^\beta] + T(k) \right\}, \\ \Psi(a) &= \bar{\Psi}(a) \left\{ [1 - T(k)] \exp[-\alpha_2 (ak/k_{eq})^\beta] + T(k) \right\}, \end{aligned} \quad (\text{A.16})$$

where α_1 , α_2 and β are fitting parameters. We also need a small correction to take into account the free streaming oscillations of the neutrino quadrupole inside the Jeans scale. A very simple approximation can be obtained by making the replacement $\bar{N}_2(a) \rightarrow \bar{N}_2(a) \cos[0.5k/(Ha)]$ in equation (A.9) for $\Psi(a)$. Here the factor 0.5 is a best fit, and the

Hubble parameter $H(a) = (\dot{a}/a)(a_0/a)$. Since it is a higher order correction, this crude approximation is sufficient for our purposes. Comparing this functional form (A.16) with numerical results, we obtain a good fit for $\alpha_1 = 0.11$, $\alpha_2 = 0.097$ and $\beta = 1.6$. In order to calculate the early ISW effect, we take the direct derivative of equations (A.16). In Fig. A.1, we compare these analytic approximations to the numerical results and find good agreement.

A.2 Analytic Construction to 5% Accuracy

A.2.1 Explicit Tight Coupling Solutions

The first step in obtaining the explicit analytic solution for the anisotropy is to calculate the photon fluctuation spectrum at last scattering. We have already seen in §5.2.1 how this may be obtained under the tight coupling approximation once the potential evolution is known. For calculational purposes, it is convenient to express the acoustic solution of equation (5.52) in a more explicit but cumbersome form. One advantage of the analytic tight coupling solutions is they do not require the use of time derivatives of the potentials despite the appearance of equation (5.52). Thus accuracy is not compromised by our lack of a detailed description for $\dot{\Phi}$ and $\dot{\Psi}$. Integrating equation (5.52) by parts twice, we obtain

$$(1 + R)^{1/4}[\hat{\Theta}_0(\eta) + \Phi(\eta)] = [\cos kr_s(\eta) + J(0)\sin kr_s(\eta)] [\Theta_0(0) + \Phi(0)] + I(\eta), \quad (\text{A.17})$$

where the overhat denotes the undamped solution,

$$J(\eta) \equiv -(1 + R)^{3/4} \frac{\sqrt{3}}{k} \frac{d}{d\eta} (1 + R)^{-1/4} = \frac{\sqrt{3}}{4k} \frac{\dot{R}}{\sqrt{1 + R}}, \quad (\text{A.18})$$

and

$$I(\eta) = \frac{k}{\sqrt{3}} \int_0^\eta d\eta' \Phi(\eta') G(\eta') \sin[kr_s(\eta) - kr_s(\eta')], \quad (\text{A.19})$$

with

$$G(\eta) = (1 + R)^{-1/4} \left[1 - (1 + R) \frac{\Psi}{\Phi} + \frac{3}{4k^2} \ddot{R} - J^2 \right]. \quad (\text{A.20})$$

Here we have employed the identity $\hat{\Theta}_0(0) = -\dot{\Phi}(0)$. Since the ISW effect predicts constant $\Theta_0 + \Phi$ at superhorizon scales, we have written these expressions in terms of that quantity.

The dipole solution $\hat{\Theta}_1$ can be similarly obtained from the photon continuity equation $k\Theta_1 = -3(\dot{\Theta}_0 + \dot{\Phi})$,

$$(1+R)^{3/4} \frac{\hat{\Theta}_1(\eta)}{\sqrt{3}} = [1+J(\eta)J(0)][\Theta_0(0) + \Phi(0)]\text{sin}kr_s(\eta) \\ + [J(\eta) - J(0)][\Theta_0(0) + \Phi(0)]\text{cos}kr_s(\eta) \\ + J(\eta)I(\eta) - \frac{k}{\sqrt{3}} \int_0^\eta d\eta' \Phi(\eta') G(\eta') \text{cos}[kr_s(\eta) - kr_s(\eta')], \quad (\text{A.21})$$

where we have used the relation $\dot{r}_s = c_s = (1/\sqrt{3})(1+R)^{-1/2}$. Notice that we do not need $\dot{\Phi}$ even in the boundary terms in either equation (A.17) and (A.21).

At large scales, $k < 0.08h^3 \text{ Mpc}^{-1}$ this WKB solution fails because the oscillation rate becomes comparable to rate at which the sound speed is changing (see §5.2.1). On the other hand, we know the large scale behavior is given by the dilation effect $\Theta(\eta) = \Theta(0) - \Phi(\eta) + \Phi(0)$. Comparison with (A.17) suggests that an approximate matching onto large scales can be obtained by dropping the explicit R dependence,

$$[\hat{\Theta}_0(\eta) + \Phi(\eta)] = [\Theta_0(0) + \Phi(0)]\text{cos}kr_s(\eta) + \frac{k}{\sqrt{3}} \int_0^\eta d\eta' [\Phi(\eta') - \Psi(\eta')] \text{sin}[kr_s(\eta) - kr_s(\eta')]. \quad (\text{A.22})$$

Here we take the true $R \neq 0$ sound horizon r_s in order to match more smoothly onto the small scale solution. In the CDM model, the error this causes at large scales is minimal. The continuity equation now implies

$$(1+R)^{1/2} \frac{\hat{\Theta}_1(\eta)}{\sqrt{3}} = [\Theta_0(0) + \Phi(0)]\text{sin}kr_s(\eta) - \frac{k}{\sqrt{3}} \int_0^\eta d\eta' [\Phi(\eta') - \Psi(\eta')] \text{cos}[kr_s(\eta) - kr_s(\eta')]. \quad (\text{A.23})$$

Finally, the following relations are useful for computation:

$$R = \frac{1}{1-f_\nu} \frac{3\Omega_b}{4\Omega_0} a, \quad \dot{R} = \dot{a}R_{eq} = \frac{k_{eq}}{\sqrt{2}} \sqrt{1+a} R_{eq}, \quad \ddot{R} = \frac{1}{4} k_{eq}^2 R_{eq}, \quad (\text{A.24})$$

and recall

$$k_{eq}r_s = \frac{2}{3} \sqrt{\frac{6}{R_{eq}}} \ln \frac{\sqrt{1+R} + \sqrt{R+R_{eq}}}{1 + \sqrt{R_{eq}}}, \quad (\text{A.25})$$

where $R_{eq} \equiv R(\eta_{eq})$ and we have employed the relation $k_{eq}\eta = 2\sqrt{2}(\sqrt{1+a} - 1)$. Here $1 + \rho_\nu/\rho_\gamma = (1-f_\nu)^{-1} = 1.68$. Note that a is normalized at equality $a_{eq}/a_0 = a_0^{-1} = 2.38 \times 10^{-5} \Theta_{2.7}^4 (\Omega_0 h^2)^{-1} (1-f_\nu)^{-1}$, and the scale which passes the horizon at equality is $k_{eq} = 1.17/\eta_{eq} = 9.67 \times 10^{-2} \Theta_{2.7}^{-2} \Omega_0 h^2 (1-f_\nu)^{1/2} \text{ Mpc}^{-1}$. Evaluating these expressions at last scattering gives the solution in the absence of diffusion damping. To account for diffusion damping through last scattering, one needs to know the ionization history through recombination.

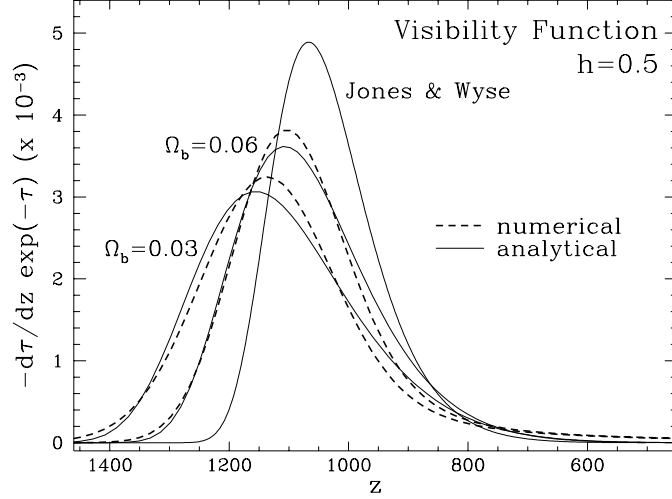


Figure A.2: Visibility Function

The redshift visibility function. Notice that the weak dependence on Ω_b of the visibility function is adequately described by the analytic fitting formula, whereas the Jones & Wyse [91] fitting formula [their equation (23)] does not.

A.2.2 Recombination Revisited

Atomic Considerations

Some care must be taken in calculating the recombination history of hydrogen. In particular, hydrogen recombines more slowly than Saha prediction presented in §6.3.4. Lyman α and Lyman continuum photons from recombination to the ground state immediately reionize another hydrogen atom leaving no net effect. It was realized long ago [123, 183] that net recombination occurs through the forbidden 2-photon decay from the $2s$ level and by the loss of Lyman α photons to the cosmological redshift. The result is that the hydrogen ionization fraction

$$x_H \equiv n_e/n_H = (1 - Y_p)^{-1} n_e/n_b = (1 - Y_p)^{-1} x_e, \quad (\text{A.26})$$

[see equation (3.7)] obeys the differential equation [123],

$$\frac{dx_H}{dt} = C_r \left[\beta(1 - x_H) - n_H \alpha_B x_e^2 \right], \quad (\text{A.27})$$

where

$$\beta = \left(\frac{m_e k_B T_b}{2\pi \hbar^2} \right)^{3/2} e^{-B_1/k_B T_b} \alpha_B \quad (\text{A.28})$$

is the ionization rate out of the ground state, with the ground state binding energy $B_1 = 13.6\text{eV}$ and

$$\alpha_B = 10^{-13} \frac{aT_4^b}{1 + cT_4^d} \text{cm}^3\text{s}^{-1} \quad (\text{A.29})$$

is the ‘case B’ recombination rate which excludes those to the ground state [129]. Here the fitting constants are $a = 4.309$, $b = -0.6166$, $c = 0.6703$, $d = 0.5300$ with $T_4 = T_b/10^4\text{K}$.

The suppression factor

$$C_r = \frac{\Lambda_\alpha + \Lambda_{2s \rightarrow 1s}}{\Lambda_\alpha + \Lambda_{2s \rightarrow 1s} + \beta e^{h\nu_\alpha/k_B T_b}}, \quad (\text{A.30})$$

takes into account the 2-photon decay rate $\Lambda_{2s \rightarrow 1s} = 8.22458\text{s}^{-1}$ [60] and the hydrogen production rate through redshifting out of the line [123]

$$\Lambda_\alpha = \frac{8\pi}{\lambda_\alpha^3(1 - x_H)n_H} H, \quad \lambda_\alpha = c/\nu_\alpha = \frac{8\pi\hbar c}{3B_1} = 1.216 \times 10^{-5}\text{cm}, \quad (\text{A.31})$$

where recall H is the Hubble parameter. Since helium recombination precedes hydrogen we can assume that at the start of hydrogen recombination $x_e = (1 - Y_p)$ or $x_H = 1$. We shall see below what effect helium recombination has on the spectrum.

From equation (3.8), the baryon temperature evolution is governed by

$$\frac{dT_b}{dt} = -\frac{1}{t_{cool}}(T_b - T) - 2\frac{da}{dt}\frac{1}{a}T_b, \quad (\text{A.32})$$

with

$$t_{cool} = 7.66 \times 10^{19} \frac{(1 + x_e)/2 - (3 + 2x_e)Y_p/8}{1 - Y_p/2} x_e^{-1} \Theta_{2.7}^{-4} (1 + z)^{-4}\text{s}. \quad (\text{A.33})$$

Since this short time scale implies that the electron temperature tracks the photon temperature until late redshifts and low ionization, we can determine its evolution away from the photon temperature iteratively by employing the $T_b = T$ solution for x_e . The two temperatures only start diverging at $z \lesssim 100$ and thus is irrelevant for CMB anisotropies [123, 77]. We can therefore replace the baryon temperature with $T_b = T_0(1 + z)$.

Ionization Fitting Formulae

It is also useful to have fitting formula to the solutions of equation (A.27). The total optical depth from the present to the critical recombination epoch $800 < z < 1200$ can be approximated as

$$\tau(z, 0) \simeq \Omega_b^{c_1} \left(\frac{z}{1000} \right)^{c_2}, \quad (\text{A.34})$$

where $c_1 = 0.43$ and $c_2 = 16 + 1.8 \ln \Omega_b$. Since the range of reasonable values for h is limited to $0.5 \lesssim h \lesssim 0.8$, we have ignored the small h dependence. For definiteness, we take last scattering to occur at z_* where the optical depth $\tau(z_*, 0) = 1$. It immediately follows from (A.34) that this occurs at¹

$$\frac{z_*}{1000} \simeq \Omega_b^{-c_1/c_2} = \Omega_b^{-0.027/(1+0.11 \ln \Omega_b)}, \quad (\text{A.35})$$

which is weakly dependent on Ω_b . The differential optical depth $\dot{\tau}$ then becomes

$$\dot{\tau}(z) = \frac{c_2}{1000} \Omega_b^{c_1} \left(\frac{z}{1000} \right)^{c_2-1} \frac{\dot{a}}{a} (1+z), \quad (\text{A.36})$$

where $\dot{\tau}$ is by definition positive since $\dot{\tau} \equiv d[\tau(\eta', \eta)]/d\eta$. Finally, the ionization fraction is given by $x_e(z) = \dot{\tau} a_0 / n_e \sigma_T a$, where

$$(n_e \sigma_T a / a_0)^{-1} = 4.3 \times 10^4 (1 - Y_p/2)^{-1} (\Omega_b h^2)^{-1} (1+z)^{-2} \text{Mpc}. \quad (\text{A.37})$$

Of course, where the formula (A.36) implies $x_e > 1$, we set $x_e = 1$, *i.e.* $\dot{\tau} = n_e \sigma_T a / a_0$. Or slightly better, impose two step functions: from $x_e = 1$ to $1 - Y_p/2$ at $z = 6000$ and $1 - Y_p$ at $z = 2500$ to account for helium recombination. To the level that we expect the analytic formulae to work, these corrections are insignificant. In Fig. A.2, we show the numerical values for the visibility function in redshift space $-(d\tau/dz)e^{-\tau}$ compared with these analytic fits.

A.2.3 Analytic Results

The decrease in ionization fraction implies an increase in the Compton mean free path and hence the diffusion length. Recall that the damping length is given by

$$k_D^{-2}(\eta) = \frac{1}{6} \int_0^\eta d\eta' \frac{1}{\dot{\tau}} \frac{R^2 + 4(1+R)/5}{(1+R)^2}. \quad (\text{A.38})$$

and fluctuations are damped as $\exp[-(k/k_D)^2]$ assuming $R\Psi \ll \Theta_0$ (see section A.3.1). To account for the evolution after last scattering, note that the Boltzmann equation in flat space has the formal solution

$$[\Theta + \Psi](\eta_0, \mu) = \int_0^{\eta_0} \left\{ [\Theta_0 + \Psi - i\mu V_b] \dot{\tau} - \dot{\Phi} + \dot{\Psi} \right\} e^{-\tau(\eta, \eta_0)} e^{ik\mu(\eta - \eta_0)} d\eta. \quad (\text{A.39})$$

¹A more general expression including variations in $\Omega_0 h^2$ is given in [84]

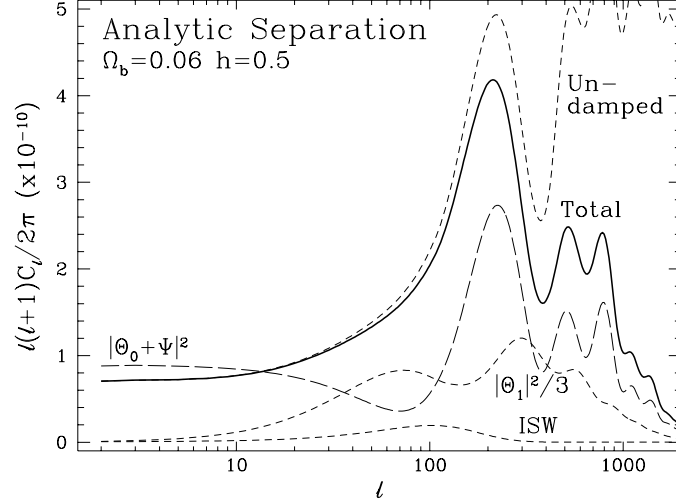


Figure A.3: Analytic Separation of Effects

Individual contributions to the anisotropy in the CDM model. At the largest scales ($\ell \lesssim 30$), the monopole $|\Theta_0 + \Psi|$ from the ordinary Sachs-Wolfe effect dominates. The 20% correction from the early ISW effect on scales larger than the first Doppler peak appears misleadingly small in power (see text). The ordinary Sachs-Wolfe effect is overpowered by the acoustic oscillations at small scales leading to a deficit at intermediate scales ($\ell \sim 70$) which is filled in by the adiabatic dipole Θ_1 and the ISW effect. Although the dipole cannot be neglected, the monopole is clearly responsible for the general structure of the Doppler peaks. Diffusion damping significantly reduces fluctuations beyond the first Doppler peak and cuts off the anisotropies at $\ell \sim 1000$.

For sufficiently large scales, we can take the slowly varying quantities out of this integral. Thus accounting for diffusion damping, the fluctuations at last scattering become $[\Theta_0 + \Psi](\eta_*) = [\hat{\Theta}_0 + \Psi](\eta_*)\mathcal{D}(k)$ and $\Theta_1(\eta_*) = \hat{\Theta}_1(\eta_*)\mathcal{D}(k)$, where

$$\mathcal{D}(k) = \int_0^{\eta_0} \dot{\tau} e^{-\tau(\eta, \eta_0)} e^{-[k/k_D(\eta)]^2} d\eta. \quad (\text{A.40})$$

Taking the multipole moments and setting $V_b = \Theta_1$, we find for $\ell \geq 2$,

$$\begin{aligned} \Theta_\ell(\eta_0) \simeq & [\Theta_0 + \Psi](\eta_*)(2\ell + 1)j_\ell(k\Delta\eta_*) + \Theta_1(\eta_*)[\ell j_{\ell-1}(k\Delta\eta_*) - (\ell + 1)j_{\ell+1}(k\Delta\eta_*)] \\ & + (2\ell + 1) \int_{\eta_*}^{\eta_0} [\dot{\Psi} - \dot{\Phi}] j_\ell(k\Delta\eta) d\eta. \end{aligned} \quad (\text{A.41})$$

Integrating over all k modes of the perturbation, we obtain

$$\frac{2\ell + 1}{4\pi} C_\ell = \frac{V}{2\pi^2} \int \frac{dk}{k} \frac{k^3 |\Theta_\ell(\eta_0, k)|^2}{2\ell + 1}. \quad (\text{A.42})$$

This completes the explicit construction of the anisotropy spectrum.

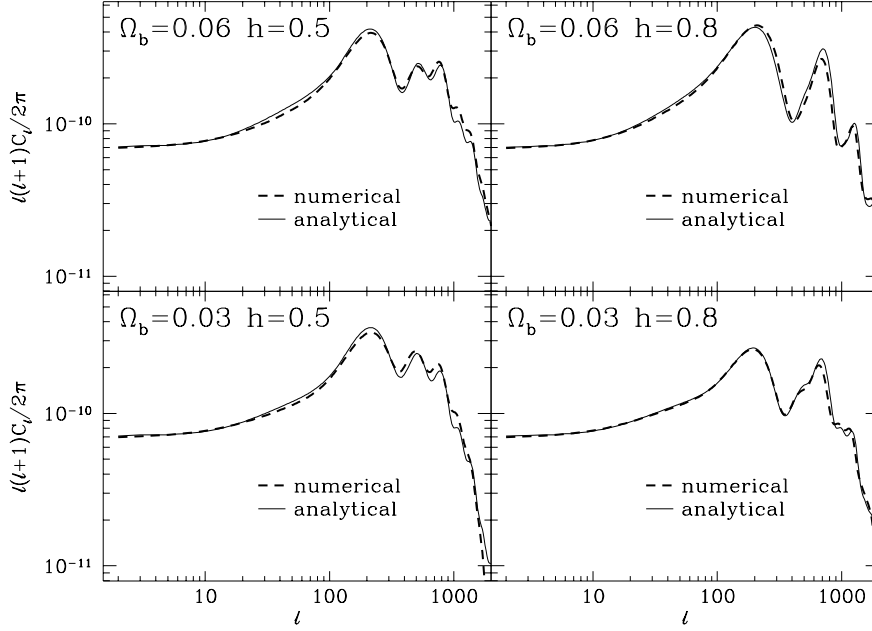


Figure A.4: Comparison of Analytic and Numerical Results
The agreement between analytic and numerical results is excellent on all scales.

In Fig. A.3, we show the analytic decomposition of the spectrum into the effective temperature perturbation at last scattering $[\Theta_0 + \Psi](\eta_*)$, the dipole or Doppler term $\Theta_1/\sqrt{3}$, the early ISW effect and diffusion damping. Notice that without diffusion damping the dilation boost of the acoustic oscillations for small scales that enter during radiation domination is clearly evident. The early ISW effect appears misleadingly small in power. In fact it adds coherently with the SW effect, whereas the dipole roughly adds in quadrature. The 20% shift in power spectrum normalization from the monopole-only solution is entirely due to the 1% ISW effect. Finally let us compare the analytic construction with the full numerical results (see Fig. A.4). The analytic approximation agrees at the 5% level to the damping scale for the range of parameters accessible to the CDM model. By extending the analysis in this section to other models, comparable accuracy can be obtained.

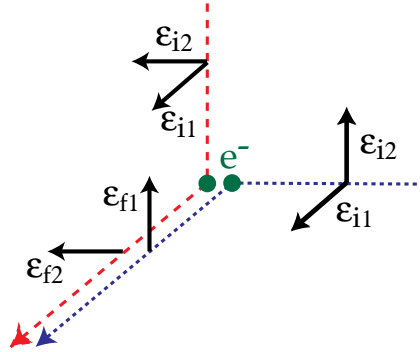


Figure A.5: Polarization Generation

A quadrupole moment in the temperature distributions sources polarization. Unless the temperature or mean energy of the radiation at ninety degree angles is the same, polarization dependent preferential scattering will cause more intensity in one polarization than the other in the outgoing scattered radiation. Reversing the arrow of time, we see that linear polarization sources a quadrupole anisotropy. The length of the dashes represents the wavelength of the photon.

A.3 Toward 1% Accuracy

The next generation of space based CMB anisotropy experiments have the potential to measure all the C_ℓ 's out to $\ell \sim 500$ to the cosmic variance limit (*i.e.* accuracy $\ell^{-1/2}$). In this case, the amount of information which may be retrieved from the CMB is truly enormous. If the inflationary CDM cosmology turns out to be correct, there is even a possibility that we can probe the physics of inflation through tensor contributions (see *e.g.* [168, 47]) and the shape of the initial power spectrum. A small difference between C_ℓ 's for neutrinos with an eV scale mass and the standard massless case appears near the damping scale and provides the possibility of an indirect measure of the neutrino mass through anisotropies. To realize these goals, we must understand the spectrum at the 1% level. Many secondary effects like those discussed in §7 can contribute at this level. As a first step toward the goal of 1% accuracy, it is also necessary to refine calculations of primary anisotropies. The following discussion draws results from [77].

A.3.1 Polarization Damping

The quadrupole moment of the temperature distribution leads to linear polarization in the microwave background (*e.g.* [135, 93]) and vice versa [16]. The precise level

of the temperature anisotropies therefore is not recovered by neglecting polarization. The Thomson cross section depends on angle as $|\epsilon_f \cdot \epsilon_i|^2$, where ϵ_f and ϵ_i are the final and initial polarization vectors respectively [16, 93]. A quadrupole temperature anisotropy therefore sources polarization (see Fig. A.5). Reversing the arrow of time, polarization also feeds back to generate a temperature quadrupole.

To formally account for polarization, a separate Boltzmann hierarchy is added for the temperature perturbation Θ^Q in the Stokes parameter Q [16, 103],

$$\begin{aligned}\dot{\Theta}_0^Q &= -\frac{k}{3}\Theta_1^Q - \dot{\tau} \left[\frac{1}{2}\Theta_0^Q - \frac{1}{10}(\Theta_2 + \Theta_2^Q) \right], \\ \dot{\Theta}_1^Q &= k \left[\Theta_0^Q - \frac{2}{5}K_2^{1/2}\Theta_2^Q \right] - \dot{\tau}\Theta_1^Q, \\ \dot{\Theta}_2^Q &= k \left[\frac{2}{3}K_2^{1/2}\Theta_1^Q - \frac{3}{7}K_3^{1/2}\Theta_3^Q \right] - \dot{\tau} \left(\frac{9}{10}\Theta_2^Q - \frac{1}{10}\Theta_2 - \frac{1}{2}\Theta_0^Q \right), \\ \dot{\Theta}_\ell^Q &= k \left[\frac{\ell}{2\ell-1}K_\ell^{1/2}\Theta_{\ell-1}^Q - \frac{\ell+1}{2\ell+3}K_{\ell+1}^{1/2}\Theta_{\ell+1}^Q \right] - \dot{\tau}\Theta_\ell^Q, \quad (\ell > 2)\end{aligned}\tag{A.43}$$

where recall $K_\ell = 1 - (\ell^2 + 1)K/k^2$ and goes to unity if $K = 0$. Notice that as expected, it is the temperature quadrupole that sources monopole and quadrupole polarization perturbations. Since the temperature quadrupole itself is suppressed in the tight coupling limit, we expect that polarization will yield only a higher order correction for primary anisotropies. Polarization feeds back to modify the quadrupole equation of the temperature hierarchy (4.54)

$$\dot{\Theta}_2 = k \left[\frac{2}{3}K_2^{1/2}\Theta_1 - \frac{3}{7}K_3^{1/2}\Theta_3 \right] - \dot{\tau} \left(\frac{9}{10}\Theta_2 - \frac{1}{10}\Theta_2^Q - \frac{1}{2}\Theta_0^Q \right).\tag{A.44}$$

Other multipole moments of the temperature hierarchy remain unmodified.

It is easy to see what effect polarization has on anisotropies. Let us expand these equations in the Compton scattering time $\dot{\tau}^{-1}$. The polarization monopole $\ell = 0$ and quadrupole $\ell = 2$ equations together imply that

$$\Theta_2^Q = \Theta_0^Q = \frac{1}{4}\Theta_2.\tag{A.45}$$

Putting these relations into equation (A.44) for the feedback effect, we see that it changes the Compton coupling quadrupole coefficient from $\frac{9}{10} \rightarrow \frac{3}{4}$. This affects the damping rate of acoustic oscillations as we shall now show.

Diffusion damping occurs to second order in the tight coupling expansion of the photon dipole and baryon Euler equations [see equations (4.54), (4.58)],

$$\Theta_1 - V_b = \dot{\tau}^{-1} [k(\Theta_0 + \Psi) - \frac{2}{5}k\Theta_2 - \dot{\Theta}_1],\tag{A.46}$$

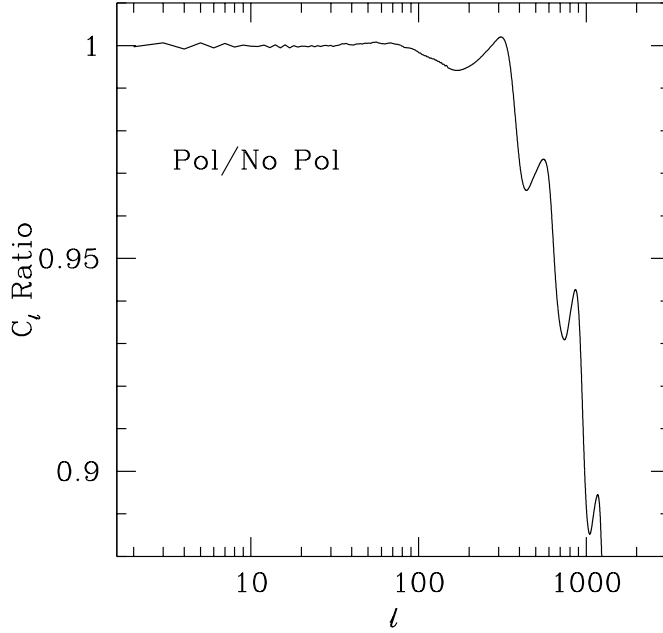


Figure A.6: Polarization Damping

The ratio of C_ℓ for a standard CDM model where polarization is explicitly followed, relative to a calculation where it is neglected. Polarization increases the damping scale of temperature anisotropies. Calculations courtesy of M. White [77].

$$\Theta_1 - V_b = \dot{\tau}^{-1} R[\dot{V}_b + \frac{\dot{a}}{a} V_b - k\Psi] \quad (\text{A.47})$$

where we have assumed that $K/k^2 \ll 1$. Notice that a quadrupole generated to first order in $\dot{\tau}^{-1}$ affects the evolution of the dipole to second order. To lowest order, equation (A.44) gives the quadrupole source as

$$\Theta_2 = \dot{\tau}^{-1} f_2^{-1} \frac{2}{3} k \Theta_1, \quad (\text{A.48})$$

where we have left the effect of polarization and the angular dependence of Compton scattering implicit in

$$f_2 = \begin{cases} 9/10 & \text{angular dependence} \\ 3/4 & \text{polarization} \end{cases} \quad (\text{A.49})$$

The photon continuity or monopole equation yields

$$\dot{\Theta}_0 = -\frac{k}{3} \Theta_1 - \dot{\Phi}. \quad (\text{A.50})$$

To solve these equations to second order in $\dot{\tau}^{-1}$, let us assume a solution of the form $\Theta_1 \propto \exp i \int \omega d\eta$ and ignore variations on the expansion time scale compared with those at

the frequency of oscillation. The electron velocity, obtained by iteration is to second order

$$V_b = \Theta_1 - \dot{\tau}^{-1} R [i\omega\Theta_1 - k\Psi] - \dot{\tau}^{-2} R^2 \omega^2 \Theta_1. \quad (\text{A.51})$$

Substituting this into the dipole equation (A.46) and eliminating the zeroth order term yields

$$i\omega(1+R)\Theta_1 = k[\Theta_0 + (1+R)\Psi] - \dot{\tau}^{-1} R^2 \omega^2 \Theta_1 - \frac{4}{15} \dot{\tau}^{-1} f_2^{-1} k^2 \Theta_1. \quad (\text{A.52})$$

The combination $\Theta_0 + (1+R)\Psi$ was shown in §5.2.2 to oscillate acoustically around zero under the assumption of a slowly varying R . This is because of the baryonic infall contribution $R\Psi$ and the photon blueshift Ψ which displaces the zero point. It is therefore natural to try a solution where $\Theta_0 + (1+R)\Psi \propto \exp i \int \omega d\eta$, since its oscillations should match with the dipole. Note also that after diffusion damping, the photon temperature retains a contribution of order $R\Psi$ due to baryonic infall.

Employing this relation in the photon continuity equation and ignoring slow changes in R , Φ and Ψ yields the dispersion relation

$$(1+R)\omega^2 = \frac{k^2}{3} + i\dot{\tau}^{-1}\omega \left(R^2\omega^2 + \frac{4}{15}k^2 f_2^{-1} \right). \quad (\text{A.53})$$

Using the lowest order solution to rewrite $\omega^3 = k^2\omega/3(1+R)$ and solving the resultant quadratic equation, we obtain [93]

$$\omega = \pm \frac{k}{\sqrt{3(1+R)}} + \frac{i}{6} k^2 \dot{\tau}^{-1} \left[\frac{R^2}{(1+R)^2} + \frac{4}{5} f_2^{-1} \frac{1}{1+R} \right]. \quad (\text{A.54})$$

In other words, the oscillations damp as $\exp[-(k/k_D)^2]$ and the damping length becomes

$$k_D^{-2} = \frac{1}{6} \int d\eta \frac{1}{\dot{\tau}} \frac{R^2 + 4f_2^{-1}(1+R)/5}{(1+R)^2}. \quad (\text{A.55})$$

In the photon-dominated $R \ll 1$ limit, the damping length increases by 5% ($f_2 = \frac{9}{10}$) through the angular dependence of Compton scattering and an additional 10% through polarization ($f_2 = \frac{3}{4}$). Closer to baryon domination, the effect of f_2 is less noticeable. Qualitatively, the polarization sources the quadrupole and generates viscosity which is then dissipated [93]. Actual numerical results of the effect of polarization are shown in in Fig. A.6 and are in good agreement with these analytic estimates of the relative effect. The fractional difference at small scales can be quite significant due to the near exponential behavior of damping.

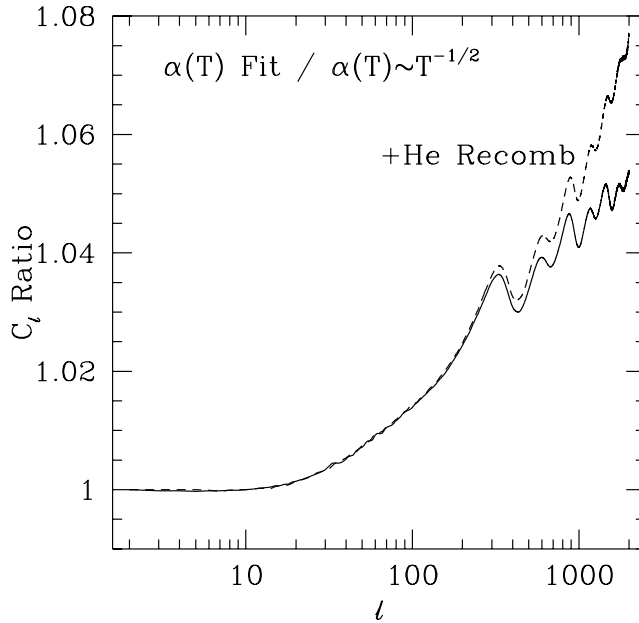


Figure A.7: Helium Recombination

Ionized helium at high redshift contributes free electrons to oppose photon diffusion and thus even at recombination has a small effect in decreasing the damping scale. Also shown here is the effect of improving the fitting formula for the ‘case B’ recombination coefficient α_B of equation (A.29) from the $T^{-1/2}$ scaling of [123]. Calculations courtesy of M. White [77].

A.3.2 Helium Recombination

One might naively expect helium recombination to have a negligible effect on the C_ℓ ’s because helium recombines while the radiation and matter are still very tightly coupled, at $z \simeq 2500$ for singly ionized and $z \simeq 6000$ for doubly ionized helium. However the diffusion damping length grows continuously and is sensitive to the full thermal history. Inclusion of helium recombination affects the 2nd, 3rd and 4th peaks at the 0.2%, 0.4% and 1% levels, as shown in Fig. A.7. Hence it *is* important to follow the recombination of the helium in order to obtain accurate C_ℓ ’s at the percent level. Note that because of atomic collisions, helium atoms are tightly coupled to the hydrogen through collisions even after helium recombination, Since they contribute to the inertia of the photon-baryon fluid, helium atoms should be kept in the baryon evolution equations. It has been shown that simple use of the Saha equation for helium is as accurate as treating helium atoms more fully [77]. The trace of neutral hydrogen, present even at redshifts $z \simeq 2500$, can absorb

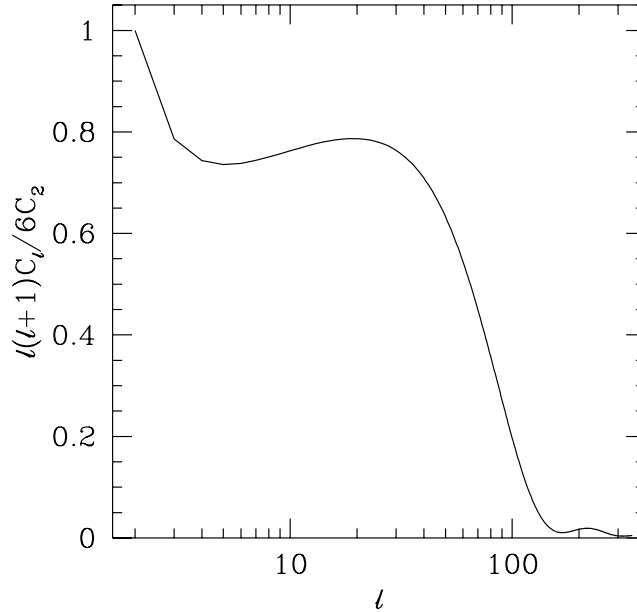


Figure A.8: Gravity Wave Spectrum

A flat spectrum of tensor generated anisotropies with for standard CDM $\Omega_0 = 1.0$, $h = 0.5$, $\Omega_b = 0.05$ $n_T = 1$. The tensor and scalar spectrum add in quadrature. Calculation courtesy of M. White [77].

the helium Ly α photons. This prevents helium recombination photons from ionizing other helium atoms, unlike their hydrogen counterparts.

A.3.3 Gravity Waves

In addition to the scalar modes with which the previous discussion has been involved, there is the possibility that inflation excites tensor (*i.e.* gravity wave) perturbations as well [154]. Early work on tensors and the CMB was performed by [155, 54, 4, 155]. There exist several semi-analytic approximations of varying accuracy, the most recent and accurate being due to [1]. To calculate the tensor spectrum numerically one uses the formalism of [132] as first worked out in detail by [37]. This leads to another set of Boltzmann equations, independent of those for the scalars, which follow the temperature and polarization anisotropies of the tensors. The final result is then $C_\ell^{(\text{tot})} = C_\ell^{(S)} + C_\ell^{(T)}$ where the relative normalization of the tensor and scalar components depends on the details of the perturbation generation scenario. In Fig. A.8, we plot the tensor contribution $C_\ell^{(T)}$, for a model with the parameters of standard CDM.

The qualitative features of this spectrum are easy to understand. The CMB couples to gravity waves through its quadrupole moment. The amplitude of the metric perturbation induced by a gravity wave h_ϵ , where ϵ represents the two possible polarizations, evolves as

$$\ddot{h}_\epsilon + 2\frac{\dot{a}}{a}\dot{h}_\epsilon + (k^2 + 2K)h_\epsilon = 8\pi G \left(\frac{a}{a_0}\right)^2 p_T \Pi_T^{(2)} \quad (\text{A.56})$$

(see [99] eqn. 4.15) where $\Pi_T^{(2)}$ is the *tensor* contribution to the anisotropic stress. Ignoring the feedback effect through the radiation quadrupoles, this is a damped oscillator equation. Inflation predicts a spectrum of initial gravity waves $k^3|h_\epsilon(0, k)|^2 \propto k^{n_T-1}$. For these initial conditions, h_ϵ remains constant outside the horizon and feels the k^2 “pressure” force near horizon crossing. The consequent changes in h_ϵ are damped by the expansion. Since $\dot{a}/a = \eta^{-1}$ in the radiation-dominated epoch and $2\eta^{-1}$ in the matter-dominated epoch, gravity waves are damped less rapidly in the former [$j_0(k\eta)$] than in the latter [$j_1(k\eta)/k\eta$].

Just like changes in the scalar spatial metric perturbation $\dot{\Phi}$, \dot{h}_ϵ sources radiation perturbations through dilation from the stretching of space. The difference is that due to the spin two nature of gravity waves, the deformation sources a quadrupole rather than a monopole fluctuation in the matter. This makes its effects unimportant for density perturbations and structure formation. Contributions to the photon temperature perturbation before last scattering are rapidly damped away by Compton isotropization. However during the free streaming epoch, the quadrupole source like the monopole projects onto higher multipoles as the photons free stream, causing anisotropies in the CMB through the ISW effect. This explains the three prominent features in the spectrum of Fig. A.8. Modes that cross the horizon recently source mainly the quadrupole, boosting the low order multipoles. Smaller scales experience the full decay of h_ϵ , leading to a small rise. However the smallest scales contribute negligibly since they enter the horizon before last scattering. Since these are exactly the scales on which acoustic oscillations appear, it is very likely that gravity waves are unimportant for small angle anisotropies. On the other hand, the ratio of large to small scale anisotropies may tell us something about the relative amplitude of the tensor to scalar initial contributions [168, 47].

A.3.4 Massive Neutrinos

The radiation content determines the amount of dilation boost the acoustic modes encounter at horizon crossing from the decay of the potential. Lowering the radiation

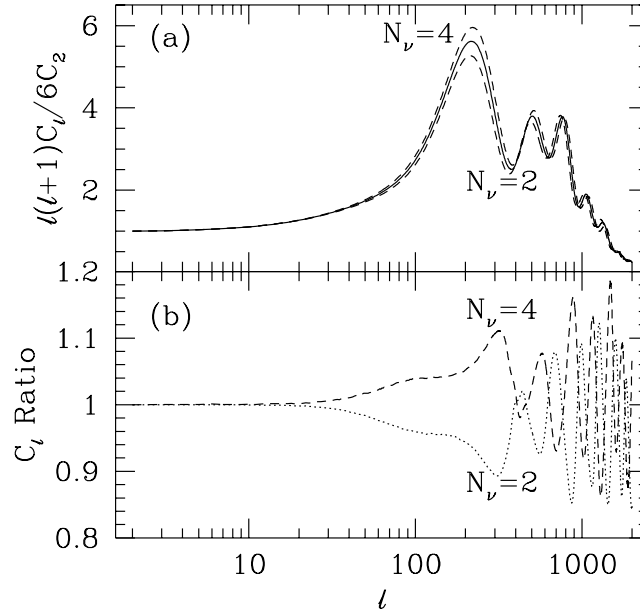


Figure A.9: Number of Massless Neutrinos

Relativistic neutrinos increase the amount of dilation boost from the potential decay that the acoustic mode encounters at horizon crossing. The prediction for massive neutrino models depends on when the neutrinos become non-relativistic. For a mass of a few eV, the horizon at this epoch projects onto $\ell \sim 500$ and the resultant spectrum will be a smooth transition from $N_\nu = 3$ to $N_\nu = 2$ near this scale. Calculation courtesy of M. White [77].

content lowers the boost. Thus the CMB is sensitive to the number of effectively massless neutrino families N_ν before last scattering (see Fig. A.9). Massive neutrinos are a promising dark matter candidate and can solve some of the problems CDM models have with large scale structure formation [42, 97]. By assuming a neutrino with a few eV mass and composing the rest of the critical density with cold dark matter, one retains many of the features of the CDM model while also lowering the excess of small scale power. A low mass neutrino is relativistic when a galaxy-sized mass enters the horizon. Thus neutrino free streaming will collisionlessly damp power on these scales. However for the degree and larger scales that the current CMB experiments probe, such neutrinos are already non-relativistic at horizon crossing and leave the same signature as CDM. The transition scale is around $\ell \simeq 500$ for a neutrino mass of a few eV. Thus the CMB anisotropy spectrum should follow the $N_\nu = 3$ CDM prediction until roughly those scales and then decrease to the lower N_ν prediction. Extracting the neutrino mass will therefore require a detailed understanding of the damping

tail and any secondary and foreground contributions – an extremely challenging, but not unthinkable task.

Appendix B

Useful Quantities and Relations

B.1 FRW Parameters

The expansion rate is given by the Hubble parameter

$$\begin{aligned} H^2 &\equiv \left(\frac{1}{a} \frac{da}{dt}\right)^2 = \left(\frac{\dot{a}}{a} \frac{a_0}{a}\right)^2 \\ &= \left(\frac{a_0}{a}\right)^4 \frac{a_{eq} + a}{a_{eq} + a_0} \Omega_0 H_0^2 - \left(\frac{a_0}{a}\right)^2 K + \Omega_\Lambda H_0^2, \end{aligned} \quad (\text{B.1})$$

where the curvature is $K = -H_0^2(1 - \Omega_0 - \Omega_\Lambda)$. The value of the Hubble parameter today, for different choices of the fundamental units (see Tab. B.1), is expressed as

$$\begin{aligned} H_0 &= 100h \text{ kms}^{-1} \text{ Mpc}^{-1} \\ &= 2.1331 \times 10^{-42} h \text{ GeV} \\ &= (2997.9)^{-1} h \text{ Mpc}^{-1} \\ &= (3.0857 \times 10^{17})^{-1} h \text{ s}^{-1} \\ &= (9.7778)^{-1} h \text{ Gyr}^{-1}. \end{aligned} \quad (\text{B.2})$$

Present day densities in a given particle species X are measured in units of the critical density $\rho_X(a_0) = \Omega_X \rho_{\text{crit}}$, where

$$\begin{aligned} \rho_{\text{crit}} &= 3H_0^2/8\pi G = 1.8788 \times 10^{-29} h^2 \text{ g cm}^{-3} \\ &= 8.0980 \times 10^{-47} h^2 \text{ GeV}^4 \\ &= 1.0539 \times 10^4 h^2 \text{ eV cm}^{-3} \end{aligned}$$

1 s	= 9.7157×10^{-15} Mpc
1 yr	= 3.1558×10^7 s
1 Mpc	= 3.0856×10^{24} cm
1 AU	= 1.4960×10^{13} cm
1 K	= 8.6170×10^{-5} eV
1 M_{\odot}	= 1.989×10^{33} g
1 GeV	= 1.6022×10^{-3} erg
	= 1.7827×10^{-24} g
	= $(1.9733 \times 10^{-14} \text{ cm})^{-1}$
	= $(6.5821 \times 10^{-25} \text{ s})^{-1}$

Planck's constant	$\hbar = 1.0546 \times 10^{-27} \text{ cm}^2 \text{ g s}^{-1}$
Speed of light	$c = 2.9979 \times 10^{10} \text{ cm s}^{-1}$
Boltzmann's constant	$k_B = 1.3807 \times 10^{-16} \text{ erg K}^{-1}$
Fine structure constant	$\alpha = 1/137.036$
Gravitational constant	$G = 6.6720 \times 10^{-8} \text{ cm}^3 \text{ g}^{-1} \text{ s}^{-2}$
Stefan-Boltzmann constant	$\sigma = ac/4 = \pi^2 k_B^4 / 60 \hbar^3 c^2$ $a = 7.5646 \times 10^{-15} \text{ erg cm}^{-3} \text{ K}^{-4}$
Thomson cross section	$\sigma_T = 8\pi\alpha^2 / 3m_e^2 = 6.6524 \times 10^{-25} \text{ cm}^2$
Electron mass	$m_e = 0.5110 \text{ MeV}$
Neutron mass	$m_n = 939.566 \text{ MeV}$
Proton mass	$m_p = 938.272 \text{ MeV}$

Table B.1: Physical Constants and Conversion Factors

$$\begin{aligned}
&= 1.1233 \times 10^{-5} h^2 \text{ protons cm}^{-3} \\
&= 2.7754 \times 10^{11} h^2 M_{\odot} \text{ Mpc}^{-3}.
\end{aligned} \tag{B.3}$$

For the CMB,

$$\begin{aligned}
n_{\gamma 0} &= 399.3 \Theta_{2.7}^3 \text{ cm}^{-3}, \\
\rho_{\gamma 0} &= 4.4738 \times 10^{-34} \Theta_{2.7}^4 \text{ g cm}^{-3}, \\
\Omega_{\gamma} &= 2.3812 \times 10^{-5} h^{-2} \Theta_{2.7}^4,
\end{aligned} \tag{B.4}$$

and for the neutrinos

$$\begin{aligned}
\rho_{\nu 0} &= [(1 - f_{\nu})^{-1} - 1] \rho_{\gamma 0}, \\
\Omega_{\nu} &= [(1 - f_{\nu})^{-1} - 1] \Omega_{\gamma},
\end{aligned} \tag{B.5}$$

with $(1 - f_\nu)^{-1} = 1.68$ for the standard model, or for the total radiation

$$\begin{aligned}\rho_{r0} &= (1 - f_\nu)^{-1} \rho_{\gamma 0}, \\ \Omega_r &= (1 - f_\nu)^{-1} \Omega_\gamma.\end{aligned}\tag{B.6}$$

B.2 Time Variables

Throughout the text we use four time variables interchangeably, they are a the scale factor, z the redshift, η the conformal time, and t the coordinate time. In addition, three dimensionless time parameterizations are useful to consider: χ the development angle in an open universe, D the relative amplitude of pressureless matter fluctuations, and τ the optical depth to Compton scattering.

B.2.1 Scale Factor and Redshift

The scale factor $a(t)$ describes the state of expansion and is the fundamental measure of time in the Hubble equation (B.1) since it controls the energy density of the universe. In this Appendix, we leave the normalization of a free to preserve generality. However, the normalization applied in §4, §5, §6, and Appendix A is $a_{eq} = 1$. The conversion factor between the more commonly employed normalization $a_0 = 1$ is

$$\begin{aligned}\frac{a_{eq}}{a_0} &= \frac{\Omega_r}{\Omega_0 - \Omega_r} \\ &= 2.38 \times 10^{-5} (\Omega_0 h^2)^{-1} (1 - f_\nu)^{-1} \Theta_{2.7}^4.\end{aligned}\tag{B.7}$$

The redshift z is defined by $(1 + z) = a_0/a$ and serves the same role as the scale factor normalized to the present. We give the scale factor normalized to 3/4 at baryon-photon equality a special symbol R given the frequency of its appearance in equations related to Compton scattering. More explicitly,

$$\begin{aligned}R &= \frac{3}{4} \frac{\rho_b}{\rho_\gamma} = (1 - f_\nu)^{-1} \frac{3}{4} \frac{\Omega_b}{\Omega_0} \frac{a}{a_{eq}} \\ &= 31.5 \Omega_b h^2 \Theta_{2.7}^{-4} (z/10^3)^{-1}.\end{aligned}\tag{B.8}$$

Epochs of interest for the CMB are listed in Tab. B.2 by their redshifts.

Epoch	Definition
$z_* = 10^3 \Omega_b^{-0.027/(1+0.11 \ln \Omega_b)} \quad \Omega_0 = 1$	Last scattering (recomb.)
$= 10^2 (\Omega_0 h^2 / 0.25)^{1/3} (x_e \Omega_b h^2 / 0.0125)^{-2/3}$	Last scattering (reion.)
$z_d = 160 (\Omega_0 h^2)^{1/5} x_e^{-2/5}$	Drag epoch
$z_{eq} = 4.20 \times 10^4 \Omega_0 h^2 (1 - f_\nu) \Theta_{2.7}^{-4}$	Matter-radiation equality
$z_{b\gamma} = 3.17 \times 10^4 \Omega_b h^2 \Theta_{2.7}^{-4}$	Baryon-photon equality
$z_H = (1 + z_{eq}) \{4(k/k_{eq})^2 / [1 + (1 + 8(k/k_{eq})^2)^{1/2}]\} - 1$	Hubble length crossing
$z = (1 - \Omega_0 - \Omega_\Lambda) / \Omega_0 - 1$	Matter-curvature equality
$z = (\Omega_\Lambda / \Omega_0)^{1/3} - 1$	Matter- Λ equality
$z = [\Omega_\Lambda / (1 - \Omega_0 - \Omega_\Lambda)]^{1/2} - 1$	Curvature- Λ equality
$z_{cool} = 9.08 \Theta_{2.7}^{-16/5} f_{cool}^{2/5} (\Omega_0 h^2)^{1/5} - 1$	Compton cooling era
$z > 4\sqrt{2} z_K$	Bose-Einstein era
$z < z_K / 8$	Compton- y era
$z_K = 7.09 \times 10^3 (1 - Y_p / 2)^{-1/2} (x_e \Omega_b h^2)^{-1/2} \Theta_{2.7}^{1/2}$	Comptonization epoch
$z_{\mu,dc} = 4.09 \times 10^5 (1 - Y_p / 2)^{-2/5} (x_e \Omega_b h^2)^{-2/5} \Theta_{2.7}^{1/5}$	Dbl. Compton therm. epoch
$z_{\mu,br} = 5.60 \times 10^4 (1 - Y_p / 2)^{-4/5} (x_e \Omega_b h^2)^{-6/5} \Theta_{2.7}^{13/5}$	Bremss. therm. epoch
$\Theta_{2.7} = T_0 / 2.7\text{K} \simeq 1.01$	Temperature Scaling
$Y_p = 4n_{He} / n_b \simeq 0.23$	Helium mass fraction
$(1 - f_\nu)^{-1} = 1 + \rho_\nu / \rho_\gamma \rightarrow 1.68132$	Neutrino density correction
$k_{eq} = (2\Omega_0 H_0^2 a_0 / a_{eq})^{1/2}$	Equality Hubble wavenumber
$= 9.67 \times 10^{-2} \Omega_0 h^2 (1 - f_\nu)^{1/2} \Theta_{2.7}^{-2} \text{Mpc}^{-1}$	
$f_{cool} = x_e^{-1} [(1 + x_e) / 2 - (3 + 2x_e) Y_p / 8] (1 - Y_p / 2)^{-1}$	Cooling correction factor

Table B.2: Critical Redshifts

Critical epochs are also denoted as the corresponding value in the coordinate time t , scale factor a , and conformal time η . The neutrino fraction f_ν is given for three families of massless neutrinos and the standard thermal history. The Hubble crossing redshift z_H is given for the matter and radiation dominated epochs.

B.2.2 Conformal Time

By definition, the conformal time $\eta = \int dt/a$ is related to the scale factor as

$$\eta = \int \frac{da}{a} \frac{1}{H} \frac{a_0}{a}. \quad (\text{B.9})$$

Note that in these $c = 1$ units, the conformal time doubles as the comoving size of the horizon. In an open universe, it is also related to the development angle by

$$\chi = \sqrt{-K} \eta. \quad (\text{B.10})$$

Asymptotic relations are often useful for converting values. Before curvature or Λ domination, the conformal time

$$\begin{aligned} \eta &= \frac{2\sqrt{2}}{k_{eq}} \left(\sqrt{1 + a/a_{eq}} - 1 \right) \\ &= 2(\Omega_0 H_0^2)^{-1/2} (a_{eq}/a_0)^{1/2} \left(\sqrt{1 + a/a_{eq}} - 1 \right), \end{aligned} \quad (\text{B.11})$$

and reduces to

$$\eta = \begin{cases} (\Omega_r H_0^2)^{-1/2} a/a_0 & \text{RD} \\ 2(\Omega_0 H_0^2)^{-1/2} (a/a_0)^{1/2}, & \text{MD} \end{cases} \quad (\text{B.12})$$

where $\Omega_r/\Omega_0 \simeq a_{eq}/a_0$. In a $\Lambda = 0$ universe, it also has an asymptotic solution for $a \gg a_{eq}$

$$\begin{aligned} \eta &= \frac{1}{\sqrt{-K}} \cosh^{-1} \left[1 + \frac{2(1 - \Omega_0)}{\Omega_0} \frac{a}{a_0} \right] & \text{MD/CD} \\ \lim_{\Omega_0 \rightarrow 0} \eta_0 &\rightarrow (-K)^{-1/2} \ln(4/\Omega_0), \end{aligned} \quad (\text{B.13})$$

and thus the horizon scale is larger than the curvature scale $(-K)^{-1/2}$ for low Ω_0 universes.

In a flat universe,

$$\eta_0 \simeq 2(\Omega_0 H_0^2)^{-1/2} (1 + \ln \Omega_0^{0.085}), \quad \Omega_0 + \Omega_\Lambda = 1 \quad (\text{B.14})$$

and the horizon goes to a constant $\eta = 2.8 H_0^{-1} \Omega_0^{-1/3} (1 - \Omega_0)^{-1/6}$ as $a/a_0 \rightarrow \infty$.

B.2.3 Coordinate Time

The coordinate time is defined in terms of the scale factor as,

$$t = \int \frac{da}{a} \frac{1}{H}. \quad (\text{B.15})$$

It also takes on simple asymptotic forms, *e.g.*

$$t = \frac{2}{3}(\Omega_0 H_0^2)^{-1/2} a_0^{-3/2} [(a + a_{eq})^{1/2} (a - 2a_{eq}) + 2a_{eq}^{3/2}]. \quad \text{RD/MD} \quad (\text{B.16})$$

Explicitly, this becomes

$$\begin{aligned} t &= \frac{1}{2}(\Omega_0 H_0^2)^{-1/2} (a_0/a_{eq})^{1/2} (a/a_0)^2 \quad \text{RD} \\ &= 2.4358 \times 10^{19} \Theta_{2.7}^{-2} (1+z)^{-2} \text{s}. \end{aligned} \quad (\text{B.17})$$

and

$$\begin{aligned} t &= \frac{2}{3}(\Omega_0 H_0^2) (a/a_0)^{3/2} \quad \text{MD} \\ &= 2.0571 \times 10^{17} (\Omega_0 h^2)^{-1/2} (1+z)^{-3/2} \text{s}. \end{aligned} \quad (\text{B.18})$$

The expansion time, defined as H^{-1} scales similarly

$$\begin{aligned} t_{exp} &= (\Omega_0 H_0^2)^{-1} (a/a_0)^2 a_0^{1/2} (a + a_{eq})^{-1/2} \\ &= 4.88 \times 10^{19} (z + z_{eq} + 2)^{-1/2} \Theta_{2.7}^{-2} (1+z)^{-3/2} \text{s}. \end{aligned} \quad (\text{B.19})$$

For $\Lambda = 0$ universes, the coordinate time at late epochs when radiation can be neglected is given by

$$t = H_0^{-1} \left[\frac{(1 + \Omega_0 z)^{1/2}}{(1 - \Omega_0)(1 + z)} - \frac{\Omega_0}{2(1 - \Omega_0)^{3/2}} \cosh \left(\frac{2(1 - \Omega_0)}{\Omega_0(1 + z)} + 1 \right) \right]. \quad \text{MD/CD} \quad (\text{B.20})$$

In particular, the age of the universe today is

$$t_0 = H_0^{-1} (1 - \Omega_0)^{-1} \left[1 - \frac{\Omega_0}{2} (1 - \Omega_0)^{-1/2} \cosh(2/\Omega_0 - 1) \right], \quad \Omega_\Lambda = 0 \quad (\text{B.21})$$

where the factor in square brackets goes to unity as $\Omega_0 \rightarrow 0$. This should be compared with the flat $\Omega_0 + \Omega_\Lambda = 1$ result

$$t_0 = \frac{2}{3} H_0^{-1} (1 - \Omega_0)^{-1/2} \ln \left[\frac{1 + \sqrt{1 - \Omega_0}}{\sqrt{\Omega_0}} \right], \quad \Omega_0 + \Omega_\Lambda = 1, \quad (\text{B.22})$$

which diverges logarithmically as $\Omega_0 \rightarrow 0$. Finally a microphysical time scale of interest for the CMB,

$$\begin{aligned} t_C &= (d\tau/dt)^{-1} = (x_e n_e \sigma_T)^{-1} \\ &= 4.4674 \times 10^{18} (1 - Y_p/2)^{-1} (x_e \Omega_b h^2)^{-1} (1+z)^{-3} \text{s}, \end{aligned} \quad (\text{B.23})$$

is the Compton mean free time between scatterings.

B.2.4 Growth Function

The amplitude of matter fluctuations undergoing pressureless growth is another useful parameterization of time. It is given by equation (5.9) as

$$D = \frac{5}{2} \Omega_0 \frac{a_0}{a_{eq}} g(a) \int \frac{da}{a} \frac{1}{g^3(a)} \left(\frac{a_0}{a} \right)^2, \quad (\text{B.24})$$

where the dimensionless, “pressureless” Hubble parameter is

$$g^2(a) = \left(\frac{a_0}{a} \right)^3 \Omega_0 + \left(\frac{a_0}{a} \right)^2 (1 - \Omega_0 - \Omega_\Lambda) + \Omega_\Lambda. \quad (\text{B.25})$$

In the matter or radiation-dominated epoch, $D = a/a_{eq}$ by construction. In a $\Lambda = 0$ universe, D becomes

$$D = \frac{5}{2x_{eq}} \left[1 + \frac{3}{x} + \frac{3(1+x)^{1/2}}{x^{3/2}} \ln[(1+x)^{1/2} - x^{1/2}] \right], \quad (\text{B.26})$$

where $x = (\Omega_0^{-1} - 1)a/a_0$. Fitting formulae for the growth factor, valid for the general case, are occasionally useful [26]:

$$\frac{D_0}{a_0} \simeq \frac{5}{2} \Omega_0 \left[\Omega_0^{4/7} - \Omega_\Lambda + \left(1 + \frac{1}{2} \Omega_0 \right) \left(1 - \frac{1}{70} \Omega_\Lambda \right) \right]^{-1}, \quad (\text{B.27})$$

$$\frac{d \ln D}{d \ln a} \simeq \left[\frac{\Omega_0(1+z)^3}{\Omega_0(1+z)^3 - (\Omega_0 + \Omega_\Lambda - 1)(1+z)^2 + \Omega_\Lambda} \right]^{4/7}. \quad (\text{B.28})$$

The latter relation is often employed to relate the velocity to the density field.

B.2.5 Optical Depth

For the CMB, the optical depth τ to Compton scattering is a useful lookback time parameterization,

$$\begin{aligned} \tau(a, a_0) &= \int_\eta^{\eta_0} d\eta' x_e n_e \sigma_T a' \\ &= 6.91 \times 10^{-2} (1 - Y_p/2) x_e \Omega_b h \int_a^{a_0} \frac{da'}{a'} \frac{H_0}{H} \left(\frac{a_0}{a'} \right)^3, \end{aligned} \quad (\text{B.29})$$

for constant ionization fraction. If $a \gg a_{eq}$, this has closed form solution,

$$\begin{aligned} \tau(a, a_0) &= 4.61 \times 10^{-2} (1 - Y_p/2) x_e \frac{\Omega_b h}{\Omega_0^2} \\ &\times \begin{cases} 2 - 3\Omega_0 + (1 + \Omega_0 z)^{1/2} (\Omega_0 z + 3\Omega_0 - 2) & \Omega_\Lambda = 0 \\ \Omega_0 [1 - \Omega_0 + \Omega_0(1+z)^3]^{1/2} - \Omega_0. & \Omega_0 + \Omega_\Lambda = 1 \end{cases} \end{aligned} \quad (\text{B.30})$$

Furthermore, since the optical depth is dominated by early contributions the distinction between open and Λ universes for $\tau \gtrsim 1$ is negligible.

B.3 Critical Scales

B.3.1 Physical Scales

Several physical scales are also of interest. We always use comoving measures when quoting distances. The most critical quantity is the horizon scale η given in the last section and the curvature scale $(-K)^{-1/2} = 2997.9h(1 - \Omega_0 - \Omega_\Lambda)^{1/2}\text{Mpc}$. There are two related quantities of interest, the Hubble scale and the conformal angular diameter distance to the horizon. The Hubble scale is often employed instead of the horizon scale because it is independent of the past evolution of the universe. The wavenumber corresponding to the Hubble scale is

$$k_H = \frac{\dot{a}}{a} = \begin{cases} (\Omega_r H_0^2)^{1/2} (a_0/a) & \text{RD} \\ (\Omega_0 H_0^2)^{1/2} (a_0/a)^{1/2} & \text{MD} \\ (-K)^{1/2} & \text{CD} \\ (\Omega_\Lambda H_0^2)^{1/2} a/a_0 & \text{LD} \end{cases} \quad (\text{B.31})$$

Comparison with the relations for η shows that $k_H \eta \sim 1$ during radiation and matter domination but not curvature or Λ domination. Indeed, due to the exponential expansion, the Hubble scale goes to zero as $a/a_0 \rightarrow \infty$, reflecting the fact that regions which were once in causal contact can no longer communicate. This is of course how inflation solves the horizon problem. Throughout the main text we have blurred the distinction between the Hubble scale and the horizon scale when discussing the radiation- and matter-dominated epochs.

The distance inferred for an object of known spatial extent by its angular diameter is known as the conformal angular diameter distance. It multiplies the angular part of the spatial metric. Moreover, in an open universe, it is not equivalent to the distance measured in conformal time. For an observer at the present, it is given by

$$r_\theta(\eta) = (-K)^{-1/2} \sinh[(\eta_0 - \eta)(-K)^{1/2}]. \quad (\text{B.32})$$

Note that the argument of \sinh is the difference in development angle χ in an open universe. Of particular interest is the angular diameter distance to the horizon $r_\theta(0)$ since many features in the CMB are generated early

$$r_\theta(0) \simeq \begin{cases} 2(\Omega_0 H_0)^{-1} & \Omega_\Lambda = 0 \\ 2(\Omega_0 H_0^2)^{-1/2} (1 + \ln \Omega_0^{0.085}). & \Omega_\Lambda + \Omega_0 = 1 \end{cases} \quad (\text{B.33})$$

In the flat case, $r_\theta(0) = \eta_0$.

A microphysical scale, the mean free path of a photon to Compton scattering, is also of interest for the CMB,

$$\lambda_C = (x_e n_e \sigma_T a / a_0)^{-1} = 4.3404 \times 10^4 (1 - Y_p/2)^{-1} (x_e \Omega_b h^2)^{-1} (1 + z)^{-2} \text{Mpc}. \quad (\text{B.34})$$

The diffusion length is roughly the geometric mean of λ_C and the horizon η . More precisely, it is given by equation (A.55) as

$$\lambda_D^2 \sim k_D^{-2} = \frac{1}{6} \int d\eta \frac{1}{\dot{\tau}} \frac{R^2 + 4f_2^{-1}(1+R)/5}{(1+R)^2}. \quad (\text{B.35})$$

where

$$f_2 = \begin{cases} 1 & \text{isotropic, unpolarized} \\ 9/10 & \text{unpolarized} \\ 3/4 & \text{polarized} \end{cases} \quad (\text{B.36})$$

where isotropic means that the angular dependence of Compton scattering has been neglected, and the polarization case accounts for feedback from scattering induced polarization. Throughout the main text, we have used $f_2 = 1$ for simplicity. If the diffusion scale is smaller than the sound horizon, acoustic oscillations will be present in the CMB. The sound horizon is given by

$$r_s = \int_0^\eta c_s d\eta' = \frac{2}{3} \frac{1}{k_{eq}} \sqrt{\frac{6}{R_{eq}}} \ln \frac{\sqrt{1+R} + \sqrt{R+R_{eq}}}{1 + \sqrt{R_{eq}}}, \quad (\text{B.37})$$

which relates it to the horizon at equality $\eta_{eq} = (4 - 2\sqrt{2})k_{eq}^{-1}$, where

$$\begin{aligned} k_{eq} &= (2\Omega_0 H_0^2 a_0 / a_{eq})^{1/2} \\ &= 9.67 \times 10^{-2} \Omega_0 h^2 (1 - f_\nu)^{1/2} \Theta_{2.7}^{-2} \text{Mpc}^{-1}, \\ \eta_{eq} &= 12.1 (\Omega_0 h^2)^{-1} (1 - f_\nu)^{1/2} \Theta_{2.7}^2 \text{Mpc}, \end{aligned} \quad (\text{B.38})$$

with k_{eq} as the wavenumber that passes the Hubble scale at equality.

B.3.2 Angular Scales

A physical scale at η subtends an angle or equivalently a multipole on the sky ℓ

$$\ell = kr_\theta(\eta) \simeq \theta^{-1}, \quad \ell \gg 1 \quad (\text{B.39})$$

where the angle-distance relation r_θ is given by equation (B.32). Three angular scales are of interest to the CMB. The sound horizon at last scattering determines the location of the

acoustic peaks

$$\begin{aligned} \ell_A &= \pi \frac{r_\theta(\eta_*)}{r_s(\eta_*)}, \\ \ell_p &= \begin{cases} m\ell_A & \text{adiabatic} \\ (m - \frac{1}{2})\ell_A, & \text{isocurvature} \end{cases} \end{aligned} \quad (\text{B.40})$$

where ℓ_p is the location of the p th acoustic peak. If $R_* \ll 1$, ℓ_A takes on a simple form

$$\ell_A = 172 \left(\frac{z_*}{10^3} \right)^{1/2} \frac{f_G}{f_R}, \quad (\text{B.41})$$

where f_R is the correction for the expansion during radiation domination

$$\begin{aligned} f_R &= (1 + x_R)^{1/2} - x_R^{1/2}, \\ x_R &= a_{eq}/a_* = 2.38 \times 10^{-2} (\Omega_0 h^2)^{-1} (1 - f_\nu)^{-1} \Theta_{2.7}^4(z_*/10^3), \end{aligned} \quad (\text{B.42})$$

and f_G is the geometrical factor

$$f_G \simeq \begin{cases} \Omega_0^{-1/2} & \Omega_\Lambda = 0 \\ 1 + \ln \Omega_0^{0.085} & \Omega_\Lambda + \Omega_0 = 1 \end{cases} \quad (\text{B.43})$$

The diffusion damping scale at last scattering subtends an angle given by

$$\ell_D = k_D(\eta_*) r_\theta(\eta_*), \quad (\text{B.44})$$

where $k_D(\eta_*)$ is the effective damping scale at last scattering accounting for the recombination process. From §6.3.4, to order of magnitude it is

$$\ell_D \sim 10^3 (\Omega_b/0.05)^{1/4} \Omega_0^{-1/4} f_R^{-1/2} f_G, \quad (\text{B.45})$$

if $\Omega_b h^2$ is low as required by nucleosynthesis. The scaling is only approximate since the detailed physics of recombination complicates the calculation of k_D (see Appendix A.2.2). The curvature radius at the horizon distance (*i.e.* early times) subtends an angle given by

$$\begin{aligned} \ell_K &\simeq \sqrt{-K} r_\theta(0) \\ &\simeq \frac{2\sqrt{1 - \Omega_0}}{\Omega_0}. \end{aligned} \quad (\text{B.46})$$

This relation is also not exact since for reasonable Ω_0 , the curvature scale subtends a large angle on the sky and the small angle approximation breaks down. Note also that at closer distances as is relevant for the late ISW effect, the curvature scale subtends an even larger angle on the sky than this relation predicts.

B.4 Normalization Conventions

B.4.1 Power Spectra

There are unfortunately a number of normalization conventions used in the literature and indeed several that run through the body of this work. Perhaps the most confusing conventions are associated with open universes. The power in fluctuations is expressed alternately per logarithmic intervals of the Laplacian wavenumber k or the eigenfunction index $\nu = \tilde{k}/\sqrt{-K}$, $\tilde{k} = (k^2 + K)^{1/2}$. The relation between the two follows from the identity $kdk = \tilde{k}d\tilde{k}$,

$$\tilde{P}_X(\tilde{k}) = \frac{k}{\tilde{k}} P_X(k), \quad (\text{B.47})$$

where P_X is the power spectrum of fluctuations in X . For example, our power law spectra

$$\begin{aligned} |\Phi(0, k)|^2 &= Bk^{n-4}, \\ |S(0, k)|^2 &= Ck^m, \end{aligned} \quad (\text{B.48})$$

become

$$\begin{aligned} |\tilde{\Phi}(0, \tilde{k})|^2 &= B(1 - K/\tilde{k}^2)^{(n-3)/2} \tilde{k}^{n-4}, \\ |\tilde{S}(0, \tilde{k})|^2 &= C(1 - K/\tilde{k}^2)^{m/2} \tilde{k}^m. \end{aligned} \quad (\text{B.49})$$

To add to the confusion, adiabatic fluctuations are often expressed in terms of the density power spectrum at present $P(k) = |\Delta_T(\eta_0, k)|^2$. The two conventions are related by the Poisson equation,

$$(k^2 - 3K)\Phi = \frac{3}{2}\Omega_0 H_0^2 (1 + a_{eq}/a) \frac{a_0}{a} \Delta_T. \quad (\text{B.50})$$

To account for the growth between the initial conditions and the present, one notes that at large scales ($k \rightarrow 0$) the growth function is described by pressureless linear theory. From equations (A.8) and (A.9),

$$\Delta_T(\eta_0, k) = \frac{3}{5}(\Omega_0 H_0^2)^{-1} \left[1 + \frac{4}{15}f_\nu\right] \left[1 + \frac{2}{5}f_\nu\right]^{-1} (1 - 3K/k^2) \frac{D}{D_{eq}} \frac{a_{eq}}{a} \Phi(0, k). \quad (\text{B.51})$$

If the neutrino anisotropic stress is neglected, drop the f_ν factors for consistency. Thus for a normalization convention of $P(k) = Ak^n$ at large scales

$$A = \frac{9}{25}(\Omega_0 H_0^2)^{-2} \left[1 + \frac{4}{15}f_\nu\right]^2 \left[1 + \frac{2}{5}f_\nu\right]^{-2} (1 - 3K/k^2)^2 \left(\frac{D}{D_{eq}} \frac{a_{eq}}{a}\right)^2 B. \quad (\text{B.52})$$

Notice that in an open universe, power law conditions for the potential do not imply power law conditions for the density,

$$\begin{aligned} P(k) &\propto (k^2 - 3K)^2 k^{n-4}, \\ \tilde{P}(\tilde{k}) &\propto \tilde{k}^{-1} (\tilde{k}^2 - K)^{-1} (\tilde{k}^2 - 4K)^2 (\tilde{k}^2 - K)^{(n-1)/2}. \end{aligned} \quad (\text{B.53})$$

$\tilde{P}(\tilde{k})$ is the form most often quoted in the literature [175, 82, 134].

The power spectrum may also be expressed in terms of the bulk velocity field. At late times, pressure can be neglected and the total continuity equation (5.6) reduces to

$$\begin{aligned} kV_T &= -\dot{\Delta}_T \\ &= -\frac{\dot{a}}{a} \frac{d \ln D}{d \ln a} \Delta_T, \end{aligned} \quad (\text{B.54})$$

and in particular

$$kV_T(\eta_0, k) = -H_0 \left. \frac{d \ln D}{d \ln a} \right|_{\eta_0} \Delta_T(\eta_0, k), \quad (\text{B.55})$$

or

$$P_V(k) \equiv |V_T(\eta_0, k)|^2 = H_0^2 \left(\left. \frac{d \ln D}{d \ln a} \right)^2 \right|_{\eta_0} P(k), \quad (\text{B.56})$$

for the velocity power spectrum. Recall from equation (B.27) that $d \ln D / d \ln a \simeq \Omega_0^{0.6}$ in an open universe.

B.4.2 Anisotropies

The anisotropy power spectrum C_ℓ is given by

$$\frac{2\ell + 1}{4\pi} C_\ell = \int \frac{dk}{k} T_\ell^2(k) \times \begin{cases} k^3 |\Phi(0, k)|^2 & \text{adiabatic} \\ k^3 |S(0, k)|^2, & \text{isocurvature} \end{cases} \quad (\text{B.57})$$

where $T_\ell(k)$ is the radiation transfer function from the solution to the Boltzmann equation. Examples are given in §6. The power measured by a given experiment with a window function W_ℓ has an ensemble average value of

$$\left(\frac{\Delta T}{T} \right)_{rms}^2 = \frac{1}{4\pi} \sum_\ell (2\ell + 1) C_\ell W_\ell. \quad (\text{B.58})$$

Only if the whole sky is measured at high signal to noise does the variance follow the ‘‘cosmic variance’’ prediction of a χ^2 with $2\ell + 1$ degrees of freedom. Real experiments make noisy measurements of a fraction of the sky and therefore require a more detailed statistical

Experiment	ℓ_0	ℓ_1	ℓ_2	$Q_{\text{flat}}(\mu\text{K})$	Ref.
COBE	–	–	18	19.9 ± 1.6	[62]
FIRS	–	–	30	19 ± 5	[57]
Ten.	20	13	30	26 ± 6	[70]
SP94	67	32	110	26 ± 6	[68]
SK	69	42	100	29 ± 6	[119]
Pyth.	73	50	107	37 ± 12	[49]
ARGO	107	53	180	25 ± 6	[43]
IAB	125	60	205	61 ± 27	[131]
MAX-2 (γ UMi)	158	78	263	74 ± 31	[2]
MAX-3 (γ UMi)	158	78	263	50 ± 11	[67]
MAX-4 (γ UMi)	158	78	263	48 ± 11	[44]
MAX-3 (μ Peg)	158	78	263	19 ± 8	[117]
MAX-4 (σ Her)	158	78	263	39 ± 8	[32]
MAX-4 (ι Dra)	158	78	263	39 ± 11	[32]
MSAM2	143	69	234	40 ± 14	[30]
MSAM3	249	152	362	39 ± 12	[30]

Table B.3: Anisotropy Data Points

A compilation of anisotropy measurements from [146]. The experimental window function peaks at ℓ_0 and falls to half power at ℓ_1 and ℓ_2 . Points are plotted in Fig. 1.3.

treatment. To employ likelihood techniques, we must assume some underlying power spectrum. In order to divorce the measurement from theoretical prejudice, experimental results are usually quoted with a model independent choice. The two most common conventions are the gaussian autocorrelation function $C_{\text{gacf}}(\theta) = C_0 \exp(-\theta^2/2\theta_c^2)$ and the “flat” power spectrum motivated by the Sachs-Wolfe tail of adiabatic models (see *e.g.* [174]),

$$\begin{aligned}
 C_{\ell\text{gacf}} &= 2\pi C_0 \theta_c^2 \exp[-\ell(\ell+1)\theta_c^2/2], \\
 C_{\ell\text{flat}} &= \frac{24\pi}{5} \left(\frac{Q_{\text{flat}}}{T_0} \right)^2 [\ell(\ell+1)]^{-1}.
 \end{aligned}
 \tag{B.59}$$

The two power estimates are thus related by

$$Q_{\text{flat}}^2 \frac{6}{5} \sum_{\ell} \frac{2\ell+1}{\ell(\ell+1)} W_{\ell} = C_0 \theta_c^2 \frac{1}{2} \sum_{\ell} (2\ell+1) \exp[-\ell(\ell+1)\theta_c^2/2] W_{\ell}.
 \tag{B.60}$$

The current status of measurements is summarized in Tab. B.3 [146].

B.4.3 Large Scale Structure

Large scale structure measurements probe a smaller scale and have yet another set of normalization conventions based on the two point correlation function of astrophysical objects

$$\xi_{ab}(\mathbf{x}) = \langle \delta\rho_a(\mathbf{x}' + \mathbf{x})\delta\rho_b(\mathbf{x}')/\bar{\rho}_a\bar{\rho}_b \rangle. \quad (\text{B.61})$$

If all objects are clustered similarly, then all $\xi_{aa} = \xi$ and the two-point correlation function is related to the underlying power spectrum by

$$\begin{aligned} \xi(r) &= \frac{V}{2\pi^2} \int \frac{dk}{k} k^3 P(k) X_\nu^0(\sqrt{-K}r) \\ &\simeq \frac{V}{2\pi^2} \int \frac{dk}{k} k^3 P(k) \frac{\sin(kr)}{kr}, \end{aligned} \quad (\text{B.62})$$

where the approximation assumes that scales of interest are well below the curvature scale. The normalization of the power spectrum is often quoted by the N th moment of the correlation function $J_N(r) = \int_0^r \xi(x)x^{(N-1)}dx$ which implies

$$J_3(r) = \frac{V}{2\pi^2} \int \frac{dk}{k} P(k)(kr)^2 j_1(kr). \quad (\text{B.63})$$

For reference, $j_1(x) = x^{-2}\sin x - x^{-1}\cos x$. Another normalization convention involves the rms density fluctuation in spheres of constant radii

$$\sigma^2(r) = \frac{V}{2\pi^2} \int \frac{dk}{k} k^3 P(k) \left(\frac{3j_1(kr)}{kr} \right)^2. \quad (\text{B.64})$$

The observed galaxy distribution implies that

$$J_3(10h^{-1}\text{Mpc}) \simeq 270h^{-3}\text{Mpc}^3 \quad (\text{B.65})$$

$$\sigma_8 \equiv \sigma(8h^{-1}\text{Mpc}) = \begin{cases} 1.1 \pm 0.15 & \text{optical [109]} \\ 0.69 \pm 0.04 & \text{IRAS [55]} \end{cases} \quad (\text{B.66})$$

The discrepancy between estimates of the normalization obtained by different populations of objects implies that they may all be biased tracers of the underlying mass. The simplest model for bias assumes $\xi_{aa} = b_a^2\xi$ with constant b . Peacock & Dodds [122] find that the best fit to the Abell cluster (A), radio galaxy (R), optical galaxy (O), and IRAS galaxy (I) data sets yields $b_A : b_R : b_O : b_I = 4.5 : 1.9 : 1.3 : 1$.

B.5 Symbol Index

Symbol	Definition	Equation
Γ_i	Entropy fluctuation in i	(4.37)
Δ_i	T gauge density fluctuation in i	(4.89)
Λ	Cosmological constant, $3H_0^2\Omega_\Lambda$	(4.62)
Θ	N Gauge CMB $\Delta T/T$	(2.25)
Θ_ℓ	CMB ℓ th multipole	(4.53)
$\Theta_{2.7}$	$T_0/2.7\text{K}$	(3.16)
$ \Theta + \Psi _{rms}$	CMB rms fluctuation	(6.3)
Π_i	Anisotropic stress in i	(4.30)
Ψ	Newtonian potential	(2.5)
Φ	Space curvature perturbation	(2.5)
Ω_i	Fraction of critical density in i	(4.62)
γ_i	Photon direction cosines	(2.10)
γ_{ij}	Comoving three metric	(2.3)
δ_i^G	G gauge density fluctuation in i	(4.71)
η	Conformal time	(B.9)
μ	Dimensionless chemical potential	(3.33)
ν	Dimensionless eigenmode index	(4.10)
ρ_{crit}	Critical density $3H_0^2/8\pi G$	(B.3)
ρ_i	Energy density in i	(4.30)
σ_T	Thomson cross section	(2.43)
τ	Thomson optical depth	(2.42)
τ_K	Comptonization optical depth $4y$	(3.28)
τ_{abs}	Thermalization optical depth	(3.49)

χ	Curvature normalized radial coordinate	(2.4)
\mathcal{D}	Diffusion damping factor	(6.29)
\mathcal{G}	Drag growth factor	(5.69)
A	Final matter power spectrum norm.	(6.12)
A^G	Time-time G gauge metric fluctuation	(4.67)
B	Initial power spectrum norm.	(6.12)
B^G	Time-space G gauge metric fluctuation	(4.67)
C_ℓ	Anisotropy power spectrum	(6.2)
D	Pressureless growth factor	(5.18)
F	Gravitational driving force	(5.44)
G	Gravitational constant	(4.60)
H	Hubble parameter	(4.62)
H_L^G	Diagonal space-space G gauge metric pert.	(4.67)
H_T^G	Traceless space-space G gauge metric pert.	(4.67)
N_ℓ	Neutrino ℓ th multipole	(4.54)
K	Curvature	(2.3)
K_ℓ	$1 - (\ell^2 - 1)K/k^2$	(4.11)
Q	General Laplacian eigenfunction	(4.1)
R	Baryon-photon norm. scale factor $3\rho_b/4\rho_\gamma$	(4.58)
S	Matter-radiation entropy fluctuation	(4.51)
T_ℓ	Radiation transfer function	(6.4)
T	CMB temperature	(2.62)
T_e	Electron temperature	(2.31)
U_A	Adiabatic mode growth function	(5.11)
U_I	Isocurvature mode growth function	(5.11)
V_i	N/T gauge velocity in i	(4.30)
X_ν^ℓ	Radial eigenfunction	(4.10)
a	Scale factor	(2.3)
c_i	Sound speed in i	(4.37)

c_s	Photon-baryon fluid sound speed	(5.43)
f	Photon distribution function	(2.2)
h	Dimensionless Hubble constant	(B.2)
k	Laplacian eigenvalue and wavenumber	(4.1)
\tilde{k}	Eigenmode number $\nu\sqrt{-K}$	(4.3)
k_D	Diffusion damping wavenumber	(A.55)
k_{eq}	Equality horizon wavenumber	(5.9)
ℓ	Multipole number	(4.53)
ℓ_A	Acoustic angular scale	(B.40)
ℓ_D	Damping angular scale	(B.45)
ℓ_p	p th acoustic peak scale	(B.40)
m	Isocurvature spectral index	(6.4)
n	Adiabatic spectral index	(6.4)
n_i	Number density in i	(4.39)
p	Photon frequency/momentum	(2.7)
p_i	Pressure in i	(4.30)
r_θ	Conf. angular diameter distance	(6.16)
r_s	Sound horizon	(5.46)
x_e	Electron ionization fraction	(2.31)
x_p	Dimensionless frequency p/T_e	(3.1)
v_i	Real space velocity in i	(2.31)
v_i^G	G gauge velocity in i	(4.71)
w_i	Equation of state for i , p_i/ρ_i	(4.32)
y	Compton- y parameter	(3.32)
z	Redshift	(2.3)
z_h	Early energy injection redshift	(3.64)
z_i	Ionization redshift	(5.70)

Table B.4: Commonly Used Symbols

T = total matter gauge, N = Newtonian gauge, G = arbitrary gauge, $i = \gamma, b, e, \nu, c, m, r, T$ for photons, baryons, electrons, neutrinos, cold collisionless matter, non-relativistic matter, radiation, and total energy density. Other redshifts of interest are listed in Tab. B.2

Bibliography

- [1] Allen, B. & Koranda, S. PRD **50**, 3713 (1994)
- [2] Alsop, D.C. *et al.* ApJ **395**, 317 (1992)
- [3] Abbott, L.F. & Schaefer, R.K. ApJ **308**, 546 (1986)
- [4] Abbott, L.F. & Wise, M.B. Nucl. Phys. **B244**, 541 (1984)
- [5] Bardeen, J.M. PRD **22**, 1882 (1980)
- [6] Bardeen, J.M., Bond, J.R., Kaiser, N. & Szalay, A.S. ApJ **304**, 15 (1986)
- [7] Bartlett, J.G. & Silk, J. ApJ **423**, 12 (1994)
- [8] Bartlett, J.G. and Stebbins, A. ApJ **371**, 8 (1991)
- [9] Bennett, C.L. *et al.* ApJ **396**, L7 (1992)
- [10] Bennett, C.L. *et al.* ApJ **436**, 432 (1994)
- [11] Bernstein, J., *Relativistic Kinetic Theory*, (Cambridge University, 1988).
- [12] Bernstein, J. & Dodelson, S. PRD **41**, 354 (1990).
- [13] Birkinshaw, M. & Hughes, J.P. ApJ **420**, 331 (1994)
- [14] Blanchard, A. & Scheider A&A **184**, 1 (1987)
- [15] Bond, J.R. in *The Early Universe*, (eds Unruh, W.G. and Semenov, G.W.) (Reidel, Dordrecht, 1988) p. 283
- [16] Bond, J.R. & Efstathiou, G. ApJL **285**, L45 (1984)

- [17] Bond, J.R. & Efstathiou, G. MNRAS **227**, 655 (1987)
- [18] Bond, J.R. *et al.* PRL **72**, 13 (1994)
- [19] Brandt, C.L. *et al.* ApJ **424**, 1 (1994)
- [20] Bucher, M., Goldhaber, A.S., & Turok hep-ph/9411206
- [21] Bunn, E. *Statistical Analysis of Cosmic Microwave Background Anisotropies*, UCB thesis (1995)
- [22] Bunn, E., Scott, D. & White, M. ApJL **441**, L9 (1995)
- [23] Bunn, E., & Sugiyama, N. ApJ **446**, 49 (1995)
- [24] Burigana, C., Danese, L. & De Zotti, G., A&A **246**, 49 (1991)
- [25] Burigana, C., Danese, L. & De Zotti, G., ApJ **379**, 1 (1991)
- [26] Carroll, S.M., Press, W.H. & Turner, E.L. ARA&A **30**, 499 (1992)
- [27] Ceballos, M.T. & Barcons, X. MNRAS **271**, 817 (1994)
- [28] Cen, R., Ostriker, J.P. & Peebles, P.J.E. ApJ **415**, 423 (1993)
- [29] Chan, K.L. & Jones, B.J.T. ApJ **195**, 1 (1975)
- [30] Cheng, E.S. *et al.* ApJL **422**, L37 (1994)
- [31] Chiba, T., Sugiyama, N. & Suto, Y. ApJ **429**, 427 (1994)
- [32] Clapp, A.C. *et al.* ApJL **433**, L57 (1994)
- [33] Colafrancesco, S., Mazzotta, P., Rephaeli, Y. & Vittorio, N. ApJ **433**, 454 (1994)
- [34] Cole, S. & Efstathiou, E. MNRAS **239**, 195 (1989)
- [35] Coulson, D., Crittenden, R.G., & Turok, N. PRL **73**, 2390 (1994)
- [36] Crittenden, R.G., Coulson, D. & Turok, N. PRD **52** R5402 (1995)
- [37] Crittenden, R. *et al.* PRL **71**, 324 (1994)
- [38] Daly, R.A. ApJ **371**, 14 (1991)

- [39] Danese, L. & De Zotti, G. Riv. Nuovo Cimento **7**, 277 (1977)
- [40] Danese, L. & De Zotti, G. A&A **84**, 364 (1980)
- [41] Danese, L. & De Zotti, G. A&A **107**, 39 (1982)
- [42] Davis, M., Summers, F.J. & Schlegel, D. Nature **359**, 393 (1992)
- [43] de Bernardis, P. *et al.* ApJL **422**, L33 (1994)
- [44] Devlin, M. *et al.* ApJL **430**, L1 (1994)
- [45] Dodelson, S. & Jubas, J.M. PRL **70**, 2224 (1993)
- [46] Dodelson, S. & Jubas, J.M. ApJ **439**, 503 (1995)
- [47] Dodelson, S., Knox, L. & Kolb, E.W. PRD **72**, 3444 (1994)
- [48] Doroshkevich, A.G., Zel'dovich, Ya.B., & Sunyaev, R.A. Sov. Astron **22**, 523 (1978)
- [49] Dragovan, M. *et al.* ApJL **427**, 67 (1993)
- [50] Efstathiou, G. *Large Scale Motions in the Universe: A Vatican Study Week*, eds. Rubin, V.C. and Coyne, G.V., (Princeton University, Princeton, 1988) pg. 299
- [51] Efstathiou, E. & Bond, J.R. MNRAS **227**, 33p (1987)
- [52] Efstathiou, G., Bond, J.R. & White, S.D.M. MNRAS **258**, P1 (1992)
- [53] Ellis, J. *et al.*, Nuc. Phys. B **373**, 399 (1992)
- [54] Fabbri, R. & Pollock, M. Ap. Phys. Lett. **B125**, 445 (1983)
- [55] Fisher, K.B., Davis, M., Strauss, M., Yahil, A. & Huchra, J. MNRAS **266**, 50 (1994)
- [56] Freedman, W.L., *et al.* Nature **371**, 27 (1994)
- [57] Ganga, K., Page, L., Cheng, E. & Meyer, S. ApJL **432**, L15 (1994)
- [58] Gnedin, N.Y. & Ostriker, J.P. ApJ **400**, 1 (1992)
- [59] Gnedin, N.Y., Ostriker, J.P., & Rees, M.J. ApJ **438**, 40 (1995)
- [60] Goldman, S.P. Phys. Rev. A **40**, 1185 (1989)

- [61] Gorski, K.M., Stompor, R. & Juskiwicz, R. ApJL **410** L1 (1993)
- [62] Gorski, K.M. *et al.* ApJL **430**, L89 (1994)
- [63] Gouda, N., Sasaki, M., Suto, Y., ApJ **341**, 557 (1989)
- [64] Gouda, N., Sugiyama, N., & Sasaki, M. Prog. Theor. Phys. **85**, 1023 (1991)
- [65] Graham, A.C. *Chuang-tzu: The Inner Chapters* (Mandala, London 1989)
- [66] Gregory, P.C., & Condon, J.J. ApJS **75**, 1011 (1991)
- [67] Gundersen, J.O. *et al.* ApJL **413**, L1 (1993)
- [68] Gundersen, J.O. *et al.* ApJL **443**, L57 (1994)
- [69] Gunn, J.E. & Peterson, B.A. ApJL **318**, L11 (1965)
- [70] Hancock, S. *et al.* Nature **367**, 333 (1994)
- [71] Harrison, E.L. Rev. Mod. Phys. **39**, 862 (1967)
- [72] Holtzman, J.A. ApJS **71**, 1 (1989)
- [73] Hu, W, in *CWRU CMB Workshop: 2 Years after COBE*, eds. L. Krauss & P. Kernan, (World Scientific, Singapore 1994) p. 188
- [74] Hu, W., Bunn, E., & Sugiyama, N. ApJL **447**, L59 (1995)
- [75] Hu, W., Scott, D. & Silk, J. PRD **49**, 648 (1994)
- [76] Hu, W., Scott, D. & Silk, J. ApJL **430**, L5 (1994)
- [77] Hu, W., Scott, D., Sugiyama, N. & White, M. PRD **52** 5498 (1995)
- [78] Hu, W. & Silk, J. PRL **70**, 2661 (1993)
- [79] Hu, W. & Silk, J. PRD **48**, 485 (1994)
- [80] Hu, W. & Sugiyama, N. PRD **50**, 627 (1994)
- [81] Hu, W. & Sugiyama, N. ApJ **436**, 456 (1994)
- [82] Hu, W. & Sugiyama, N. ApJ **444**, 489 (1995)

- [83] Hu, W. & Sugiyama, N. PRD **51**, 2599 (1995)
- [84] Hu, W. & Sugiyama, N. ApJ **471**, 542 (1996)
- [85] Hu, W., Sugiyama, N., & Silk, J. Nature **386** 37 (1997)
- [86] Hu, W. & White, M. A&A **315**, 33 (1996)
- [87] Illarionov, A.F. & Sunyaev, R.A. Sov. Astron. **18**, 413 (1975)
- [88] Illarionov, A.F. & Sunyaev, R.A. Sov. Astron. **18**, 691 (1975)
- [89] Jacoby, G.H. *et al.* PASP **104**, 599 (1992)
- [90] Jones, M, *et al.* Nature **365**, 320 (1993)
- [91] Jones, B.J.T. & Wyse, R.F.G. A&A **149**, 144 (1985)
- [92] Jørgensen, H.E., Kotok, E., Naselsky, P., & Novikov, I. A&A **294**, 639 (1995)
- [93] Kaiser, N. MNRAS **202**, 1169 (1983)
- [94] Kaiser, N. ApJ **282**, 374 (1984)
- [95] Kamionkowski, M. & Spergel, D.N. ApJ **432**, 7 (1994)
- [96] Kamionkowski, M., Spergel, D.N., & Sugiyama, N. ApJL **434**, L1 (1994)
- [97] Klypin, A., Holtzmann, J., Primack, J. & Regos, E. ApJ **416**, 1 (1993)
- [98] Kofman, L.A. & Starobinskii, A.A. Sov. Astron. Lett. **9**, 643 (1985)
- [99] Kodama, H. & Sasaki, M. Prog. Theor. Phys. Supp. **78**, 1 (1984)
- [100] Kodama, H. & Sasaki, M. Int. J. Mod. Phys. **A1**, 265 (1986)
- [101] Kodama, H. & Sasaki, M. Int. J. Mod. Phys. **A2**, 491 (1987)
- [102] Kompaneets, A.S. Sov. Phys.-JETP **4**, 730 (1957)
- [103] Kosowsky, A. Ann. Phys. **246**, 49 (1996)
- [104] Krauss, L.M. and Kernan, P., ed. *CMB Anisotropies Two Years After COBE*, (World Scientific, Singapore 1994)

- [105] Larson, E.W. *et al.* J. Comput. Phys. **61**, 359 (1985)
- [106] Lifshitz, E.M. & Khalatnikov, I.M. Adv. Phys. **12**, 185 (1963)
- [107] Lightman, A.P. ApJ **244**, 392 (1981)
- [108] Linder, V.E. MNRAS **243**, 362 (1990)
- [109] Loveday, J., Peterson, B.A., Efstathiou, G. & Maddox, S.J. ApJ **390**, 338 (1992)
- [110] Lyth, D.H. & Stewart, E.D. Phys. Lett. B **252**, 336 (1990)
- [111] Lyth, D.H. & Woszczyna, A. PRD **52**, 3338 (1995)
- [112] Makino, N. & Suto, Y. ApJ **405**, 1 (1993)
- [113] Mandl, F. & Shaw, G., *Quantum Field Theory* (Wiley, New York, 1984) pg. 157
- [114] Markevitch, M, Blumenthal, G.R., Forman, W., Jones, C. & Sunyaev, R.A. ApJ **378**, L33 (1991)
- [115] Martinez-Gonzalez, E., Sanz, J.L. & Silk, J. PRD **46**, 4193
- [116] Mather, J.C. *et al.* ApJL **420**, 439 (1994)
- [117] Meinhold, P.R. ApJL **409**, L1 (1993)
- [118] Mukhanov, V.F., Feldman, H.A., & Brandenberger, R.H. Phys. Rep. **215**, 203 (1992)
- [119] Netterfield, C.B., Jarosik, N.C., Page, L.A., Wilkinson, D., & Wollack, E. ApJL **445**, L69 (1995)
- [120] Ostriker, J.P. ARA&A **31**, 689 (1993)
- [121] Ostriker, J.P. & Vishniac, E.T. ApJ **306**, 51 (1986)
- [122] Peacock, J.A. & Dodds, S.J. MNRAS **267**, 1020 (1994)
- [123] Peebles, P.J.E. ApJ **153**, 1 (1968)
- [124] Peebles, P.J.E. *Large Scale Structure of the Universe*, (Princeton University, Princeton 1980)

- [125] Peebles, P.J.E. ApJL **315**, L73 (1987)
- [126] Peebles, P.J.E. Nature **327**, 210 (1987)
- [127] Peebles, P.J.E. & Yu, J.T. ApJ **162**, 815 (1970)
- [128] Penzias, A.A. & Wilson, R.W. ApJ **142**, 419 (1965)
- [129] Pequignot, D., Petitjean, P. & Boisson, C. A&A **251**, 690 (1991)
- [130] Peyraud, J. J. Physics **29**, 88 (1968)
- [131] Piccirillo, L. & Calisse, P. ApJ **411**, 529 (1993)
- [132] Polnarev, A.G. Sov. Astron. **29**, 607 (1985)
- [133] Press, W. & Vishniac, E.T. ApJ **239**, 1 (1980)
- [134] Ratra, B. & Peebles, P.J.E. ApJL **432**, L5 (1994)
- [135] Rees, M.J. ApJL **153**, L1 (1968)
- [136] Rees, M.J. & Sciama, D.N. Nature **519**, 611 (1968)
- [137] Ressel, M. & Turner, M. Comm. Astrophys. **14**, 323 (1990)
- [138] Sachs, R.K. & Wolfe, A.M. ApJ **147**, 73 (1967)
- [139] Saha, A., *et al.* ApJ **438**, 8 (1995)
- [140] Sandage, A.R. AJ **106** 719 (1993)
- [141] Shi, X., Schramm, D.N., Dearborn, D.S.P. & Truran, J.W. Comm. Astrophys. **17**, 343 (1995)
- [142] Sarkar, S. & Cooper, A.M. Phys. Lett. B **148**, 347 (1983)
- [143] Sasaki, M. MNRAS **240**, 415 (1989)
- [144] Schneider, D.P., Schmidt, M. & Gunn, J.E. AJ **98**, 1951 (1989)
- [145] Schuster, J. *et al.* ApJL **419**, L47 (1993)
- [146] Scott, D., Silk, J. & White, M. Science **268**, 829 (1995)

- [147] Seljak, U. *ApJL* **435**, L87 (1994)
- [148] Seljak, U. *ApJL* **463**, L1 (1996)
- [149] Seljak, U. *ApJ* **460**, 549 (1996)
- [150] Silk, J. *ApJ* **151**, 459 (1968)
- [151] Smith, M.S., Kawano, L.H., & Malaney, R.A. *ApJ* **85**, 219 (1993)
- [152] Smoot, G., *et al.* *ApJL* **371**, L1 (1991)
- [153] Smoot, G., *et al.* *ApJL* **396**, L1 (1992)
- [154] Starobinskii, A.A. *JETP Lett.* **30**, 682 (1979)
- [155] Starobinskii, A.A. *Sov. Astron. Lett.* **11**, 113 (1985)
- [156] Strauss, M.A. & Willick, J.A. *Phys. Rep.* **261**, 271 (1995)
- [157] Sugihara, T. & Suto, Y., *ApJ* **387**, 431 (1992)
- [158] Sugiyama, N. & Gouda, N., *Prog. Theor. Phys.* **88**, 803 (1992)
- [159] Sugiyama, N. & Silk, J. *PRL* **73**, 509 (1994)
- [160] Sugiyama, N., Silk, J. & Vittorio, N. *ApJL* **419**, L1 (1993)
- [161] Sunyaev, R.A. & Zel'dovich, Ya.B. *Comments Ap. Space Phys.* **4**, 79 (1972)
- [162] Sunyaev, R.A. & Zel'dovich, Ya.B. *Ap. Space Sci.* **7**, 3 (1970)
- [163] Sunyaev, R.A. & Zel'dovich, Ya.B. *Ap. Space Sci.* **9**, 368 (1970)
- [164] Tegmark, M., Bunn, E. & Hu, W. *ApJ* **434**, 1 (1994)
- [165] Tegmark, M. & Silk, J. *ApJ* **423**, 529 (1994); errata **423**, 529 (1994)
- [166] Tomita, K. & Watanabe, K. *Prog. Theor. Phys.* **82**, 563
- [167] Tuluie, R. & Laguna, P. *ApJL* **445**, L73 (1995)
- [168] Turner, M.S., White, M., & Lidsey, J.E. *PRD* **48**, 4613 (1993)

- [169] Vishniac, E.T. ApJ **322**, 597 (1987)
- [170] Vittorio, N. & Silk, J. ApJL **285**, L39 (1984)
- [171] Walker, T.P., Steigman, G., Schramm, D.N., Olive, K.A., & Kang, H.-S. ApJ **376**, 51 (1991)
- [172] Webb, J.K., Barcons, X., Carswel, R.F., & Parnell, H.C. MNRAS **244**, 319 (1992)
- [173] Weinberg, S. *Gravitation and Cosmology*, (Wiley, New York, 1972)
- [174] White, M., Scott, D., & Silk, J. ARA&A **32**, 319 (1994)
- [175] Wilson, M.L. ApJ **273**, 2 (1983)
- [176] Wilson, M. & Silk, J. ApJ **243**, 14 (1981)
- [177] Weymann, R. ApJ **145**, 560 (1966)
- [178] Wilkinson, D. in *Proceedings of the 9th Lake Louise Winter Institute*, ed. A. Astbury *et al.* (World Scientific, Singapore, 1995)
- [179] Wright, E., *et al.* ApJ **420**, 450 (1994)
- [180] Yamamoto, K., Sasaki, M., & Tanaka, T. ApJ **455**, 412 (1995)
- [181] Zdziarski, A.A. ApJ **335**, 768 (1988)
- [182] Zel'dovich, Ya. B., Illarionov, A.F. & Sunyaev, R.A. Sov. Phys.-JETP **33**, 643 (1972)
- [183] Zel'dovich, Ya. B., Kurt, V.G., & Sunyaev, R.A. Sov. Phys.-JETP **28**, 146 (1969)
- [184] Zel'dovich, Ya. B. & Levich, E.V. Sov. Phys.-JETP Lett. **11**, 35 (1970)
- [185] Zel'dovich, Ya. B. & Sunyaev, R.A. Ap. Space Sci. **4**, 301 (1969)